Metastable Phosphates of 3d Metals

Illuminating Fundamental Crystallization and Nucleation Processes

Dissertation

zur Erlangung des Grades
„Doktor der Naturwissenschaften“
im Promotionsfach Chemie

am Fachbereich Chemie, Pharmazie und Geowissenschaften
der Johannes Gutenberg-Universität Mainz

Sven Bach

geb. in Wiesbaden

Mainz, 2015

Dekan: [redacted]

Erster Berichterstatter: [redacted]

Zweiter Berichterstatter: [redacted]

Tag der mündlichen Prüfung: 21.12.2015

Erklärung

Hiermit erkläre ich,

dass die vorliegende Arbeit in der Zeit von Januar 2013 bis November 2015 unter der Leitung von [redacted] am Institut für Anorganische Chemie und Analytische Chemie der Johannes Gutenberg-Universität Mainz angefertigt wurde.

Ich versichere, das Manuskript selbständig verfasst zu haben und keine weiteren als die von mir angegebenen Quellen verwendet zu haben.

Mainz, den 25.11.2015

ABSTRACT

The present work studies the formation of metastable intermediates of 3d metal phosphate hydrates during precipitation and under influence of mechanical stress. It was the goal of this manuscript to obtain a better understanding of the underlying mechanisms including non-equilibrium phases, which are still subject of controversial discussions.

The first part of the thesis deals with the early stages of the precipitation of 3d metal phosphate hydrates. The formation of amorphous precursors followed by dissolution and recrystallization ending up with the respective crystalline modifications was observed for the iron, cobalt, nickel, copper, and zinc phosphate hydrate systems. The amorphous nanoparticles were determined to be 5–30 nm in size and revealed a lower content of structural water than their crystalline counterparts. The amorphous solids were stabilized kinetically in the absence of water. Simulations of CREDOR NMR spectra displayed a rather stiff hydrogen-bounded network to be responsible for this behavior. This fact was utilized to inhibit crystallization even in the presence of water by encapsulation the amorphous nanoparticles by a silica shell. Next, the synthesized compounds were characterized comprehensively in terms of composition, recrystallization kinetics (*in situ* IR spectroscopy), and short-range order (EXAFS and XANES).

Furthermore, the role of water as active reaction partner during nucleation and crystal growth was investigated by precipitation in anhydrous solvents. The anhydrous amorphous phosphates adsorb water provided by humidity according to a Langmuir mechanism, which was determined *in situ*. Further, application of a highly concentrated HPO_4^{2-} solution resulted in the dissolution of crystalline phosphate hydrates that involved the formation of a macroscopic dense liquid. First results of SS-NMR measurements displayed a hydrogen-bonded network and suggested the formation of metal hydrogen phosphate complexes. In addition, prenucleation clusters of the copper phosphate system were detected prior to the formation of an amorphous solid in solution with a constant-pH titration setup and an ion-sensitive electrode. The clusters were formed upon undercritically concentrated solution and densified towards nanoscopic liquid-condensed phases (LCP) during titration. 3d metal phosphate hydrates represent well-suited model systems for the investigation of nucleation and crystal growth in a more complex way because the reversible hydration of the metal ions allows multistage crystallization processes with different hydrated intermediates, which can be isolated.

The second part of the present thesis addresses the mechanochemical amorphization of thermodynamically stable phosphate hydrates. This unusual solid-state reaction was studied quantitatively by IR spectroscopy and X-ray diffraction *ex situ*. Structural water was expelled during the reaction which results in the loss of crystallinity. The comparison of (i) the treatment of $Co_3(PO_4)_2 \times 8\ H_2O$ in a planetary ball mill with (ii) an *in situ* high-pressure study revealed hydrostatic pressure not to be responsible for amorphization.

In addition, the influence of impurities on the stabilization of amorphized zinc phosphate hydrate was examined according to the different recrystallization behavior of solid bodies synthesized in a stainless steel jar and in a zirconia jar. Impurities of iron (after oxidation to Fe^{2+}- and Fe^{3+}-compounds) inhibited the crystallization in water to the thermodynamically stable crystalline phase, hopeite, effectively. The oxidation state and chemical surrounding of iron in the amorphous zinc phosphate hydrate and its annealing products were determined by ^{57}Fe Mössbauer spectroscopy. Incorporation of Fe in the structure was accompanied by the generation of zinc vacancies. Water which was needed for crystallization of hopeite was bound to iron species at particles' surface due to its higher Pearson hardness. As a result, an effective inhibition of the crystallization of hopeite was achieved. Using the amorphous product, crystalline *α*- and *γ*-$Zn_3(PO_4)_2$ were selectively synthesized by controlling heating conditions.

KURZZUSAMMENFASSUNG

Die vorliegende Arbeit untersucht die Bildung metastabiler Intermediate von Phosphathydraten der 3d-Metalle während Fällung als auch unter der Einwirkung von mechanischer Beanspruchung. Ziel war ein verbessertes Verständnis der zugrundeliegenden Mechanismen, welche zu Nichtgleichgewichtsphasen führen und gegenwärtig sehr kontrovers diskutiert werden.

Im ersten Teil der Arbeit werden die Frühstadien der Fällung von Phosphathydraten der 3d-Metalle untersucht. Die Bildung amorpher Präkursoren der Systeme Eisen-, Cobalt, Nickel-, Kupfer- und Zinkphosphathydrat in wässriger Lösung wurde beobachtet, welche sich durch Auflösung und Rekristallisation zu den jeweiligen kristallinen Modifikationen umwandelten. Die amorphen Nanopartikel waren 5–30 nm groß und wiesen eine verminderte Menge an strukturellem Wasser auf im Vergleich zu ihren kristallinen Pendants. In Abwesenheit von Feuchtigkeit waren die amorphen Festkörper über lange Zeiträume kinetisch stabilisiert. Simulation von CREDOR-NMR-Spektren zeigte als Begründung ein recht starres Wasserstoffbrückennetzwerk auf. Diese Tatsache wurde ausgenutzt, um durch Ummantelung mit einer Silikahülle die amorphen Festkörper auch in wässriger Lösung gegen Kristallisation zu stabilisieren. Weiterhin wurden die hergestellten Verbindungen umfassend charakterisiert bezüglich ihrer Zusammensetzung, ihres Rekristallisationsverhaltens (*in situ*-IR-Spektroskopie) und der vorliegenden Nahumgebung (EXAFS und XANES).

Des Weiteren wurde die Rolle von Wasser als aktiver Reaktionspartner während Keimbildung und Kristallwachstum untersucht, indem die Fällungsreaktionen in wasserfreien Lösungsmitteln durchgeführt wurden. Die wasserfreien amorphen Phosphathydrate adsorbierten Wasser aus der Atmosphäre nach einem Langmuir-Mechanismus, was *in situ* verfolgt wurde. Weiterhin wurden die kristallinen Phosphathydrate in hochkonzentrierter HPO_4^{2-}-Lösung unter der Bildung einer makroskopischen dichten Flüssigkeit gelöst. Erste Ergebnisse der SS-NMR-Messungen zeigten ein Wasserstoffbrückennetzwerk auf und legten das Vorhandensein von Metallhydrogenphoshatkomplexen nahe. Zusätzlich wurden Pränukleationscluster für das System Kupferphosphat vor der Bildung eines amorphen Festkörpers mit einem Titrationssetup mit ionenselektiver Elektrode detektiert. Die Cluster bildeten sich in unterkritischer Lösung und verdichteten sich im Verlauf der Titration zu nanoskopischen flüssig-kondensierten Phasen (LCP). Phosphathydrate der 3d-Metalle erwiesen sich als sehr gut geeignete Modellsysteme zur Untersuchung von Keimbildung und

Kristallwachstum, da die reversible Hydratation der Metallkationen zu mehrstufigen Kristallisationsprozessen über verschieden stark hydratisierte Intermediate führte, welche isoliert werden konnten.

Der zweite Teil der Arbeit befasst sich mit der mechanochemischen Amorphisierung der thermodynamisch stabilen Phosphathydrate. Diese ungewöhnliche Festphasenumwandlung wurde durch IR-Spektroskopie und Röntgenbeugung *ex situ* quantitativ untersucht. Während der Reaktion wurde strukturelles Wasser aus den Strukturen gepresst, was einen verminderten Grad an Kristallinität bedingte. Durch Vergleich (i) der Behandlung von $Co_3(PO_4)_2 \times 8\ H_2O$ in einer Kugelmühle (ii) mit einem *in situ*-Hochdruckstudie konnte bestätigt werden, dass nicht der vorherrschende Druck Auslöser eines Amorphisierungsprozesses war.

Zusätzlich wurde der Einfluss von Verunreinigungen auf die Stabilität von amorphisiertem Zinkphosphat untersucht, da unterschiedliches Rekristallisationsverhalten beobachtet wurde, je nachdem ob in Mahlbechern aus gehärtetem Stahl oder Zirconiumdioxid amorphisiert wurde. Verunreinigungen von Eisen, welche zu Fe^{2+} und Fe^{3+} oxidiert wurden, zeigten einen enormen inhibierenden Effekt bezüglich der Kristallisation in Wasser zur thermodynamisch stabilen Phase, dem Hopeit. Über ^{57}Fe-Mößbauerspektrosopie konnten die Oxidationsstufe und die chemische Umgebung der Eisenspezies in der amorphisierten Struktur sowie in den auf thermischem Wege kristallisierten Produkten bestimmt werden. Die Aufnahme von Eisen in die Verbindung geht mit der Generierung von Zinkfehlstellen einher. Zusätzliches Wasser, welches zur Kristallisation zum Hopeit in die Struktur eingebaut werden musste, wurde durch die Eisenspezies an der Partikeloberflächen gebunden aufgrund ihrer höheren Pearson-Härte, was zu einem effektiven Inhibieren der Kristallisation führte. Durch Kontrolle der Heizbedingungen konnten die *a*- und die *γ*-Modifikation von wasserfreiem Zinkphosphat selektiv aus der amorphen Substanz kristallisiert werden.

LIST OF PUBLICATIONS

[1] **Bach, S.**; Celinski, V. R.; Dietzsch, M.; Panthöfer, M.; Bienert, R.; Emmerling, F.; Schmedt auf der Günne, J.; Tremel, W., "Thermally Highly Stable Amorphous Zinc Phosphate Intermediates during the Formation of Zinc Phosphate Hydrate", *Journal of the American Chemical Society* **2015**, *136*, 2285–2294.

[2] Gehl, A.; Mondeshki, M.; **Bach, S.**; Häger, T.; Panthöfer, M.; Barton, B.; Kolb, U.; Tremel, W., „Anhydrous Amorphous Calcium Oxalate Nanoparticles from Ionic Liquids: Stable Crystallization Intermediates of the Formation of Whewellite", *Chemistry - A European Journal* **2015**, *21*, accepted.

[3] **Bach, S.**; Panthöfer, M.; Bienert, R.; Guilherme, A.; Emmerling, F.; Tremel, W., "The Role of Water During the Crystallization of Amorphous Cobalt Phosphate Nanoparticles", *submitted.*

[4] **Bach, S.**; Visnow, E.; Panthöfer, M.; Gorelik, T.; Guilherme, A., Gurlo, A.; Kolb, U.; Emmerling, F.; Lind, C.; Tremel, W., "Amorphization of $Co_3(PO_4)_2 \times 8\ H_2O$ under Mechanical Stress", *submitted.*

[5] **Bach, S.**; Shylin, S. I.; Panthöfer, M.; Barton, B.; Dinnebier, R.; Ksenofontov, V.; Kolb, U.; Tremel, W., "Understanding the Recrystallization Behavior of Amorphous Zinc Phosphate Prepared by Mechanochemical Ball-Milling", *in preparation.*

[6] **Bach, S.**; Mondeshki, M.; Tremel, W., "Silica Shells as Tool to Stabilize Amorphous Compounds", *in preparation.*

[7] **Bach, S.**; Tremel, W. "Prenucleation cluster of Copper Phosphate in Undercritical Solution", *in preparation.*

[8] Bach, S.; Emmerling, F.; Tremel, W., "Amorphous Intermediates during the Precipitation of 3d Metal Phosphates", *in preparation.*

[9] **Bach, S.**; Emmerling, F.; Tremel, W., "Synthesis of Anhydrous Amorphous Cobalt Phosphate in Methanol", *in preparation.*

[10] **Bach, S.**; Mondeshki, M.; Roncal-Herrero, T.; Kröger, N.; Tremel, W., "Liquid-Condensed Precursors of Metal Phosphates", *in preparation*.

Acknowledgments

List of Contents

Abstract V

Kurzzusammenfassung VII

List of Publications IX

Acknowledgments XI

List of Contents XIII

List of Figures XVII

List of Tables XXIII

List of Abbreviations and Symbols XXIV

1 Nucleation and Crystal Growth 1

1.1 Nucleation Theories 1

1.2 Crystal Growth Theories 14

2 Motivation 21

3 Amorphous Zinc Phosphate Hydrate: The Role of Coordinating Water 31

3.1 Introduction 31

3.2 Experimental 34

3.3 Results and Discussion 36

3.4 Conclusion 53

4 Amorphous Cobalt Phosphate Hydrate: Short-range ordering 55

4.1 Introduction 55
4.2 Experimental 57
4.3 Results and Discussion 58
4.4 Conclusion 72

5 Amorphous Phosphate Hydrates of Iron, Nickel, and Copper 75

5.1 Introduction 75
5.2 Experimental 78
5.3 Results and Discussion 79
5.4 Conclusion 91

6 Synthesis of Amorphous Cobalt Phosphate under Anhydrous Conditions 93

6.1 Introduction 93
6.2 Experimental 95
6.3 Results and Discussion 97
6.4 Conclusion 104

7 Stabilizing Amorphous Nanoparticles by Silica Shells 105

7.1 Introduction 105
7.2 Experimental 107
7.3 Results and Discussion 108
7.4 Conclusion 116

8 Formation of Liquid-Condensed Phases at High Supersaturation . 117

8.1 Introduction 117
8.2 Experimental 119
8.3 Results and Discussion 121
8.4 Conclusion 129

9 PRENUCLEATION CLUSTERS OF COPPER PHOSPHATE HYDRATE 131

9.1 Introduction 131
9.2 Experimental 133
9.3 Results and Discussion 135
9.4 Conclusion 145

10 AMORPHIZATION OF $Co_3(PO_4)_2 \times 8\ H_2O$ UNDER MECHANICAL STRESS 149

10.1 Introduction 149
10.2 Experimental 152
10.3 Results and Discussion 154
10.4 Conclusion 168

11 RECRYSTALLIZATION OF AMORPHOUS ZINC PHOSPHATE PREPARED BY BALL-MILLING 169

11.1 Introduction 169
11.2 Experimental 172
11.3 Results and Discussion 174
11.4 Conclusion 186

12 CONCLUSION AND OUTLOOK 189

13 SUPPORTING INFORMATION 195

Instrumental Details 195
Additional Declaration 201

14 BIBLIOGRAPHY 203

CURRICULUM VITAE 217

LIST OF FIGURES

Figure 1.1: Free enthalpy contributions of nucleus formation according to CNT. 2
Figure 1.2: Nucleation and crystal growth as described by the LaMer model. 4
Figure 1.3: Enthalpic pathways in the formation of solid nuclei according to CNT and assuming PNC. 6
Figure 1.4: Illustration of 2-step nucleation. 8
Figure 1.5: Free enthalpy pathways for the formation of solid nuclei assuming prior nucleation of a dense liquid. 9
Figure 1.6: Non-equilibrium $CaCO_3$ morphology achieved via a PILP process. 10
Figure 1.7: Illustration of spinodal decomposition. 12
Figure 1.8: Possibilities for a crystal unit to attach on a growing crystal. 15
Figure 1.9: Illustration of spiral growth and island growth in $BaSO_4$ 16
Figure 1.10: Mechanism of classical crystal growth in comparison to one dominated by oriented attachment. 18
Figure 1.11: TEM image of anatase formed by oriented attachment. 18
Figure 1.12: SEM image of a $CaCO_3$ mesocrystal. 19
Figure 2.1: Polyphosphates, cyclophosphates, and ultraphosphates – structural motifs. 22
Figure 3.1: XRD patterns of AZP, hopeite, and their heating products. 37
Figure 3.2: Quantitative analysis of AZP. 38
Figure 3.3: SEM and TEM images of AZP particles. 39
Figure 3.4: SAXS curve of RT-AZP. 39
Figure 3.5: IR spectra of AZP, hopeite, and their heating products. 40
Figure 3.6: Thermogravimetric trace and DTA signal of AZP and hopeite under argon. 43
Figure 3.7: SEM images of α-$Zn_3(PO_4)_2$ and TEM image of HT-ACP. 44
Figure 3.8: XRD patterns of RT-AZP after heating in air at 200, 400, and 600 °C. 45
Figure 3.9: ^{31}P MAS NMR spectrum of AZP a) as-synthesized and b) after 4 weeks exposed to humidity. 45
Figure 3.10: ^{1}H MAS NMR spectrum of (A) RT-AZP before and after heating at 200 °C (B) and 400 °C (C) under argon for one week. 46

Figure 3.11: $^{1}H\{^{31}P\}$ C-REDOR curve of RT-AZP. 47
Figure 3.12: Experimental and simulated $^{31}P\{^{1}H\}$ C-REDOR curves. 48
Figure 3.13: Excerpt from the crystal structure of hopeite. 50
Figure 3.14: Static ^{1}H spin-echo NMR spectrum of RT-AZP. 52
Figure 4.1: XRD patterns of ACP, $Co_3(PO_4)_2 \times 8\ H_2O$, HT-ACP and $Co_3(PO_4)_2$. 59
Figure 4.2: Quantitative analysis of ACP. 60
Figure 4.3: SEM and TEM images of ACP particles. 61
Figure 4.4: Scattering curve of ACP. 61
Figure 4.5: IR spectra of ACP, and $Co_3(PO_4)_2 \times 8\ H_2O$, HT-ACP, and $Co_3(PO_4)_2$. 62
Figure 4.6: Left: Extinctions of the water bands of the IR spectra of different cobalt phosphates and the resulting water content. Right: Thermogravimetric trace and DTA signal of HT-ACP under argon. 63
Figure 4.7: (A) TEM image of HT-ACP under argon. (B) SEM image of $Co_3(PO_4)_2$. 63
Figure 4.8: UV-Vis spectra of RT-ACP, HT-ACP, $Co_3(PO_4)_2 \times 8\ H_2O$, and anhydrous $Co_3(PO_4)_2$. 65
Figure 4.9: a) XANES spectrum of $Co_3(PO_4)_2 \times 8\ H_2O$ and ACP. b) EXAFS profile-amplitude of the Fourier transform. 65
Figure 4.10: Possible pre-peak transitions for $Co_3(PO_4)_2 \times 8\ H_2O$. 66
Figure 4.11: Thermogravimetric and DTA trace of ACP and $Co_3(PO_4)_2 \times 8\ H_2O$. 67
Figure 4.12: XRD patterns of the precipitation products of 10 mM PO_4^{3-} and 15 mM Co^{2+} 5 min after mixing at room temperature and at elevated temperatures. 68
Figure 4.13: a) IR spectra of the precipitation products of 10 mM PO_4^{3-} and 15 mM Co^{2+} 5 min after mixing at at room temperature and at elevated temperatures. b) Analysis of the dependence of the mass fraction crystalline to amorphous on the temperature. 69
Figure 4.14: Standards for quantification: Mixtures of crystalline and amorphous phases of cobalt phosphate hydrate. a) Extinction of the symmetric stretching mode and b) splitting of asymmetric stretching mode. 70
Figure 4.15: Crystallization kinetics of ACP in water. 71

Figure 5.1: XRD patterns and ATR-FTIR spectra of (A) amorphous iron phosphate hydrate, crystallizing to (B) in aqueous solution. (C) is achieved after heating amorphous solid under argon at 800 °C. 80
Figure 5.2: XRD patterns ATR-FTIR spectra of (A) amorphous nickel phosphate hydrate, crystallizing to (B) in aqueous solution. (C) is achieved after heating amorphous solid under argon at 800 °C. 81
Figure 5.3: XRD patterns ATR-FTIR spectra (right) of (A) amorphous copper phosphate hydrate, crystallizing to (B) in aqueous solution. (C) is achieved after heating amorphous solid under argon at 800 °C. 82
Figure 5.4: DTA and TG curves of as-synthesized amorphous phosphate hydrates. 84
Figure 5.5: SEM images of amorphous phosphate hydrates of (A) iron, (B) nickel, and (C) copper as well as of (D) vivianite, (E) arupite, and (F) mixture of libethenite and $Cu_3(PO_4)_2 \times 3\ H_2O$. 87
Figure 5.6: TEM images of amorphous phosphate hydrates of (A) iron, (B) nickel, and (C) copper. 88
Figure 5.7: UV-Vis spectra of amorphous and crystalline iron phosphate hydrate. 89
Figure 5.8: UV-Vis spectra of amorphous and crystalline nickel phosphate hydrate. 89
Figure 5.9: UV-Vis spectra of amorphous and crystalline copper phosphate hydrate.. 90
Figure 6.1: IR spectra of MeOH-ACP, hydr-MeOH-ACP, ACP, and $Co_3(PO_4)_2 \times 8\ H_2O$. ... 97
Figure 6.2: XRD patterns of MeOH-ACP in a capillary and hydr-MeOH-ACP. 98
Figure 6.3: TEM images of MeOH-ACP. 98
Figure 6.4: a) IR measurements of MeOH-ACP in the wet state. b) Evolving of the water vibrations (extinctions) of MeOH-ACP in the wet state together with a Langmuir plot. 99
Figure 6.5: TEM images of hydr-MeOH-ACP. 100
Figure 6.6: Crystallization kinetics of hydr-MeOH-ACP. 101
Figure 6.7: TEM images of $Co_3(PO_4)_2 \times 8\ H_2O$ achieved after crystallization experiment in climate chamber. 101
Figure 6.8: DTA and TGA curves of MeOH-ACP measured in the wet state. 103
Figure 7.1: Synthesis scheme for silica-encapsulated AZP nanoparticles. 108

Figure 7.2: TEM images of AZP@SiO_2 particles. 109
Figure 7.3: ^{31}P MAS NMR spectrum, XRD pattern, and IR spectrum of AZP and AZP@SiO_2 nanoparticles. 109
Figure 7.4: IR spectra of experiments resulting in large quantities of silica. 110
Figure 7.5: TGA and DTA of AZP nanoparticles and AZP@SiO_2 nanoparticles. 111
Figure 7.6: IR spectra of wet AZP and AZP@SiO_2 measured *in situ*. 112
Figure 7.7: Splitting of the asymmetric phosphate stretching mode for mixtures of AZP and hopeite measured by ATR-FTIR spectroscopy. 113
Figure 7.8: a) Quantitative analysis of AZP crystallization kinetics by ATR-FTIR spectroscopy. b) Double-logarithmic plot of crystallization kinetics showing the underlying Avrami mechanism. 113
Figure 7.9: ^{31}P MAS NMR spectrum, XRD pattern, and ATR-FTIR spectrum of AZP@SiO_2 nanoparticles after incubation in water for one week. 114
Figure 7.10: Scheme how silica shell may prohibit further uptake of water which is needed to crystallize hopeite. 115
Figure 8.1: IR spectra of the ternary system K_2HPO_4, H_2O, EtOH. 121
Figure 8.2: Synthesis of LCP in the two-phase system water +K_2HPO_4/ethanol. 122
Figure 8.3: ^{31}P MAS NMR spectra of highly concentrated K_2HPO_4 solution and of liquid-condensed phases of zinc phosphate. 124
Figure 8.4: Viscosity of LCP in dependence of the amount of added Zn solution. 126
Figure 8.5: Results of liquid-TEM measurements for Co-LCP. 127
Figure 8.6: Dissolving experiments using highly-concentrated K2HPO4 solution and a NaOH solution (pH=9). 127
Figure 8.7: Formation and liquefaction of a Co-LCP gel. 128
Figure 9.1: Titration of Cu^{2+} in 1 mM phosphate buffer at different constant pH-values. 136
Figure 9.2: TEM images at the three distinguished stages during titration. 137
Figure 9.3: XRD pattern and IR spectrum of species isolated from the third stage of the titration experiment. 138
Figure 9.4: Distribution of the different phosphate species as a function of pH value. 140

Figure 9.5: Number of OH^- equivalents ω_{OH} necessary to keep the pH constant when one PO_4^{3-} is removed from equilibrium due to cluster formation. 141
Figure 9.6: Amount of phosphate and copper bound due to cluster formation during constant pH titration. 142
Figure 9.7: Amount of free calcium ions in 10 mM phosphate buffer (red) and 1 mM oxalate (blue) at pH=8.0, respectively. 143
Figure 10.1: XRD patterns of mech-ACP synthesized by 260 min ball milling and $Co_3(PO_4)_2 \times 8\ H_2O$. 154
Figure 10.2: 11-BM XRD data of $Co_3(PO_4)_2 \times 8\ H_2O$ after different milling durations. 155
Figure 10.3: IR spectra of $Co_3(PO_4)_2 \times 8\ H_2O$ before milling, after 60 min of milling, and after 260 min of milling (mech-ACP). 156
Figure 10.4: Amorphization kinetics of $Co_3(PO_4)_2 \times 8\ H_2O$ in a planetary ball mill monitored with XRD and ATR-FTIR spectroscopy. 156
Figure 10.5: a) DTA curves of cobalt phosphate hydrates after different milling durations. b) Corresponding TG curves. 157
Figure 10.6: UV-Vis spectra of cobalt phosphate hydrates with different degrees of "IR-crystallinity". 158
Figure 10.7: Evolution of the X-ray powder diffraction patterns of $Co_3(PO_4)_2 \times 8\ H_2O$ at pressures up to 8.18 GPa. 159
Figure 10.8: Illustration of performed high-pressure and ball milling experiments. 160
Figure 10.9: a) Relative change in unit cell axis length a/a_0, b/b_0, and c/c_0 as a function of pressure in $Co_3(PO_4)_2 \times 8\ H_2O$ up to 8.18 GPa. b) Corresponding unit cell volumes. 161
Figure 10.10: SEM image of mech-ACP and HT-mech-ACP. 163
Figure 10.11: TEM images and STEM images of cobalt phosphate hydrate after 30 min of milling. 164
Figure 10.12: a) XANES spectra of $Co_3(PO_4)_2 \times 8\ H_2O$, ACP, and mech-ACP. b) EXAFS profile-amplitude of the Fourier transform. 165
Figure 10.13: IR spectra of mech-ACP and HT-mech-ACP. 166

Figure 10.14: a) Crystallization kinetics of mech-ACP. b) Double-logarithmic plot of crystallization kinetics showing the validity of an Avrami mechanism. 167

Figure 11.1: a) IR spectra of hopeite after different process (milling) times of 2, 80, and 340 min in the absence of Fe impurities. b) Amorphization kinetics derived by quantitative analysis of the IR spectra. 174

Figure 11.2: Amorphization kinetics of $Zn_3(PO_4)_2 \times 4\ H_2O$ in the presence of iron impurities (2 mol%). 175

Figure 11.3: XRD pattern of hopeite in the presence of Fe impurities (2 mol%) after different milling times. 175

Figure 11.4: SEM images of mech-AZP in the absence of iron. 177

Figure 11.5: a) Crystallization kinetics in water of mech-AZP with different amounts of iron. b) "IR-Crystallinity" at saturation limit according to a Langmuir plot..... 178

Figure 11.6: TGA measurements of mech-AZP(0 m% Fe) and hopeite. 179

Figure 11.7: a) DTA of hopeite milled with 2 m% of Fe for different milling durations. b) DTA of hopeite and its milling end products (mech-AZP) with different amounts of Fe used during reaction. 180

Figure 11.8: (A) XRD patterns of γ-$Zn_{3-x}Fe_x(PO_4)_2$ formed by heating a sample mech-AZP in the presence of 2 mol% ^{57}Fe at 700 °C under argon. (B) Heating up on air leads to α-$Zn_3(PO_4)_2$ containing α-Fe_2O_3 impurities. 181

Figure 11.9: Mössbauer spectra of mech-AZP and its annealing products..... 182

Figure 11.10: Hysteresis loops (5 K) for mech-AZP ball-milled in the presence of 2 mol% ^{57}Fe after annealing at 700 °C under Ar and in air. 184

Figure 11.11: EPR spectra of mech-AZP (synthesized with 2 mol% of ^{57}Fe) at room temperature and cooled with N_2..... 184

Figure 13.1: Schematics of the experiments for XANES/EXAFS in transmission. 199

LIST OF TABLES

Table 3.1: Extinctions of the water bands in the IR spectra of different zinc phosphate hydrates and resulting water content. 41

Table 3.2: Results of IR and Raman spectroscopy of different zinc phosphate hydrates in detail. 42

Table 3.3: Thermal analysis of HT-AZP and resulting water content. 44

Table 3.4: Square roots of second Moments of hydrates calculated for rigid structures and a few of the shortest H–H distances..... 51

Table 4.1: Experimental conditions during precipitation of cobalt phosphate hydrates. 58

Table 4.2: Results of IR spectroscopy of different cobalt phosphate hydrates in detail. 64

Table 5.1: Solubility products and supersaturation for the synthesis of amorphous solids.... 79

Table 5.2: ICP-MS and ICP-OES results of different amorphous metal phosphate hydrates isolated as intermediates during precipitation. 83

Table 5.3: Results of TGA for amorphous and crystalline metal phosphate hydrates. 85

Table 5.4: Crystallization temperature of amorphous phosphate hydrates. 86

Table 6.1: ICP-MS, ICP-OES, and EDX results of hydr-MeOH-ACP. 102

Table 7.1: Reaction conditions for synthesis of silica encapsulated AZP nanoparticles. 100 mg of AZP nanoparticles were applied respectively. 108

Table 8.1: Amount of Zn and Co located in the down phase during different experiments as determined by AAS. 123

Table 9.1: Intercept and slope for the Cu sensitive electrode determined by titration of Cu^{2+} in deionized water. 136

Table 10.1: Results of ICP-MS, ICP-OES, and EDX of mech-ACP. 161

Table 10.2: Water content of mech-ACP and HT-mech-ACP. 162

Table 11.1: Milling reaction with different amounts of iron. 176

Table 11.2: ICP-MS, ICP-OES, and EDX results of mech-AZP synthesized without Fe. .. 177

Table 11.3: Water content of zinc phosphates based on the extinctions of the water bands in normalized IR spectra. 180

Table 11.4: Hyperfine parameters of ^{57}Fe in Fe substituted $Zn_{3-x}Fe_x(PO_4)_2 \times n\ H_2O$. 183

LIST OF ABBREVIATIONS AND SYMBOLS

abbreviation or symbol	meaning
a	activity
A	Arrhenius factor
AAS	atomic absorption spectroscopy
a.u.	arbitrary units
ACC	amorphous calcium carbonate
ACP	amorphous cobalt phosphate hydrate
ATR	attenuated total reflectance
AUC	analytical ultracentrifugation
AZP	amorphous zinc phosphate hydrate
c	concentration
c_{crit}	critical concentration
CNT	classical nucleation theory
c_s	saturation concentration
DOLLOP	dynamically ordered liquid-like oxyanion polymer
DTA	differential thermal analysis
EDX	energy-dispersive X-ray
EPR	electron parametric resonance
EXAFS	extended X-ray absorption fine structure
FTIR	Fourier transformed infrared
HT-	high temperature-
I	ionic strength
ICP-MS	inductively coupled plasma mass spectrometry
ICP-OES	inductively coupled plasma optical emission spectroscopy
ISE	ion-selective electrode

J	nucleation rate
K	equilibrium constant
k_B	Boltzmann constant
K_{SP}	solubility product
LCP	liquid condensed phase
MAS	magic angle spinning
mech-ACP	amorphous cobalt phosphate hydrate synthesized mechanochemically
mech-AZP	amorphous zinc phosphate hydrate synthesized mechanochemically
MeOH-ACP	amorphous cobalt phosphate synthesized in methanol
PILP	polymer-induced liquid precursor
pK_a	pKa value
PNC	prenucleation cluster(s)
r	radius
R	ideal gas constant
r_{crit}	critical radius
S	supersaturation
SAXS	small-angle X-ray scattering
S_{crit}	critical supersaturation
SEM	scanning electron microscopy
SQUID	superconducting quantum interference device
SS-NMR	solid state-nuclear magnetic resonance
STEM	scanning transmission electron microscopy
T	temperature
TEM	transmission electron microscopy

TEOS	tetraethyl orthosilicate
TGA	thermogravimetric analysis
V	volume
V_m	mole volume
XANES	X-ray absorption near edge structure
XRD	X-ray diffraction
α	fraction of solute species
γ	surface tension
ΔG	free enthalpy
Δg	free enthalpy of bulk phase per unit volume
ΔG_{crit}	free enthalpy barrier
μ_{mix}	chemical potential of mixing
χ_A	molar fraction of species A
ω	amount of individual phosphate species

1

NUCLEATION AND CRYSTAL GROWTH

Crystallization is the precipitation of solid crystals from a supersaturated solution, a melt, or from the gas phase. Basically, crystallization is divided in two main events: nucleation and crystal growth. Here, nucleation is the formation of a second phase in the original one-phase system, followed by the growth of the formed species.[1]

1.1 Nucleation Theories

Nucleation is the very essential physicochemical process to gain new phases. According to the classification of Ehrenfest, this process is classified as a first order transition induced by changes of state variables (*e.g.*, pressure, temperature, etc.).[2] Nucleation only occurs when a system is brought out of the stable region of its respective phase diagram (composition versus state variable). Every phase transition requires a nucleation event, *e.g.*, the condensation of water droplets in a supersaturated steam atmosphere. Furthermore, nucleation is a sub-event of crystallization and emulsion polymerization. There are several theories how nucleation events proceed. Besides the classical nucleation theory (CNT), non-classical approaches exist including prenucleation clusters, two-step nucleation, liquid-liquid phase separation, or spinodal decomposition. In the following paragraph, the CNT is described first to show that it is a suitable starting point to explain nucleation, but far away from a complete package to describe nucleation adequately.

1.1.1 Classical Nucleation Theory

Figure 1.1 describes a nucleation event according to CNT on thermodynamic considerations. A characteristic feature of nucleation events is the associated enthalpy barrier, which prevents precipitation to set in immediately at low or even zero supersaturations. Upon nucleation, a homogeneous system becomes heterogeneous. A second phase is formed, accompanied with a gain in interfacial surface leading to an increase in free enthalpy. However, the formation of a second phase also causes a decrease in free enthalpy due to the higher

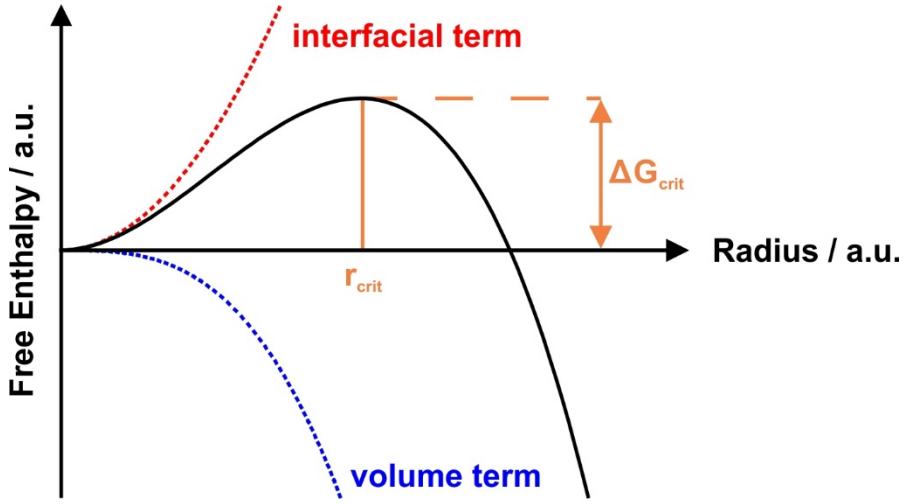

Figure 1.1. Free enthalpy contributions of nucleus formation according to CNT.

packing density of the bulk phase resulting in an increased number of attractive interactions. CNT assumes that even the nanoscopic nuclei of the new phase can be described by a volume term and an interfacial term (see Equation 1.1). A nucleation event happens when the free enthalpy ΔG of the whole system is decreased by this process.

$$\Delta G_{total} = \Delta G_{surface} - \Delta G_{volume} \qquad 1.1$$

The assumption of a spherical nucleus with radius r to be formed first by homogeneous nucleation, seems reasonable as this form provides the smallest ratio of surface to volume and is therefore the most favorable in terms of free enthalpy.

$$\Delta G = 4\pi r^2 \cdot \gamma - \frac{4}{3}\pi r^3 \cdot \Delta g \qquad 1.2$$

In Equation 1.2, γ is the surface tension of the interface between nucleus and surrounding phase and Δg the free enthalpy per unit volume. For heterogeneous nucleation with a nucleus at a surface, the effective interfacial surface is reduced (less than $4\pi r^2$) leading to lower enthalpy barriers for a nucleation phenomenon and thus to much easier nucleation. However, the surface term is dominating for small radii of nucleus. For a growing nucleus, the volume term grows much faster becoming the dominating influence due to its r^3 dependence. Hence, the superposition of both terms result in an effective free enthalpy diagram with a pronounced maximum. This maximum represents the free enthalpy barrier ΔG_{crit} which has to be overcome in order to achieve a nucleus growth instead of dissolution. Although ΔG is still positive for radii bigger than the radius at ΔG_{crit} (called critical radius r_{crit}), the derivation of free enthalpy with respect to the radius becomes negative at this point. This leads to smaller values of free enthalpy for a growing nucleus favoring the growth towards larger particles. The formation of

nuclei with a radius smaller than r_{crit} is endergonic resulting in dissolution of the nucleus. The critical radius and the free enthalpic barrier are:

$$r_{crit} = \frac{2\gamma}{\Delta g} \quad 1.3$$

$$\Delta G_{crit} = \frac{4}{3}\pi\gamma r_{crit}^2 \quad 1.4$$

The height of profile for the nucleation barrier ΔG_{crit} for a given system depends essentially on its supersaturation and temperature. Supersaturation S is defined as the activity a of the solved compound divided by the activity at the point of saturation (equilibrium) a^*.

$$S = \frac{a}{a^*} \quad 1.5$$

It is important to note that supersaturation is a variable linked to a certain crystalline polymorph of the final solid. For example, anhydrous calcium carbonate exists in three crystalline polymorphs and some additional amorphous solids. Each of these crystalline/ amorphous solids has a characteristic free enthalpy linked to a certain solubility and thus the supersaturations with respect to the different crystalline/amorphous solids are different. The Gibbs Thomson equation[3]

$$\ln S = \frac{2\gamma V_m}{\mathrm{R}Tr} \quad 1.6$$

where V_m is the mole volume of the crystalline building blocks, T the thermodynamic temperature, and R the ideal gas constant, relates the radii of nuclei formed to the supersaturation. Insertion of Equation 1.6 in Equation 1.4 results in:

$$\Delta G_{crit} = \frac{16\pi}{3}\frac{\gamma^3 V_m^2}{(\mathrm{R}T\ln S_{crit})^2} \quad 1.7$$

It can be seen that the free enthalpy barrier for nucleation is connected to a critical degree of supersaturation S_{crit} as driving force for nucleation. High supersaturations decrease the free enthalpy barrier for nucleation and a nucleation phenomenon becomes much more probable at a given system. In other words, the critical radius that has to be reached to form a nucleus with the potential for further growth is decreased at high supersaturations.

Besides the thermodynamic aspects of a nucleation process, supersaturation also determines kinetics of nucleation events according to an Arrhenius approach.[4] The nucleation rate J is described as:

$$J = A \cdot \exp\left(-\frac{-\Delta G_{crit}}{k_B T}\right) \quad 1.8$$

where k_B is the Boltzmann constant, and A the pre-exponential factor. This indicates that a metastable system may never nucleate in years, whereas a small increase in supersaturation can trigger nucleation immediately.

LaMer Model

The LaMer model is systematic approach showing how increasing supersaturation can cause an ensemble of nuclei followed by growth.[5] Figure 1.2 describes a typical crystallization event (nucleation followed by crystal growth) according to the LaMer model. As reported in LaMer's original work, he uses $Na_2S_2O_3$ as precursor in water which disproportionates into S_2 and HSO_3^- in the presence of HCl. The ongoing disproportionation results in an increasing concentration of sulfur which is slightly soluble in water. In the first stage, concentration of sulfur in solution increases linearly upon critical supersaturation (c_{crit}) is reached. In this prenucleation stage, no nuclei are formed despite reached supersaturation (c_s). According to Equation 1.7, supersaturation S>1 does not require consequently nucleation as the free enthalpy barrier for nucleation has a finite value but may not be reached in the given system. In other words, the critical radius to form a nucleus with the potential for growth may be too big despite present supersaturation. Going further to the second stage, the critical concentration c_{crit} is reached initiating homogeneous nucleation. The formed nuclei grow instantly consuming new formed sulfur. Therefore, the concentration curve flattens. During

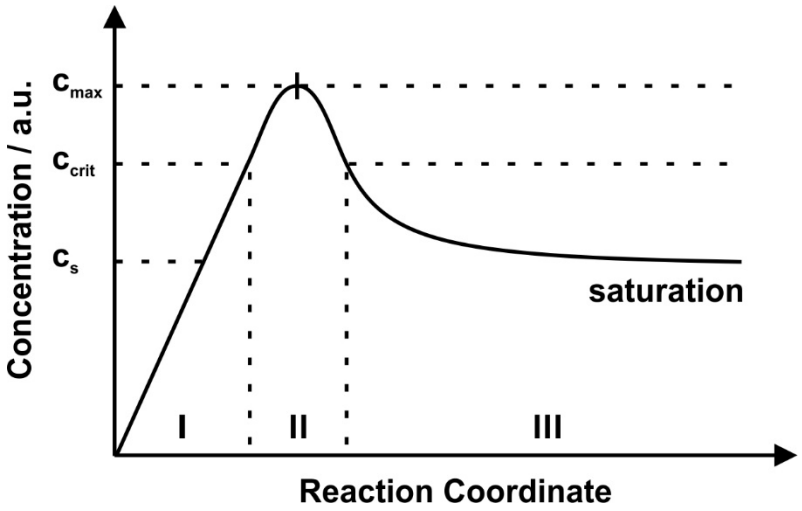

Figure 1.2. Development of the measured concentration of solved sulfur during the reaction $2\ Na_2S_2O_3 + HCl \rightarrow 2\ HSO_3^- + S_2 + 4\ Na^+ + 2\ Cl^-$ in water considering nucleation and crystal growth as described by the LaMer model. S_2 is formed with a constant rate. Based on [5].

stage II, prior formed nuclei grow but there is also formation of new nuclei as the concentration is higher than c_{crit}. Reaching the maximum supersaturation, all further released sulfur is consumed by nucleation and growth of nuclei. The increasing number of nuclei leads to a higher amount of consumed sulfur. Thus, the concentration of free sulfur in solution drops down again. In the third stage, concentration falls below c_{crit} so that no nucleation events take place any more. In this stage, the present monomer concentration is determined by growth of particles exclusively. The limit of concentration is given by the solubility product (supersaturation=1).

Ostwald-Volmer Rule

Regarding a polymorphic system, different modifications have different surface and bulk energies depending on their structure. Normally, the densest modification represents the thermodynamically stable one because in dense solids an increased number of attractive interactions are realized leading to a minimization of free enthalpy. This argumentation is based on the bulk values of the chemical potential for the different modifications because surface effects may be neglected for bulk material. As the dense solids reveal a high number of surface degrees of freedom, the trend of stability may be reversed for free enthalpy of surface. This might lead to a crossover in thermodynamic stabilities at the nanoscale where surface effects dominate. Furthermore, the number of monomers which has to be arranged for reaching the critical radius for nucleation is decreased for less dense modifications. This assumption is known as the Ostwald and Volmer's rule.[6] It implies that in a polymorphic system the least dense modification (with the lowest enthalpy of formation) forms first and cascades down to the thermodynamically stable modification via metastable states. This assumption is rather a rule of thumb than a strict law. As surface energies of solids cannot be measured, there is no quantitative foundation for this theory. Additionally, there is no statement about different hydrated modifications and intermediates which differ from their anhydrous counterparts in the chemical composition.

Qualitatively, CNT describes a lot of nucleation processes sufficiently. However, quantitative predictions are often quite wrong with difference to some orders of magnitude. The intrinsic problem of the CNT is the assumption of continuous thermodynamics. Energies/enthalpies of nanometer sized nuclei are calculated based on the thermodynamic values of bulk material. In addition, solvents have a subordinated role within this theory and are only important for calculating surface tensions.

1.1.2 Non-Classical Approaches

As explained above the CNT is not sufficient for describing all nucleation processes adequately due to discontinuous thermodynamics and nanoscale effects (maybe crossovers in the thermodynamic stabilities of polymorphs).

Prenucleation Cluster

One non-classical approach is described by the existence of stable clusters in solution which are still solved, so-called prenucleation clusters (PNC) introduced by Gebauer *et al.*[7] Clusters display an intermediate between a molecule and a bulk solid. These PNC are predicted to be present even in the homogeneous region of phase diagrams and their existence has been proofed for calcium carbonate[7] and phosphate,[8] silica (more pronounced covalent character),[9–11] and iron(oxy)(hydr)oxides,[12–14] and especially for organic compounds like amino acids. For calcium phosphate amorphous precursors with small clusters as structural building blocks were found already in the 1970's. The so-called Posner cluster are predicted to be spherical and form amorphous calcium phosphate via cluster aggregation.[8] It is assumed that PNC are very small and have no clear phase boundary to the solution. Anyway, it is difficult to draw a clear line between hydration of a cluster and the phase boundary of a bigger agglomerate to the surrounding solution. PNC are highly dynamic species comparable with molecular complexes changing their coordination. The occurrence of solved clusters is nothing new in principle. For instance, different sized but well-defined CdSe cluster can be synthesized starting with cadmium benzoate, *bis*(trimethylsilyl)selenide and *n*-butylamine. Benzoate and *n*-butylamine units act as stabilizing ligands for the growing clusters so that they can be isolated.

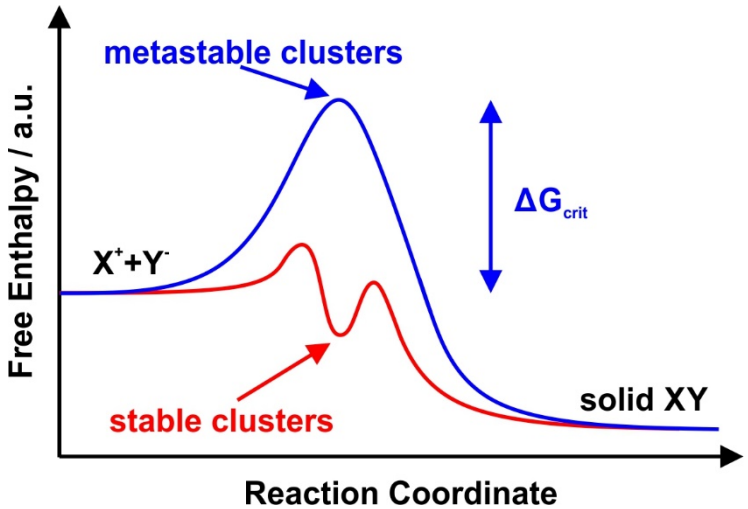

Figure 1.3. Enthalpic pathways in the formation of solid nuclei of XY according to CNT (blue line) and assuming PNC (red line). Based on [7].

These quantum dots consist of a series of pyramidal nanostructures with Cd terminated {111} facets.[15] Furthermore, Zintl cluster and polyoxometalates (POM) like molybdates or vanadates are known for more than 150 years. Depending on the set pH range, various metal oxide cluster structures can be realized like the Keggin structure[16]. The polyanions precipitate selectively as salts with respective cations (*e.g.*: $Na_6[V_{10}O_{28}]$). In contrast to the PNC mentioned above, these metal clusters are defined precisely or rather stabilized by ligands and therefore not ordered dynamically. However, one has to note that the polyoxometalates reveal a covalent character rather than clusters of $CaCO_3$. PNC of $CaCO_3$ or similar biominerals are coordinated by water in aqueous solution. As Ca^{2+} is in the intermediate range of hardness according to Pearson's concept of hard and soft acids and bases, binding of water is a reversible event making the PNC ill-defined and a highly dynamic species.

As the PNC are predicted to be a thermodynamic stable species, they are not a kinetic artifact and can be described according to Le Chatelier's principle:[17]

$$\mathrm{n\ Ca^{2+} + n\ CO_3^{2-} \leftrightharpoons (CaCO_3)_n} \qquad 1.9$$

with cluster formation constant $K_{Cluster}$:

$$K_{Cluster} = \frac{[(\mathrm{CaCO_3})_\mathrm{n}]}{[\mathrm{Ca^{2+}}]^n\,[\mathrm{CO_3^{2-}}]^n} \qquad 1.10$$

In Equation 1.10 $[Ca^{2+}]$, $[CO_3^{2-}]$, and $[(CaCO_3)_n]$ stand for the concentrations of respective species in solution under the assumption that all activity constants are equal to 1. The existence of PNC is reported by Gebauer *et al.* on the basis of a titration experiments. In their work, they titrate $CaCl_2$ into a carbonate buffer and use a Ca^{2+} sensitive electrode for monitoring $[Ca^{2+}]$. The measured concentration of Ca^{2+} is always lower than it should be according to the added amounts, even in the undersaturated solution. The pH value is kept constant and differences in ionic strength are excluded. The discrepancy in measured concentration is explained by the formation of PNC of calcium carbonate which cannot be detected by the ionic sensitive electrode. Consequently, this experiment was performed at different pH values resulting in different concentrations of CO_3^{2-} species in the carbonate buffer. Hence, the deviation from concentration of dosed amount is in agreement with Equation 1.10. Furthermore, the authors performed measurements at different temperatures. Isothermal titration monitors calorimetrically leads them to the conclusion that the formation of PNC is endothermic and basically an entropy driven process. Due to the formation of PNC, parts of the original hydration layers of the solved ions are peeled away leading to the gain in entropy. Hence, water as coordinating agent seems to play an essential role in nucleation processes.

Furthermore, the PNC for the calcium carbonate system are detected by analytical ultracentrifugation (AUC). The clusters are approximately 2 nm in size in accordance with the results of cryo-TEM and thus consist of nearly 70 calcium and 70 carbonate ions per cluster.

But the question is how the PNC act as intermediate during the nucleation event. It is assumed that with growing supersaturation the PNC form bigger aggregates by peeling away their respective hydration layers. As the inner parts of the aggregates contain less water, there are density differences with respect to the surrounding solution. Upon reaching a critical supersaturation, density differences are in fact so high that the PNC represent a new phase (nucleation event has happened). The final products of the titration experiments are amorphous calcium carbonates (ACC). Interestingly, depending on the set pH value, two different amorphous species can be distinguished. At pH 9.00, ACC I is obtained which is less soluble than ACC II produced at pH=9.75. The authors claim that the short range order of vaterite and calcite is encoded in the PNC and the amorphous precursors respectively, which is supported by NMR measurements.[18]

Computer simulations reported by Gale *et al.* suggest a model of dynamically ordered liquid-like oxyanion polymers (DOLLOP) for the formation of PNC. According to this, PNCs (oxyanion polymers) are stable but rapidly exchanging.[19]

2-Step Nucleation

A further non-classical approach explaining nucleation events is the 2 step nucleation. Before a solid crystal forms in supersaturated solution, there is a dense liquid phase formation taking place within the parent phase. Within this dense liquid the second nucleation event takes place to generate the final nucleus (see Figure 1.4) Therefore, two energetic barriers have to be overcome. As a result, the dense liquid is metastable with respect to the final crystal but can either be metastable or unstable with respect to the species in solution (see Figure 1.5). This was experimentally found for nucleation of proteins from solution,[20] colloid crystals,[21] organic crystals,[22] and biomineral crystals.[23] Free enthalpy pathways for the formation of

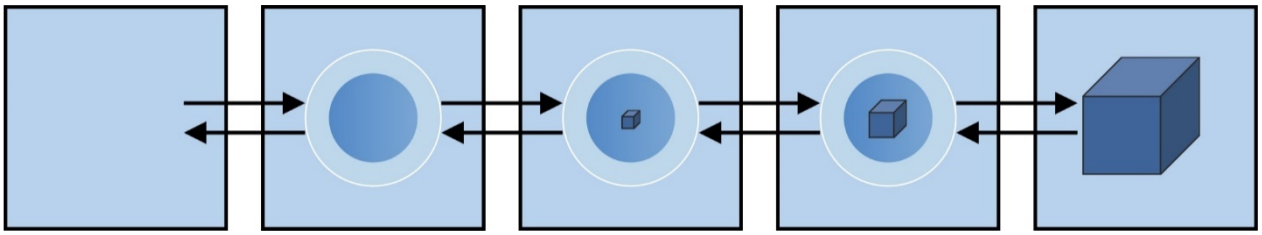

Figure 1.4. Illustration of 2-step nucleation: Nucleation of a solid particle proceeds via nucleation of a dense liquid species in homogeneous solution. Based on [23].

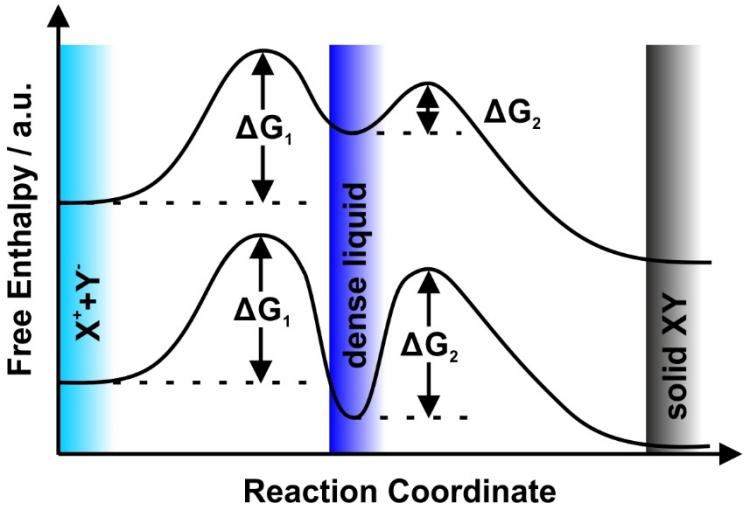

Figure 1.5. Free enthalpy pathways for the formation of solid nuclei of XY assuming prior nucleation of a dense liquid, which can be metastable (upper graph) or stable (lower graph) with respect to solute species X^+ and Y^-. Based on [23].

PNC and for 2-step nucleation seem to be very similar. It has to be noted that in fact the free enthalpy barrier is very low in case of PNC formation. Hence, PNC exist already in the undersaturated region as thermodynamically stable species coexisting with ions in solution. In contrast, the first nucleation event in a 2-step nucleation with a sufficient high free enthalpy barrier leads to a dense liquid, including phase separation. A possible combination of both theories is present when aggregating and densifying of PNC lead to a dense liquid before a solid nucleus is formed. A final answer whether clusters aggregate towards the final particles or grow classically by single ion attachment is still not found.

The dense liquids, also called liquid condensed phases (LCP), can be stabilized by polymers. Originally, phases synthesized by this effect were called polymer-induced liquid-precursors (PILPs). But the occurrences of LCP without polymer additives suggested that the appearance of PILPS is indeed a polymer-stabilized LCP phenomenon.[24]

The use of charged polypeptides during the precipitation of biominerals may promote nucleation via a multi-step process including an intermediate liquid phase (PILP). An instance is reported by Gower *et al.* who used poly(α, L-aspartate) during precipitation of calcium carbonate. Poly(α, L-aspartate) induces a liquid-liquid phase separation of droplets of mineral precursors most-probably by ionic interactions with the Ca^{2+} and CO_3^{2-}. Solidification of the liquid droplets leads to the formation of solid crystals instead of crystallization from solution. As a result of the solidification process, calcium carbonate crystals display a "molten" appearance with unique non-equilibrium morphologies (see Figure 1.6).[25,26] Instances for liquid precursors in the absence of additives are provided by Wolf *et al.* A liquid-phase of

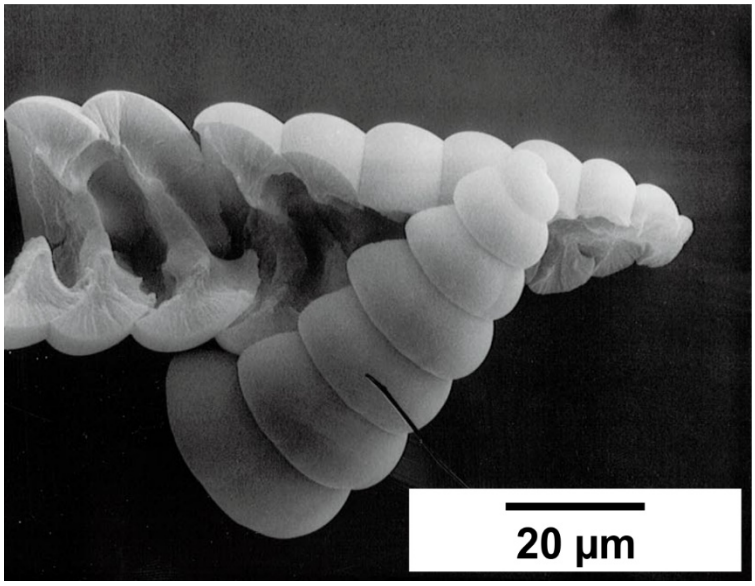

Figure 1.6. Non-equilibrium $CaCO_3$ morphology achieved via a PILP process using poly(α, L-aspartate). Reproduced from [26] with permission of Elsevier.

$CaCO_3$ forms in a levitated droplet at pH=6.3 while supersaturation is increased by release of CO_2.[27] Basically, dense liquids mostly occur in system with low lattice energies like proteins or other organic crystals leading to far extended species (several 100 nm). Liquid-like precursor phases are an interesting explanatory approach how nature realizes complex morphologies in narrow space by using additives and templates to stabilize intermediates.

Amorphous intermediates

At first sight, the appearance of an amorphous phase is not directly in conflict with classical nucleation theory.[6] At sufficiently high supersaturations, amorphous phases may form first and transform to the thermodynamically stable polymorph afterwards probably via further (amorphous or crystalline) metastable intermediates according to Ostwald's rule. However, the classical model of nucleation and crystal growth is based on equilibrium states. At high supersaturations accompanied by high nucleation and growth rates, the system is far away from equilibrium and the application of classical theories is limited.[28] Nonetheless, amorphous solids (not PNC) can be intermediates on the way towards the thermodynamically stable polymorph.

Amorphous calcium carbonate (ACC) has a great meaning in biomineralization processes as intermediate during the formation of crystalline calcium carbonate modifications. Crystalline calcium carbonate displays the most commonly employed material for the construction of hard tissue in invertebrates. In literature, ACC is described as amorphous

$CaCO_3 \times n\ H_2O$ with various degrees of hydration while near-stoichiometric $CaCO_3 \times H_2O$ is dominating.[29] ACC may act as structural component, *e.g.*, in calcitic sponge spicules.[30] Further, it may act as substance reservoir for (i) future availability of calcium and carbonate, which is observed for earthworms,[31] and (ii) crystallizing a desired polymorph quickly (*e.g.*, observed for sea urchins).[32–35] ACC appears to be stabilized by water, macromolecules, ionic additives, or membranes. Biogenic stabilized ACC typically contains water and transforms to the crystalline polymorphs of $CaCO_3$ (non-hydrated) via anhydrous ACC. Anhydrous ACC is reported to be a short-lived intermediate.[36]

To sum up, water plays an essential role in these non-classical approaches and acts not only as solvent, but as active part of the nucleation process.[37] It stabilizes amorphous and liquid-like intermediates as coordinating molecule. Also the release of hydration layers and the accompanied gain of entropy appear to be the main reasons for PNC formation.

Spinodal Decomposition

One further mechanism by which an one-phase system becomes two-phase is the spinodal decomposition.[38] In this process, forming a new phase is no discrete nucleation event under certain conditions but a uniform process throughout the whole volume of supersaturated solution. Figure 1.7 illustrates a phase diagram of a binary mixture of component A and B with a miscibility gap where single-phase mixtures of the components are metastable or unstable. At high temperatures, entropy dominates the free enthalpy and thus A and B are mixable at any ratio. Moderate temperatures, where the free enthalpy of mixing ΔG_{mix} becomes positive, can lead to decomposition into an A-rich and B-rich phase. The dividing line between a thermodynamically stable mixture and one which is metastable or unstable with respect to decomposition is called coexistence or binodal curve. The binodal can be determined by calculating the minimum of free enthalpy of mixing at the respective temperature. Crossing the binodal curve leads to a system where a phase transition may occur and is thermodynamically favored. However, the state without decomposition is metastable and thus stabilized against small concentration fluctuations. Decomposition appears randomly in place and time and can be described by nucleation events according to CNT. Growth of

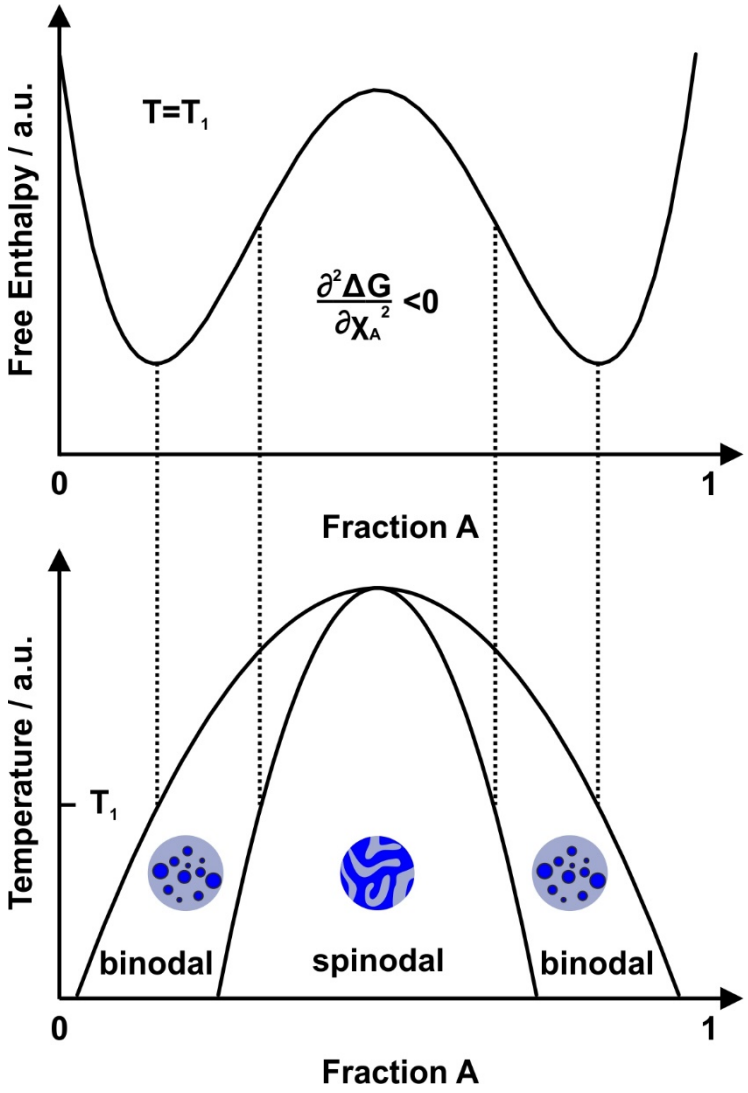

Figure 1.7. Bottom image: Phase diagram for two components A and B, which are mixable partially. Top image: Free enthalpy of the system for a given temperature T1. Minima and turning points of free enthalpy determine the position of binodal and spinodal curve. Based on [38].

nuclei proceeds contrary to the direction of diffusion which is caused by a concentration gradient. Within the binodal region, there is a region called spinodal. It can be calculated by the turning points of the free enthalpy of mixing (see Equation 1.11).

$$\frac{\partial^2 \Delta G_{mix}}{\partial \chi_A^2} = 0 \qquad 1.11$$

where χ_A represents the fraction of species A. Above this line, the second derivation of the free enthalpy of mixing becomes negative. Applying the definition of the chemical potential $\Delta\mu_{mix}$ leads to Equation 1.12.

$$\frac{\partial \mu_{mix}}{\partial \chi_A} < 0 \qquad 1.12$$

According to a modified Fick's law, the diffusion is proportional to the derivation of the chemical potential with respect to the fraction of one species.

$$J = -K \frac{\partial \mu_{mix}}{\partial \chi_A} \qquad 1.13$$

K is a coefficient proportional to the diffusion coefficient *D*. This results in a diffusion flux proceeding via concentration gradient in the spinodal region. Diffusion of material causes further diffusion leading to a chain reaction. The homogeneous solution is unstable against microscopic fluctuations in composition. Thus, the barrier for the growth of a new phase vanishes and a uniform decomposition process occurs throughout the whole volume. Phase separation is only controlled by diffusion. To reach the spinodal region in the miscibility gap at a fixed temperature, one has to start in the homogeneous region and pass through the binodal point. Therefore, supersaturation has to increase dramatically to avoid phase separation by nucleation within the binodal region.

1.2 Crystal Growth Theories

Crystal growth describes the formation of the final crystal after nucleation has taken place. Crystals continue growing until supersaturation has dropped to the critical concentration determined by the solubility product of the final crystal. Besides the classical crystal growth theory, where crystal growth proceeds by single-ion/molecule attachment in layers, non-classical approaches based on particle mediated aggregation are discussed.

1.2.1 Classical Crystal Growth

Classically, a crystal seed grows layer wise by the addition of single ions/molecules on ideal conditions. At very low supersaturations the crystallization rate is very low and thus thermodynamically controlled. On these conditions, crystal growth is determined by the surface energies of the different crystal faces. Low-energy crystal faces will be preferred while high-energy crystal faces occur only to a small extent giving the crystal its shape. One possibility to predict this equilibrium morphology of a crystal is the Wulff construction.[39]

As crystallization in biological environments normally occurs in the presence of additives or at higher supersaturations, it is often kinetically controlled. Crystallization under strict thermodynamic control is in fact very rare. Under kinetic control, the final crystal morphology is not only determined by the surface energy of individual crystal faces but by its growth rate. As high growth rates do not increase the surface of the growing facet but surface of the surrounding facets, the final crystal morphology is determined by the crystal face with the lowest growth rate. Controlling the growth rate of certain crystal faces therefore allows the formation of crystals with various morphologies. Using additives which selectively bind on one certain crystal facet is one way to control crystal growth. It is reported that carboxylated polyelectrolytes strongly interact with Ca^{2+} ions by double layer interaction and by the formation of complexes along the chain of the polyelectrolyte.[40] In addition, additives may be incorporated into the crystal structures as impurities. Dissolution of these impurities may result in porous crystals with a high specific surface.

As mentioned above, crystal growth proceeds via single ion/molecule attachment. A present layer can grow by forming a nucleus of the next layer on its surface by single ion/molecule attachment. This is in fact a 2-dimensional nucleation event and a critical block size can be calculated. It is possible that a crystal grows monolayer-by-monolayer (Frank-van-der-Merwe growth).[41] Thereby, the adhesion on the new monolayer is equal to flat surface's adhesion. More common is the case that adsorbed units are not integrated into the

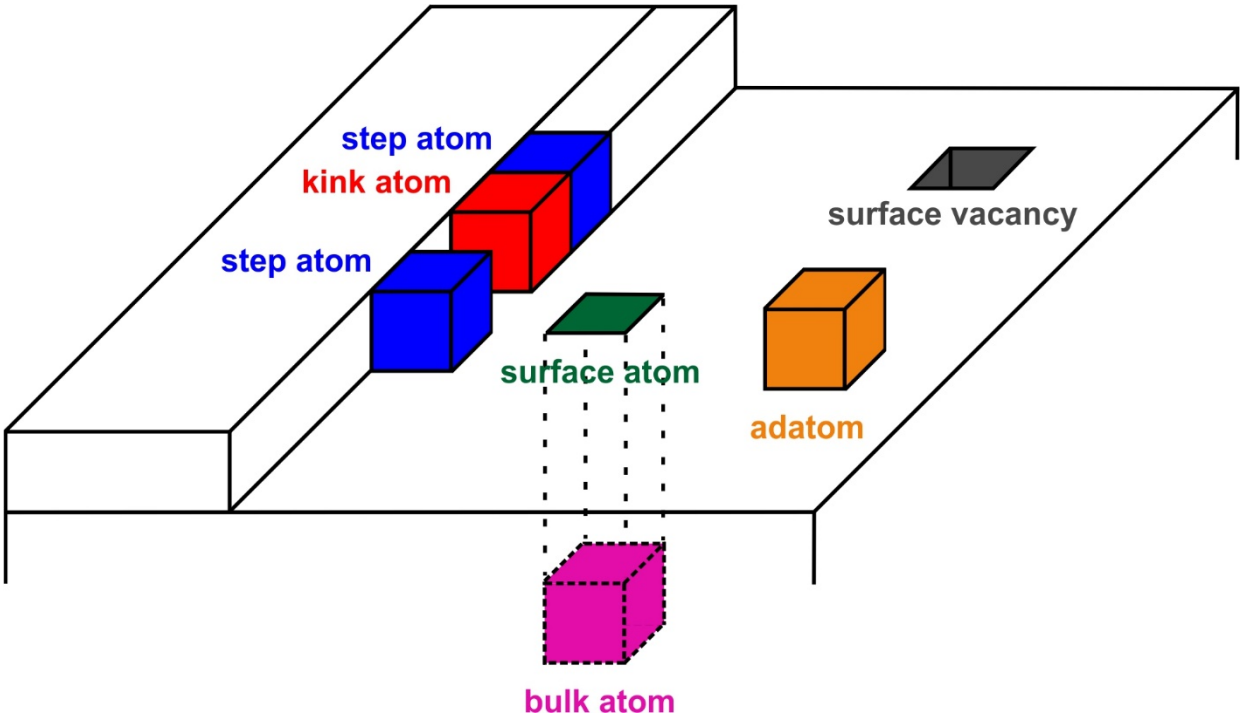

Figure 1.8. Various possibilities for a crystal unit to attach on a growing crystal. Different positions result in different numbers of next neighbors and thus in different binding enthalpy.

crystal lattice directly as they are able to migrate in two dimensions on the crystal facet. Steps and kinks on the crystal surface provide an increased number of binding neighbors resulting in a preferred attachment at these points in comparison to the attachment on the flat surface (see Figure 1.8). Further attachment of building units to the steps and kinks finally leads to the formation of a new layer. At high supersaturations, attached building blocks tend to be integrated into the crystal lattice on the flat surface directly, which is called island growth (see Figure 1.9 f). This behavior is caused by the flat surface dominating and a low free enthalpy barrier according to Equation 1.7. Island growth may also be the case when adatom-adatom interactions are stronger than those of the adatoms with the surface (Volmer-Weber growth).[42]

The BCF model (named after Burton, Cabrera, and Frank) predicts crystal growth taking place mainly at natural defects (*e.g.*, screw dislocations) as nucleation of the first building block on a perfect crystal facet is in fact an improbable event at moderate supersaturations. Growth of steps along screw dislocations lead to spirals growing, which are called hillocks (see Figure 1.9 a–e).[43]

However, crystal growth is never a perfect process. Instead, there is a certain number of imperfections in form of impurities, vacancies, and (screw) dislocations. Impurities may have

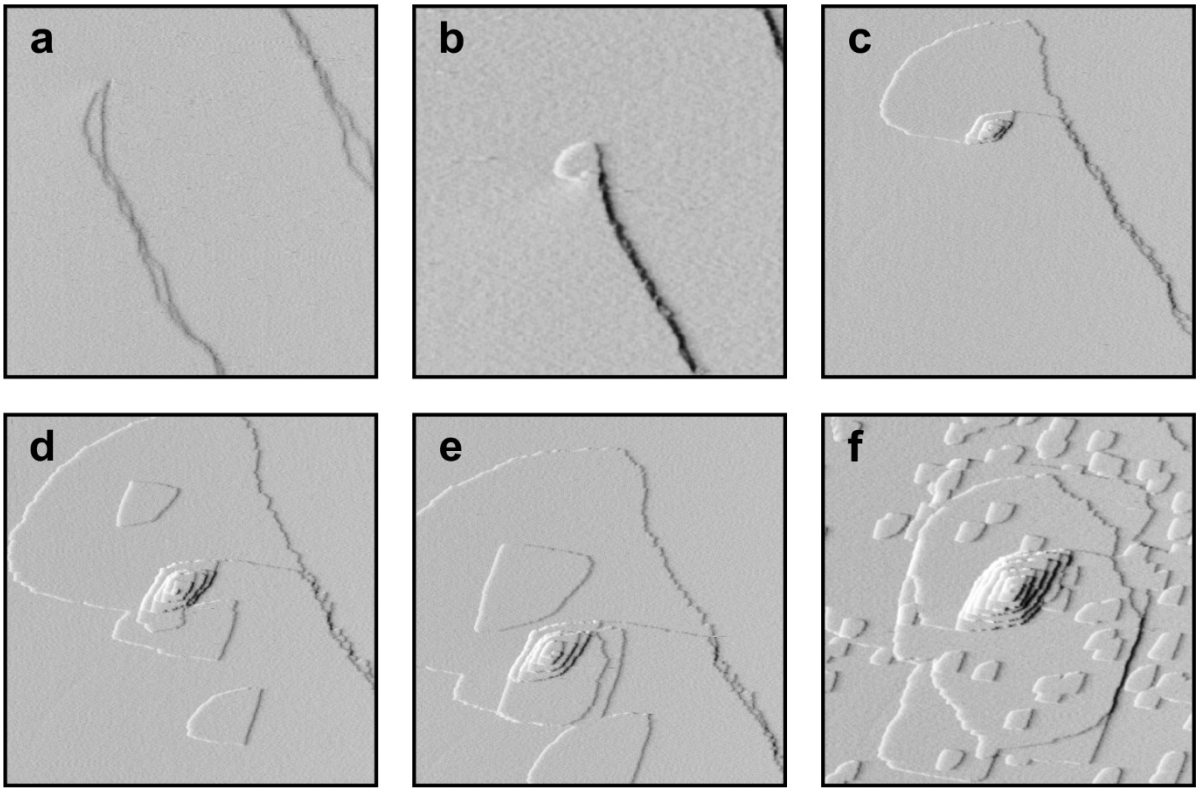

Figure 1.9. Crystal growth on an (001) cleavage plane in $BaSO_4$. Images a–e show the spiral growth beginning at a dislocation core. f: Fresh injection leading to massive supersaturation. Resulting low free enthalpy barrier allows high nucleation rate (island growth). Reprinted by permission from Macmillan Publishers Ltd: Nature [43], copyright 1998.

great influence on the layer-by-layer growth as they inhibit step edges from further growing (kinetic) and lower crystal faces surface energy (thermodynamic). Thus, the selective adsorption of additives onto crystal surfaces/kink sites leading to imperfections is a key mechanism to control crystal morphology as well as crystallization kinetics.

One further question is which of the sub-process of the crystal growth is rate determining. As the ions/molecules that attach later on have to be sufficiently close to the growing crystal, diffusion to the crystal surface is one of the essential steps of crystal growth. Thereafter, the new growth unit has to diffuse along the surface to a kink site followed by a desolvation process. Growth units as well as the attachment site have to be free from solvent to generate new chemical bonds. Finally, the growth unit is incorporated into the kink site. As the desolvation process is the only one which requires dissociation of chemical bonds or at least their weakening, it is the rate determining step during crystal growth by attachment of ions/molecules. One consequence is that changes in the solvents have a great influence on the crystal growth kinetics. Many chemical reactions take place in aqueous solution while the degree of hydration can by controlled by changes in ionic strength and pH value.

Growth of large particles proceeds classically at the expense of smaller particles according to the phenomenon of Ostwald ripening. Larger particles have a decreased surface tension and a decreased number of surface atoms in comparison to the bulk material, which is favored energetically. For Ostwald ripening, there has to be a sufficiently high molecular solubility of the crystal units as well as a high specific surface energy, which makes a reduction of the number of surface atoms essential in terms of thermodynamics. Consequently, systems with a very low solubility or very low specific surface energies (*e.g.*, achieved by using additives) tend to crystallize not strictly according to classical crystallization theories.

Non-Classical Approaches

Many crystal morphologies are too complex to be explained by a layer-by-layer growth of crystalline units. In contrast to the classical crystal growth theory, non-classical approaches are mainly particle mediated. As mentioned above, crystallization via aggregation of nanoscopic sub-units (amorphous or crystalline) is favored at high nucleation rates (high supersaturations) and in the presence of stabilizing additives. It is difficult to speak about crystal growth exclusively proceeding via non-classical mechanisms. Hybrid forms between classical layer-by-layer growth and particle mediated growth are much more common.

Oriented Attachment

Classically, already formed nanoparticles grow at the expense of smaller particles by Ostwald ripening which results in a minimization of surface energy. This recrystallization process is decelerated if the molecular solubility of particles is low. Further, low surface energies present for the nanoparticles result in a lack of thermodynamic driving force for Ostwald ripening. Low surface energies may be achieved by using stabilizing additives. In these cases, nanoparticles may grow by oriented attachment. This mechanism is described by self-assembly of nanoparticles along a common crystallographic axis that is followed by joining at planar interfaces (see Figure 1.10). The self-assembly and fusing lead to the reduction of surface energy which is crucial especially in the early stages of the crystal growth.[44,45] Oriented attachment only may occur when the particles are in an intermediate range in terms of interaction. Thus, stabilization of particle's surface have to be sufficiently weak that nanoparticles approach each other and mutually attract by van der Waals forces. However, particle's dynamics must be sufficiently high so that they may rearrange in the low-energy configuration.[46] Consequently, appropriate conditions for crystallization processes basically dominated by oriented attachment are provided by additives for surface functionalization in most cases. Crystals that form by oriented attachment reveal various non-equilibrium

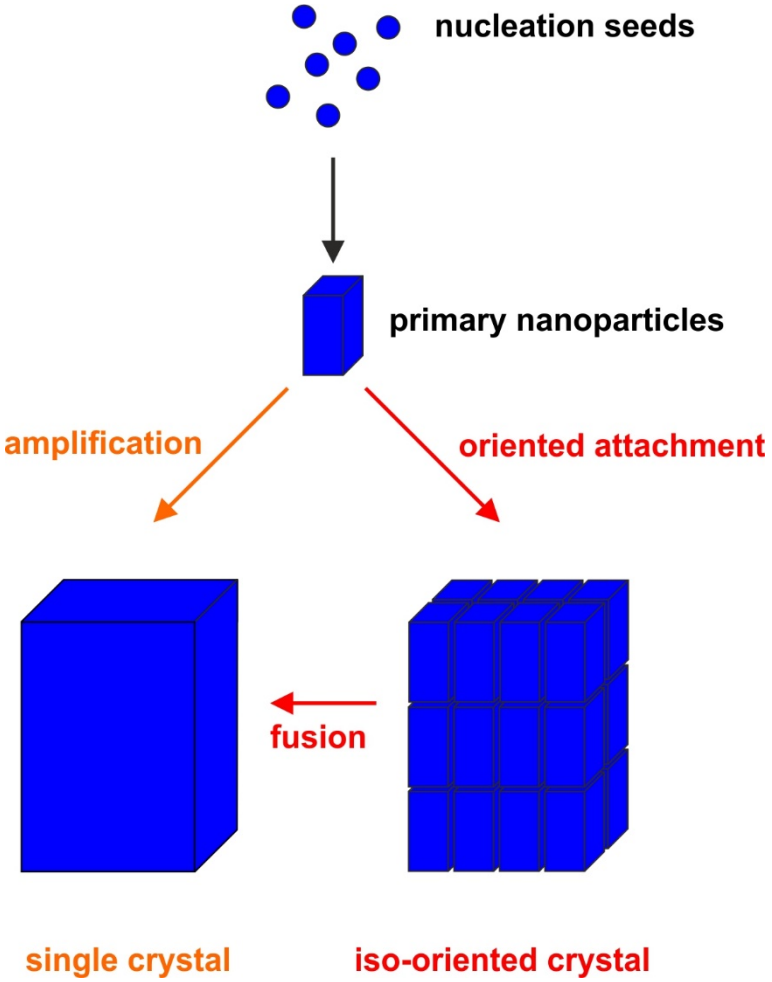

Figure 1.10. Mechanism of classical crystal growth (left, orange) in comparison to one dominated by oriented attachment. Based on [45].

morphologies including nanofibers,[47] rods,[48] and hexapods.[49] They have in common that X-ray as well as electron diffraction investigations show their single crystalline nature but

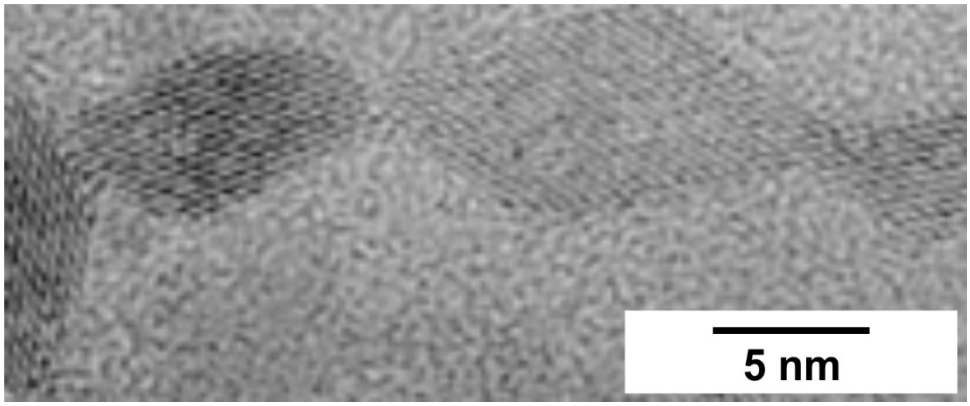

Figure 1.11. TEM image of anatase that was hydrothermally coarsened. Primary crystallites form an iso-oriented crystal by oriented attachment. Reprinted from [50] with permission from Elsevier.

electron micrographs display their tectonic sub-units which is not explainable by a layer by layer growth.

One interesting instance for oriented attachment can be observed during hydrothermal synthesis of TiO_2 nanoparticles. Nanoparticles generated at early stages may align along crystallographic directions and fuse afterwards (Figure 1.11). The highest energy surfaces are identified as the ones fusing and forming the unexpected morphology.[50]

Mesocrystals

Mesocrystal is an abbreviation for mesoscopically structured crystal. They are composed of individual nanocrystals which are aligned along crystallographic directions but are spatially separated. Mesocrystals reveal a similar scattering behavior like single crystals despite their hierarchical structure. It is important to note that the appearance of mesocrystals does not reveal their formation process.

Mesocrystals may form via alignment of nanocrystals by physical forces,[51] alignment by spatial constraints,[52] alignment by an organic matrix[53] or by mineral bridges.[54] In biomineralization processes, mesocrystals are basically observed in the presence of an organic skeleton. For instance, corals are suggested to grow mediated by an organic matrix.[55] The formation of mesocrystals by application of polymers *in vitro* is also reported.[56] As a results,

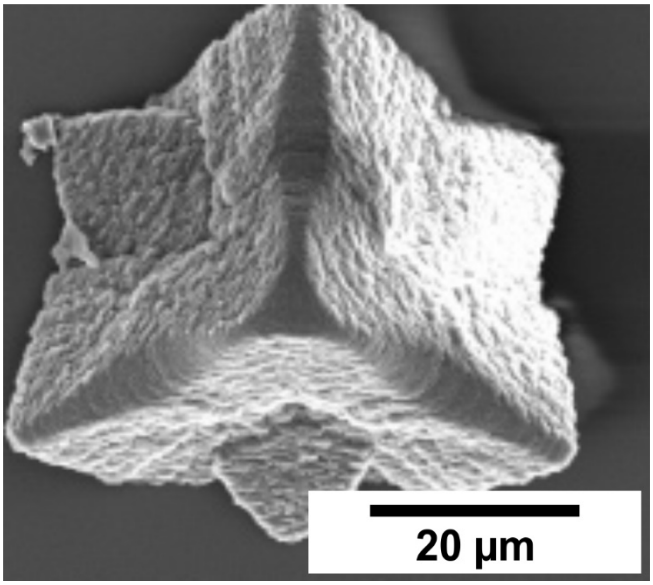

Figure 1.12. $CaCO_3$ mesocrystal precipitated in the presence of the diblock copolymer PEO_{22}-$PNaStS_{49}$ (a poly(ethylene oxide)-*b*-poly(sodium 4-styrenesulfonate) diblock copolymer). Reprinted with permission from [56]. Copyright 2015 American Chemical Society.

inorganic-organic composite superstructures with periodic orientation of nanocrystals are generated (see Figure 1.12).

Besides organic molecules, amorphous phases can be in between the aligned individual nanocrystals, which seems to be common for biominerals. Due to their aligned nanocrystals, biominerals often appear to be single crystals but their fracture behavior indicates amorphous interparticle phases.[57] In general, mesocrystals are supposed to play a key role during a lot of crystallization processes as the theory of nanoparticular sub-units forming an anisotropic structure delivers new possibilities to explain complex morphologies.[58]

2

MOTIVATION

Phosphates display one of the most important inorganic classes of compounds due to their enormous range of possible industrial applications and their role in biomineralization processes. Metal phosphates are used as batteries,[59–63] corrosion resistance coatings[64–67], catalysts, [68–70] and glasses[71–74]. In the past decades, plenty of phosphate based zeolite materials have been successfully synthesized.[75–78]

Basically, crystallization of metal phosphates is a highly complex process due to the big structural diversity. Different degrees of protonation may occur depending on the present pH value. In addition, condensation products like polyphosphates ($P_nO_{3n+1}^{(n+2)-}$) (pyrophosphates ($P_2O_7^{4-}$) for n=2), cyclophosphates ($P_nO_{3n}^{n-}$), and ultraphosphates ($P_{(2m+n)}O_{(5m+3n)}^{n-}$) may be present as structural units (see Figure 2.1). This enormous variety of structural sub-units depends on the degree of protonation and temperature sensitively.[79]

A large part of the research was focused on the synthesis of well-defined crystals of metal phosphates for crystallographic investigations.[80] The synthesis of many anhydrous crystalline phosphates by transport reactions in gaseous phase under equilibrium conditions are reported with well-defined products. However, the question which intermediates appear in the gas phase during the transport reaction remains unanswered. The big number of crystal structures determined of simple orthophosphates as well as of condensed phosphates suggest erroneously that synthesis, crystal chemistry, and physical properties are well understood.[80] However, there is still a big lack of knowledge concerning the early stages of crystallization (nucleation and early crystal growth) as well as on intermediates appearing during these processes.

Model systems for the investigation of crystallization of metal phosphates should be very easy which is achieved by a low number of possible experiment parameters. Therefore, this thesis basically deals with metal phosphates in solution where the degree of protonation and the formation of condensed phosphates can be adjusted quite precisely by the pH value

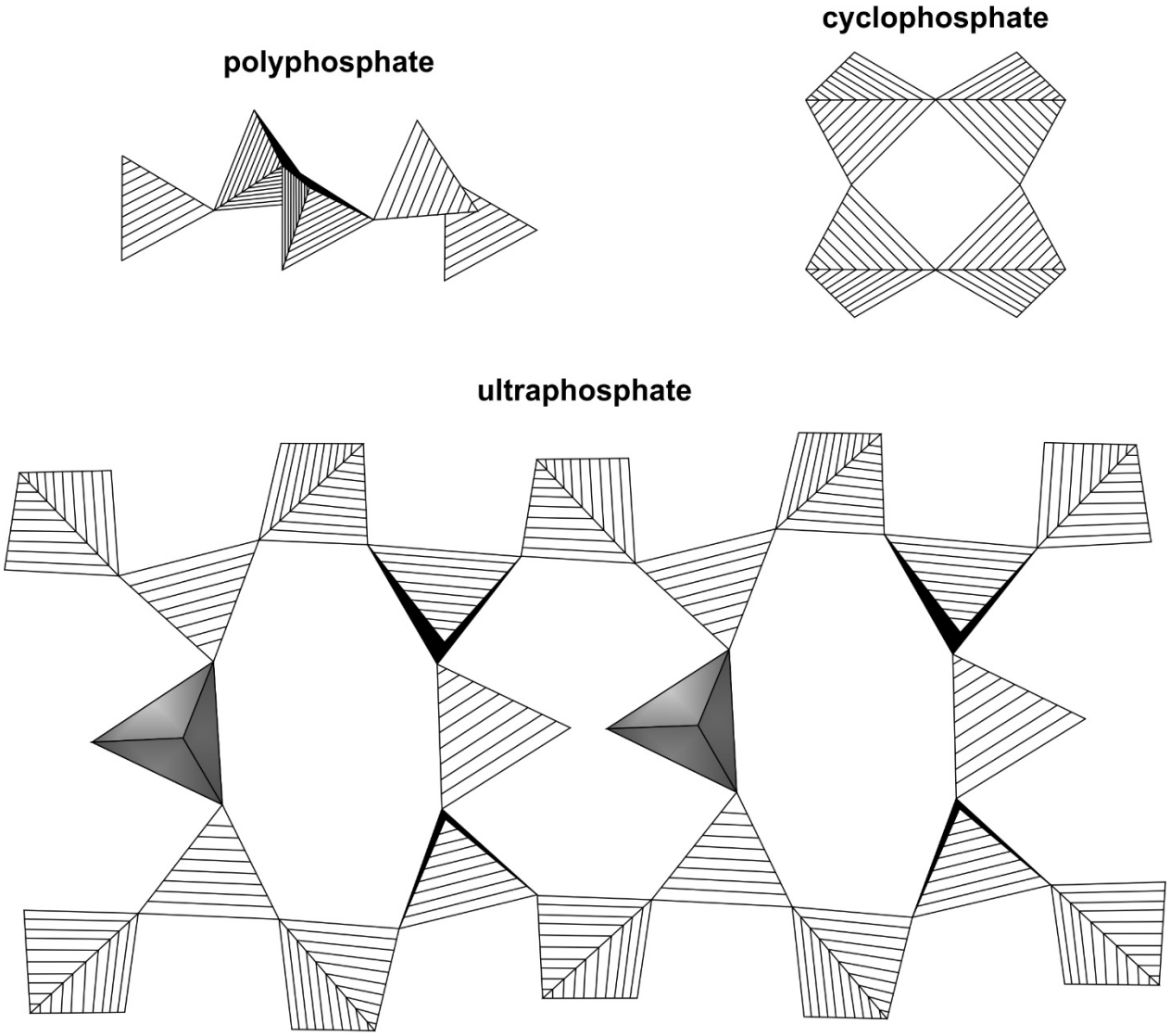

Figure 2.1. Illustration of the respective structures of polyphosphates, cyclophosphates, and ultraphosphates. Based on [79].

and temperature. Due to the low solubility of the most metal phosphates, they can easily be prepared from aqueous solution. Despite the simplicity of reactions in solution with regards to solid state reactions in terms of understanding the mechanisms, there are hardly any fundamental studies of nucleation and crystal growth reported on metal phosphates. The studies are basically restricted to calcium phosphates (*e.g.*, apatite/hydroxylapatite) due to their role in biomineralization processes.[81]

Calcium orthophosphates represents the majority of naturally occurring hard tissue in vertebrates[82] occurring in bones,[83–85] teeth,[86,87] and tendons. Most of the known modifications are slightly soluble in water but dissolve in dilute acids due to the protonation

of the phosphate groups. It is reported that metastable precursor phases appear during the precipitation of calcium orthophosphates. These intermediates transform to the final crystals basically by dissolution and recrystallization.[88,89] Furthermore, the presence of peptides[90] and additives[91] during *in vivo* precipitation has a strong influence on stabilization and crystallization of the different metastable intermediates which complicates a prediction of intermediates formed during the multi-stage crystallization processes. Brushite ($CaH[PO_4] \times 2\ H_2O$) and octacalcium phosphate ($Ca_8H_2(PO_4)_6 \times 5\ H_2O$) are often observed as precursors during *in vitro* formation of apatite,[90] whereas amorphous calcium phosphate is observed as precursor for apatite ($Ca_5(PO_4)_3(F,Cl,OH)$) *in vivo*.[92] Nevertheless, sufficiently high supersaturations and pH values results in the formation of amorphous calcium phosphate *in vivo* as well as *in vitro*. The ratio of Ca^{2+} to PO_4^{3-} in amorphous calcium phosphate varies in the range from 1.18–2.50 depending on the pH value.[93] The amount of coordinating water molecules is reported to be 10–20 m%. Drying at elevated temperatures allows removing the tightly bound coordinated water without crystallization to apatite.[8]

Amorphous calcium phosphate is hypothesized to consist of sub-nanometer Posner clusters $Ca_9(PO_4)_6$, which are roughly spherical and closed packed with water molecules in the interstices.[8] *Ab initio* calculations using the restricted Hartree-Fock scheme showed that this structural motif in fact is more energetically favored in comparison to $Ca_3(PO_4)_2$ and $Ca_6(PO_4)_4$ units due to a specific bonding pattern. Within this pattern, Ca^{2+} is coordinated by 6 PO_4^{3-} groups which is also the case for apatite. This structural similarity also supports the theory that apatite is formed by aggregation of Posner cluster[94]. The occurrence of these nanometer-sized building blocks challenges classical nucleation theory anyway and may also complicate the underlying nucleation processes.

The amorphous phases are metastable and hydrolyze to the more stable phases, whereby the lifetime of the amorphous phase is a function of pH, ionic strength, and the presence of additives. Interestingly, precipitation experiments at high supersaturations and pH>10 showed an induction period for the formation of amorphous calcium phosphates depending on concentration, pH value, and ionic strength.[95] For moderate supersaturations, the lifetime of the amorphous phases were increased. At the first sight, higher supersaturations are supposed to cause rather the formation of amorphous phases accompanied with a longer lifetime. It is assumed that amorphous phases act as a template for the growth of the final crystals. However, apatite forms by consuming ions from solution rather than from direct hydrolysis of the amorphous solid. Consumption of ions in solution is driven by diffusion and is favored at

highly supersaturated solutions leading to an increased tendency to crystallize (shorter lifetime of amorphous solid).[95]

Furthermore, it is reported that a complex phosphate-water interplay tunes the metastability of ACC *in vivo*.[96] Phosphate ions were found in biogenic ACC to be molecularly dispersed as a solid solution.[97] The presence of phosphate ions reduces the chance of a nucleus forming.[98] In addition, the bulky ion PO_4^{3-} can disrupt the lattice of calcium carbonate which contains planar CO_3^{2-} ions which is known as "geometric frustration".[99] In the absence of phosphate, stepwise dehydration of hydrous ACC leads to phase separation and crystallization of calcite, whereas in the presence of phosphate, the geometric frustration increases the lifetime of the metastable ACC. Here, ACC has to diffuse first to particle's surface where it can dissolve partially and grow by ion-by-ion crystal growth. As a result, mixtures of calcite and hydroxyapatite are achieved. However, the mechanisms by which additives govern ACC stability are not well understood.[96]

Despite investigations in aqueous solution, there are some reports using solvothermal syntheses of metal phosphates and electrosyntheses. In addition, the direct melting of metals/metal oxides with P_2O_5/H_3PO_4 was investigated. One instance is the well-known formation of the so-called microcosmic salt beads used in qualitative analysis. For this purpose, $NaNH_4HPO_4 \times 4\ H_2O$ is molten forming a bead. A sodium metaphosphate ($(NaPO_3)_x$ with x=3–8) is formed by desorption of H_2O and NH_3. By adding heavy metal salts, heavy metal phosphates are formed, which reveal characteristic colors.[100] However, these synthesis routes reveal an increased number of possible experiment parameters in comparison to reactions in solution as well as a greater degree of freedom. Further, *in situ* studies are hardly possible.

In order to gain fundamental knowledge concerning nucleation, crystal growth, and metastable phases formed as intermediates during the formation of metal phosphates, we choose 3d metal phosphates as model systems. To the best of our knowledge, there are no general investigations of metastable intermediates formed during precipitation of 3d metal phosphates in aqueous solution. The goal of the project presented in this thesis was to gather more information about the early precipitation stages of 3d metal phosphates. Especially, the appearance of metastable intermediates is focused. Furthermore, it was our aim to understand the role of metastable phases during mechanochemical treatment of 3d metal phosphates.

In the first part of the thesis, the following questions are addressed:

(i) Do metastable metal phosphate hydrates occur as precursor for the formation of the crystalline modifications $Fe_3(PO_4)_2 \times 8\ H_2O$, $Co_3(PO_4)_2 \times 8\ H_2O$, $Ni_3(PO_4)_2 \times 8\ H_2O$ $Cu_3(PO_4)_2 \times 3\ H_2O$, and $Zn_3(PO_4)_2 \times 4\ H_2O$ in aqueous solution?

No additives are used for the stabilization but rather we try to isolate the intermediates by interrupting the precipitation process in early stages. The possible intermediates have to be comprehensively characterized in terms of composition and long-range/short-range order. Due to the transition metal character of Fe^{2+}, Co^{2+}, Ni^{2+}, and Cu^{2+}, changes in coordination environment and hydration state should influence significantly the respective absorption spectra. If intermediates exist, which are most probably amorphous, the following question will be opened:

(ii) What degree of hydration is present for the metal ions in the amorphous solids? What influence has a hydration network on the metastability of the solids?

This question is addressed by thermogravimetric analysis, ATR-FTIR, and NMR spectroscopy. A special focus lies on the dynamics of hydration networks in the possible amorphous intermediates as well as in the crystalline modifications.

(iii) What are the underlying mechanisms leading to the respective crystalline phosphate hydrates in aqueous solution? What are products of thermally induced crystallization processes?

Amorphous precursors are well-known as intermediates of complex crystallization processes in literature but the processes by which they transform to crystalline compounds are still poorly understood. Recrystallization kinetics of different amorphous phosphate hydrates may be observed quantitatively using ATR-FTIR spectroscopy *in situ*. The thermally induced crystallization can be monitored *ex situ* by thermogravimetric analysis and DTA.

(iv) Which role does water play during the precipitation of 3d metal phosphates?

For a long period of time it was assumed that water acts just as a solvent during nucleation and early crystal growth of biominerals instead of being an active ligand. Recent results show the diverse role of water during stepwise densification and dehydration.[37] 3d metal phosphates are very interesting model systems *a fortiori* because their thermodynamically stable crystalline modifications are hydrates. The role of coordinating water in the 3d metal phosphate systems is addressed by comparison of

precipitation in aqueous solution with anhydrous setups. For this purpose, silica shells and non-aqueous solvents are applied. Further, the precipitation behavior of 3d metal phosphates in the presence of massive supersaturation in phosphate is object of investigation.

(v) Do prenucleation clusters exist for the 3d metal phosphate systems?

This question is approached by using a constant pH titration setup with an ionic sensitive electrode. A solution containing Cu^{2+} is titrated into a phosphate buffer while the concentration of Cu^{2+} in solution can be monitored by the electrode. Comparison of the measured concentration and the "theoretical" concentration based on the titrated amount of solution will verify if Cu^{2+} is bound by a phosphate species in clusters in the prenucleation stage. The postnucleation stage will give essential information about the first solid species appearing during precipitation.

The second part of the thesis devotes metastable phases during mechanochemical treatment of crystalline 3d metal phosphate hydrates by focusing on the following questions:

(vi) What metastable phases occur during mechanochemical treatment of crystalline 3d metal phosphate hydrates in a planetary ball mill?

Interrupting the milling process after different time durations allows *ex situ* detection and characterization of possible metastable phases. Again, the role of coordinating water in the crystalline starting material and the possible intermediates is focused.

(vii) What are the underlying mechanism during mechanochemical treatment in a planetary ball mill?

The combination of static pressure and high shearing forces in a ball mill maybe accompanied by the formation of a plasma[101] is difficult to access. In literature, different *in situ* studies of mechanochemically induced transformations are reported using synchrotron X-ray diffraction.[102–104] A reference experiment applying high hydrostatic pressure in a diamond anvil will help to verify if the processes in planetary ball mills are dominated by pressure or by the present shearing forces.

(viii) Are the metastable phases generated under mechanochemical treatment different from the intermediates during precipitation?

This question is investigated by the recrystallization kinetics in water which may be different for metastable metal phosphates generated mechanochemically or trapped as

precursor during precipitation. Further, the influence of impurities during ball milling on the recrystallization behavior is addressed. Using ^{57}Fe enables high-precision Mössbauer measurements. This study provides experimental access to the local surrounding in non-equilibrium states.

Part I

3

AMORPHOUS ZINC PHOSPHATE HYDRATE: THE ROLE OF COORDINATING WATER

This chapter contains an adapted reproduction of *Journal of the American Chemical Society* **2015**, *136*, 2285–2294[105] reproduced with permission of the American Chemical Society Copyright 2015.

3.1 Introduction

As discussed in Chapter 1, classical crystallization pathways have their limitations and new model systems for crystallization are needed. A guideline for identifying candidates where non-classical crystallization routes might play an important role appears to be (i) the presence of cations whose charge density makes the hydration enthalpy comparable to the binding energy of counter-anions (*e.g.*, carbonates and phosphates), and/or (ii) the presence of anions whose acidity (pKs values) allows protonation, as hydrogen bonds may play an important role in packing and crystal chemistry. As a result polymorphs, which exhibit a distinctly different thermal behavior, may differ only in the position of a few hydrogen atoms, *i.e.*, in the orientation of water molecules coordinated to anions or cations. The different water orientations lead to different hydrogen-bonding patterns and small energy differences which, in turn, leads to the formation of metastable hydrated or eventually non-hydrated polymorphs as intermediates of a multi-stage crystallization process: (i) homogeneous precipitation of nanocrystalline hydrated phases, (ii) self-assembly of aggregates by condensation/dehydration via joint crystal faces, and finally (iii) transformation into thermodynamically stable end products. The moderate charge density of Ca^{2+} cations makes apatite[106] and $CaSO_4$[107,108] (besides $CaCO_3$) especially well-documented cases. Similarly, the charge density of Zn^{2+}

indicates the possibility to form a variety of hydrated polymorphs in compounds like zinc sulfate[109] or zinc phosphate.[110–115]

In nature, zinc phosphate occurs as tetrahydrate in two polymorphs, orthorhombic hopeite and triclinic parahopeite. Hopeite arises in three different modifications (*a*-, *β*-, and *γ*-hopeite) that differ only in the order of crystal water molecules.[116–122] Zinc hydrogen phosphate trihydrate (ZHPT) forms by slightly changing the synthesis conditions used to obtain *a*-hopeite.[115] Stepwise dehydration first leads to the formation of zinc phosphate dihydrate and later to anhydrous zinc phosphates.[115,123]

Crystallization of zinc phosphate in the presence of organic templates[75,124] leads to the formation of microporous zinc phosphates with zeolite-like topologies,[124–127] although the formation mechanism of these open framework structures is still poorly understood. Furthermore, zinc phosphates have important technical applications such as cements, filling material in plastics, as corrosion inhibitors, and for the prosthetic and conservative therapy of bones and teeth.[128–132] Hopeite ($Zn_3(PO_4)_2 \times 4\ H_2O$) and phosphophyllite ($Zn_2Fe(PO_4)_2 \times 4\ H_2O$) are important phases used in the formation of corrosion resistant coatings on steel[133–139] and as a host lattice for fluorescent materials or long-lasting phosphors.[140–142]

Inorganic nanoparticles tend to form polymorphs different from the thermodynamically stable one for small particle sizes, although hydrated and/or dehydrated amorphous phases are metastable with respect to their crystalline counterparts.[143] Calorimetric measurements by Navrotsky and coworkers[144] have shown the competition between lattice and surface energy to be responsible for this polymorph change,[145] and it could be shown that the stability regime of metastable polymorphs can be extended significantly for small particle sizes.

Therefore, the formation of amorphous zinc phosphate as a transient precursor during the early stages of crystallization may be preferred for nanoparticles, but so far there are only few reports on zinc phosphate nanoparticles. All synthetic approaches reported so far were concerned with confining the particle size. $Zn_3(PO_4) \times 2\ H_2O$ nanoparticles have been synthesized at room temperature by grinding sodium phosphate dodecahydrate and zinc sulfate heptahydrate in the presence of a non-ionic surfactant. However, these nanoparticles are crystalline with a diameter of 40–50 nm, a broad size distribution and a high degree of agglomeration.[146] In addition, $Zn_3(PO_4)_2$ nanoparticles have been prepared from microemulsions.[147] Amorphous zinc phosphate hydrate nanoparticles have been obtained in anhydrous media via the polyol method,[148] and solid-state NMR proved an important

analytical tool of characterization for both, amorphous and crystalline nanoparticles[148,149] because of its ability to probe local atomic environments. It delivered accurate and precise information on the water content of the samples[150] and the coordination of the phosphate moieties as demonstrated in a case study of non-crystalline zinc phosphate nanoparticles,[148] where a core-shell model was demonstrated with the aid of double resonance techniques. The size of the crystalline core was estimated using C-REDOR techniques.[151,152]

There are several challenges concerning the characterization of amorphous intermediates:

(i) Composition: The assumption of a single amorphous species may be too simplified, as more than one composition may exist. Besides impurities or surface active molecules[25] that may stabilize the amorphous phase water appears to be a key variable in the composition.

(ii) Configuration: The formation and configuration of the amorphous phase is difficult to unravel. An appealing model of the formation of a hydrated amorphous phase is the agglomeration of small cluster nuclei with water molecules of their solvation shell trapped by hydrogen bonding in between. This implies the loss and/or reorganization of hydration water and the reorganization of the clusters the rate determining steps during crystallization. There are several approaches to the configuration of amorphous phases. While techniques such as EXAFS typically probe the local coordination environment of the metal atoms, the pair distribution function (PDF) analysis provides information on local atomic order. A comparison of the PDF patterns for amorphous calcium carbonate[153] with those of its crystalline hydrous and anhydrous counterparts showed little resemblance.

(iii) The stability of the amorphous phase as a function of conditions is difficult to define. So far, only the transition enthalpy from ACC to calcite with a concomitant loss of water has been determined.[154] Although amorphous intermediates are assumed to be unstable with respect to the crystalline counterparts, little is known about the thermodynamics during nucleation and the early stages of nanoparticle formation.

Aim of the project presented in this chapter was to investigate the early stages of zinc phosphate formation in solution in the absence of additives. Assumed amorphous intermediates of zinc phosphate hydrate (AZP) should be isolated and characterized in terms of morphology, composition, missing crystallinity, and configuration. Thermal analysis and SS-NMR spectroscopy differentiated between surface water and configurational water in order to understand the role of water networks during precipitation of hydrated polymorphs.

3.2 Experimental

3.2.1 Synthesis

AZP nanoparticles were prepared by direct precipitation from solution. $Zn(NO_3)_2 \times 6\ H_2O$ (>98%, Sigma-Aldrich) (10 mL) (solution 1), and Na_3PO_4 (>96%, Sigma-Aldrich) were dissolved in deionized water (10 mL) (solution 2, both at ambient temperature), and solution 1 was stirred with 400 rpm in a beaker, while solution 2 was added. To instantly separate the precipitated solids from solution the mixture was centrifuged (9000 rpm, 5 min) immediately. Subsequently, the solid was resuspended in and centrifuged from reagent-grade acetone (≥99.5 %, Sigma-Aldrich) three times to remove adsorbed water. The solid was dried at room temperature under dynamic vacuum ($p=3\times10^{-3}$ mbar) for 2 d.

3.2.2 Characterization

The morphology of AZP nanoparticles was determined by TEM and SEM. SAXS measurements provided a size distribution of the particles. Information about the configuration of AZP were gained by ATR-FTIR spectroscopy and Raman spectroscopy. AZP's composition was determined by ICP-MS, ICP-OES, and EDX spectroscopy. High-resolution XRD at the 11-BM beamline at the Advanced Photon Source (APS), Argonne National Laboratory, confirmed the amorphous character of AZP. For further experimental details see Chapter 13.

In this chapter, solid-state NMR experiments were not performed as described in the Supporting Information. Instead, experiments were carried out on a Bruker Avance III-500 spectrometer equipped with a 1.3 and a 2.5 mm double resonance MAS probe at a ^1H frequency of 500.13 MHz (magnetic field 11.7 T) and on a Bruker Avance II spectrometer equipped with a 4 mm homemade double resonance MAS probe at a ^1H frequency of 200.0 MHz (magnetic field 4.74 T). Saturation combs were used before all repetition delays. The chemical shifts of ^1H were reported using the δ scale, relatively to 1% tetramethylsilane (TMS) in $CDCl_3$. The ^1H resonance of 1% TMS in $CDCl_3$ was also used as an external secondary reference for the ^{31}P resonance of 85% H_3PO_4 using the Ξ-values for ^{31}P as reported by the IUPAC.[155] The $^{31}P\{^1H\}$ MAS NMR spectrum was obtained at a sample spinning frequency ν_r of 40 kHz with repetition delays of 128 s and 16 transients. The ^1H MAS NMR spectrum was obtained at a sample spinning frequency ν_r of 40 kHz with a repetition delay of 1 s and 128 transients. Proton decoupling was implemented using PPM decoupling

with a nutation frequency of 100 kHz. The channels used in the C-REDOR[151,151] experiments are denoted as S{I}, where S refers to the observed nucleus and I to the recoupled one. The $^{31}P\{^{1}H\}$ C-REDOR experiment was performed at a sample spinning frequency ν_r of 40 kHz with a recycle delay set to 27 s, accumulated 32 transients/FID and was implemented using two-pulse phase-modulation (TPPM) decoupling with a nutation frequency of 16 kHz. The crystal structure of hopeite used for the calculation of C-REDOR curves was taken from [156].

3.3 Results and Discussion

3.3.1 Synthesis

Our initial attempts to synthesize AZP followed the approach of Faatz *et al.*[157] for the synthesis of ACC using the hydrolysis of a trialkyl phosphate in aqueous solution because ester hydrolysis proceeds on a time scale ideally suited for monitoring the reaction *in situ*. However, when trialkyl phosphates were hydrolyzed at a fixed pH in an aqueous solution of zinc chloride, ZnO (zincite) rather than AZP precipitated because at pH 11 (required for the ester hydrolysis) the solubility product (3.0×10^{-17} mol^{-3})[158] of $Zn(OH)_2$ was reached. $Zn(OH)_2$ quickly transforms in a follow-up reaction to ZnO.

Therefore, we attempted the precipitation of AZP by fast mixing of aqueous solutions of $Zn(NO_3)_2 \times 6\ H_2O$ and Na_3PO_4 (final pH=6.86). The precipitates were separated by centrifugation, resuspended in acetone, centrifuged, and finally dried to remove physisorbed water. According to Ostwald's rule,[6,46,109] the least stable (amorphous) polymorph should be formed first and transform subsequently to the thermodynamically stable hopeite (solubility product: 2.51×10^{-35} $mol^5\ L^{-5}$).[159] The thermodynamic driving force for the crystallization from solution is given by the difference in the chemical potential of zinc phosphate in a supersaturated solution and in the crystal. To precipitate specific polymorphs, the rate of nucleation and growth must be controlled by the degree of supersaturation. Classically, low supersaturations and long reaction times favor the formation of the thermodynamically stable polymorph at a given temperature. The formation of amorphous compounds at high supersaturations is not in conflict with a classical kinetic crystallization pathway,[6] but the classical model of equilibrium states appears to have limitations.[28] To understand the formation of amorphous zinc phosphate and its transformation in solution with time, the precipitation experiments were conducted at time intervals ranging from 5 s to 1 d with different starting concentrations (ranging from 10 to 300 mM) of the zinc nitrate and sodium phosphate solutions.

However, for short reaction times (5 s) and low concentrations (15 mM Zn^{2+} and 10 mM PO_4^{3-}) pure AZP was obtained as demonstrated by the absence of reflections in the X-ray diffractogram (Figure 3.1 A), whereas longer reaction times (>4 min) lead to the formation of crystalline hopeite (Figure 3.1 B). In contrast, crystalline hopeite was obtained even for the shortest reaction times from concentrated solutions (300 mM Zn^{2+} and 200 mM PO_4^{3-}), which might be due to another precipitation mechanism at higher concentrations.

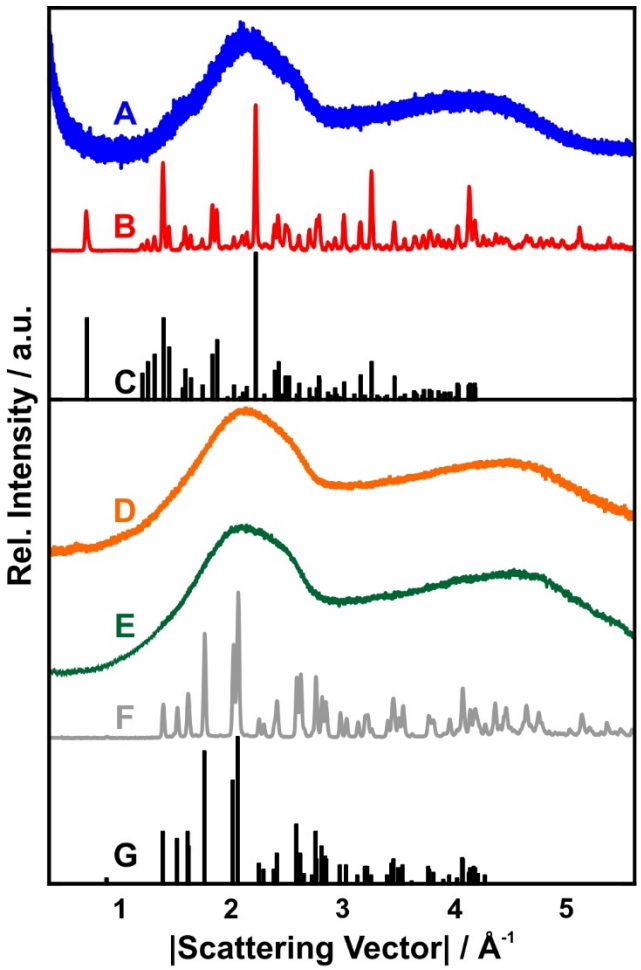

Figure 3.1. X-ray diffractograms of **(A)** amorphous zinc phosphate measured with high-energy synchrotron radiation and **(B)** hopeite. **(C)** Calculated line pattern of hopeite. **(D and E)** After heating A to 200 and 400 °C under argon for 1 week, the amorphous phase is still preserved. **(F)** At 600 °C only α-$Zn_3(PO_4)_2$, the thermodynamically stable phase at that temperature with **(G)** the calculated line pattern, was formed. Based on [105].

3.3.2 Composition

The results of ICP-MS and ICP-OES analyses performed with 30.3 mg of AZP are compiled in Figure 3.2 (left). They showed a Zn:P ratio of 3.00:1.98 in good agreement with the composition $Zn_3(PO_4)_2 \times n\ H_2O$. EDX spectroscopy (Figure 3.2, right) showed the presence of zinc, oxygen, and phosphorus without impurities from other precipitates. As the samples were coated with a thin layer sputtered carbon coating, a carbon signal appears in the spectrum as well. Semiquantitative analysis showed a Zn:P ratio of 3:2.

TEM snapshots of the product sampled after 5 s and prior to centrifugation (Figure 3.4 C, D) showed noncrystalline species of coalesced nanoparticles crystallizing under strong

ICP-MS	^{64}Zn	^{66}Zn	^{31}P
mean conc. / µg L^{-1}	131.1 ±2.9	130.7 ±3.4	41.3 ±0.9
mean conc. / µmol L^{-1}	2.05 ±0.05	1.98 ±0.05	1.33 ±0.03
ICP-OES	Zn		P
mean conc. / µg L^{-1}	132		41
mean conc. / µmol L^{-1}	2.02		1.32

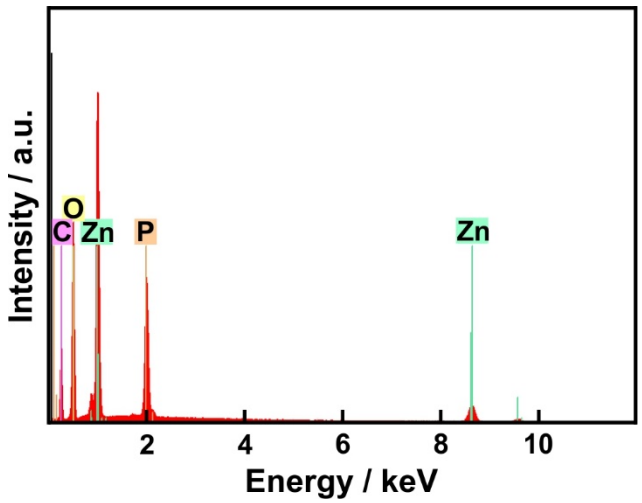

Figure 3.2. Quantitative analysis. **Left:** Results of the ICP-MS and ICP-OES measurements[a] for AZP; **Right:** EDX spectrum of AZP. Spectrum shows carbon due to sputtering with a layer of graphite. Based on [105].

[a]Mean concentrations (µg L^{-1}) and standard deviations for Zn and P in AZP; relative standard deviation of all the samples (RSD) are included.

electron radiation, reminiscent of liquid-like ACC particles obtained from related studies on $CaCO_3$.[160]

The nearly spherical nanoparticles had an average diameter of 22(2) nm and revealed a high degree of agglomeration, as can be seen in the SEM images (Figure 3.4 A, B) of the product sampled after 5 s and centrifuged subsequently. These observation are supported by SAXS measurements (Figure 3.3). The scattering curve of AZP shows no pronounced minima, indicating a high degree of aggregation (and/or polydispersity). From the central part of the scattering curve the radius of gyration as well as the zero-angle intensity can be deduced according to $I(q)=I_0 e^{-\frac{R_g}{3}q^2}$. Traditionally, the two structure parameters are determined by straight-line fitting in a so-called Guinier plot (see inset of Figure 3.3). Assuming spherical particles the average diameter can be calculated by $D=2\sqrt{5/3}\,R_g$.

For RT-AZP a radius of gyration of 20.0 nm was calculated, resulting in an average diameter of 51.6 nm. However, for particle systems with a high degree of agglomeration the Guinier plots do not display a sufficiently large linear region.

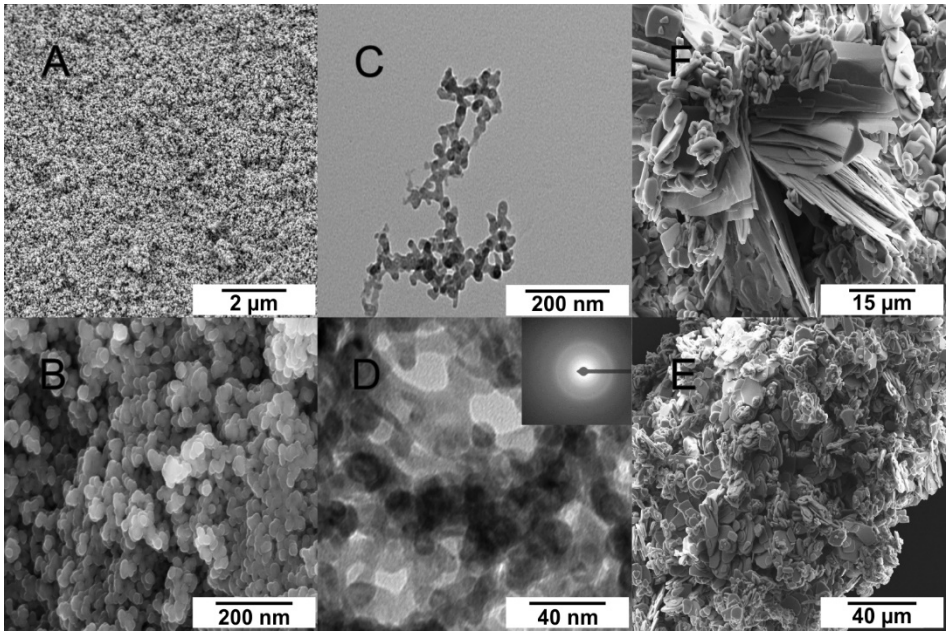

Figure 3.4. (A, B) SEM images of the precipitated AZP particles sampled 5 s after rapid mixing equal volumes of 15 mM $Zn(NO_3)_2$ and of 10 mM Na_3PO_4 solutions. **(C, D)** TEM images of AZP particles. The electron diffraction pattern shown in the inset of (D) is featureless, indicating the amorphous nature of the precipitate. **(E, F)** SEM images of hopeite sampled 4 min after rapid mixing equal volumes of 15 mM $Zn(NO_3)_2$ and of 10 mM Na_3PO_4 solutions. Based on [105].

A good approximation of the weight average particle volume that uses the entire scattering curve can be obtained by applying $V=2\pi^2 \frac{I_0}{Q}$ (Kratky approximation). Here I_0 is the forward scattering obtained from the Guinier fit and Q is the Porod invariant that can be calculated by $Q= \int_0^\infty q^2 I(q)dq$. From the particle volume the average diameter was determined

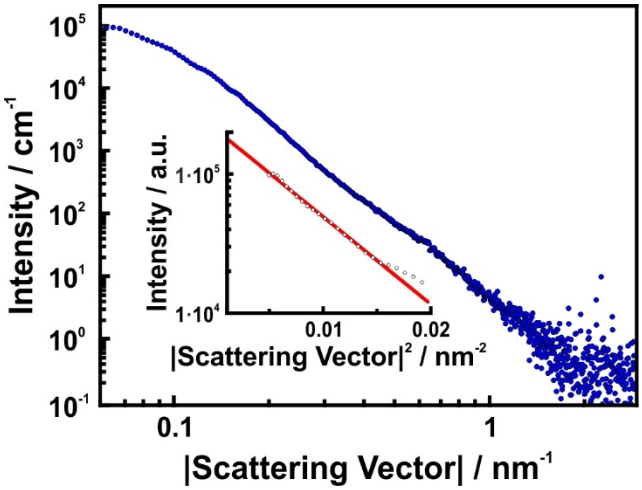

Figure 3.3. SAXS curve of RT-AZP. The inset shows a Guinier plot of the SAXS intensities (dotted black curves) with the Guinier fit (red line) for determination of the radius of gyration. Based on [105].

with 44.8 nm. The results of SAXS measurements should not be over-interpret due to the high degree of agglomeration of the particles.

However, the featureless SAED pattern shown in the inset of Figure 3.4 D supports the absence of long-range order in as-prepared zinc phosphate hydrate. Samples collected 4 min after rapid mixing of equal volumes of 15 mM $Zn(NO_3)_2$ and 10 mM Na_3PO_4 showed agglomerated plate-like crystals of hopeite (Figure 3.4 E, F).

As vibrational spectroscopy provides direct access to the structure of the different phosphates, we measured the IR spectra normalized to the phosphate stretching mode of AZP (Figure 3.5, trace A) and hopeite (Figure 3.5, trace B) together with the spectra of the annealing products at 200, 400, and 600 °C under argon for 1 week (traces C–E). The two bottom traces

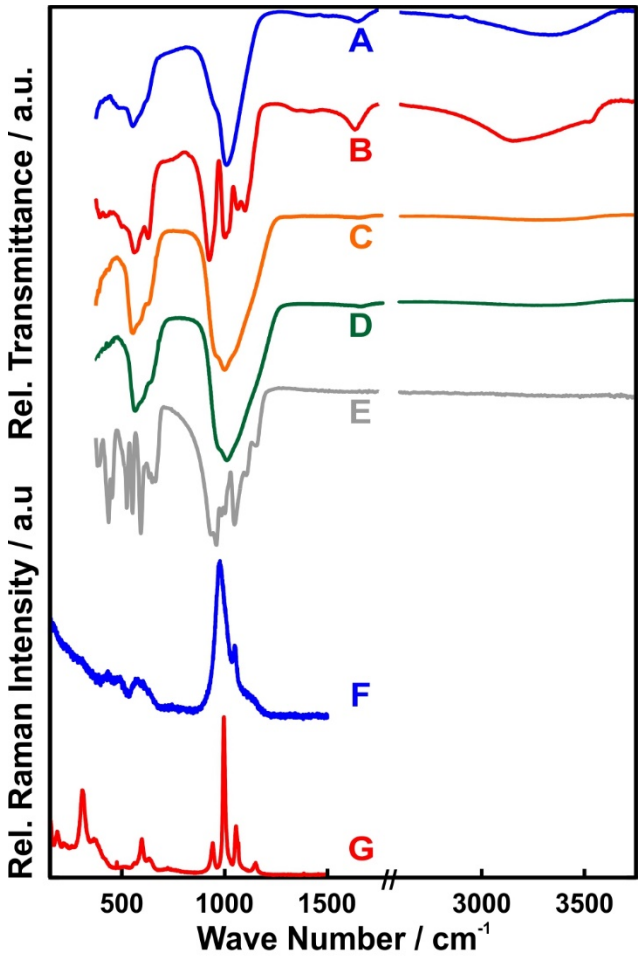

Figure 3.5. IR spectra normalized to the phosphate stretching mode of AZP **(A)** and hopeite **(B)**. At 200 and 400 °C (under argon, for 1 week) AZP is still amorphous but contains less water **(C and D)**. At 600 °C the thermodynamically stable phase at that temperature α-$Zn_3(PO_4)_2$ **(E)** exhibits a well-resolved band pattern. Raman spectra normalized to the phosphate stretching mode of hopeite **(G)** and AZP **(F)**. The bands of hopeite and α-$Zn_3(PO_4)_2$ are split because of lattice symmetry constraints Based on [105].

show the Raman spectra of hopeite (trace G) and AZP (trace F). Signals observed in both, IR and Raman spectra at 1000 cm^{-1} can be related to the stretching vibrations of the phosphate groups. The bands of free phosphate anions and water molecules are split due to factor group splitting and the lower site symmetry in the crystal structure of hopeite (traces B–G).[161] In AZP (traces A and F) no splitting occurs, and the bands ν_{as}(P–O) and δ_{as}(O–P–O) are broad but not split.

The water bands ν(O–H) and δ(H–O–H) become increasingly smaller in the spectra of the samples obtained at elevated temperatures (200, 400, and 600 °C) under argon. The non-split phosphate bands in traces D and E reveal that the samples are still amorphous, which can be seen by missing Bragg reflections in the corresponding XRD patterns as well (Figure 3.1 D, E). The annealed phases (HT-AZP) contained less water than the AZP at room temperature (RT-AZP), as extracted from the calculated extinctions of the bands of the stretching and deformation modes of water ν(O–H) and δ(H–O–H) in the IR spectra (normalized to the PO_4^{3-} stretching mode, Table 3.1). According to the Beer–Lambert law the extinction of vibrations arising from water is proportional to the concentration of structural water within the sample. From the compositions for RT-AZP derived by IR spectroscopy ($Zn_3(PO_4)_2 \times 1.9\ H_2O$), thermal analysis (*vide infra*, $Zn_3(PO_4)_2 \times 2.5\ H_2O$), and ^{1}H MAS NMR spectroscopy (*vide infra*, $Zn_3(PO_4)_2 \times 1.7 \pm 0.2\ H_2O$) we assume an averaged value of $Zn_3(PO_4)_2 \times 2\ H_2O$. For the HT-AZP polymorph we deduced an averaged composition of $Zn_3(PO_4)_2 \times 0.5\ H_2O$ (IR spectroscopy showed: $Zn_3(PO_4)_2 \times 0.4\ H_2O$, thermal analysis *vide infra*: $Zn_3(PO_4)_2 \times 0.5\ H_2O$, ^{1}H MAS NMR spectroscopy *vide infra*: $Zn_3(PO_4)_2 \times 0.5\ H_2O$). At 600 °C the anhydrous crystalline polymorph *a*-$Zn_3(PO_4)_2$ was formed (trace E). The bands of the phosphate groups are split and well resolved in the IR spectrum. No water bands were observed.

Table 3.1. Extinctions of the water bands in the normalized IR spectra of different zinc phosphate hydrates and resulting water content (formula units).

substance	E(ν(O–H)) / a.u.	water content	E(δ(H–O–H)) / a.u.	water content
hopeite	0.125	4.0	0.070	4.0
AZP	0.067	2.1	0.029	1.7
AZP, 200 °C	0.013	0.4	0.009	0.5
AZP, 400 °C	0.013	0.4	0.006	0.3
a-$Zn_3(PO_4)_2$	0.000	0.0	0.000	0.0

Table 3.2. Results of IR and Raman spectroscopy of different zinc phosphate hydrates in detail.

IR	δ_{as}(O–P–O)	Lit.	ν_{as}(P–O)	Lit.	δ(H–O–H)	Lit.	ν(O–H)	Lit.
AZP	557	n.a.	1005	n.a.	1643	n.a.	2580–3660	n.a.
hopeite	658, 561	635, 579	1099, 1003, 925	1107, 1009, 948	1643	1645	2600–3630	3000–3500
HT-AZP (200 °C)	559	n.a.	993	n.a.	1635	n.a.	2720–3730	n.a.
HT-AZP (400 °C)	557	n.a.	994	n.a.	1635	n.a.	2710–3720	n.a.
$Zn_3(PO_4)_2$	391, 436, 452, 524, 552, 592	n.a.	960, 984, 1005, 1047, 1153	n.a.	*		*	

Raman	δ_s(O–P–O)	Lit.	δ_{as}(O-P-O)	Lit.	ν_{as}(P–O)	Lit.	ν_s(P–O)	Lit.
AZP	§	n.a.	597	n.a.	977	n.a.	1051	n.a.
hopeite	307	310	597	598	942, 996, 1151	941, 997, 1150	1055	1055

n.a. – no data available
* – do not occur in spectrum
§ – cannot be resolved in spectrum due to background noise
Literature values for IR based on [161], values for Raman based on [162]

The Raman spectra of AZP and hopeite (bottom traces) show more bands than the corresponding IR spectra because all normal modes of the phosphate anion are Raman active. However, bands of AZP (traces F) are broad and non-split whereas the bands of hopeite (trace G) are split due to symmetry constraints in the crystalline structure.[162] For a complete listing of the vibration modes of the different phosphates see Table 3.2.

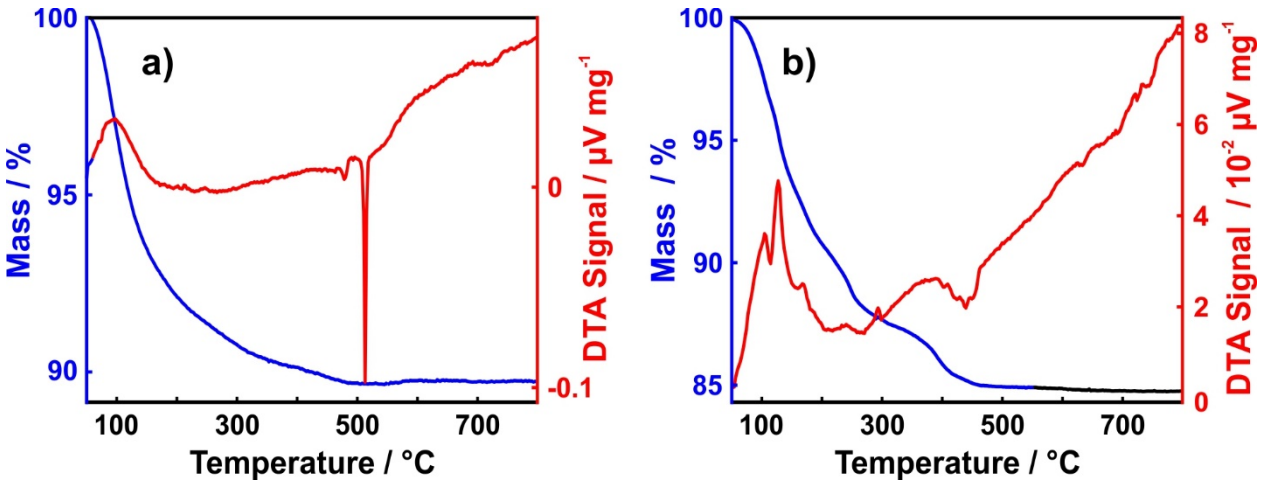

Figure 3.6. Thermogravimetric trace (blue line) and DTA signal (red line) of **a)** AZP and **b)** hopeite under argon. Based on [105].

3.3.3 Thermal Stability

The thermogravimetric and DTA traces of AZP under argon are displayed in Figure 3.6. A continuous weight loss of 10.28% (accompanied by an endothermic DTA signal at 97 °C) occurred during heat-up, which is attributed to the loss of structural water because (i) no other volatile components are present and (ii) XRD and vibrational spectroscopy showed that at 600 °C only anhydrous *a*-$Zn_3(PO_4)_2$ is present. Surface bound water was removed prior to the heating step by drying the sample *in vacuo*. The weight loss lead to an approximate composition $Zn_3(PO_4)_2 \times 2.5\ H_2O$ in agreement with the IR spectroscopic results ($Zn_3(PO_4)_2 \times 1.9\ H_2O$), *i.e.*, the amorphous phase contained less water than *a*-hopeite, the thermodynamically stable phase in this temperature range. Two exothermic signals in the DTA curve at 480 and 510 °C indicate a crystallization of AZP, where the anhydrous zinc phosphate *a*-$Zn_3(PO_4)_2$ is formed as demonstrated by XRD and IR spectroscopy (Figure 3.1 F and Figure 3.5 E). *a*-$Zn_3(PO_4)_2$ revealed a sintered structure as can be seen by SEM (Figure 3.7, left).

AZP had a high thermal stability up to 480 °C; even annealing at 200 and 400 °C for 1 week under argon left the amorphous character unchanged (see Figure 3.1 D, E). However, the annealing products (HT-AZP) at 200 and 400 °C contained less water than RT-AZP, which could be extracted from a quantitative analysis of the IR spectra (see Table 3.1) and derived by the weight loss observed in the thermal analysis (see Table 3.3). HT-AZP revealed exothermic signals at nearly the same temperature than AZP. As the differences in free enthalpy of formation of the different amorphous solids are minimal, all ensemble crystallize at the same temperature within the measuring accuracy. HT-AZP consists of coalesced spherical

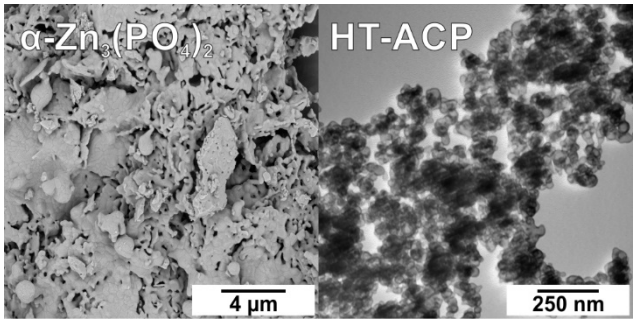

Figure 3.7. SEM images of α-$Zn_3(PO_4)_2$ synthesized by heating up RT-AZP one week at 600 °C under argon and TEM image of HT-ACP synthesized by heating up RT-AZP one week at 400 °C under argon. Based on [105].

nanoparticles slightly bigger than RT-AZP (Figure 3.7, right). The surprising stability of the amorphous nanoparticles can be explained either by very small volume diffusion coefficients in the solid state (kinetic barrier)[163] or by a crossover in thermodynamic stability at the nanoscale.[164] The presence of water during heat up in air leads to the formation of a mixture of zinc phosphate dihydrate, hopeite (which in fact contains more water than RT-AZP), and a large amount of amorphous phase at 200 °C. At 400 °C mixtures of *a*-$Zn_3(PO_4)_2$ and *β*-$Zn_3(PO_4)_2$ were obtained (Figure 3.8). *a*-Hopeite has been reported to release its crystal water in three steps,[123] (Figure 3.6 b) and *β*-hopeite is dehydrated via two metastable dehydration products, $Zn_3(PO_4)_2 \times 3\ H_2O$ and $Zn_3(PO_4)_2 \times H_2O$.[123]

As AZP contains less water than hopeite we assume that the transformation from AZP to hopeite must occur in aqueous solution or requires at least atmospheric moisture or surface water as a mineralizer and crystal building block.[163] Crystalline hopeite was obtained even after very short reaction times (approximately 1 min) by resuspending (RT or HT)-AZP nanoparticles in water and separating them by centrifugation. In contrast, AZP transformed to hopeite in air after days. AZP is stable for months when stored under dry conditions. A possible reason for this behavior is the significantly lower activation energy for surface diffusion than for diffusion in the solid state.[163] As surface diffusion coefficients are nearly

Table 3.3. Thermal analysis of HT-AZP and resulting water content (formula units).

substance	weight loss / %	water content
AZP	10.28	2.5
AZP, 200 °C	2.75	0.6
AZP, 400 °C	1.82	0.4

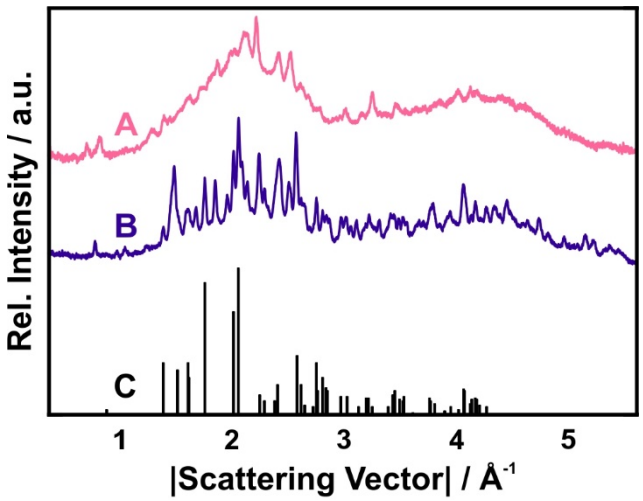

Figure 3.8. X-ray diffractograms of RT-AZP after heating in air for one week. **(A)** At 200 °C there is still a big amount of amorphous material in combination with zinc phosphate dihydrate and hopeite. **(B)** At 400 °C reflections of α-$Zn_3(PO_4)_2$ and *β*-$Zn_3(PO_4)_2$ can be observed with a smaller amount of amorphous material. **(C)** Calculated line pattern of α-$Zn_3(PO_4)_2$. Based on [105].

equivalent to those for diffusion in solution, adsorbed water leads to a high ion mobility of Zn^{2+} and PO_4^{3-} so that rearrangement and addition of water molecules lead to crystallization. Even a water film provided by atmospheric moisture may have this effect.[163]

3.3.4 Water Content and Mobility

The main goals of the solid-state NMR study were to (i) provide evidence of the amorphous structure of AZP, (ii) identify water of hydration and to quantify its amount, (iii) demonstrate that the transformation of AZP to hopeite is triggered by the uptake of

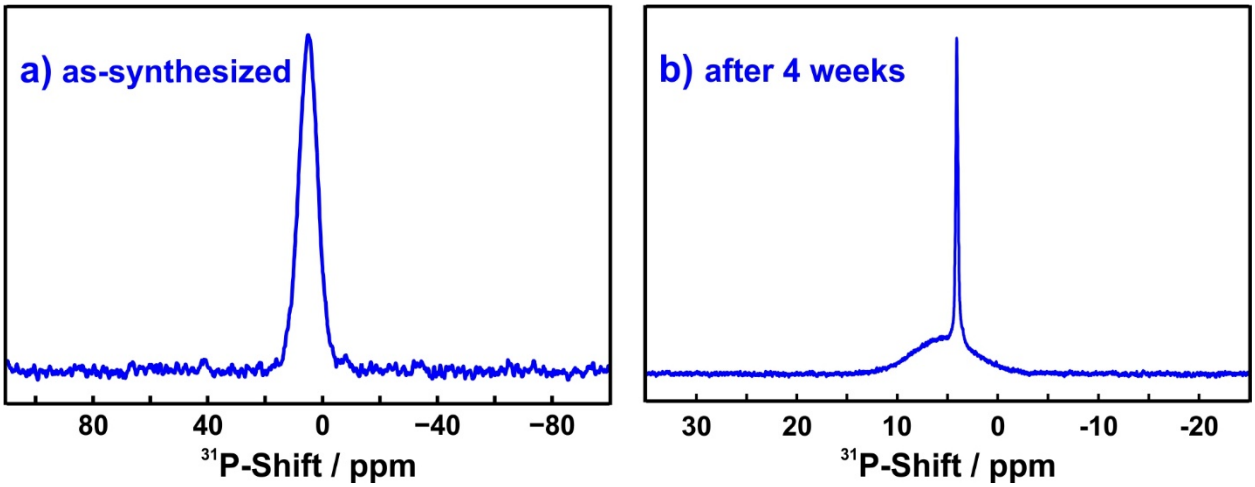

Figure 3.9. ^{31}P MAS NMR spectrum of AZP **a)** as-synthesized and **b)** after 4 weeks exposed to humidity. Data were measured at ν_r =40 kHz. Based on [105].

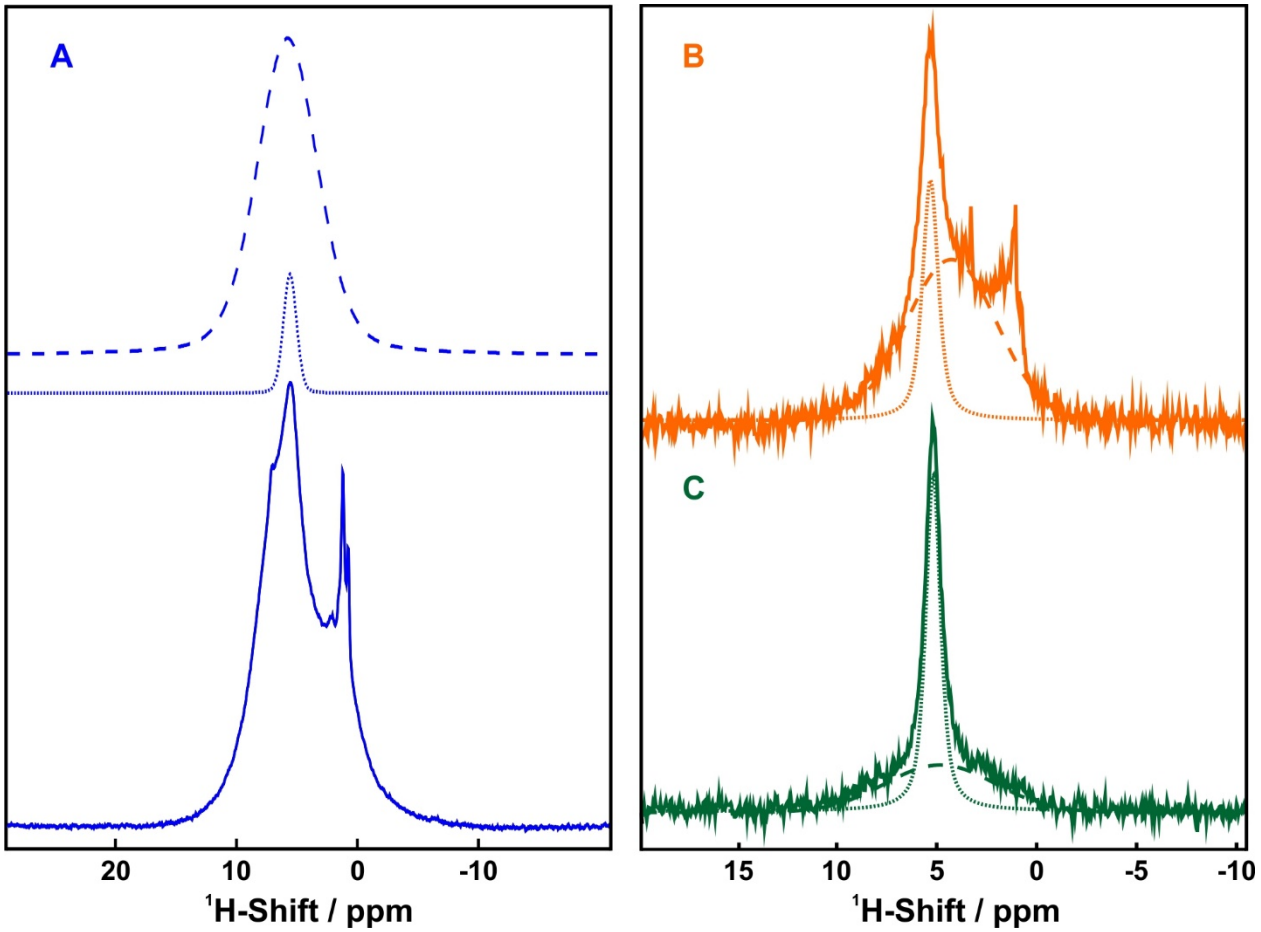

Figure 3.10. ^{1}H MAS NMR spectrum of **(A)** RT-AZP before and after heating at 200 °C **(B)** and 400 °C **(C)** under argon for one week. Spectra were background corrected and measured at υ_r=40 kHz with a repetition delay of 16 s and transients. The broad peak (dashed line) was assigned to structural water, while the sharper peak (dotted line) to mobile water adsorbed on the surface of the nanoparticles (see main text); peaks at≈1 ppm were assigned to acetone (used in the washing step) and the shoulder centered at≈7 ppm to an unknown phase, while the peaks at 1 and 7 ppm do not contain P-atoms according to the absence of dephasing observed in the ^{1}H{^{31}P} C-REDOR experiments (Figure 3.11). Based on [105].

atmospheric moisture, and (iv) study the stiffness of the hydrogen-bonding network which stabilizes AZP against crystallization. The ^{31}P MAS NMR spectrum of AZP (Figure 3.9 a) displayed a broad signal, which is characteristic of amorphous materials but can also be obtained from small nanosized crystalline structures. Its chemical shift at ≈5 ppm is typical for zinc orthophosphates.[148,165] The same spectrum, taken after a few weeks, showed a similar broad signal of the amorphous phase and an additional sharp peak that was assigned to crystalline hopeite (Figure 3.9 b). Unlike thermogravimetry, 1H MAS NMR is able to differentiate between and quantify structural and surface water in AZP. The 1H MAS NMR spectrum of AZP (Figure 3.10 A) showed mainly two peaks. One broad signal at 5.8 ppm

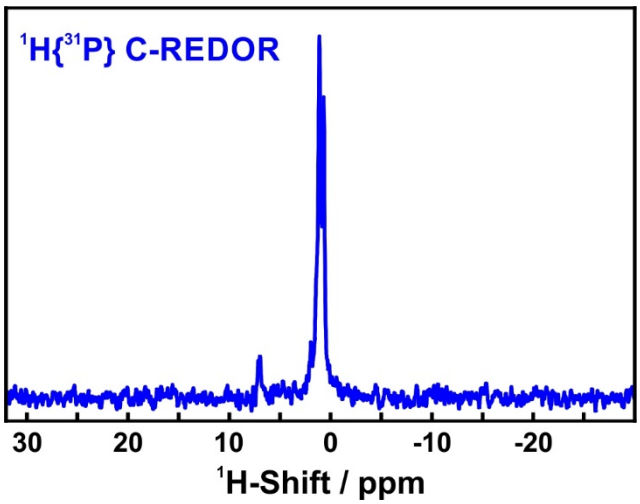

Figure 3.11. ^{1}H{^{31}P} C-REDOR curve of RT-AZP after a dephasing time τ=1.6 ms. Data were measured at ν_r=25 kHz with a repetition delay of 1 s and 16 transients/FID. Based on [105].

(dashed line) was assigned to structural water, while a sharper peak at 5.5 ppm (dotted line) to mobile water adsorbed on the surface of the nanoparticles because of the absence of spinning side-bands observed for the peak assigned to mobile water. Both line shape and assignment were confirmed by ^{1}H{^{31}P} C-REDOR experiments (Figure 3.11). These values are well within the range of chemical shifts reported for crystal water in inorganic materials.[165] The ^{1}H NMR quantification of the peak associated with structural water led to a composition $Zn_3(PO_4)_2 \times (1.7\pm0.2)\ H_2O$. The proton quantification of HT-AZP showed a composition with less structural water than RT-AZP (Figure 3.10 B → $Zn_3(PO_4)_2 \times (0.7\pm0.1)\ H_2O$ and C → $Zn_3(PO_4)_2 \times (0.3\pm0.1)\ H_2O$). We assume an averaged composition for HT-AZP of $Zn_3(PO_4)_2 \times 0.5\ H_2O$ calculated by NMR, which is in agreement with the results of IR spectroscopy and thermal analysis (see Table 3.3). In order to corroborate the hypotheses that AZP is stabilized by a rigid hydrogen-bonding network and that it transforms to *a*-hopeite by absorbing atmospheric moisture, C-REDOR[151,152] experiments and a moment-based line shape analysis were performed. The curve of AZP (crosses in Figure 3.12 a) showed a slower dephasing toward the value $\Delta S/S_0 = 1$ than the curve of *a*-hopeite (circles in Figure 3.12 b). Simulations helped to understand these results, which we will discuss in the following.

C-REDOR is one flavor of the prominent REDOR[166] experiment. Both are used to determine internuclear distance constraints and study spatial proximities between NMR-active nuclei.[167] In the case of a multispin system the use of C-REDOR is more advantageous, since it is able to suppress to first order average Hamiltonian theory[168] unwanted homonuclear dipole–dipole interaction.[151,152] Analytical expressions for the investigation of multispin

systems have been derived for the REDOR[169,170] experiment and adapted to C-REDOR (Equation 3.1 and 3.2).[171]

$$\langle \frac{S_D}{S_0} \rangle = \langle \prod_{k=1}^{n} \cos\left[\sqrt{2/3}\, \pi |\kappa| \nu_{dip,k} \tau \varepsilon_k \right] \rangle \qquad 3.1$$

$$\nu_{dip,k} = -\frac{\mu_0 \gamma_I \gamma_S \hbar}{8\pi^2 r_k^3} \qquad 3.2$$

Explanation of symbols used in Equation 3.1 and 3.2:

The normalized dipolarly dephased signal of the C-REDOR experiment of a powder $\langle S_D/S_0 \rangle$ is analytically determined by Equation 3.1. It is the product of cosine terms integrated over the set of Euler angles that connect crystal frame and rotor frame (powder average) indicated by angle brackets. There are n cosine terms, one for every pair made out of the observed spin S and one of the spins I in a SI_n spin system. Each of these terms is a function of: (i) the time during which the C-REDOR sequence is applied, also called dephasing time; (ii) the scaling factor $\varkappa$ that reflects the efficiency of a pulse sequence; (iii) a factor ε_k that depends on Euler angles that connect four (or more) different frames of reference to one another, ultimately defining the orientation of the dipole-dipole interaction towards the static magnetic field of the spectrometer; and (iv) the dipole coupling constant $\nu_{dip,k}$. The latter is a function of the gyromagnetic ratios of the nuclei (γ_I and γ_S) and the internuclear distance r_k

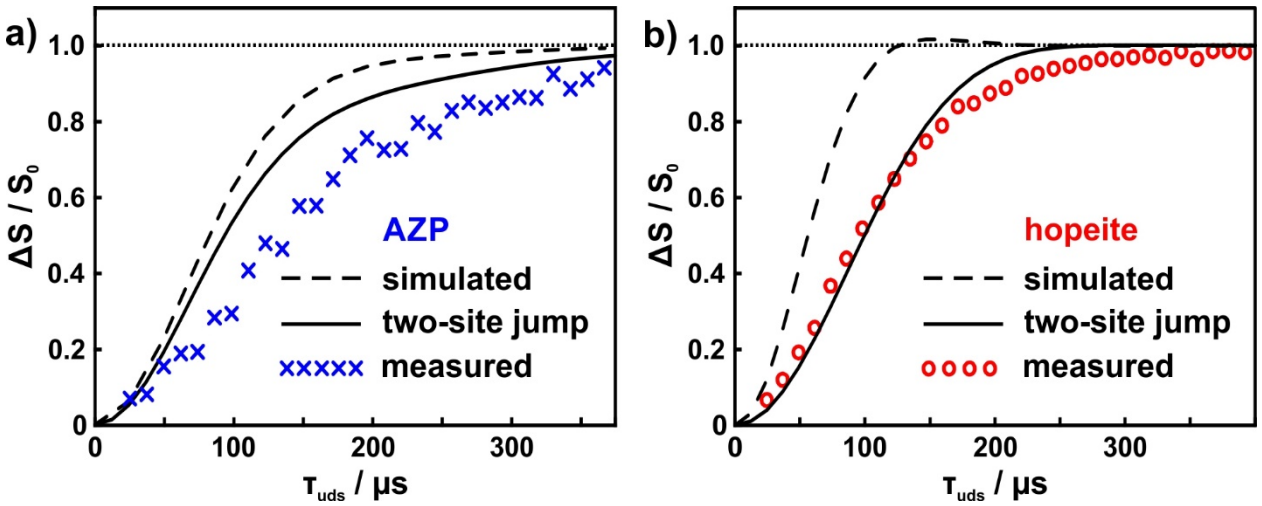

Figure 3.12. Experimental and simulated $^{31}P\{^1H\}$ C-REDOR curves. Experimental curve of the amorphous component (crosses) and crystalline α-hopeite (circles). Simulated curve for α-hopeite: static model (dashed line) and one under consideration of the two-site jump between hydrogen atoms in structural water molecules (solid line). Data were measured at ν_r=40 kHz. Based on [105].

between the two spins (Equation 3.2). The vacuum permeability constant is given by $\mu_0=4\pi\times10^{-7}$ Hm^{-1} and ħ is Planck's constant. γ is the gyromagnetic ratio of the nucleus; I is the nuclear spin quantum number; N is the number of resonant spins; and r_{ij} is the distance between the i nucleus and the j nucleus. Based on this knowledge it is possible to predict accurate C-REDOR curves of a crystal up to full dephasing with a home-written Fortran90 program, which can handle the interactions between thousands of spins. It turns out that the simulation converges for spin systems with around 80 spins or more, where the atomic positions can be retrieved from crystallographic data.

The dashed line in Figure 3.12 b) displays the analytically calculated $^{31}P\{^1H\}$ C-REDOR curve of *a*-hopeite based on Equation 3.1 using the universal dephasing scale τ_{uds}.[148] A better agreement between experimental and simulated data is achieved after incorporating a two-site jump process (illustrated in Figure 3.13) between the two hydrogen atoms in a water molecule into the calculation (solid line) according to Equation 3.3.[171]

$$\left\langle \frac{S_D}{S_0} \right\rangle = \left\langle \prod_{k=1}^{n} \cos\left[\sum_{j=1}^{N} p_{eq}(j) \left[\sqrt{2/3}\,\pi |\kappa| \nu_{dip,k} \tau \varepsilon_k \right] \right] \right\rangle \qquad 3.3$$

In this model, the two hydrogen atoms of the water molecule switch places infinitely fast as in an N-stepped jump process. The difference between Equation 3.1 and 3.3 is in the cosine's argument that is now the weighted sum of the N possible positions of the kth spin, in this case one of the hydrogen atoms. The weighting factor is given by the probability $p_{eq}(j)$ of finding an atom in a certain position, where $\sum_{j=1}^{N} p_{eq}(j) = 1$. Clearly, the experimental curve for *a*-hopeite can be described neither by a static spin-system nor by a completely mobile arrangement of H–atoms. The truth is somewhere in between. We attribute the deviations between experiment and simulation to random local motional processes like the shown two-site jump, where $\sum_{j=1}^{N} p_{eq}(j) = 1$. Clearly, the experimental curve for *a*-hopeite can be described neither by a static spin-system nor by a completely mobile arrangement of H–atoms. The truth is somewhere in between. We attribute the deviations between experiment and simulation to random local motional processes like the shown two-site jump.

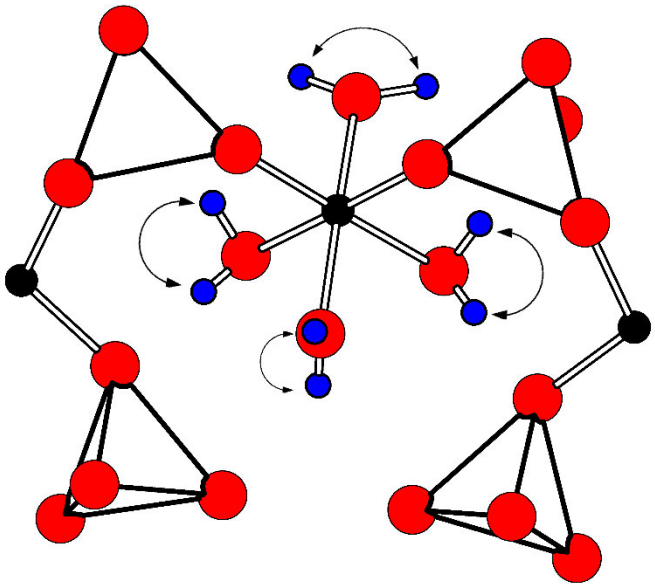

Figure 3.13. Excerpt from the crystal structure of hopeite, showing the two-site jump process between the two hydrogen atoms of crystal water molecules, which was taken into account to simulate the $^{31}P\{^{1}H\}$ C-REDOR curve (gray spheres, O; empty spheres, H; black spheres, Zn atoms; P atoms are located in the center of the tetrahedron formed by the O atoms). Based on [105].

The $^{31}P\{^{1}H\}$ C-REDOR curve of AZP slower dephases than that of *a*-hopeite (Figure 3.12 a) and b). This translates to a lower value of the so called effective dipole dipole constant.[172] In principle this can be explained by a lower water content, longer $^{31}P–^{1}H$ distances, dynamics or a combination thereof. Since AZP is amorphous, the prediction of its $^{31}P\{^{1}H\}$ C-REDOR curve is not trivial. Taking *a*-hopeite as a model for AZP the lower content of H-atoms in form of structural water offers a simple explanation for the slower dephasing of the respective REDOR curves. We took the structure of *a*-hopeite with only half of the amount of structural water as a model for AZP and predicted the average static C-REDOR curve and the average one accounting for two-site jumps. We conclude that the REDOR experiments give evidence for hydrogen-bonding network where local H-motions are partially activated and lead to less efficient dephasing than that of a rigid hydrogen-bonding network.

In the following we will analyze the second moment of the static ^{1}H NMR spectra of AZP and *a*-hopeite as a second tool to study the stiffness of the hydrogen bonding network. Second moments of the line shape are sensitive to dynamics in solids and can be calculated according to the Van Vleck formula:[173,174]

$$M_2^{II} = \frac{3}{5}\left(\frac{\mu_0}{4\pi}\right)^2 \gamma^4 \hbar^2 I(I+1) \frac{1}{N} \sum_{i \neq j}^{N} \frac{1}{r_{ij}^6} \qquad 3.4$$

In Equation 3.4 M_2 is given in angular frequency. Based on crystallographic data, we calculated the square roots of the second moments $\sqrt{M_{2,calc}^{II}}/(2\pi)$ of gypsum[175] ($CaSO_4 \times 2\ H_2O$), chalcanthite[176] ($CuSO_4 \times 5\ H_2O$), and *a*-hopeite as rigid structures (Table 3.4).

For a single structural water molecule in gypsum Equation 3.4 features $\sqrt{M_{2,calc}^{II}}/2\pi = 22.4\ \mathrm{kHz}$. Comparing this value to the case of some hydrated minerals (Table 3.4), it becomes clear that the value of the intramolecular interaction is already close to the value calculated for a whole crystal structure. For this reason, many other hydrates (not shown) feature a value $\sqrt{M_{2,calc}^{II}}/2\pi$ in this range. Here it should be noted, that the observable experimental values at room temperature and even at lower ones are often a lot smaller due to the dynamics of structural water.[177–179]

The experimental value of $\sqrt{M_{2,calc}^{II}}/2\pi = 40\ \mathrm{kHz}$ for *a*-hopeite (spectrum not shown) is therefore very large. The calculated value is also large, although the best crystal structure we found for calculation was solved by XRD, which leads to controversial hydrogen positions. Taking into account contributions from heteronuclear interactions (≈1 kHz), ^{1}H chemical shift

Table 3.4. Square roots of second Moments $\sqrt{M_{2,calc}^{II}}/2\pi$ of hydrates calculated for rigid structures and a few of the shortest H–H distances.

substance	$\sqrt{M_{2,calc}^{II}}/2\pi$/ kHz	r_{HH} / Å
$CaSO_4 \times 2\ H_2O$[a]	24.4[a,c]	1.533
$CuSO_4 \times 5\ H_2O$[a]	23.9[a,c]	1.552/1.540/1.567/1.600
$Zn_3(PO_4)_2 \times 4\ H_2O$[b]	33.9[b,c]/40.0[d]	1.249/1.315/1.853

[a] Neutron diffraction data.
[b] XRD data.
[c] Calculated value according to Equation 3.4.
[d] Experimental value, this work.

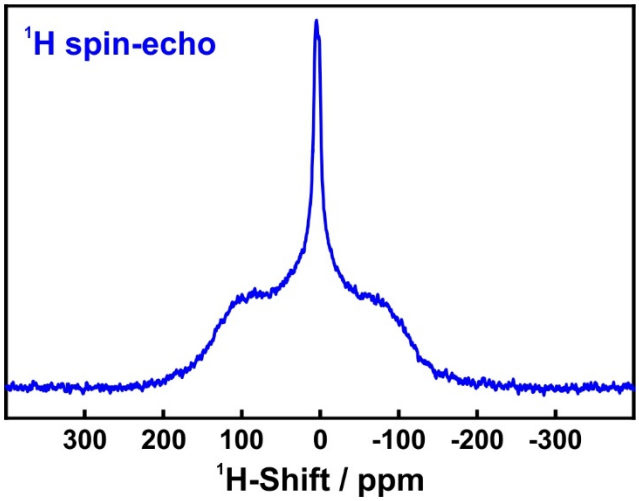

Figure 3.14. Static ^{1}H spin-echo NMR spectrum of RT-AZP measured with a repetition delay of 2 s, 1024 transients and an evolution time of 20 μs. Based on [105].

anisotropy (up to ≈4.3 kHz), and transverse relaxation (≈1 kHz), we conclude that the motion in *a*-hopeite can be described as a two-site jump which does not reduce the main contribution[180] to the second moment and explains both the observed C-REDOR curve and the static ^{1}H line shape.

The experimental value of $\sqrt{M_{2,calc}^{II}}/2\pi = 17$ kHz for RT-AZP was estimated from a ^{1}H spin–echo spectrum of a static sample (Figure 3.14) while neglecting the contribution from the distribution of chemical shifts in a noncrystalline sample. This value is already close to the calculated ones for other hydrates, which represent models featuring rigid structural water molecules (Table 3.4). In fact, such experimental values are often only achieved at lower temperatures. Thus, structural water in AZP seems to show only little dynamics at room temperature as compared to other hydrates. Thus, the observations made in the NMR experiment indicate a stiff hydrogen-bonding network, which explains that AZP is relatively stable against crystallization.

3.4 Conclusion

Zinc phosphate is an attractive example for examining fundamental processes of crystallization. (i) It is polymorphous, and we were able to synthesize (ii) amorphous zinc phosphate hydrate nanoparticles (AZP) with diameters of≈20 nm by direct precipitation from aqueous solutions of Zn^{2+} and PO_4^{3-} at low concentrations and short reaction times (subsequent annealing results in a high-temperature phase). (iii) Zinc phosphates are structurally still simple enough to serve as model compounds for a fundamental understanding of nucleation and crystallization processes from aqueous solution.

The synthesis of the AZP nanoparticles supports the hypothesis that the formation of the metastable over the thermodynamically stable polymorph (with higher lattice energy) is favored because of surface energy. The precipitation must be fast in order to avoid the precipitation of $Zn(OH)_2$ ($K_{SP}=3.0\times10^{-17}$ mol^{-3}) which is formed in a competing reaction even at neutral pH. Furthermore, the separation of AZP must be fast enough to avoid the transformation to hopeite via dissolution–recrystallization. This could be demonstrated by resuspending AZP nanoparticles in water and monitoring their transformation to hopeite.

In agreement with thermoanalytical results, hydrogen quantification using ^1H solid-state NMR and heteronuclear dipolar recoupling experiment (C-REDOR) showed lower water content in AZP than in *a*-hopeite. Simulations of C-REDOR curves and a second moment analysis indicated dynamics in *a*-hopeite and AZP to be described as an infinitely fast two-site jump process, with an otherwise rather rigid structural water network.

AZP was characterized by electron microscopy, XRD and SAXS, vibrational, MAS NMR spectroscopy, and thermal analysis. It is extraordinarily stable in the absence of water. Annealing RT-AZP with the approximate composition $Zn_3(PO_4)_2 \times 2\ H_2O$ at 400 °C resulted in the formation of HT-AZP with lower water content ($Zn_3(PO_4)_2 \times 0.5\ H_2O$). Anhydrous *a*-$Zn_3(PO_4)_2$ was formed at 600 °C by release of structural water. The "water deficient" amorphous phase may provide a starting point for further structural investigations. However, it would not be accurate to say that zinc phosphate shows polyamorphism because RT-AZP and HT-AZP differ in their water content and therefore do not have the same composition.[181–183]

What is the reason for the thermal stability of AZP with respect to hopeite? First, hopeite ($Zn_3(PO_4)_2 \times 4\ H_2O$), the thermodynamically stable crystalline polymorph, contains more structural water than the AZP. In addition, the transformation from the amorphous to the crystalline phase may occur (i) via dissolution and recrystallization or (ii) as a direct solid–solid

transformation. During the crystallization of AZP water serves as a mineralizer that facilitates the transport of the insoluble "nutrient" to a seed crystal, *i.e.*, it acts as catalysts for crystallization by enhancing the mobility of the ionic constituents.[184] Upon heating in the absence of water this process is blocked, and AZP is stabilized kinetically. Loss of coordinating water leads to variety of different hydrated amorphous solids, while the amount of water does not influence the thermally induced crystallization in a significant way. We assume that a variety of other systems exist where amorphous polymorphs play an important role as crystallization intermediates. Good indicators should be (i) the cation charge density, which makes the hydration enthalpy comparable to the binding energy of the counter-anions. (ii) Anions whose acidities allow the formation of hydrogen-bonded networks may favor multistage crystallization processes involving the homogeneous precipitation of nanocrystalline hydrated phases, and an assembly of aggregates by condensation/dehydration with subsequent transformation into thermodynamically stable end products. The moderate charge densities of Zn^{2+} and PO_4^{3-} allow the formation of hydrogen-bonded networks in hydrated polymorphs of zinc phosphate.

4

AMORPHOUS COBALT PHOSPHATE HYDRATE: SHORT-RANGE ORDERING

This chapter contains a manuscript submitted to *Crystal Growth and Design*.[185]

4.1 Introduction

As described in the previous chapter, water has an essential role during crystallization of hydrated polymorphs. Moderate charge densities of the respective cation allow reversible hydration and therefore intermediates with various degrees of coordinating water may be a consequence. Inspired by the synthesis of amorphous zinc phosphate hydrate, we present here a facile method for preparing an amorphous cobalt phosphate hydrate.

Following our idea of various hydrated intermediates, cobalt phosphate hydrates represents an interesting substance class as $Co_3(PO_4)_2 \times 8\ H_2O$[186] is the thermodynamically stable modification of cobalt phosphate hydrates at ambient conditions with a high content of crystal water. Besides as octahydrate, cobalt phosphate occurs as tetrahydrate,[187] two monohydrates[187,188] and an anhydrous cobalt phosphate.[189] A special feature of the cobalt phosphate system is the dependence of the optical absorption on differences of the hydration state and the coordination number of Co^{2+}, allowing even a visual discrimination of the cobalt coordination. This has been utilized in inorganic pigments labeled "cobalt violet" (a general term for a group of pigments including cobalt phosphate, cobalt phosphate octahydrate, lithium cobalt phosphate, and ammonium cobalt phosphate) in paintings of the 19th century, whose colors range from light pink-purple to deep purple-violet.[190] Preparing cobalt phosphates in presence of gelatin gained Liesegang banding. Depending on the uptake of surrounding water, different hydrated cobalt phosphates and cobalt oxides are formed differing strongly in the color and structure.[191]

Research on cobalt phosphate hydrates is mainly focused on its catalytic properties, especially for oxygen evolving.[192–195] The formation of cobalt phosphate (analogous to zinc phosphate)[105,148] nanoparticles as a transient intermediate during the early stages of crystallization has been analyzed theoretically,[153] but there is no experimental evidence so far. Even more, there are additional challenges concerning our understanding of its composition, configuration and stability.

Within the scope of this work, we synthesized an amorphous cobalt phosphate hydrate (ACP) by an easy precipitation experiment. Besides a comprehensive characterization of the amorphous material, we followed crystallization kinetics induced by the presence water provided by humidity to gain knowledge about the molecular ordering processes and the essential role of water. Different coloring of ACP and $Co_3(PO_4)_2 \times 8\ H_2O$ gave first hints for different coordination and hydration. EXAFS and XANES measurements provided insights into coordination of Co^{2+} within the solids as well as into bond lengths present. These results will help to understand the role of amorphous intermediates with less coordinating water during precipitation of hydrates polymorphs.

4.2 Experimental

4.2.1 Synthesis

Amorphous cobalt phosphate hydrate was prepared by precipitation from solution. $Co(NO_3)_2 \times 6\ H_2O$ (>99%, Acros) and Na_3PO_4 (>96%, Sigma-Aldrich) were dissolved in 10 mL of deionized water at room temperature (solution 1 and 2), respectively. Solution 1 was stirred with 400 rpm in a beaker and solution 2 was added. The precipitation was carried out at different temperatures (20–60 °C). The precipitate was separated immediately by centrifugation (9000 rpm, 5 min). Subsequently, the solid was resuspended in and centrifuged from reagent-grade acetone (≥99.5%, Sigma-Aldrich) 3 times in order to remove adsorbed water. Finally, the solids were dried at room temperature and under dynamic vacuum ($p=3\times10^{-3}$ mbar) for 2 d.

4.2.2 Characterization

Composition of ACP was determined by ICP-MS, ICP-OES, and EDX spectroscopy. Its morphology was observed by SEM and TEM, while SAXS provided a size distribution of nanomaterial. UV-Vis spectroscopy gave first hints for a different coordination number of Co^{2+} in ACP as well as different bond lengths. This was investigated in more detail by EXAFS and XANES spectroscopy.

The degree of crystallinity of partially crystalline samples was determined quantitatively by IR spectroscopy. Mixtures with known ratios of crystalline $Co_3(PO_4)_2 \times 8\ H_2O$ and ACP were measured by IR spectroscopy for calibration. Therefore, the density of ACP was determined pycnometrically, the density of $Co_3(PO_4)_2 \times 8\ H_2O$ roentgenographically. By normalizing the spectra to the asymmetric stretching mode of phosphate and measuring the extinction of the symmetric stretching mode (only occurring in $Co_3(PO_4)_2 \times 8\ H_2O$), we obtained standards for the quantification. For reactions in water the splitting of the PO_4^{3-} was considered instead because the symmetric stretching mode was superimposed by water vibrational bands.

For further experimental details see Chapter 13.

4.3 Results and Discussion

4.3.1 Synthesis

The early stages of the precipitation of cobalt phosphate octahydrate were synthesized by fast mixing of aqueous solutions of $Co(NO_3)_2 \times 6\ H_2O$ and Na_3PO_4. In order to prevent crystallization according to Ostwald's rule, the precipitates were separated quickly by centrifugation, resuspended in acetone, centrifuged, and dried *in vacuo*. Also here, the least stable (amorphous) polymorph is expected to form first and to transform subsequently into cobalt phosphate octahydrate, the thermodynamically stable polymorph at room temperature (solubility product: $2.05 \times 10^{-35}\ mol^5\ L^{-5}$).

Therefore, we performed precipitation experiments with different starting concentrations, reaction times and temperatures during precipitation (see Table 4.1). We are aware that the reaction will proceed to a certain extent during centrifugation. Still, the results were unaffected by shorter centrifugation times (1 min and 3 min). Therefore, we assume that crystallization is interrupted at very early stages by centrifugation. Pink crystalline $Co_3(PO_4)_2 \times 8\ H_2O$ was precipitated from concentrated starting solutions (300 mM Co^{2+} and 200 mM PO_4^{3-}) at every temperature even at the shortest reaction times. In contrast, deep-blue ACP was precipitated for low concentrations (15 mM of Co^{2+} and 10 mM of PO_4^{3-}) at room temperature for reaction times ≤5 min, whereas mixtures of ACP and $Co_3(PO_4)_2 \times 8\ H_2O$ were obtained for longer were obtained for longer reaction times (Figure 4.1 A, B). This may suggest that at higher concentrations the precipitation of cobalt phosphate follows a different mechanism.

Table 4.1. Experimental conditions during precipitation.

reaction time	reaction temperature / °C	concentration Co^{2+}—PO_4^{3-} / mM	result
5 s	25	15—10	amorphous
5 min	25	15—10	amorphous
5 min	≥30	15—10	partially crystalline[a]
≥20 min	25	15—10	partially crystalline
≥5 s	25	300—200	partially crystalline

[a] for detailed analysis see Section 4.3.5.

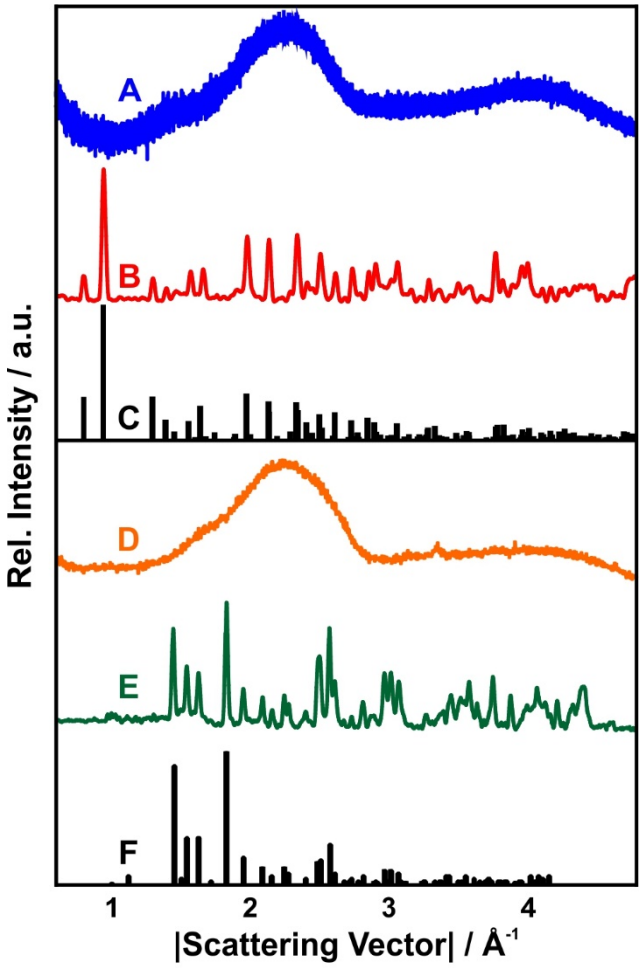

Figure 4.1. X-ray diffractograms of **(A)** amorphous cobalt phosphate (ACP) (measured with high-energy synchrotron radiation) and **(B)** $Co_3(PO_4)_2 \times 8\ H_2O$ with its calculated line pattern **(C)**. **(D)** After heating to 500 °C under argon for 1 week the amorphous phase is still preserved. **(E)** At 600 °C only anhydrous $Co_3(PO_4)_2$, the thermodynamically stable phase at that temperature was present. **(F)** Calculated line pattern of $Co_3(PO_4)_2$. Based on [185].

4.3.2 Composition

In order to determine the composition of the as-synthesized amorphous intermediate, ICP-MS and ICP-OES measurements were performed with 25.7 mg of ACP. The results, compiled in Figure 4.2, show a Co:P ratio of 3:2.01 in good agreement with a composition $Co_3(PO_4)_2 \times n\ H_2O$. An EDX spectrum confirmed the presence of cobalt, oxygen, and phosphorous (and the absence of impurities). Signals of carbon and silver arise from the TEM carbon grid and a thin layer of sputtered silver coating. A Co:P ratio of 3.00:2.04 could be determined by semiquantitative analysis.

ICP-MS	^{59}Co	^{31}P
mean conc. / µg L^{-1}	99.4±3.4	33.6±0.7
mean conc. / µmol L^{-1}	1.68±0.06	1.08±0.02
ICP-OES	Co	P
mean conc. / µg L^{-1}	102	26
mean conc. / µmol L^{-1}	1.7	1.2

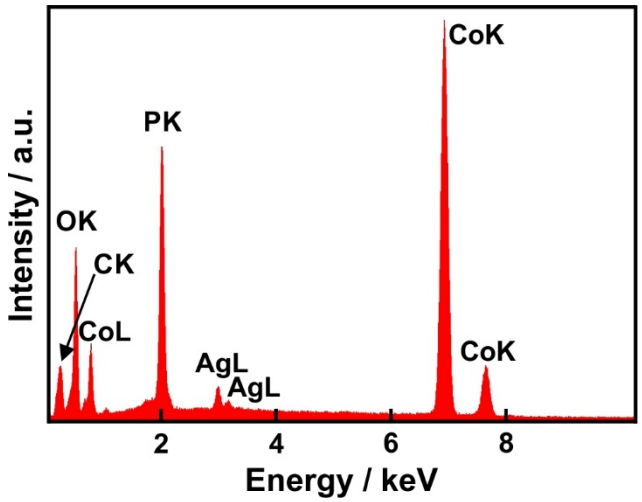

Figure 4.2. Quantitative analysis. **Left**: Results of the ICP-MS and ICP-OES measurements[a] for ACP; **Right**: EDX spectrum of ACP. Spectrum shows silver due to sputtering with a layer of silver and carbon due to the used carbon grid. Based on [185].

[a] Average concentrations (µg L^{-1}) and standard deviations for Co and P in ACP; relative standard deviation of all the samples (RSD) are included.

4.3.3 Configuration

ACP consists of nearly spherical nanoparticles with a high degree of agglomeration (Figure 4.3 A, B). The samples were collected 1 min after mixing 15 mM $Co(NO_3)_2$ and 10 mM Na_3PO_4 at room temperature. The nanoparticles have an average diameter of 23(1) nm. SAXS was performed in order to confirm the particle size and homogeneity of the sample.

By dispersing ACP in water-free ethanol and treating with a sonication probe, only a small fraction of aggregates could be disrupted. This is manifested in the scattering curve (Figure 4.4) that shows in the small *q*-range an increase in intensity. Furthermore, the sample seems to be highly polydispers or agglomerated. For fitting the scattering curve, a unified fit model was used. In the high *q*-range a Porod law slope of 4 was determined, indicating the presence of solid particles. From the kinked region the radius of gyration can be deduced according to $I(q) = I_0 e^{-\frac{R_g}{3}q^2}$. Assuming spherical particles, the average diameter can be calculated by $D = 2\sqrt{5/3}\,R_g$.

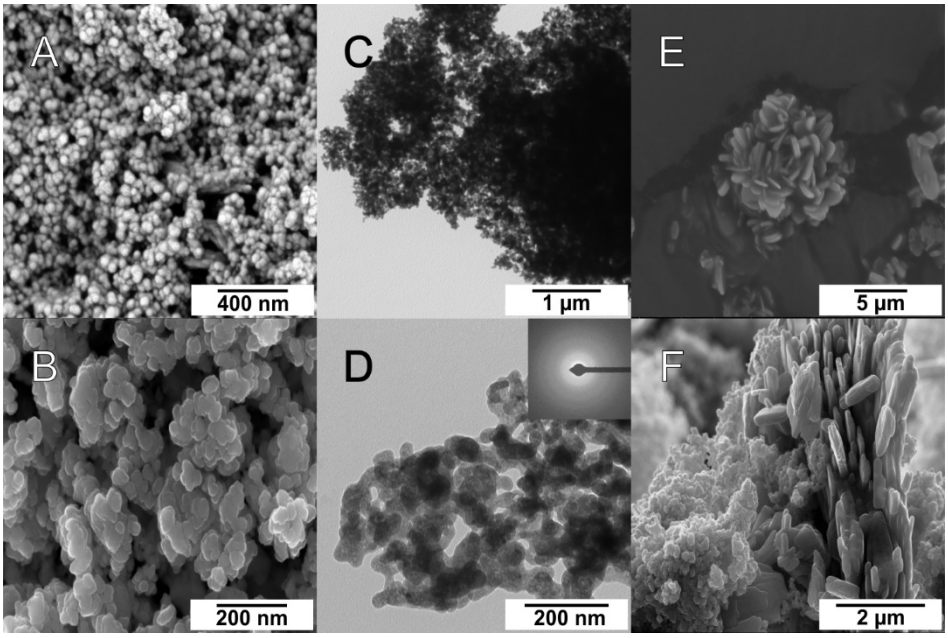

Figure 4.3. (A, B) SEM images of precipitated ACP particles sampled 1 min after rapid mixing equal volumes of 15 mM $Co(NO_3)_2$ and 10 mM Na_3PO_4 solutions. **(C, D)** TEM images of ACP particles. The SAED pattern shown in the inset of (D) is featureless, indicating the amorphous nature of ACP. **(E, F)** SEM images of $Co_3(PO_4)_2 \times 8\ H_2O$ sampled 10 min after rapid mixing equal volumes of 15 mM $Co(NO_3)_2$ and 10 mM Na_3PO_4 solutions. Based on [185].

For ACP a radius of gyration of 9.5 nm was calculated, resulting in an average diameter of 24.5 nm.

In addition, TEM snapshots of ACP sampled 30 s after mixing the starting solutions and prior to centrifugation showed coalesced liquid-like ACP particles (Figure 4.3 C, D). SAED confirmed the product to be non-crystalline; crystallization could be induced under the strong

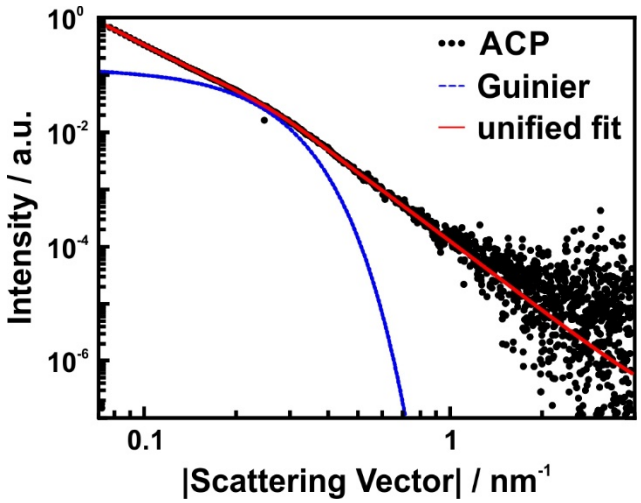

Figure 4.4. Scattering curve of ACP (black circles). The SAXS curve was fitted using a unified fit model with two levels (red line). The blue line indicates the Guinier fit. Based on [185].

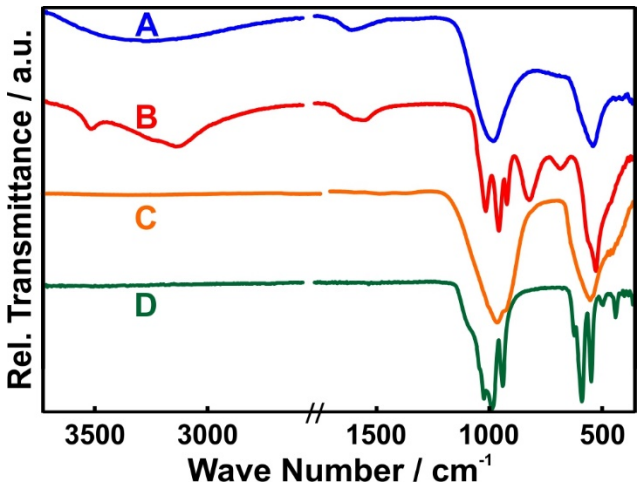

Figure 4.5. IR spectra normalized to the phosphate stretching mode of ACP **(A)** and $Co_3(PO_4)_2 \times 8\ H_2O$ **(B)**. At 500 °C (under argon, 1 week) ACP is still amorphous, but contains less water **(C)**. At 600 °C $Co_3(PO_4)_2$ **(D)**, the thermodynamically stable phase at that temperature, was formed. The bands of $Co_3(PO_4)_2 \times 8\ H_2O$ and $Co_3(PO_4)_2$ are split because of lattice symmetry constraints. Based on [185].

radiation of the electron beam. The liquid-like character of the as-synthesized nanomaterial is reminiscent of related studies on $CaCO_3$.[160] Samples collected 10 min after mixing 15 mM $Co(NO_3)_2$ and 10 mM Na_3PO_4 after separation from solution and drying, showed flower-like agglomerates of $Co_3(PO_4)_2 \times 8\ H_2O$ (Figure 4.3 E). Higher magnifications (Figure 4.3 F) revealed that the "petals" develop by coalescing of the nanomaterial, which might indicate an oriented attachment.

Figure 4.5 shows the IR spectra (normalized to the asymmetric phosphate stretching mode) of ACP (trace A), crystalline $Co_3(PO_4)_2 \times 8\ H_2O$ (trace B), and the annealing products at 500 and 600 °C (HT-ACP, trace C and $Co_3(PO_4)_2$, trace D). Bands observed at ≈1000 cm^{-1} are related to the asymmetric stretching mode of the phosphate groups, bands at around 550 cm^{-1} to the symmetric deformation mode, and signals at 1570–1650 and 3000–3500 cm^{-1} to water vibrations.

The bands of free phosphate anions are split for the crystalline compounds $Co_3(PO_4)_2 \times 8\ H_2O$[142] and $Co_3(PO_4)_2$[196] due the lower site symmetry within the crystal structure and factor group splitting. As ACP is amorphous, no splitting was observed. The bands ν_{as}(P–O) and δ_{as}(O–P–O) are broad, but not split.

compound	E(δ(H–O–H))	water content
$Co_3(PO_4)_2 \times 8\ H_2O$	0.097	8.0
ACP	0.061	5.1
ACP, 500 °C	0.004	0.3
$Co_3(PO_4)_2$	0.000	0.0

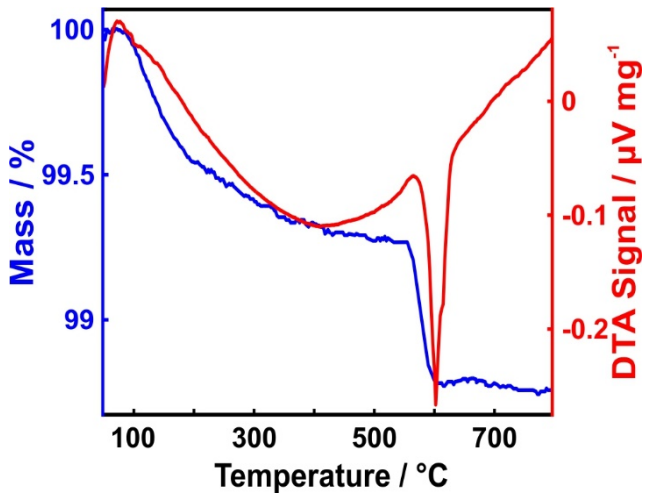

Figure 4.6. Left: Extinctions of the water bands of the IR spectra normalized to the asymmetric phosphate stretching mode of different cobalt phosphates and the resulting water content (formula inits). **Right:** Thermogravimetric trace (full line) and DTA signal (dashed line) of synthesized HT-ACP under argon. The water loss of 0.51% at around 600 °C leads in crystallization of HT-ACP to $Co_3(PO_4)_2$ showing that a completely anhydrous ACP cannot be synthesized. Quantitative analysis results in a composition of $Co_3(PO_4)_2 \times 0.25\ H_2O$ for HT-ACP. Based on [185].

Samples treated at elevated temperatures (500 and 600 °C) for 1 week under argon had a lower water content. This can be seen by the increasing transmittance of the water bands in the IR spectra (traces C, D). The phosphate bands in trace C are not split revealing that the phase is still amorphous. The absence of Bragg reflections in the corresponding X-ray diffractogram confirmed this result (Figure 4.1 D). The water content of the high-temperature amorphous phase (HT-ACP) was smaller than that of ACP at room temperature (RT-ACP). This was quantified by IR spectroscopy and TGA (Figure 4.6). The extinction of the ν(O–H) valence band arising from coordinating water is proportional to its concentration in the respective solid. RT-ACP had an averaged composition of $Co_3(PO_4)_2 \times 5.0\ H_2O$ (based on IR spectroscopy ($Co_3(PO_4)_2 \times 5.1\ H_2O$) and thermal analysis (*vide infra*, $Co_3(PO_4)_2 \times 4.8\ H_2O$).

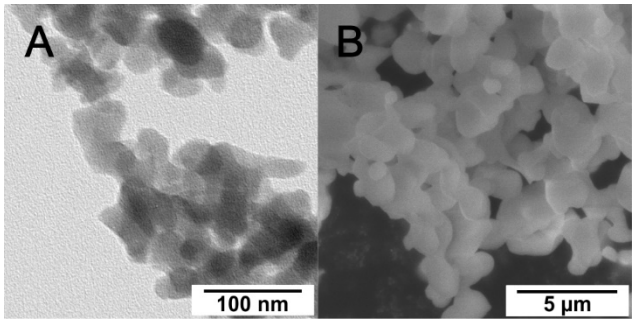

Figure 4.7. (A) TEM image of HT-ACP synthesized by heating up RT-ACP one week at 500 °C under argon. **(B)** SEM image of $Co_3(PO_4)_2$ synthesized by heating up RT-ACP one week at 600 °C under argon. Based on [185].

Table 4.2. Results of IR spectroscopy of different cobalt phosphate hydrates in detail (all values in cm^{-1})

	ACP	$Co_3(PO_4)_2 \times 8\ H_2O$	HT-ACP	$Co_3(PO_4)_2$
δ_{as}(O–P–O)	552	539	540	636, 600, 559, 510, 451
Lit.[186, 187]	n.a.	570	n.a.	605, 560, 510, 452
ν_s(P–O)	*	699, 838	*	*
Lit[186, 187]	n.a.	703, 854	n.a.	n.a.
ν_{as}(P–O)	999	1033, 974, 938	999	1042, 999, 954
Lit.[186, 187]	n.a.	triple split band at 1032	n.a.	1045, 1008, 956
δ(H–O–H)	1634	1579	1527	*
Lit. [186, 187]	n.a.	1627	n.a.	n.a.
ν(O–H)	2880–3600	2800–3600 with sharp signal at 3450	2740–3646	*
Lit. [186, 187]	n.a.	sharp signal at 3454	n.a.	n.a.

n.a. – no data available
* – do not occur in spectrum

For HT-ACP an average composition of $Co_3(PO_4)_2 \times 0.3\ H_2O$ was calculated. HT-ACP also consists of nearly spherical nanoparticles with an average diameter of 25 nm, but shows some facets and corners indicating the onset of crystallization (Figure 4.7. A). At higher temperature (600 °C) anhydrous $Co_3(PO_4)_2$ was formed (trace D). $Co_3(PO_4)_2$ consists of rounded particles different in shape having an average diameter of 1 μm (Figure 4.7. B). Detailed results of the IR measurements are provided in Table 4.2.

Figure 4.8 displays the UV-Vis spectra of the different cobalt phosphates. $Co_3(PO_4)_2 \times 8\ H_2O$ and $Co_3(PO_4)_2$ are pink/purple salts (traces C, D), whereas (RT and HT)-ACP had a deep-blue color (traces A, B). Based on the different spectra and color, differences in coordination number and hydration states are apparent. In the crystal structures of $Co_3(PO_4)_2 \times 8\ H_2O$ and $Co_3(PO_4)_2$ the Co^{2+} cations are octahedrally coordinated, which - based on the crystal field splitting - requires a higher excitation energy than tetrahedrally coordinated Co^{2+}. The deep-blue color of the amorphous phases points to a tetrahedral coordination of Co^{2+} (or at least to a lower coordination than for the crystalline phases). In addition, optical transitions are Laporte forbidden for octahedral coordination, as

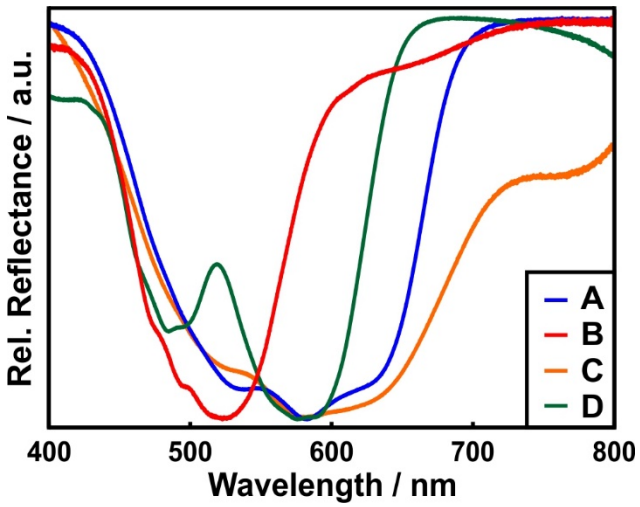

Figure 4.8. UV-Vis spectra of **(A)** RT-ACP, **(B)** $Co_3(PO_4)_2 \times 8\ H_2O$, **(C)** HT-ACP and **(D)** anhydrous $Co_3(PO_4)_2$. Based on [185].

apparent from the weak pink/violet color for the crystalline compounds. In contrast, optical transitions are permitted in amorphous compounds with ill-defined coordination, because the lower symmetry suspends the Laporte selection rule. The result is in an intense blue color for the amorphous phases.

While optical spectroscopy gave first indications on the metal coordination, XANES and EXAFS spectroscopy (at a synchrotron beamline) provide more quantitative information concerning coordination and bond lengths. XANES is sensitive to differences in the oxidation state. Figure 4.9 a) shows XANES spectra of ACP and $Co_3(PO_4)_2 \times 8\ H_2O$. ACP has an edge position at 7723 eV and the crystalline substance at 7727 eV. The pre-edge structure, a

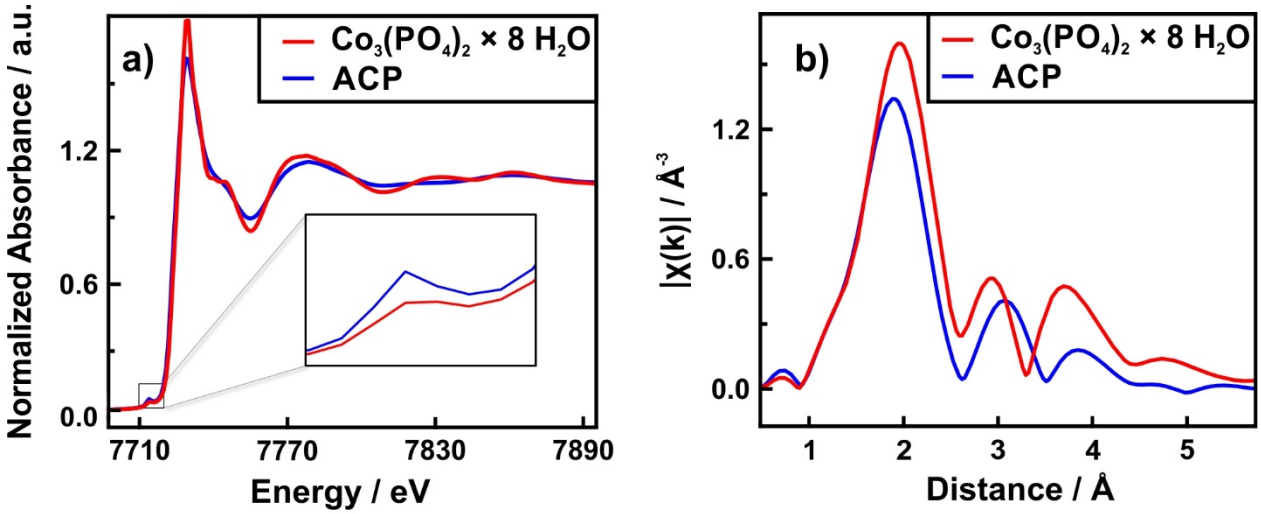

Figure 4.9. a) XANES spectrum of $Co_3(PO_4)_2 \times 8\ H_2O$ and ACP. Inset shows the pre-peak region. **b)** EXAFS profile-amplitude of the Fourier transform. Based on [185].

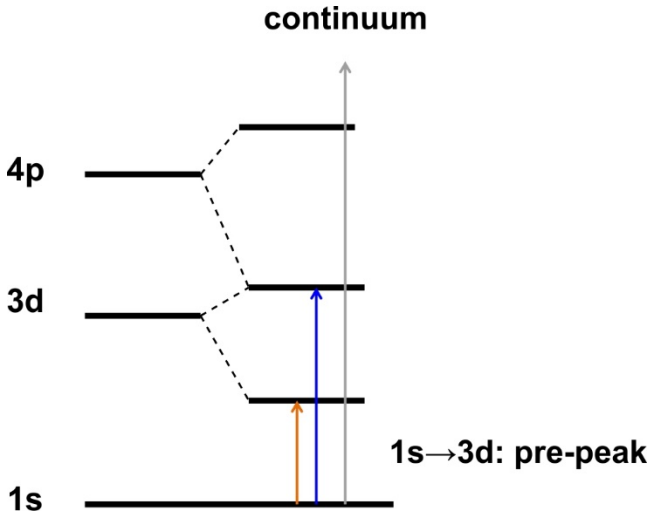

Figure 4.10. Possible pre-peak transitions for $Co_3(PO_4)_2 \times 8\ H_2O$. Based on [185].

pronounced "white-line" accompanied by a slightly lower pre-peak, can be interpreted as quadrupole transitions from the 1s core state to empty 3d states. In case of inversion symmetry of the transition metal is broken, the pre-edge gains additional intensity due to the local 3d 4p wave function mixing, effectively allowing dipole transitions to the 4p character of the 3d-band (see Figure 4.10). The presence of a strong pre-edge peak and a smooth white line are typical of a non-centrosymmetric structure (tetrahedral coordination), whereas a reduced intensity of a pre-edge peak and a more pronounced white line are an indicative of octahedral symmetry. Following this explanation, we assume that Co^{2+} in ACP tends to have a tetrahedral coordination in accordance with the results of UV-Vis spectroscopy.

Furthermore, EXAFS is sensitive to the local environment of the probed atom: the distance to its nearest neighbors (position of the peaks), the number and type of neighboring atoms (coordination number CN) at a given separation, (amplitude of the peaks). Figure 4.9 b) shows EXFAS signals after Fourier transformation of $\chi(k)$. The first peak, at a distance of about R=2.1 Å corresponds to a Single Scattering (SS) from the oxygen (O) neighbor and differs only slightly for the two investigated species. ACP has a lower number of oxygen neighbors for Co^{2+} in accordance with the results of UV-Vis and XANES spectroscopy. In addition, the signals at around 3.0 Å and between 3.5 and 4.0 Å show that in ACP distances of Co^{2+} to its next neighbors are larger than for the crystalline compound. To sum up this section, we have shown that besides its missing long-range order ACP also shows up a different short range order than $Co_3(PO_4)_2 \times 8\ H_2O$ leading to a very different color of amorphous and crystalline compound.

4.3.4 Thermal Stability

Figure 4.11 displays the thermogravimetric and DTA traces of ACP under argon. A nearly continuous weight loss of about 20% was observed in the range between 100 and 700 °C together with an endothermic DTA signal, which is caused by the loss of coordinating water. Surface bound water was removed prior by drying the sample under dynamic vacuum.

Upon heating anhydrous $Co_3(PO_4)_2$ was formed, as demonstrated by XRD (Figure 4.1 E) and IR spectroscopy (Figure 4.5 D). An approximate composition of $Co_3(PO_4)_2 \times 5.0\ H_2O$ was calculated from the weight loss determined by TGA in agreement with the IR spectroscopic results ($Co_3(PO_4)_2 \times 5.1\ H_2O$). The amorphous compound contained less water than crystalline $Co_3(PO_4)_2 \times 8\ H_2O$, the thermodynamically stable phase in that temperature range. The release of coordinating water at 120 °C is associated with a broad endothermic DTA signal. An exothermic signal at 600 °C indicates crystallization of ACP to anhydrous $Co_3(PO_4)_2$. In contrast, $Co_3(PO_4)_2 \times 8\ H_2O$ loses its crystal water in two well-defined steps (Figure 4.11 b). No signal indicating recrystallization was observed. $Co_3(PO_4)_2 \times 8\ H_2O$ reacts gradually to anhydrous $Co_3(PO_4)_2$. $Co_3(PO_4)_2$ transforms to $Co_3(PO_4)_2 \times 8\ H_2O$ by suspending in water for 10 d, but it is stable under ambient conditions for more than 2 a. The very high stability of $Co_3(PO_4)_2$ under ambient conditions indicates that this reaction proceeds via a dissolution/ recrystallization process, as the different crystal structures of $Co_3(PO_4)_2$ and $Co_3(PO_4)_2 \times 8\ H_2O$ require decomposition and reconstruction. Therefore, this rearrangement is very slow and requires a large amount of water.

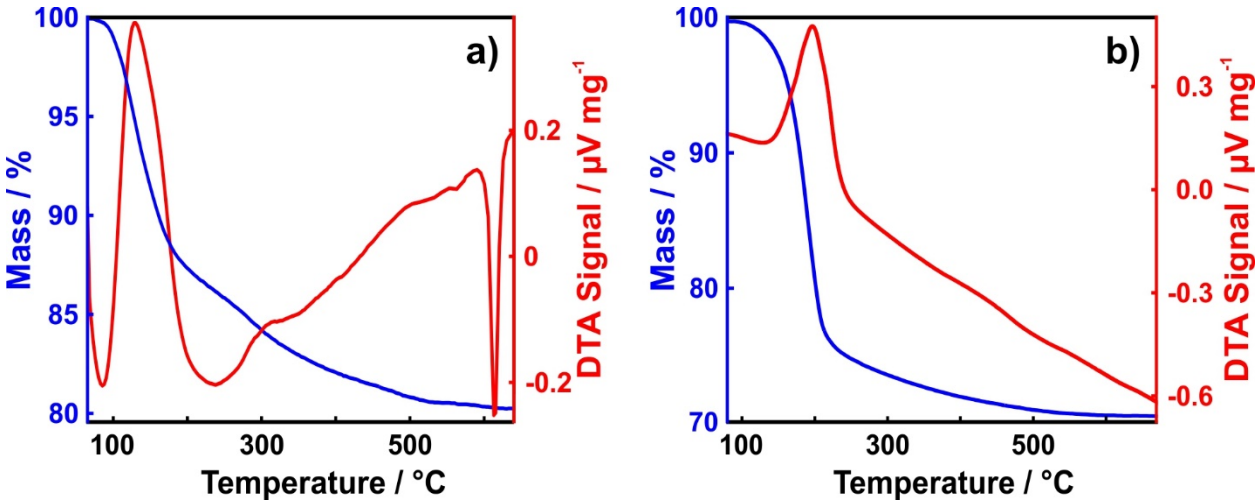

Figure 4.11. Thermogravimetric (blue line) and DTA trace (red line) of ACP **a)** and $Co_3(PO_4)_2 \times 8\ H_2O$ **b)** under argon. Based on [185].

The amorphous nanomaterial showed a very high thermal stability up to 600 °C. Even annealing to 500 °C for 1 week under argon left the compound amorphous (Figure 4.1 D and Figure 4.5 C).

In contrast, ACP is stable for months when stored under anhydrous conditions, but it crystallizes within weeks in air. This behavior is explained by the lower activation energy for surface diffusion than for diffusion in the solid state.[163,197] The high ion mobility of Co^{2+} and PO_4^{3-} is caused by adsorbed water because surface diffusion coefficients are nearly equivalent to those for diffusion in solution. Rearrangement and addition of water leads to crystallization, also in a water film from atmospheric moisture.[163]

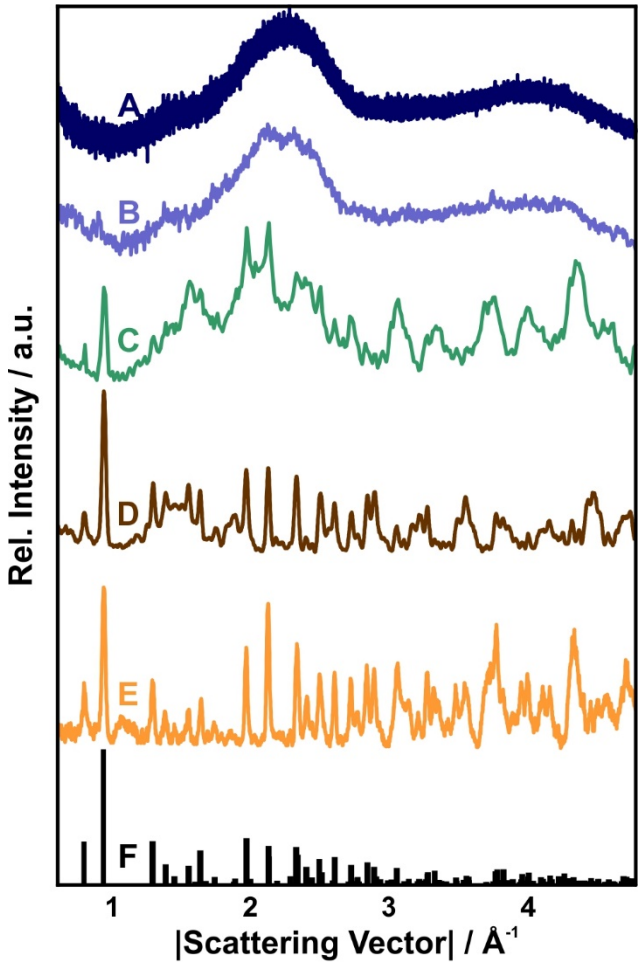

Figure 4.12. X-ray diffractograms of the precipitation products of 10 mM PO_4^{3-} and 15 mM Co^{2+} 5 min after mixing at **(A)** room temperature, **(B)** 30 °C, **(C)** 40 °C, **(D)** 50 °C, and **(E)** 60 °C showing the increasing degree of crystallinity. **(F)** Calculated pattern. Based on [185].

4.3.5 Effect of Reaction Temperature

As higher temperature should promote a transformation from the amorphous to the crystalline state, the precipitation of cobalt phosphate hydrate was performed at different temperatures. X-ray powder diffraction of the precipitates (Figure 4.12) of 10 mM PO_4^{3-} and 15 mM Co^{2+} after 5 min at different temperatures showed the degree of crystallinity of the precipitated cobalt phosphate hydrates to increase with the reaction/precipitation temperature. The corresponding IR spectra (Figure 4.13 a) reveal a similar trend. The bands of the symmetric stretching vibration (present only in the $Co_3(PO_4)_2 \times 8\ H_2O$) allow to determine the ratios of the amorphous and crystalline phases for different temperatures (Figure 4.13 b). It is critical to speak about crystallinity in this context. Crystallinity is defined as a translationally invariant tiling of space. However, IR spectroscopy probes the symmetry of the first coordination spheres. As the long-range order also has influence on the symmetry of

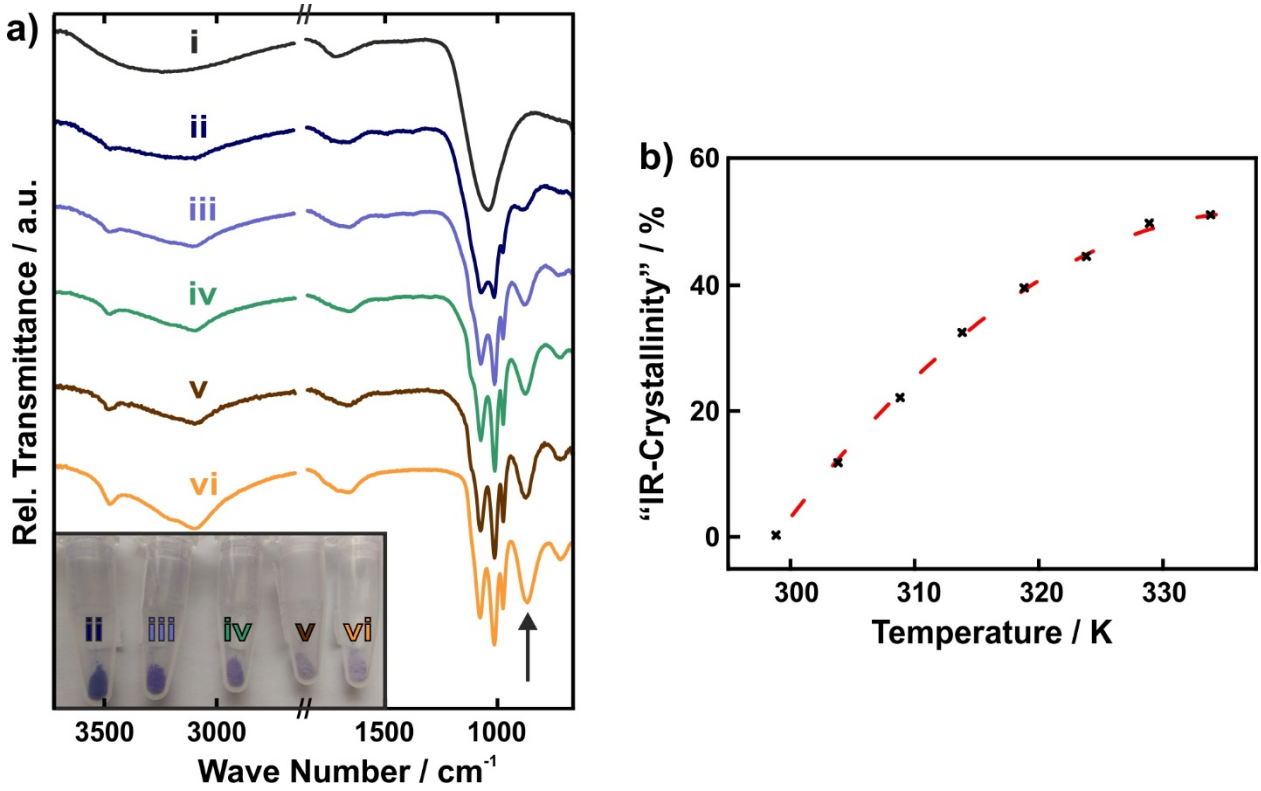

Figure 4.13. a) IR spectra normalized to the phosphate stretching mode of the precipitation products of 10 mM PO_4^{3-} and 15 mM Co^{2+} 5 min after mixing at **(i)** 25 °C, **(ii)** 30 °C, **(iii)** 40 °C, **(iv)** 50 °C, and **(v)** 60 °C showing the increasing degree of crystallinity. **(vi)** Complete crystalline $Co_3(PO_4)_2 \times 8\ H_2O$ synthesized with 200 mM PO_4^{3-} and 300 mM Co^{2+} 10 min after mixing. The arrow highlights the symmetric stretching mode. The inset shows the visual appearance of the samples. **b)** Analysis of the dependence of the mass fraction crystalline to amorphous on the temperature showing an exponential dependence. Based on [185].

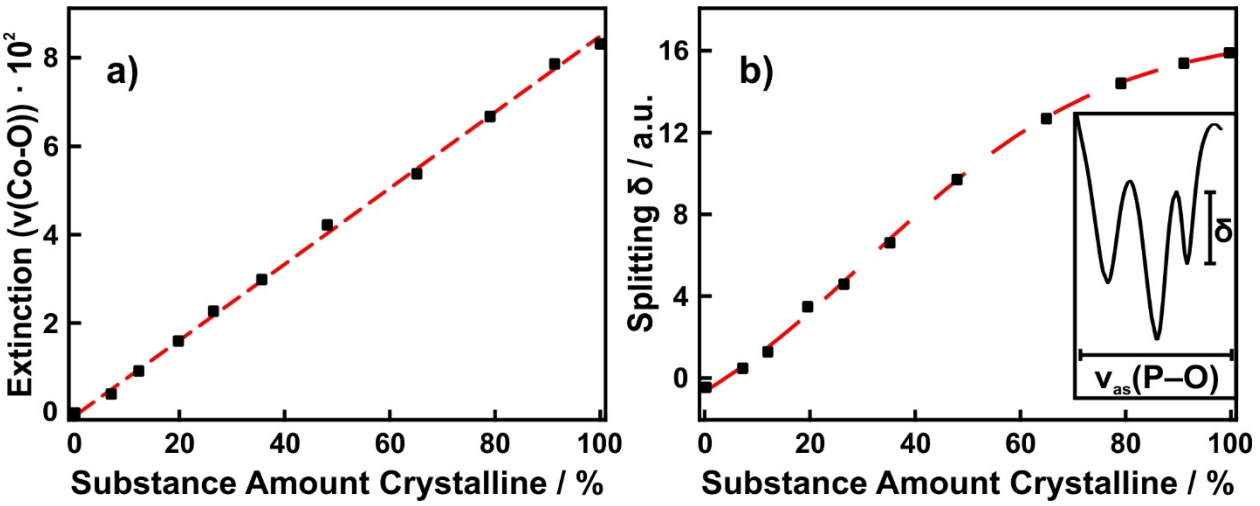

Figure 4.14. Standards for quantification: Mixtures of crystalline and amorphous phases of cobalt phosphate hydrate. **a)** Extinction of the symmetric stretching mode and **b)** splitting of asymmetric stretching mode. Based on [185].

coordination spheres, vibrational spectroscopy is suitable to monitor crystallization indirectly. Amorphous compound has a lower transmittance (higher extinctions) than the crystalline counterpart and thus mixtures with known ratios of amorphous to crystalline phase were used as standards (see Figure 4.14). For the standardization we used the measured density of ACP (ϱ=2.911±0.016 g/cm³) and the roentgenographic density of $Co_3(PO_4)_2 \times 8\ H_2O$ (ϱ=2.812 g/cm³). As shown in Figure 4.13 b) the ratio of the amorphous to crystalline phases depends on temperature in an exponential manner. However, we assume a dissolution/ recrystallization process to be responsible for the crystallization of ACP, which is accelerated by higher temperature. The higher density of the amorphous compound is counterintuitive albeit only at first glance. Amorphous compounds are normally less dense compared to their crystalline counterparts. However, amorphous and crystalline cobalt phosphate hydrate vary in their degree of hydration and therefore in their composition. As the van der Waals radius of H_2O (3.1 Å) is larger than the thermochemical radius of PO_4^{3-} (2.3±0.42 Å) and ionic radius of Co^{2+} (0.65 Å, coordination number=6) in the solid state despite their smaller molar mass, replacing Co^{2+} and PO_4^{3-} with H_2O leads to lower density.[198,199]

4.3.6 Water as Building Block and Mineralizer

As ACP contains less water than its crystalline counterpart, water is needed as a building block for crystallization. The crystallization kinetics of ACP was determined *in situ* by monitoring the splitting of the asymmetric phosphate IR stretch for wet ACP (Figure 4.15). Again, mixtures of ACP and $Co_3(PO_4)_2 \times 8\ H_2O$ were used as standards (see Figure 4.14). The

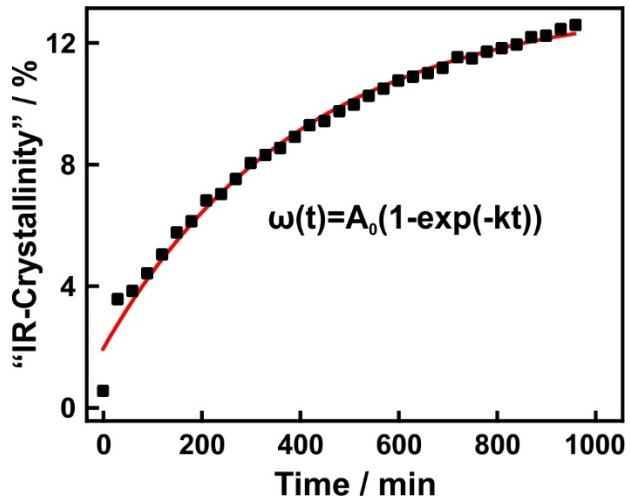

Figure 4.15. Crystallization kinetics of ACP in water. The red line is an exponential fit. Based on [185].

crystallization of ACP stirred in water proceeded much faster, but could not be monitored *in situ* because of insufficient sample homogeneity in the beam of the evanescent wave of the ATR-FTIR. The crystallization of ACP in D_2O showed a partial replacement of H_2O by D_2O during crystallization. As the oxygen atoms of the PO_4^{3-} groups are strongly involved in hydrogen bonding, the splitting of the PO_4^{3-} bands strongly depends on the hydrogen network. The PO_4^{3-} groups are involved in both, O–H–O and O–D–O hydrogen bonds. The resulting complex splittings could not be analyzed with our standards and the kinetics of the crystallization in D_2O could not be determined. Due to H/D exchange with (atmospheric) moisture, crystalline $Co_3(PO_4)_2 \times x\ H_2O \times y\ D_2O$ (x+y=8) undergoes a fast reaction to $Co_3(PO_4)_2 \times 8\ H_2O$.

4.4 Conclusion

Cobalt phosphate hydrates are an intriguing example for studying fundamental crystallization processes. (i) Besides the crystalline polymorphs $Co_3(PO_4)_2 \times 8\ H_2O$ and $Co_3(PO_4)_2$, there are two different amorphous cobalt phosphate hydrates: Amorphous cobalt phosphate hydrate nanoparticles (ACP containing approx. 5 H_2O molecules per formula unit) with diameters of approx. 20 nm were prepared by direct precipitation from aqueous solutions of Co^{2+} and PO_4^{3-} at low concentrations and short reaction times. An amorphous HT-phase with a lower water content (0.3 H_2O) could be obtained by subsequent annealing. (ii) The dependence of the optical absorption spectrum on the coordination and hydration state of Co^{2+} allows differentiating between different polymorphs. (iii) The crystal structures of the different cobalt phosphate hydrates are simple enough to gain fundamental knowledge of the nucleation and crystallization processes from aqueous solution.

The synthesis of ACP nanoparticles from aqueous solutions lends support to the hypothesis that metastable phases form prior to the thermodynamically stable polymorphs (with higher lattice energy) because surface energy dominates the total energy balance. However, to avoid the kinetically controlled transformation of metastable ACP into crystalline $Co_3(PO_4)_2 \times 8\ H_2O$ its separation must be fast. This could be demonstrated by resuspending ACP nanoparticles in water and monitoring their transformation to crystalline $Co_3(PO_4)_2 \times 8\ H_2O$.

ACP is extraordinary stable in the absence of water up to 500 °C as determined by XRD, electron microscopy, SAXS, vibrational and UV-Vis spectroscopy, as well as thermal analysis. Annealing RT-ACP with the approximate composition $Co_3(PO_4)_2 \times 5.1\ H_2O$ at 500 °C leads initially to the formation of a second amorphous polymorph, HT-ACP ($Co_3(PO_4)_2 \times 0.3\ H_2O$). Anhydrous $Co_3(PO_4)_2$ was formed at still higher temperature after full release of coordinating water. Since RT-ACP and HT-ACP differ in their composition, cobalt phosphate is not polyamorphous.

The high thermal stability of ACP against crystallization may be attributed to two facts: (i) $Co_3(PO_4)_2 \times 8\ H_2O$, the thermodynamically stable crystalline polymorph, contains more coordinating water than the ACP; therefore ACP requires additional water molecules as structural components in order to crystallize. (ii) This decomposition and reconstruction from the amorphous to the crystalline phase must occur via dissolution and recrystallization. During the crystallization of ACP water is assumed to serve as a mineralizer that facilitates the transport of the insoluble "nutrient" to the seed crystal, *i.e.*, it accelerates crystallization by

increasing the mobility of the ionic constituents.[200] When heating in the absence of water crystallization is inhibited because ACP is stabilized kinetically. The degree of crystallinity could be adjusted through the precipitation/reaction temperature. Higher temperatures accelerate the crystallization process of ACP in solution through enhanced dissolution and crystallization.

The charge density of the Co^{2+} cation, which makes the hydration enthalpy comparable to the binding energy of the counter-anions and the moderate acidity of the phosphate anions that allows the formation of hydrogen-bonded networks favor a multistage crystallization processes involving the homogeneous precipitation of nanocrystalline hydrated precursor phase. These phases may aggregate by condensation/dehydration.

5

AMORPHOUS PHOSPHATE HYDRATES OF IRON, NICKEL, AND COPPER

5.1 Introduction

In order to generalize our approach for the synthesis of amorphous 3d metal phosphates, further metal ions, namely Fe^{2+}, Ni^{2+}, and Cu^{2+}, were tested. Reaction conditions for the synthesis of amorphous zinc phosphate hydrate (Chapter 3) and cobalt phosphate hydrate (Chapter 4) were considered as basic protocol. Moderate initial concentrations of 3d metal ions and phosphate as well as short reaction times were applied for synthesis. A short overview about Fe, Ni, and Cu phosphate is given in the following paragraphs.

$Ni_3(PO_4)_2 \times 8\ H_2O$ is the thermodynamically stable hydrated modification of nickel phosphate at ambient conditions. It can be synthesized in an easy precipitation experiment analogous to $Co_3(PO_4)_2 \times 8\ H_2O$.[201] Both compounds are isostructural and crystallize in the monoclinic crystal system. Consequently, single phase $Co_{3x}Ni_{3-3x}(PO_4)_2 \times 8\ H_2O$ with x=1, 0.8, 0.6, 0.4, 0.2, 0 can be precipitated from aqueous solution. The dehydration behavior during heating is different for $Co_3(PO_4)_2 \times 8\ H_2O$ and $Ni_3(PO_4)_2 \times 8\ H_2O$. Structural water is evaporated from the $Co_3(PO_4)_2 \times 8\ H_2O$ structure in several defined steps leading to different crystalline hydrates. In contrast, the structural water of $Ni_3(PO_4)_2 \times 8\ H_2O$ is evaporated in one step that makes $Ni_3(PO_4)_2 \times 8\ H_2O$ and $Ni_3(PO_4)_2$ the only accessible crystalline phases of nickel orthophosphate.[201] Nickel phosphates are well known for their catalytic properties,[202] and they are suitable for fabrication of electrodes for electrochemical capacitors.[203–206]

Iron phosphates basically reveal iron in the oxidation state II or III. Iron(II) phosphates occur naturally as the mineral vivianite ($Fe_3(PO_4)_2 \times 8\ H_2O$), which has application as Schuessler salt.[207] Although Fe(II) is the stable oxidation state in aqueous solution, Fe(III)

phosphates are investigated more frequently. Iron(III) phosphate reveals several hydrated modifications ($FePO_4 \times n\ H_2O$ (n=1–4)) that differ with respect to their respective structure.[208] Therefore, they may display promising candidates for the investigation of the role of coordinating water in phosphates.

Iron phosphates are precursors for lithium iron phosphate, which is an important electrode material for the application of lithium ion batteries.[209–213] Furthermore, iron phosphate glasses provide suitable host lattices for toxic and nuclear waste immobilization.[71] Moreover iron(III) phosphates both anhydrous and hydrates are known for their catalytic activities.[208–215]

Copper phosphates are also well-known for catalyzing the oxidation of alcohols and the dehydration of monosaccharides.[216,217] Further, many copper complexes with organic ligands and bridging PO_4^{3-} were synthesized and characterized in the past decade resulting in interesting hybrid compounds with open-framework structures.[218–220] Investigations of the optical properties of lithium phosphate glasses doped with Cu^{2+} under gamma irradiation are also reported. Cu^{+} is not colorimetrically active whereas Cu^{2+} has a broad absorption band in the visible region. Therefore, optical spectroscopy provides insights into the amount of Cu^{2+} and its specific coordination depending on the respective synthesis conditions.[221]

This chapter emphasizes our general idea that a moderate charge density/Pearson hardness of the metal ion provides a guideline for identifying candidates where non-classical crystallization routes might play an important role. As a result of moderate charge density, different hydrated intermediates may appear during a multistage process, which may result in non-equilibrium phases. Besides Ca^{2+}, 3d metal ions like Fe^{2+}, Co^{2+}, Ni^{2+}, Cu^{2+}, and Zn^{2+} are promising candidates to probe this hypothesis. For calcium phosphate (more precisely hydroxylapatite), the occurrence of an amorphous hydrated precursor phase ($Ca_3(PO_4)_2 \times n\ H_2O$ with n=3–4.5)[222] during crystallization is already reported.[223] Furthermore, this amorphous phases are predicted to consist of roughly spherical Posner clusters, which are close-packed.[8] A crucial difference between hydroxylapatite and 3d metal phosphate hydrates is given by their respective crystalline products. As the crystal structure of hydroxylapatite contains no water molecules, dehydration of hydrated amorphous precursors has to take place prior to crystallization. In contrast, the respective thermodynamically stable modifications of 3d metal phosphates exhibit a huge amount of structural water (*e.g.*, $Co_3(PO_4)_2 \times 8\ H_2O$) making an uptake of water essential for crystallization of the amorphous intermediates. Intermediates during precipitation of 3d metal phosphate hydrates can be

trapped by quenching the crystallization in solution. A rather rigid hydrogen-bonded network in the amorphous solids (as pointed out in Chapter 3) displays a free enthalpy barrier for crystallization of the amorphous states. Pearson hardness is just a first hint for identifying possible candidates and does not explain all aspects of the hydration behavior. The transition metals Fe^{2+}, Co^{2+}, Ni^{2+}, and Cu^{2+} reveal partially filled d-orbitals. Thus, crystal/ligand field effects determine the first coordination sphere. In contrast, Zn^{2+} and Ca^{2+} act more like charged spheres without directed bonding interactions. Thus, the initial idea based on the concept of Pearson may fit best for the zinc phosphate hydrate system.

5.2 Experimental

5.2.1 Synthesis

Crystalline and amorphous phosphates of the transition metals Fe, Cu, and Ni were synthesized by precipitation from solution. Therefore, a Na_3PO_4 solution (>96%, Sigma-Aldrich) was mixed with solutions of the respective metal chlorides: $FeCl_2$ (>99.99%, Sigma Aldrich), $CuCl_2$ (>99%, Sigma Aldrich), and $NiCl_2$ (> 99.99%, Sigma Aldrich) at room temperature. Crystalline phosphates were prepared in water with initial concentration of 200 mM PO_4^{3-} and 300 mM M^{2+} (M=Fe, Ni, Cu) and under constant stirring for one week. Amorphous phosphates were prepared at lower concentrations (20 mM PO_4^{3-} and 30 mM M^{2+} (M=Fe, Ni, Cu)) and short stirring times of ≈5 s. The precipitation from solution was interrupted by centrifugation (9000 rpm, 3 min). The products were dried by washing in reagent-grade acetone (>99.5%, Sigma-Aldrich) and centrifuging again 3 times and finally drying *in vacuo* for 2 d ($p=3\times10^{-3}$ mbar). Crystallization may proceed further during centrifugation, but it is worth to mention that varying the centrifugation time does not have a significant effect on the results.

5.2.2 Characterization

The synthesized metal phosphates were investigated regarding their crystallinity using XRD and ATR-FTIR spectroscopy. TEM and SEM displayed their morphology while ICP-MS and ICP-OES were used to determine their composition. As the transition metals with their partially filled d-orbitals show characteristic coloring depending on their first coordination sphere in the solid state and their hydration state, UV-Vis spectroscopy was performed to get insights into the amorphous configuration.

5.3 Results and Discussion

5.3.1 Synthesis

Mixing of solutions with initial concentrations of 20 mM PO_4^{3-} and 30 mM M^{2+} (M=Fe, Ni, Cu) resulted in precipitation. Due to the enormous free enthalpy of formation along with low solubility products, supersaturation with respect to the respective crystalline modification was relatively high (see Table 5.1). The products of precipitation were analyzed by XRD and ATR-FTIR spectroscopy respectively (see Figure 5.1 A, Figure 5.2 A, and Figure 5.3 A). XRD patterns mainly displayed a modulated halo without defined reflections. ATR-FTIR spectra revealed a broad, non-split band centered at approximately 1000 cm^{-1} which is assigned to the asymmetric phosphate stretching mode ν(P–O) respectively. Further, a very broad band between 2500 and 3500 cm^{-1} and a band at approximately 1600 cm^{-1} indicate the presence of coordinating water within the amorphous solids. Both XRD and ATR-FTIR spectroscopy suggest the absence of long-range order in the precipitated solids. It is assumed that amorphous phosphate hydrates formed under these synthetic conditions. In contrast, longer crystallization times (1 week) and higher initial concentrations (200 mM for PO_4^{3-} and 300 mM for M^{2+}) resulted in the precipitation of crystalline phosphate hydrates of iron, nickel, and copper.

As reported in literature, amorphous solids may precipitate at high supersaturations which are present at any tested concentration. However, the crystallization of amorphous solids to their crystalline counterparts may be accelerated at increased supersaturation and thus intermediates may not be isolated.[95] Using concentrations in the range of 10 mM at room temperature seems to be adequate for isolation of amorphous intermediates probably due to a sufficiently low diffusion in solution. For high initial concentrations, a phase pure vivianite ($Fe_3(PO_4)_2 \times 8\ H_2O$) was synthesized as indicated by XRD (see Figure 5.1 B). In case of nickel,

Table 5.1. Solubility products and present supersaturation during the precipitation of amorphous 3d metal phosphate hydrates. Initial concentrations were 30 mM PO_4^{3-} and 30 mM M^{2+} (M=Fe, Ni, Cu).

compound	solubility product[a]	supersaturation
$Fe_3(PO_4)_2 \times 8\ H_2O$	$1.71\times10^{-36}\ mol^5\ L^{-5}$	6.3×10^{27}
$Ni_3(PO_4)_2$	$4.74\times10^{-32}\ mol^5\ L^{-5}$	2.28×10^{23}
$Cu_3(PO_4)_2$	$1.40\times10^{-37}\ mol^5\ L^{-5}$	7.71×10^{28}

[a] Values at 25 °C

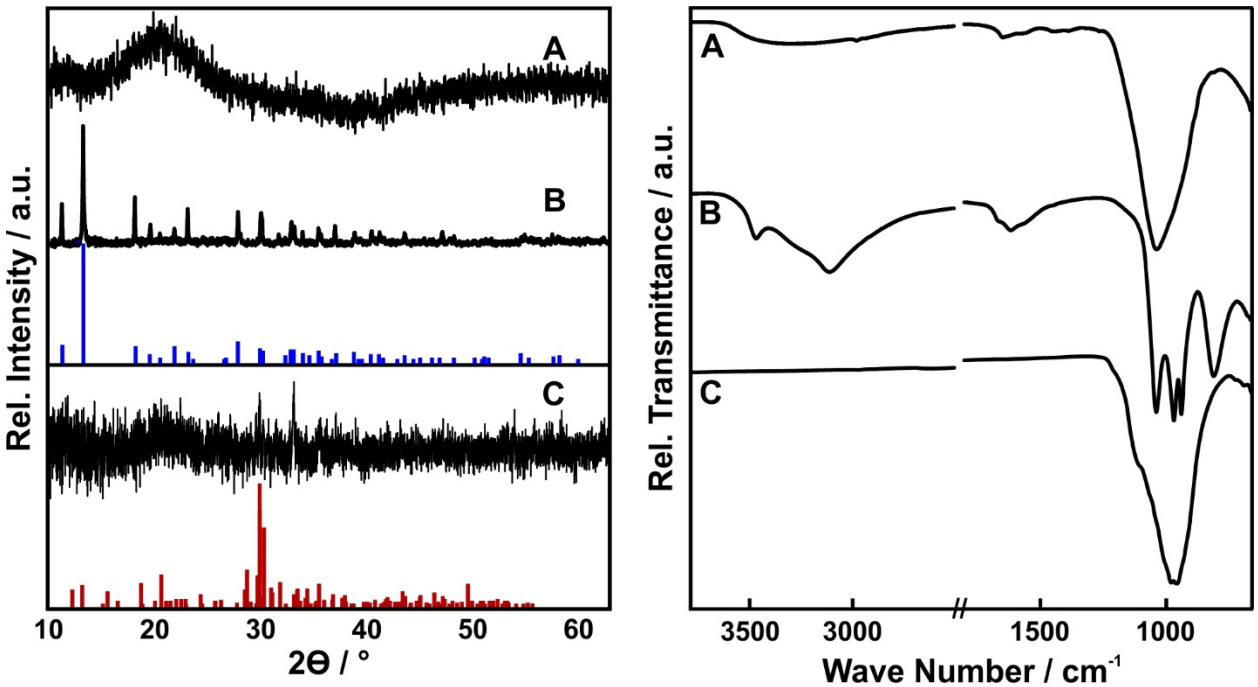

Figure 5.1. XRD patterns (left) and corresponding ATR-FTIR spectra (right) of **(A)** amorphous iron phosphate hydrate, crystallizing to **(B)** in aqueous solution (in blue literature reflections of vivianite ($Fe_3(PO_4)_2 \times 8\ H_2O$). **(C)** is achieved after heating amorphous solid under argon in a DTA device at 800 °C. (C) is basically amorphous with some very weak reflections of $Fe_7(PO_4)_6$ (red literature reflections).

phase pure arupite ($Ni_3(PO_4)_2 \times 8\ H_2O$) was achieved (Figure 5.2 B). However, for the Cu^{2+} cation, mixtures of libethenite ($Cu_2(PO_4)(OH)$) and $Cu_3(PO_4)_2 \times 3\ H_2O$ were precipitated (Figure 5.3 B). The corresponding IR spectra displayed split phosphate stretching modes due to present site symmetry and factor group splitting. Resuspending the respective amorphous solids in water for one week resulted in the same crystalline modifications. Therefore, it is assumed that the amorphous solids are intermediates during the precipitation of crystalline 3d metal phosphate hydrates.

The different hydration levels realized for the crystalline phosphate hydrates – $M_3(PO_4)_2 \times 8\ H_2O$ (M=Fe, Co, Ni), $Zn_3(PO_4)_2 \times 4\ H_2O$, and $Cu_3(PO_4)_2 \times 3\ H_2O$ (, which in fact was not precipitated phase pure) – may be explained by electrostatic and electronic reasons. First, an explanation is needed why the phosphates of many metals are hydrated. The oxygen of PO_4^{3-} is a poor Lewis base and it is not favored as ligand. In a simplified ionic approach, P^{5+} is a significant better electron acceptor than the transition metal M^{2+} leading to strong P–O bonds and thus little electron density can be donated to the M–O bond. During precipitation in solution the oxygen of H_2O, which in fact is a significantly better electron pair donator than

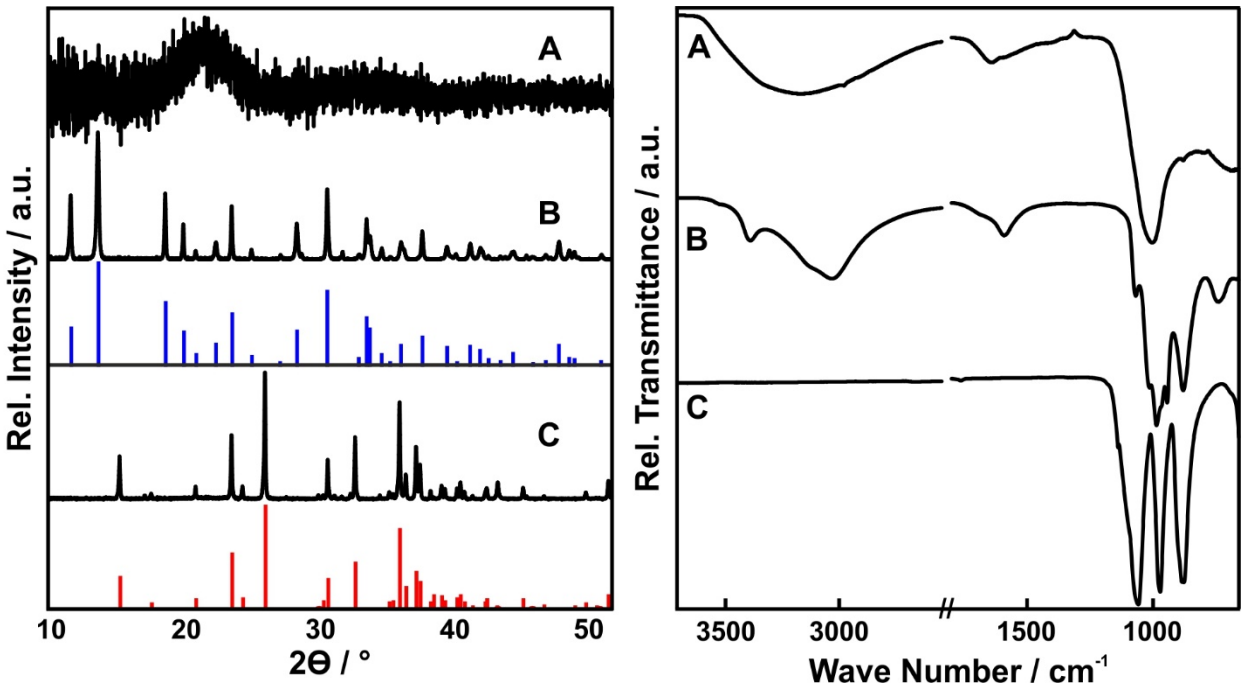

Figure 5.2. XRD patterns (left) and corresponding ATR-FTIR spectra (right) of **(A)** amorphous nickel phosphate hydrate, crystallizing to **(B)** in aqueous solution (in blue literature reflections of arupite ($Ni_3(PO_4)_2 \times 8\ H_2O$). **(C)** is achieved after heating amorphous solid under argon in a DTA device at 800 °C (in red literature reflections of anhydrous $Ni_3(PO_4)_2$).

the anion phosphate, acts as competitive ligand for the metal ion. Therefore, the metal ions are coordinated by the solvent H_2O as well as by the anion PO_4^{3-}.

Furthermore, Fe^{2+}, Co^{2+}, and Ni^{2+} prefer octahedral surrounding due to their ligand field effects. For possible anhydrous phosphates a limited number of binding partners is accessible to achieve octahedral coordination of the respective metal without reducing the electrostatic bond-valence. In addition, coordination of the central metal ion exclusively by phosphate units may not be favored due to increased steric demands.

Due to the preferred octahedral coordination of Fe^{2+}, Co^{2+}, and Ni^{2+}, it is not surprising that they are exclusively coordinated octahedrally in the crystal structures of the respective phosphate hydrates. High hydration states (octahydrates) are realized to achieve the desired octahedral coordination as water molecule are much better electron pair donating ligands than phosphate ions. In contrast, Zn^{2+} is not a transition metal in the narrow sense due to its filled d-orbitals. Thus, there is no preference for octahedral coordination due to ligand field splitting. Coordination of Zn^{2+} is basically determined by the electrostatic valence rule (1. rule of Pauling[224]) leading to a flexibility in its coordination. The crystal structure of hopeite illustrates this fact as there are two different Zn species present – one with tetrahedral and one with

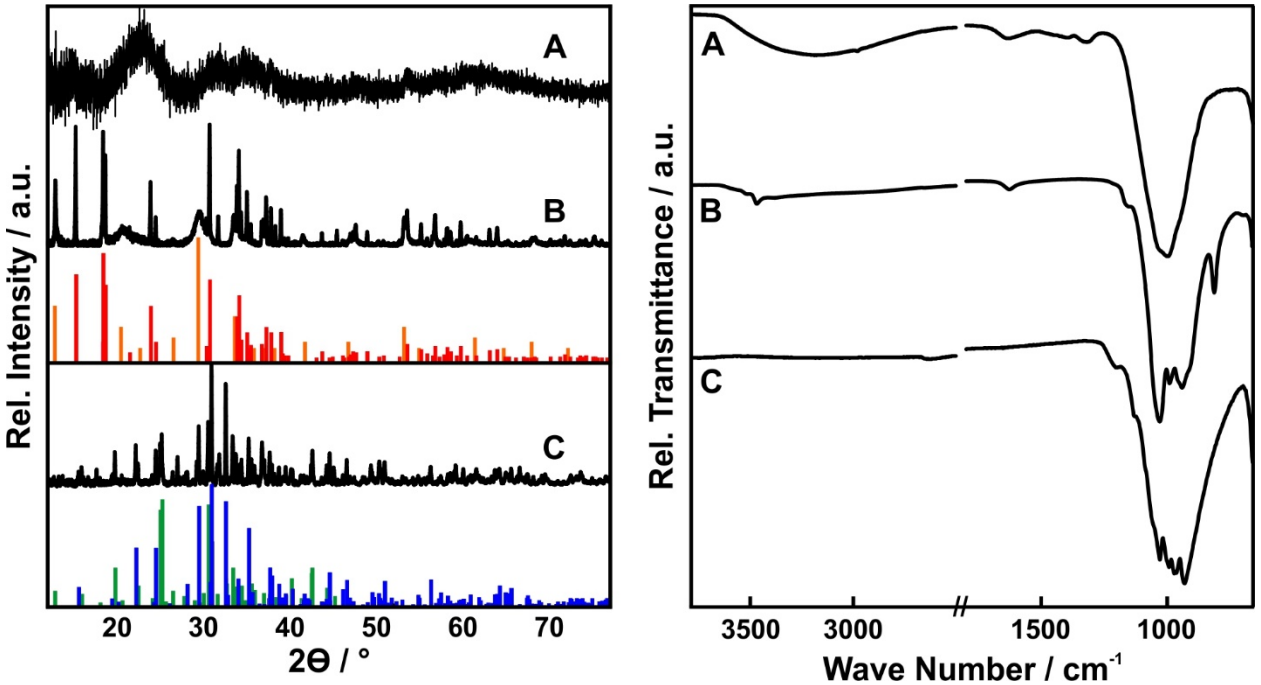

Figure 5.3. XRD patterns (left) and corresponding ATR-FTIR spectra (right) of **(A)** amorphous copper phosphate hydrate, crystallizing to **(B)** in aqueous solution (in green literature reflections of libethenite, in red literature reflections of $Cu_3(PO_4)_2 \times 3\ H_2O$). **(C)** is achieved after heating amorphous solid under argon in a DTA device at 800 °C (in blue literature reflections of anhydrous $Cu_3(PO_4)_2$, in orange literature reflections of $Cu_4O(PO_4)_2$).

octahedral coordination.[119] One Zn species is coordinated by four oxygens of PO_4^{3-} groups which is obviously possible without steric demands. Thus, less structural water is needed to achieve the desired coordination of Zn leading to a tetrahydrate. Our initial idea to identify possible candidates with the potential of reversible hydration due to moderate Pearson hardness may fit best for Zn^{2+} as no electronic restrictions because of its d metal character are present.

Copper holds a special position among the 3d metals. The stable oxidation state of copper in solution is Cu^{2+} whereas Cu^{+} should be favored due to ligand field stabilization. Cu^{2+} is in fact a very small ion (73 pm for octahedral coordination[225]) and reveals an enormous free enthalpy of hydration, which causes its stability in solution. As a possible consequence, hydroxo phosphates may occur during precipitation experiments as the hydroxo ligands acts as strong electron pair donors and stabilizes Cu^{2+}. Libethenite was precipitated besides $Cu_3(PO_4)_2 \times 3\ H_2O$ at high initial concentrations in accordance to this hypothesis.

5.3.2 Composition

Table 5.2. ICP-MS and ICP-OES results of different amorphous metal phosphate hydrates isolated as intermediates during precipitation of their crystalline modifications.

amorphous iron phosphate hydrate			
ICP-MS	^{57}Fe	^{58}Fe	^{31}P
mean conc. / µmol L^{-1}	8.02±0.14	8.15±0.09	5.98±0.05
ratio		3.00:2.20	
ICP-OES	Fe		P
mean conc. / µmol L^{-1}	32.9		21.7
ratio		3.0:2.0	
amorphous nickel phosphate hydrate			
ICP-MS	^{60}Ni	^{64}Ni	^{31}P
mean conc. / µmol L^{-1}	9.04±0.05	8.99±0.07	5.86±0.09
ratio		3.00:1.95	
ICP-OES	Ni		P
mean conc. / µmol L^{-1}	37.9		25.8
ratio		3.0:2.0	
amorphous copper phosphate hydrate			
ICP-MS	^{63}Cu	^{65}Cu	^{31}P
mean conc. / µmol L^{-1}	8.56±0.09	8.48±0.12	4.86±0.03
ratio		3.00:1.71	
ICP-OES	Cu		P
mean conc. / µmol L^{-1}	35.2		20.5
ratio		3.0:1.7	

[a]Mean concentrations (µg L^{-1}) and standard deviations for Zn and P in mech-AZP; estimated standard deviations of all the samples (ESD) are included.

The chemical composition of the as-synthesized amorphous solids was determined using ICP-MS and ICP-OES (see Table 5.2). The Ni:P ratio in the respective amorphous sample was determined to be 3.0:2.0 which is in agreement with a composition of $Ni_3(PO_4)_2$ n × H_2O.

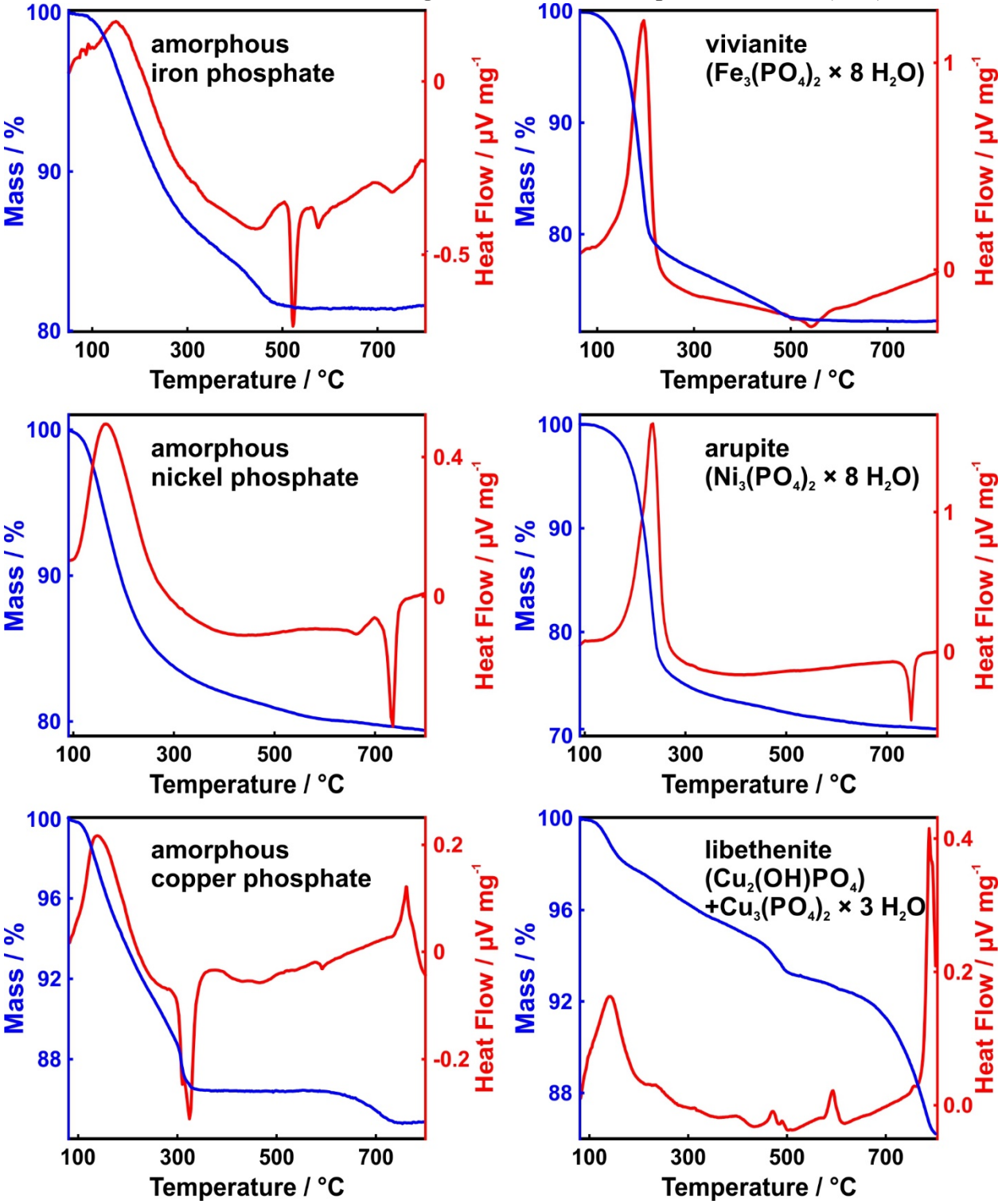

Figure 5.4. DTA and TG curves of as-synthesized amorphous phosphate hydrates.

The ratio of Fe:P is slightly smaller than 3:2 maybe due to oxidation of Fe^{2+} in the solid, what is also indicated by the brown color of the substance. Further, the "ideal" ratio was increased (3.0:1.7) for the "amorphous copper phosphate hydrate". This may suggest that their might be other ligands of Cu^{2+} in the amorphous solid besides phosphate. As the intermediate amorphous phase crystallizes to a mixture of libethenite, $Cu_2(PO_4)(OH)$, and $Cu_3(PO_4)_2 \times 3\ H_2O$, it is assumed that even in the amorphous state hydroxo groups are bound to Cu^{2+} as well as phosphate.

5.3.3 Thermally Induced Crystallization

In order to get insights into the thermally induced crystallization of the as-synthesized amorphous and crystalline products, DTA and TGA measurements were performed (see Figure 5.4). A broad endothermic signal between 100 and 300 °C was observed for all amorphous compounds accompanied with the main loss of weight which is indicative for the evaporation of coordinated water. The final loss of crystal water/coordinating water provided information on the degree of hydration of the individual species (see Table 5.3). We exclude the copper phosphate system due to the complexity of the system based on to the extraordinary hydration enthalpy and redox potential of Cu^{2+}. The amorphous intermediates

Table 5.3. Results of TGA for amorphous and crystalline metal phosphate hydrates which appear as intermediates during precipitation in aqueous solution. Deduced compositions are displayed as well.

compound	weight loss / %	deduced composition
vivianite	71.93	$Fe_3(PO_4)_2 \times 7.9\ H_2O$
amorphous iron phosphate hydrate	81.57	$Fe_3(PO_4)_2 \times 4.5\ H_2O$
$Co_3(PO_4)_2 \times 8\ H_2O$	70.74	$Co_3(PO_4)_2 \times 8.4\ H_2O$
amorphous cobalt phosphate hydrate	80.21	$Co_3(PO_4)_2 \times 5.0\ H_2O$
arupite	70.65	$Ni_3(PO_4)_2 \times 8.4\ H_2O$
amorphous nickel phosphate hydrate	79.39	$Ni_3(PO_4)_2 \times 5.3\ H_2O$
libethenite +$Cu_3(PO_4)_2 \times 3\ H_2O$	86.59	"$Cu_3(PO_4)_2 \times 3.3\ H_2O$"
amorphous copper phosphate hydrate	84.86	"$Cu_3(PO_4)_2 \times 3.8\ H_2O$"
hopeite	84.73	$Zn_3(PO_4)_2 \times 3.9\ H_2O$
amorphous zinc phosphate hydrate	89.72	$Zn_3(PO_4)_2 \times 2.5\ H_2O$

isolated during precipitation contain a significantly lower amount of coordinated water than their crystalline counterparts (all in the range of 56–66%). We assume that a certain fixed degree of hydration has to be realized in the amorphous solids to form a hydrogen-bond network that exert a stabilizing effect. Afterwards, the respective coordination spheres of the metal ions are filled up with the electron density donating ligand water. This generates crystal structures with metal ions surrounded by the desired coordination sphere.

Furthermore, DTA determined the crystallization temperature of the amorphous solids during heating. The crystallized products were also characterized by XRD and ATR-FTIR spectroscopy (see Figure 5.1 C, Figure 5.2 C, and Figure 5.3 C). Crystallization of amorphous iron phosphate was indicated by an exothermic signal at 522 °C, but the reaction product was hardly crystalline. Some weak reflections of $Fe_7(PO_4)_6$ were observed for the products obtained by heating amorphous iron phosphate hydrate and vivianite (see Figure 5.1 C). As the DTA measurement was performed under argon, the mixed valence of Fe in the structure of $Fe_7(PO_4)_6$ may be achieved by an internal redox reaction. A very broad exothermic signal for heating vivianite supports the idea of an internal redox reaction. As a result, phosphor species with different oxidation states may be present resulting in a poorly crystalline structure.

Amorphous nickel phosphate crystallize to anhydrous $Ni_3(PO_4)_2$ (see Figure 5.2 C). $Ni_3(PO_4)_2$ is also the reaction product of heating arupite. Interestingly, arupite also revealed an exothermic recrystallization signal at 660 °C in the DTA. This may point out that arupite become amorphous during heating. This may be supported by the fact that no other crystalline nickel phosphate hydrate with a lower degree of hydration is known.[201] The product of annealing "amorphous copper phosphate hydrate" under argon in the DTA is a mixture of crystalline $Cu_3(PO_4)_2$ and $Cu_4O(PO_4)_2$ (see Figure 5.3 C). The same products were achieved by

Table 5.4. Crystallization temperature for thermally induced crystallization of amorphous phosphate hydrates.

compound	crystallization temperature (first minimum) / °C
amorphous copper phosphate hydrate	324
amorphous zinc phosphate hydrate	480
amorphous iron phosphate hydrate	522
amorphous cobalt phosphate hydrate	600
amorphous nickel phosphate hydrate	660

heating up the mixture of crystalline $Cu_3(PO_4)_2 \times 3\ H_2O$ and $Cu_2(PO_4)OH$. This result also supports the idea that within "amorphous copper phosphate" hydroxo ligands are present which resulted in an oxo phosphate species during heating.

The temperature of the first exothermic signal (local minimum) was measured respectively which were comparable due to equal heating rates (see Table 5.4).It is worth to mention that even though Fe, Co, and Ni have very similar crystal structures the crystallization temperature increases dramatically from Fe to Ni. This may be explained by an increase in M–O (M=Fe, Co, Ni) bond strength from Fe to Ni. The increasing bond strength may be observed in the M–O bond length of the respective crystalline structures (Fe–O has the longest bond length and Ni–O the shortest). Removal of water molecules is achieved by breaking M–O bonds. Also, the recrystallization of an amorphous solid is a reconstructive phase transition where chemical bonds are broken according to the Ehrenfest classification.[2] Therefore, stronger M–O bonds result in an increased stability against thermally induced crystallization accompanied by an exothermic recrystallization signal at higher temperatures.

The amount of coordinating water is lower for amorphous zinc phosphate hydrate than for the amorphous solids of the other 3d metals resulting in a decreased number of bonds that have to be broken for removal of coordinating water. In addition, one of the Zn species in hopeite is coordinated tetrahedrally. As a consequence, only four bonds have to be broken

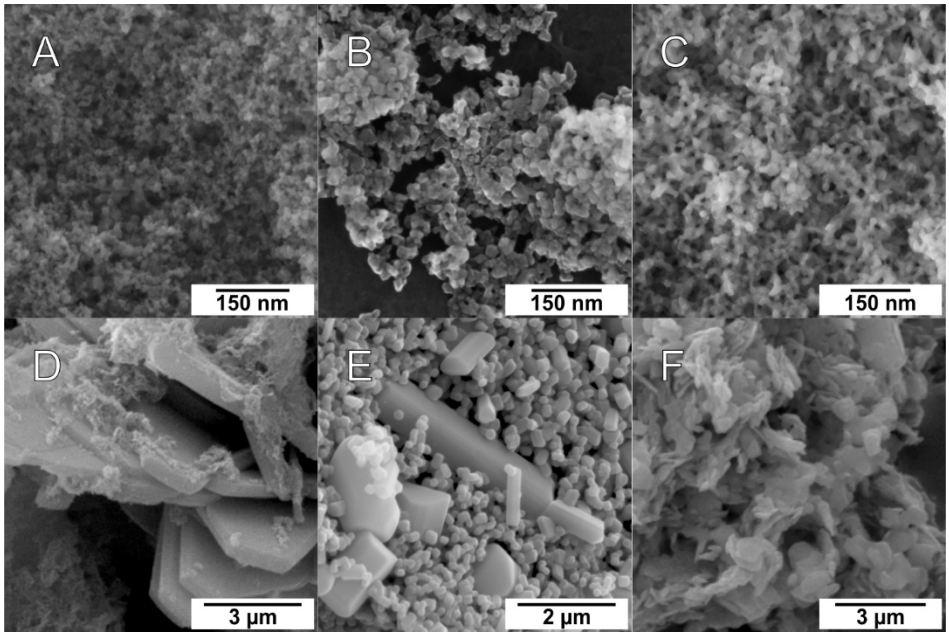

Figure 5.5. SEM images of amorphous phosphate hydrates of **(A)** iron, **(B)** nickel, and **(C)** copper. Also SEM images of **(D)** vivianite, **(E)** arupite, and **(F)** mixture of libethenite and $Cu_3(PO_4)_2 \times 3\ H_2O$ are displayed.

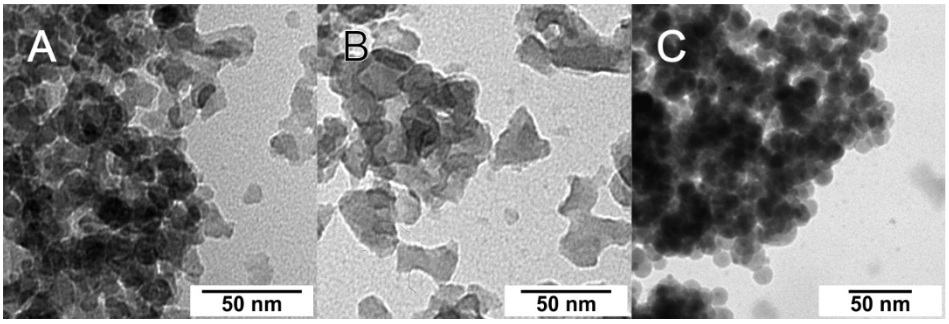

Figure 5.6. TEM images of amorphous phosphate hydrates of **(A)** iron, **(B)** nickel, and **(C)** copper.

instead of six under the assumption that a proto-crystalline order is intrinsic to AZP. The crystal structure of *a*-$Zn_3(PO_4)_2$ reveals just tetrahedrally coordinated Zn species so that a smaller number of chemical bonds has to be generated during recrystallization. Following these explanations, the reconstructive crystallization process requires less energy. As a result, the exothermic signal in the DTA is observed at lower temperatures for AZP than for the amorphous iron/cobalt/nickel phosphate hydrate.

5.3.4 Morphological Characterization and Optical Properties

Morphology of the as-synthesized amorphous and crystalline phosphate hydrates was determined using electron microscopy. SEM and TEM images displayed spherical nanoparticles 15–20 nm in size for amorphous copper phosphate hydrate (see Figure 5.5 C and Figure 5.6 C). Nanoparticles of amorphous iron and nickel phosphate hydrate display more corners and edges with particle sizes depending on the metal ion: Fe - 8–10 nm, Ni - 25–30 nm (Figure 5.5 A and B, Figure 5.6 A and B). Interestingly, the spherical nanoparticles observed for amorphous copper phosphate hydrate were well-defined and not as coalesced as for other amorphous phosphate hydrates (see also Figure 3.4, and Figure 4.3).

Crystallization of the amorphous phosphate hydrates in water leads to the formation of vivianite and libethenite (accompanied by $Cu_3(PO_4)_2 \times 3\ H_2O$) with plate-like morphologies (Figure 5.6 D and F) and arupite with a prismatic morphology (Figure 5.6 E).

UV-Vis spectra and even the physical appearance allowed to distinguish between crystalline and amorphous solids respectively. Amorphous nickel phosphate hydrate reveals a light green color whereas arupite is mint green. Amorphous iron phosphate hydrate has a brown color and vivianite reveals a grey-blue color. This indicates the oxidation of Fe^{2+} in the respective solids as freshly prepared vivianite appears colorless and transparent.[226] These colors are in agreement with a slightly decreased ratio of Fe:P determined by ICP-MS and ICP-OES (see Table 5.2). The color of amorphous copper phosphate hydrate and the

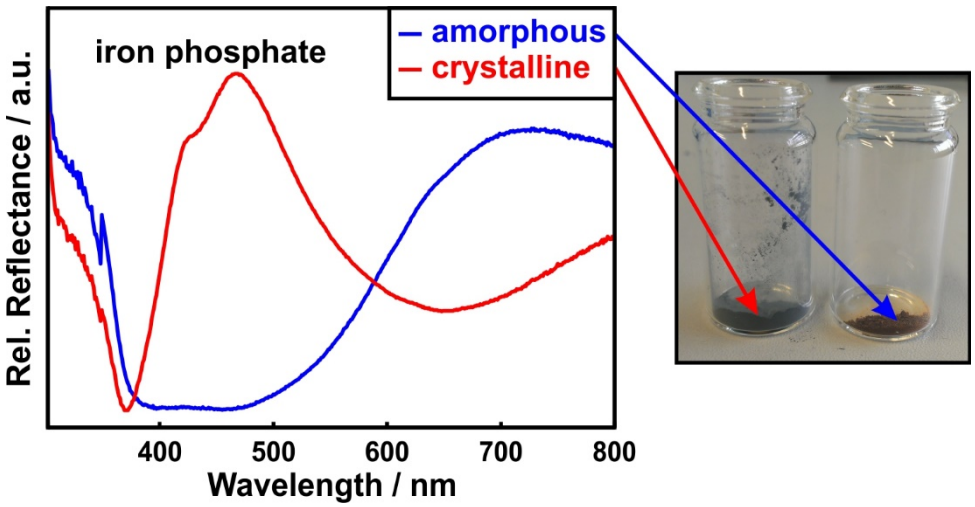

Figure 5.7. Left: UV-Vis spectra of amorphous iron phosphate hydrate and crystalline vivianite, $Fe_3(PO_4)_2 \times 8\ H_2O$. **Right:** Physical appearance of respective substances.

crystalline product (a mixture of libethenite and $Cu_3(PO_4)_2 \times 3\ H_2O$) appear very similar so that distinguishing by eye observation is hardly possible.

The absorption bands in the UV-Vis spectra of amorphous nickel and iron phosphate hydrate are broadened in comparison to their crystalline counterparts. In the crystal structure of vivianite and arupite defined coordination octahedral surrounding the metal ion exist that determine the ligand field splitting. Thus, absorption occurs at defined wavelengths. For the amorphous solids, a defined structure does not exist but rather a broad distribution of metal–oxygen distances. Consequently, the ligand field splitting itself reveals a broad distribution resulting in broad absorption bands. In addition, less selection rules for optical transitions are

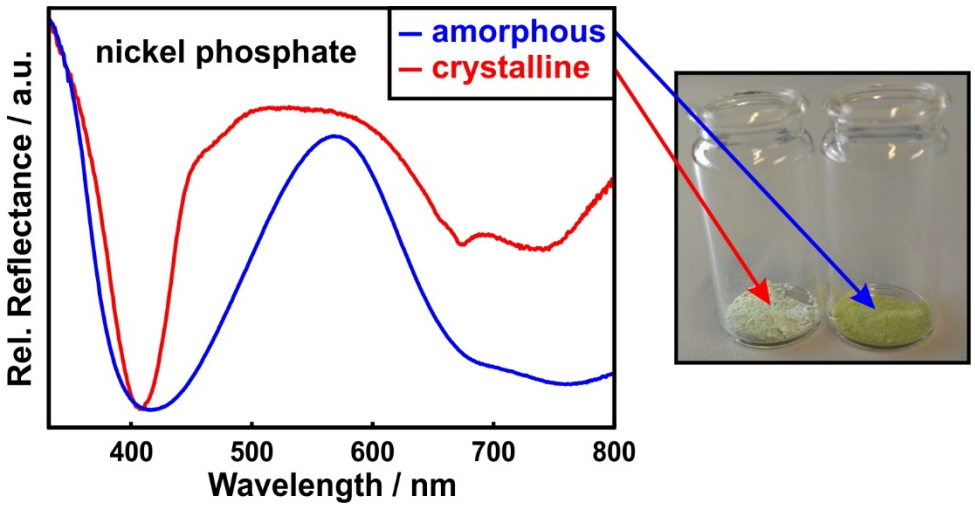

Figure 5.8. Left: UV-Vis spectra of amorphous nickel phosphate hydrate and crystalline arupite, $Ni_3(PO_4)_2 \times 8\ H_2O$. **Right:** Physical appearance of respective substances.

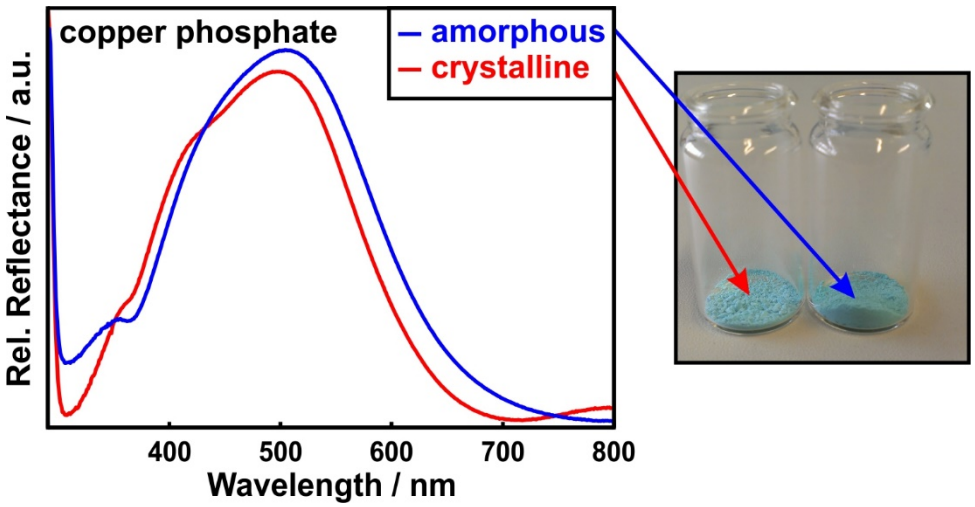

Figure 5.9. Left: UV-Vis spectra of amorphous copper phosphate hydrate and crystalline product ($Cu_3(PO_4)_2 \times 3\ H_2O$ and $Cu_2PO_4(OH)$). **Right:** Physical appearance of respective substances.

valid for the amorphous solids due to the lower symmetry and ill-defined coordination spheres, resulting in more intense optical transitions. It is assumed that partial crystallization of the amorphous solids display a possibility to tune absorption properties selectively.

5.4 Conclusion

Amorphous intermediates during the precipitation of iron, nickel, and copper phosphate hydrate were successfully isolated. The amorphous solids are precursors for the crystalline modifications vivianite ($Fe_3(PO_4)_2 \times 8\ H_2O$) and arupite ($Ni_3(PO_4)_2 \times 8\ H_2O$). In the copper phosphate hydrate system libethenite, $Cu_2PO_4(OH)$, and $Cu_3(PO_4)_2 \times 3\ H_2O$ are achieved by crystallization. This may indicate the presence of hydroxo ligands besides phosphate in the precursor "amorphous copper phosphate hydrate", which is supported by ICP-MS and ICP-OES. The amorphous phases are stabilized under anhydrous conditions and crystallize in the presence of water.

Due to the preferred octahedral coordination of Fe^{2+}, Co^{2+}, and Ni^{2+}, a high degree of hydration must be realized in the crystal structure of the phosphate hydrates. As Zn^{2+} is no transition metal, no electronic effects leading to a preferred coordination are present and so lower degrees of hydration are realized. Cu^{2+} holds a special position due to its enormous free enthalpy of hydration, resulting in mixed hydroxo phosphates.

Thermal analysis displayed the degree of hydration in the crystalline and amorphous solids. The amorphous solids reveal a lower content of coordinating water than their crystalline counterparts. The amorphous and crystalline solids crystallize during heating to the respective anhydrous crystalline phosphates. The trend in crystallization temperature is explained metal-oxygen bond lengths in the structures of the respective crystalline metal phosphate hydrates.

In addition, the amorphous solids were characterized systematically in terms of composition and configuration (UV-Vis). For nickel a 3:2 ratio of Ni:P was detected. In contrast, the Cu:P ratio in amorphous copper phosphate hydrate is higher than 3:2 probably due to the formation of hydroxo phosphates. For amorphous iron phosphate hydrate the ratio was slightly decreased maybe due to partial oxidation of Fe^{2+}. UV-Vis spectra displayed broad absorption bands for amorphous nickel and iron phosphate hydrate in accordance with a broad distribution of ligand field splittings for the various coordination polyhedra.

This chapter points out that crystalline phosphate hydrates of late 3d metals form via an amorphous precursor phase at suitable initial concentrations (range of 10 mM). Higher initial concentrations may propagate the formation of amorphous solids. However, it also may accelerate diffusion and thus the following crystallization process. To the best of our knowledge, amorphous precursors of iron, cobalt, nickel, copper, and zinc phosphate hydrate

were synthesized for the first time. The results support our initial idea that phosphates of cations with the potential to bind water reversibly crystallize via a multi-stage process with different hydrated (amorphous) intermediates. The guideline is a moderate Pearson hardness which explained the situation of Zn^{2+} (besides Ca^{2+} in literature) very well. The situation is more complex for the 3d metals with transition metal character as crystal/ligand field effects have to be taken into account. However, a moderate Pearson hardness of the metal ion turned out to be an excellent first hint for identifying crystals that crystallize via an amorphous precursor phase.

6

SYNTHESIS OF AMORPHOUS COBALT PHOSPHATE UNDER ANHYDROUS CONDITIONS

6.1 Introduction

Water is a unique solvent due to its extended hydrogen bonded network. The different crystallization pathways in aqueous solution are mainly characterized by the hydration layers of the respective ions. Cations/metals behave as Lewis acids, whereas oxyanions like in phosphates, carbonates, or water act as Lewis bases. The metals interact with lone electron pairs on the oxygen forming a dative bond resulting in a complex.[227] The coordination number and the strength of the metal–oxygen bond depend sensitively on the Pearson hardness of the metal, and on its concentration in solution. For instance, Mg^{2+} ions tend to bind 6 water molecules forming a very rigid octahedral coordination. Therefore, Mg^{2+} ions act as rather stationary units *in vivo*, for example in chlorophyll. However, Ca^{2+} ions bind water molecules reversibly due to their moderate Pearson hardness. Therefore, Ca^{2+} ions act as rather mobile units *in vivo*, *e.g.*, as trigger for nerve impulses.[228] Water is reported to be an active participant in mineralization/mineral densification including the formation of PNC and LCP. Precipitation of anhydrous modifications requires to peel away the respective hydration layers which may result in different mechanisms (or at least different time scales for sub processes) depending on how strong the hydration layers are bond.[37] The question arises whether the mechanisms of crystallization in water are also valid (perhaps in modified manner) for crystallization processes in other media.

Recently, the synthesis of ACC was reported using ionic liquids as solvent and surfactant. Ionic liquids are salts in the liquid state whose melting point is typically below 100 °C.[229] The

low melting point is typically caused by high steric requirements and mesomeric charge delocalization resulting in weak Coulomb interactions. The whole solubilizing potential of the ionic liquids is still not clear. With the aid of ionic liquids as weakly coordinating solvents it is possible to precipitate an IL-ACC (IL=ionic liquid) that is nearly anhydrous and exhibits an enormous stability against crystallization. NMR measurements give hints that proto calcite order is intrinsic of IL-ACC. Nonetheless, the difference in free enthalpy of formation is quite small for calcite and vaterite. As a result, a phase selection during the crystallization of IL-ACC was not observed.[230]

As mentioned in Chapter 4, amorphous cobalt phosphate hydrate occurs as intermediate during the precipitation of $Co_3(PO_4)_2 \times 8\ H_2O$. It displays a reduced content of coordinating water. Due to the moderate charge density of Co^{2+}, hydration is a reversible process and an entire range of different hydrated phases are accessible in theory. This is supported by a continuous weight loss during TGA measurements due to the evaporation of H_2O.

The remaining question is whether it is possible to synthesize an anhydrous amorphous cobalt phosphate in a non-aqueous medium that may also be representative for further hydrated 3d phosphates. As pointed out in the previous chapters, the amorphous phosphates are in deficit of coordinating water, which is the main reason for the inhibition of crystallization. This was shown by heating the amorphous solids in the absence of water. They crystallize in the presence of water provided by solution or even by humidity. Hence, synthesis conditions should be as dry as possible.

For this purpose, precipitation in ionic liquids may be one promising approach. However, a weakly-coordinating solvent like an ionic liquid is not necessary for crystallization under anhydrous conditions. Various alcohols may act as polar protic solvent that is anhydrous.

In the following chapter, various alcohols will be tested as solvents for Co^{2+} and PO_4^{3-} in order to precipitate an anhydrous cobalt phosphate. If the synthesis under anhydrous conditions is successful, the amorphous material will be characterized comprehensively in terms of composition and configuration. As the amorphous solid is water deficient with regards to $Co_3(PO_4)_2 \times 8\ H_2O$, following the uptake of water and its crystallization behavior *in situ* will gather more information about crystallization of hydrated modifications. Further, comparison may be made between the anhydrous amorphous cobalt phosphate and the hydrated one (ACP) as intermediate during precipitation in aqueous solution.

6.2 Experimental

6.2.1 Synthesis

Anhydrous amorphous cobalt phosphate was synthesized by precipitation in methanol (MeOH-ACP) using $CoCl_2$ (anhydrous, >99.999%, Sigma Aldrich) and Cs_3PO_4 (MP Biomedicals). In order to achieve anhydrous synthesis conditions, we dried 60 µmol (7.79 mg) $CoCl_2$ and 40 µmol (19.74 mg) Cs_3PO_4 for 3 d using a Schlenk tube at 120 °C and 3×10^{-3} mbar. The compounds were solved in respective 10 mL dry methanol (≥99.9%, Sigma Aldrich) under ultrasonication for 4 h at 40 °C. The solutions were mixed and centrifuged under inert conditions. The precipitated MeOH-ACP was dried for 3 d *in vacuo* (3×10^{-3} mbar) at room temperature.

6.2.2 Water Uptake

The amount of coordinating water of MeOH-ACP was monitored by ATR-FTIR spectroscopy. The substance was stored under vacuum until the measurement. Measurements were carried out every 30 s to monitor the increasing amount of water *in situ*. The experiments were repeated with MeOH-ACP in the wet state without removing MeOH in vacuum because MeOH prevents the uptake of water.

6.2.3 Crystallization

As MeOH-ACP crystallizes in the presence of water, crystallization experiments were performed in a climate chamber (50 °C and 70% humidity). MeOH-ACP stored under air conditions for 2 weeks (hydr-MeOH-ACP) with the final uptake of water in air at ambient conditions was used for this purpose. ATR-FTIR spectra were recorded every 10 min after storing in the climate chamber respectively.

6.2.4 Further Characterization

The morphology of MeOH-ACP was determined using TEM. Additionally, TEM micrographs were recorded from hydr-MeOH-ACP stored for two weeks under air conditions and of $Co_3(PO_4)_2 \times 8\ H_2O$ after crystallization in the climate chamber.

A XRD pattern of MeOH-ACP was collected in a fused capillary to avoid any uptake of water. Hydr-MeOH-ACP stored for 2 weeks under air was measured as well. Both XRD measurements were performed at synchrotron beamline BESSY II.

TGA and DTA measurements were performed up to 800 °C simultaneously to determine the crystallization temperature for thermally induced crystallization of MeOH-ACP and its amount of water. MeOH-ACP was used in the wet state without removing methanol to avoid uptake of water. It was heated to 85 °C for 30 min under Ar flow to remove any adsorbed MeOH.

Further characterization including ICP-MS, ICP-OES, and EDX were carried out for hydr-MeOH-ACP stored under air conditions for 2 weeks. There was no possibility to perform these measurements under exclusion of humidity and therefore the substance with a known and constant uptake of water was investigated instead. Unlike the amount of water, the ratio of PO_4^{3-} to Co^{2+} should not change under air conditions.

For additional experimental details see Chapter 13.

6.3 Results and Discussion

6.3.1 Synthesis

Many crystalline modifications of metal phosphates are very stable compounds from a thermodynamic point of view and thus reveal very low solubility products. Therefore, various combinations of phosphate salts (M_3PO_4 with M=Na, K, Li, Cs) and solvents (methanol, ethanol, 2-propanol) had to be tested in order to generate an alcoholic solution containing phosphate. As PO_4^{3-} is a hard anion according to Pearson's concept of hard and soft acids and bases, increasing ionic size of the alkali metal (softer character) leads to solid metal phosphates with lower free enthalpy of formation and thus higher solubility in water. Due to the high polarizability of Cs^+, Cs_3PO_4 provides the highest solubility in water of all tested compounds. Anhydrous MeOH was used as protic anhydrous solvent having similar solvent properties as H_2O. $CoCl_2$ as well as Cs_3PO_4 were solved in methanol successfully. Analogue experiments with other short-chain alcohols like ethanol and 2-propanol failed. The starting salts were dried for 3 d under inert conditions. Mixing $CoCl_2$ and Cs_3PO_4 that were solved in methanol respectively led to precipitation. Centrifuging the product under inert conditions resulted in a deep blue solid (MeOH-ACP), which was dried under vacuum. ATR-FTIR spectroscopy displayed the phosphate stretching mode in the region of 650 to 1220 cm^{-1}. For MeOH-ACP one very broad, non-split band was observed most probable due to the missing short-range order of MeOH-ACP (see Figure 6.1 A). Very weak water vibrations indicated by low intensity vibration bands were observed in comparison to ACP synthesized in water (see Figure 6.1

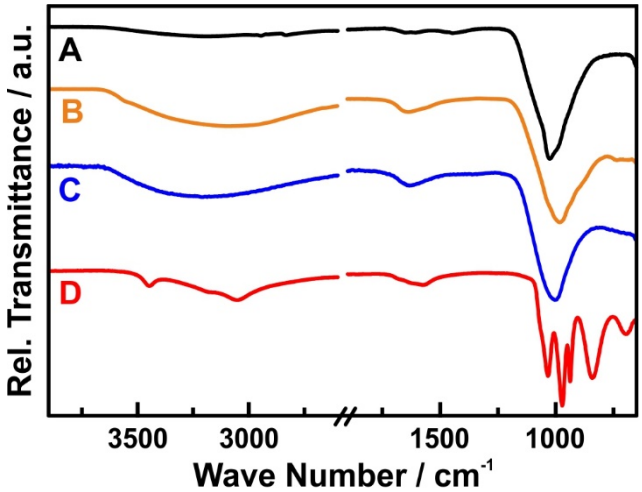

Figure 6.1. IR spectra of **(A)** MeOH-ACP synthesized in methanol after drying, **(B)** hydr-MeOH-ACP after 2 weeks on air, **(C)** ACP synthesized by precipitation in H_2O and **(D)** $Co_3(PO_4)_2 \times 8\ H_2O$, synthesized by stirring hydr-MeOH-ACP for 1 week in H_2O.

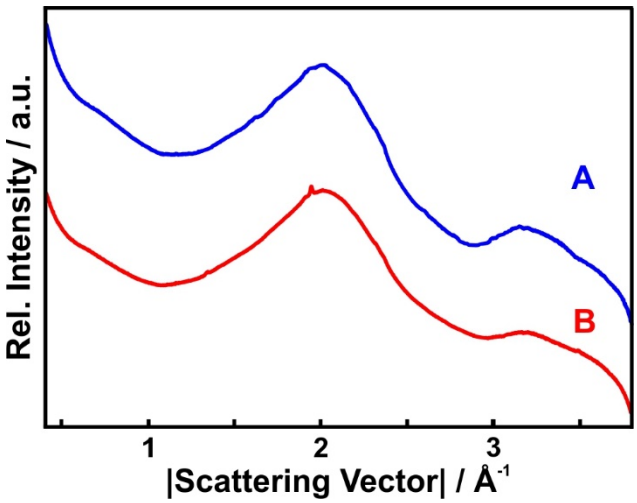

Figure 6.2. XRD patterns measured with high-intensity synchrotron radiation at BESSY II of **(A)** MeOH-ACP in a capillary (scattering of capillary was subtracted) and **(B)** hydr-MeOH-ACP.

C/Chapter 4) indicating the successfulness of the synthesis. Time dependent ATR-FTIR measurements displayed an uptake of water even in very early stages after the storage under vacuum. Measuring MeOH-ACP in the wet state without removing MeOH suggested the absence of water in the amorphous solid (deformation vibration of water is observable also in the presence of MeOH) (*vide infra*, Figure 6.4 a). The XRD pattern of MeOH-ACP recorded in a capillary resulted in a broad modulated intensity without defined reflections (see Figure 6.2 A) indicating the amorphous character of MeOH-ACP.

The morphology of MeOH-ACP was determined using TEM. Freshly prepared product, still dispersed in MeOH (no centrifugation), was dropped on a TEM grid. MeOH-ACP appears as coalesced ("molten") aggregates of "particles" in small areas 10 to 40 nm (see Figure 6.3 B) in size. Further, big areas 70 to 200 nm in size reminiscent of a liquid (see Figure 6.3 A) were detected. No defined particles were observed.

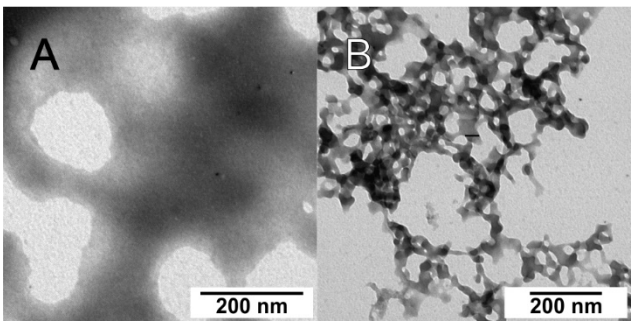

Figure 6.3. TEM images of MeOH-ACP.

ACP synthesized from aqueous solution with a higher amount of structural water appears also as coalesced aggregates of particles but with a decreased degree of structural flexibility (see Figure 4.3).The visual contrast of MeOH-ACP to the carbon grid in the TEM images is relatively low and varying. This may indicate density fluctuations in MeOH-ACP, reminiscent of a LCP at the nanoscale.

6.3.2 Water uptake

As MeOH-ACP takes up water very fast, we measured time dependent IR spectra. Figure 6.4 b) shows the evolution of the extinction of water stretching and deformation vibration for MeOH-ACP with increasing time on air. IR measurements were performed in the wet state without removing MeOH, in order to monitor ACP with a minimum amount of coordinating water. The stretching mode of water cannot be resolved in the presence of MeOH because MeOH absorbs in the same region. However, monitoring the deformation mode of water allowed to observe the water uptake in the very first stages. MeOH-ACP takes up water very fast and reaches a plateau approximately after 25 min. The evolution of extinction was described by a Langmuir-like behavior indicating that the uptake of water proceeds via adsorption/desorption of water to distinct surface sites. The plot suggests the absence of water at t=0 within the scope of measurement.

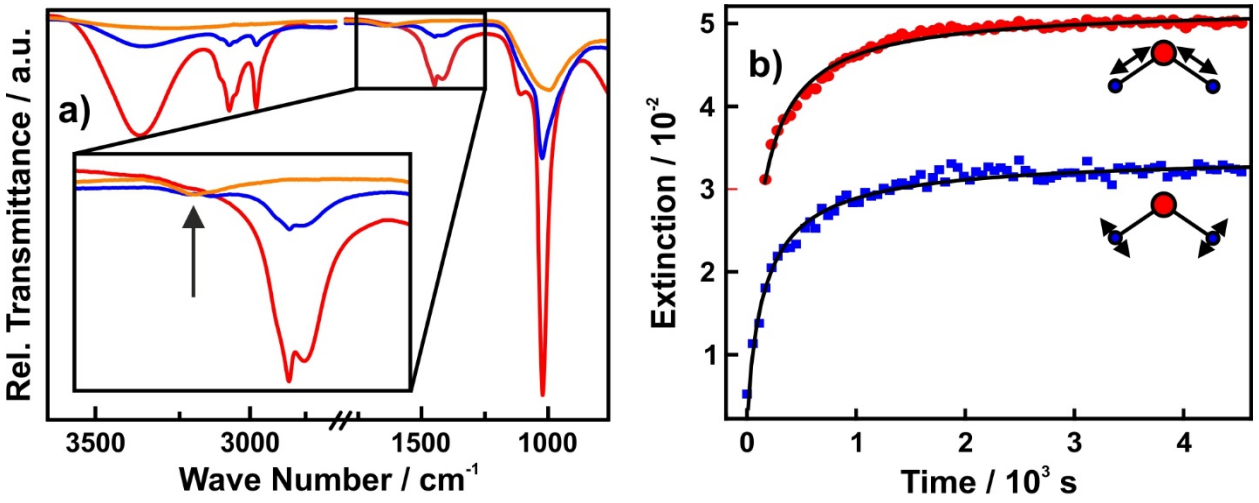

Figure 6.4. a) IR measurements of MeOH-ACP in the wet state. Red: Direct measurement; blue: 1 min on air, orange: 4 min on air. Arrow in the inset indicates the water deformation mode observable in the presence of MeOH. **b)** Evolving of the water vibrations (extinctions) of MeOH-ACP in the wet state. The stretching vibration (red circles) cannot be observed in the presence of methanol. However, deformation vibration (blue squares) can be observed from the beginning of the experiment. Black lines represent Langmuir plots of the IR data.

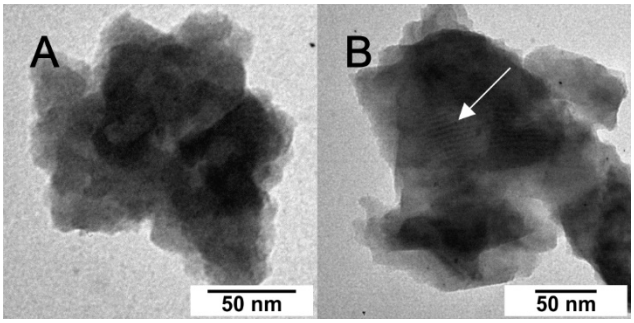

Figure 6.5. TEM images of hydr-MeOH-ACP.

According to the Langmuir mechanism, a saturation limit may be reached for longer reaction times. Therefore, a final uptake of water under ambient conditions is indicated leading to a hydrated hydr-MeOH-ACP (2 weeks after synthesis of MeOH-ACP). The uptake of water does not cause crystallization which is observed by a non-split phosphate band in the respective IR spectrum (see Figure 6.1 B) and by missing Bragg reflections in the corresponding XRD pattern (see Figure 6.2 B). IR spectroscopy revealed a water content of 5.2 formula units of H_2O per formula unit of $Co_3(PO_4)_2$. This value is really close to ACP synthesized in aqueous solution with a sum formula of $Co_3(PO_4)_2 \times 5.0\ H_2O$ (Figure 6.1 C). Hydr-MeOH-ACP is formed from MeOH-ACP by uptake of water. However, the coalesced aggregates observed for MeOH-ACP densify resulting in denser aggregates with small subunits about 20 nm in size (see Figure 6.5 A). A few particles showed lattice planes which were strongly restricted locally (see Figure 6.5 B). This is indicative for crystallization of hydr-MeOH-ACP to crystalline $Co_3(PO_4)_2 \times 8\ H_2O$. Consequently, a small reflection is observed in the corresponding XRD pattern at approximately 1.9 $Å^{-1}$ (Figure 6.2 B). ATR-FTIR measurements still displayed an amorphous sample (Figure 6.1 B).

6.3.3 Crystallization

As MeOH-ACP takes up water to the sum formula $Co_3(PO_4)_2 \times 5.2\ H_2O$ without crystallization when exposed to ambient humidity, additional water is needed for crystallization. Therefore, crystallization experiments were performed in a climate chamber at 70% humidity (50 °C). Increased temperature and humidity may promote crystallization. Figure 6.6 displays the crystallization kinetics of hydr-MeOH-ACP in a climate chamber using quantitative ATR-FTIR spectroscopy. MeOH-ACP itself transforms to hydr-MeOH-ACP in nearly 30 min under ambient conditions. Thus, it is not necessary to run experiments with MeOH-ACP because there is only water uptake in the early stages indicated by the non-split phosphate stretching mode. Again, we prepared mixtures of crystalline $Co_3(PO_4)_2 \times 8\ H_2O$ and

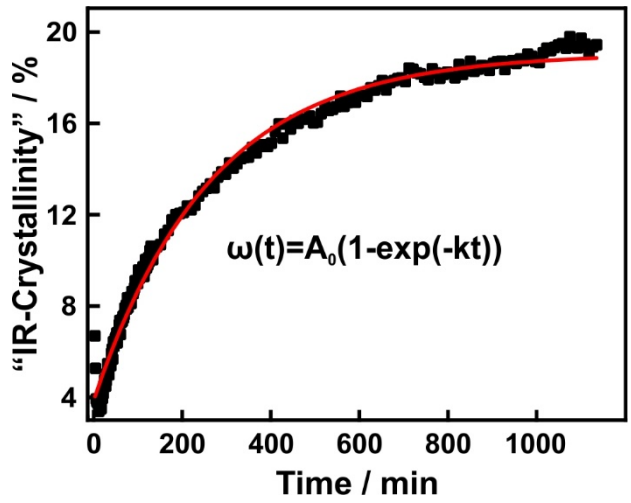

Figure 6.6. Crystallization kinetics of hydr-MeOH-ACP measured by ATR-FTIR spectroscopy. "IR-crystallinity" ω depends on the time t in an exponential manner.

hydr-MeOH-ACP as standards for the quantification. Water uptake in the climate chamber led to crystallization while an amorphous phase with a higher amount of water was not detected. This suggests that hydr-MeOH-ACP (stored for 2 weeks on air) is an amorphous cobalt phosphate hydrate with maximum content of coordinating water before crystallization (beginning splitting of the phosphate modes). Fitting the results of ATR-FTIR measurements display an exponential dependence of the degree of crystallinity on the time. Basically, crystallization kinetics are the same for hydr-MeOH-ACP and ACP (see Chapter 4). This is not a surprise as MeOH takes up water very fast forming hydr-MeOH-ACP with nearly the same composition than ACP. TEM images revealed the polycrystalline character of the as-synthesized $Co_3(PO_4)_2 \times 8\ H_2O$ (see Figure 6.7). The crystalline sub-units were small in size and poorly aligned.

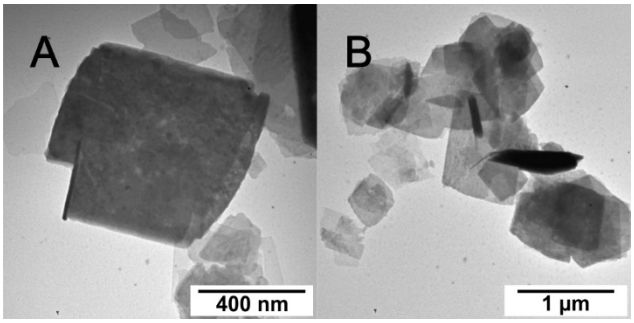

Figure 6.7. TEM images of $Co_3(PO_4)_2 \times 8\ H_2O$ achieved after crystallization experiment in climate chamber.

6.3.4 Composition

The composition of hydr-MeOH-ACP was determined using ICP-MS, ICP-OES, and EDX. The results obtained from these techniques are displayed in Table 6.1 separately. The average ratio of Co to P is 3:2.0. As hydr-MeOH-ACP forms from MeOH-ACP, only the amount of coordinating water may change most probably but not the ratio of Co to P. However, determination of the MeOH-ACP composition *in situ* without uptake of water was not possible.

Table 6.1. ICP-MS, ICP-OES, and EDX results of hydr-MeOH-ACP synthesized in MeOH and stored for 2 weeks on air.

ICP-MS	^{59}Co	^{31}P
mean conc. / μg L^{-1}	98.2±2.7	33.0±1.0
mean conc. / μmol L^{-1}	1.67±0.04	1.06±0.3
ratio		3.00:1.91±0.1
ICP-OES	Co	P
mean conc. / μg L^{-1}	105	36
mean conc. / μmol L^{-1}	1.8	1.2
ratio		3.0:2.0
EDX	CoK	PK
at%	24.8	17.0
ratio		3.0:2.1

6.3.5 Thermal Analysis

In addition, we probed the thermally induced crystallization of MeOH-ACP. TGA in combination with DTA was performed with freshly synthesized MeOH-ACP in the wet state without removing MeOH (Figure 6.8) because MeOH prevents the uptake of water as indicated by the results of ATR-FTIR measurements. The sample was heated up to 80 °C and held at this temperature for 15 min to remove all traces of methanol under argon flow. The DTA signal of MeOH-ACP is similar to the signal of ACP synthesized from aqueous solution (see Chapter 4). A broad endothermic signal between 100 and 300 °C was detected which is

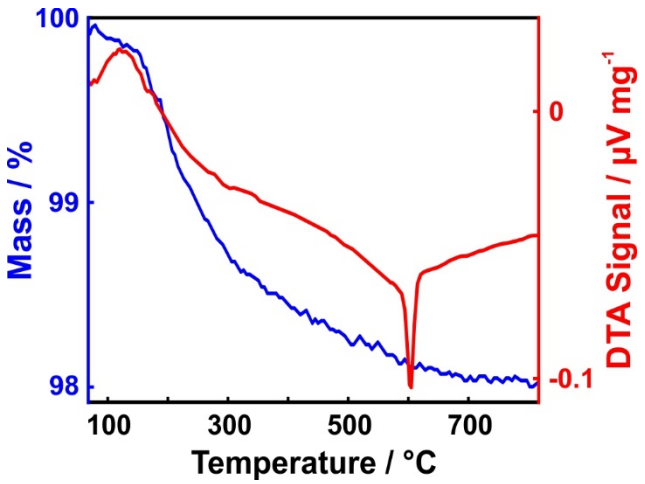

Figure 6.8. DTA and TGA curves of MeOH-ACP measured in the wet state while removing MeOH under argon flow at 80 °C for 15 min in the DTA device.

assigned to the loss of weight by evaporation of a minimal amount of water. Furthermore, an exothermic signal observed at 603 °C indicates the crystallization to anhydrous $Co_3(PO_4)_2$. As already pointed out in Chapter 3, the amount of coordinating water has no significant influence on the thermally induced crystallization to the anhydrous modification within the accuracy of a DTA measurement. This may be explained by very small differences in the free enthalpy of formation for different amorphous solids.

An obvious difference in the TGA curves of ACP and MeOH-ACP is the significantly less loss of water during heating for MeOH-ACP. A chemical composition of MeOH-ACP is calculated from the weight loss of approximately 2% to be $Co_3(PO_4)_2 \times 0.5\ H_2O$. Due to the very fast uptake of water (more than one formula unit of water in the first minute as determined by ATR-FTIR spectroscopy) even filling the crucible of the TGA/DTA device may lead to evaporation of methanol and incorporation of water in MeOH-ACP. Thus, the results of TGA are not taken into account for determination of MeOH-ACP's degree of hydration. Based on the results using ICP-MS, ICP-OES, EDX, and quantitative ATR-FTIR spectroscopy an average composition of $Co_3(PO_4)_2$ can be assumed for MeOH-ACP.

6.4 Conclusion

Anhydrous amorphous cobalt phosphate was prepared by precipitation in methanol (MeOH-ACP). To the best of our knowledge, this is the first report for the synthesis anhydrous amorphous phosphates in an alcoholic solution. Syntheses in water-free systems may be a general procedure to generate amorphous intermediates for systems whose thermodynamically stable modification at ambient conditions results in hydrates. The way to the thermodynamically stable (hydrated) polymorph is blocked due to the lack of water, and the anhydrous crystalline modifications are only accessible at elevated temperatures. Therefore, the formation of amorphous solids may be the logical consequence.

Electron micrographs display aggregates of coalesced species at the nm to μm scale as morphology of MeOH-ACP. Further, MeOH-ACP takes up water provided by humidity very fast to a final amount of $Co_3(PO_4)_2 \times 5.2\ H_2O$ (hydr.-MeOH-ACP) according to a Langmuir-like behavior. According to our measurements, hydr.-MeOH-ACP is basically the same product than ACP which occurs as intermediate in aqueous solution.

No crystallization to $Co_3(PO_4)_2 \times 8\ H_2O$ was observed for hydr.-MeOH-ACP under ambient conditions. Additional uptake of water along with crystallization can be achieved by regulating the moisture atmosphere in a climate chamber or by aqueous solution. Crystallization proceeds via agglomeration and densification of MeOH-ACP. The fact that MeOH-ACP takes up water very fast but does not crystallize under ambient conditions, indicates that a certain amount of coordinating water is essential for stabilizing amorphous intermediates probably via hydrogen-bonded networks. Thermally induced crystallization during heating resulted in anhydrous crystalline $Co_3(PO_4)_2$.

Nucleation and crystal growth is sensitively influenced by water not only as solvent but also as active participant in complex aggregation and densifying steps. In order to understand the essential role of water during these processes, it is necessary to perform crystallization experiments also in non-aqueous systems as crucial reference.

7

STABILIZING AMORPHOUS NANOPARTICLES BY SILICA SHELLS

7.1 Introduction

As the mechanisms by which amorphous intermediates transform to crystalline polymorphs are still poorly understood, it is essential to determine the crystallization kinetics of such intermediates. One of the most investigated model system for nucleation and crystallization processes is calcium carbonate.[231–234] Amorphous calcium carbonate (ACC) plays a key role for crystallization of calcite, both *in vivo*[234] and *in vitro*.[235] Using additives, the metastable ACC can be stabilized *in vitro*.[236,237] Recently, synthetic amorphous calcium carbonate was reported to dehydrate before crystallizing, both in solution and in air.[238] It is essential to expel structural water prior to crystallization, as the thermodynamically stable polymorph of calcium carbonate, calcite, is an anhydrous polymorph. The metastability of synthesized ACC is largely independent of the amount of coordinating water, but it plays an essential role in lowering the energy barrier during precipitation.

In the case of AZP (see Chapter 3), its crystalline counterpart hopeite is a hydrated polymorph. AZP contains less coordinated water (approximately 2 units of water per formula unit of zinc phosphate) than hopeite. Thus, crystallization does not proceed via expelling of coordinated water, but by incorporation of additional water. The moderate charge density of Zn^{2+} allows the formation of a hydrogen-bonded network that may trigger the crystallization process.

However, changes in the degree of hydration may be decelerated by encapsulation with a silica shell as diffusion of surface water towards the AZP core may be reduced. A large body of research has been carried out on the encapsulation of nanoparticles with SiO_2, especially in

the field of biomedicine. Silica shells provide suitable mechanical stability, optical transparency, and fair biocompatibility.[239]

Goal of this chapter is to gather more information about the recrystallization process of AZP to hopeite in aqueous solution. Crystallization is induced by water provided by an aqueous solution or by humidity as shown in the previous chapters. Water molecules are part of hopeite's crystal structure but may also act as mineralizer providing surface mobility of ions. Determination of recrystallization kinetics in solution can be addressed by using a quantitative *in situ* ATR-FTIR spectroscopy protocol. In order to determine the influence of water on the crystallization kinetics, reference experiments are needed where the effect of surrounding water is limited. For this purpose, one further aim is the synthesis of silica shells around already formed AZP nanoparticles (AZP@SiO_2). If this synthetic approach is successful, AZP@SiO_2 particles are tested as reference. Encapsulation with a silica shell may limit the contact of AZP cores with surrounding water which may have an influence on the recrystallization behavior of AZP.

7.2 Experimental

7.2.1 Synthesis of Silica Shell

Following the approach developed by Stöber,[240] we dispersed 100 mg of amorphous zinc phosphate hydrate nanoparticles (see Chapter 3) in 5 mL of reagent-grade ethanol (≥99.8%, Sigma-Aldrich) and added various amounts of NH_3 (28% in water, ≥99.99%, Sigma-Aldrich) and tetraethyl orthosilicate (TEOS) (≥99.0%, Aldrich) while stirring. The dispersion was stirred for half an hour to allow formation of silica shells around the nanoparticles. Afterwards, the particles were centrifuged (9000 rpm) and washed 3 times with reagent-grade ethanol to remove excess NH_3.

7.2.2 Characterization

In order to verify the formation of silica shells, TEM measurements were performed. Samples were sonicated in reagent-grade ethanol and dropped on a carbon-coated copper TEM grid. Ethanol was removed *in vacuo*.

ATR-FTIR spectroscopy, XRD, and SS-NMR spectroscopy were used to verify the amorphous character of AZP@SiO_2 particles synthesized under different conditions.

7.2.3 Crystallization Behavior

The crystallization kinetics of AZP and AZP@SiO_2 particles in water were monitored quantitatively by ATR-FTIR spectroscopy. For these experiments, wet AZP and AZP@SiO_2 were placed on the ATR element of a FTIR spectrometer and measured *in situ*. For quantitative analysis, standards with known ratios of AZP to hopeite were used. An Avrami approach was employed for further analysis. In addition, XRD, TEM, and NMR measurements were repeated after one week of stirring AZP@SiO_2 in water.

A combination of TGA and DTA was used to determine the amount of coordinating water in the samples and the onset of thermally induced crystallization during heating.

For further experimental details see Chapter 13.

7.3 Results and Discussion

7.3.1 Synthesis

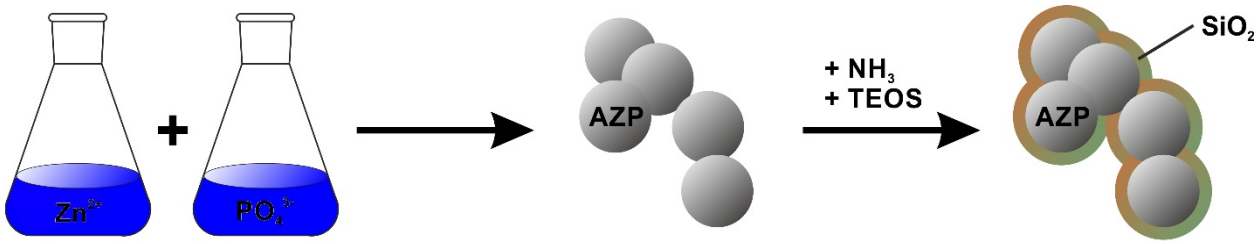

Figure 7.1. Synthesis scheme for silica-encapsulated AZP nanoparticles.

The synthesis scheme for the preparation of silica coated AZP nanoparticles is displayed in Figure 7.1. First, we synthesized AZP nanoparticles by a simple precipitation experiment at moderate concentrations and short reaction times as outlined in Chapter 3. In the second step, the basic hydrolysis of TEOS was used in order to synthesize shells of SiO_2. The commonly used method of reverse micro emulsion[241] was not suitable for the synthesis of silica shells as the initial W/O micro emulsion led to crystallization of AZP. In general, controlled hydrolysis and condensation of the silicon alkoxide TEOS result in the formation of a sol at pH<7. For pH>7 the sol particles grow to form silica nanoparticles instead.[242]

As AZP nanoparticles provide an already formed surface, heterogeneous nucleation may take place, leading to silica shells at pH>7. 100 mg AZP nanoparticles were stirred in reagent-grade ethanol while different volumes of TEOS and NH_3 were added. A variation of the amount of TEOS and NH_3 was performed to obtain homogeneous silica shells with an adequate thickness (see Table 7.1). For large quantities of NH_3 and TEOS, massive precipitation of silica (homogeneous nucleation) was observed by TEM with little or no observable AZP particles. For low amounts of NH_3 and TEOS, a negligible amount of silica

Table 7.1. Reaction conditions for synthesis of silica encapsulated AZP nanoparticles. 100 mg of AZP nanoparticles were applied respectively.

V(TEOS) / µL	V(NH_3) / µL	result
28.6	115	homogeneous silica shells
85	200	mainly silica particles
5	100	no shells

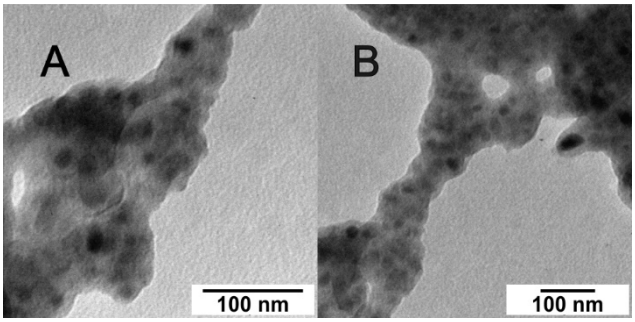

Figure 7.2. TEM images of AZP@SiO_2 particles. Silica shell formed over AZP agglomerates.

was detected. Use of 28.6 µL TEOS and 115 µL NH_3 resulted in the most homogeneous shells. TEM images confirmed that a 15 to 20 nm thick silica shell formed around the 22 nm AZP cores (Figure 7.2). No isolated AZP@SiO_2 particles were observed but a silica shell formed over entire agglomerates of AZP.

In order to verify that AZP is still amorphous after encapsulation, we performed XRD, ^{31}P MAS NMR, and ATR-FTIR measurements of AZP and AZP@SiO_2 (Figure 7.3). ^{31}P MAS NMR spectroscopy displayed very broad signals centered at 5.3 ppm and 5.6 ppm respectively. A broad ^{31}P MAS NMR signal is characteristic for an amorphous phosphates, but

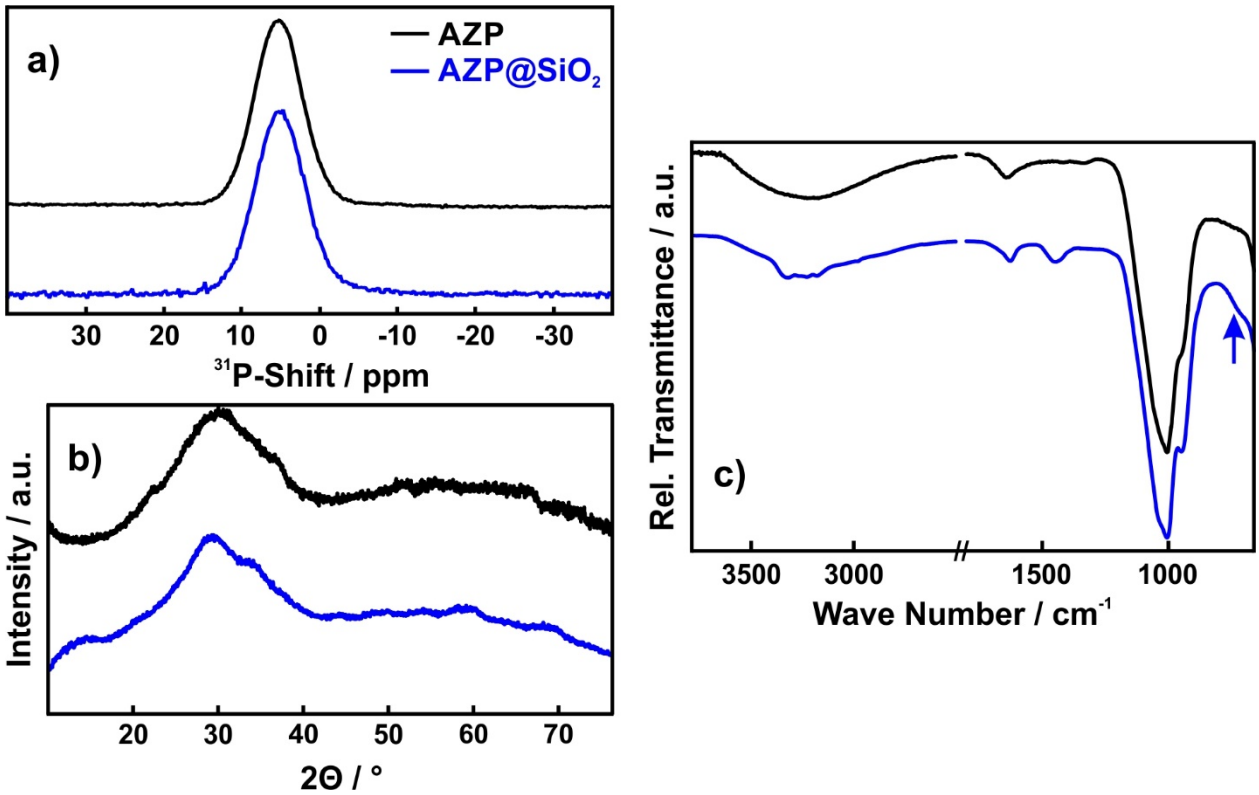

Figure 7.3. a) ^{31}P MAS NMR spectrum, **b)** XRD pattern, and **c)** IR spectrum of AZP and AZP@SiO_2 nanoparticles.

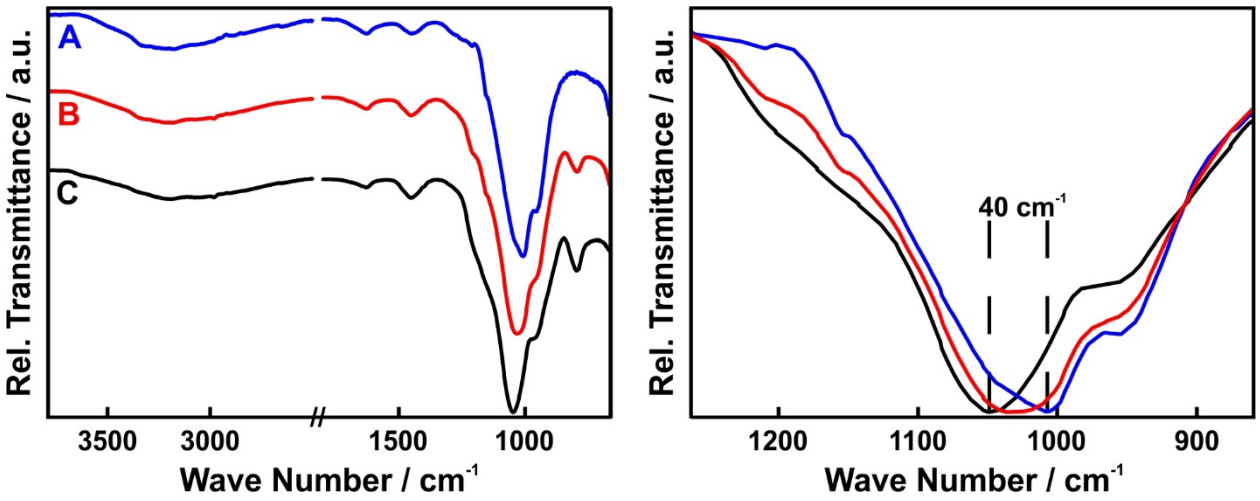

Figure 7.4. IR spectra of experiments resulting in large quantities of silica. **(A)** 0.5 mL NH_3 and 28.6 µL TEOS; **(B)** 0.5 mL NH_3 and 140 µL TEOS; **(C)** 0.5 mL NH_3 and 285 µL TEOS. The growth of the ν_s(Si–O–Si) band at 792 cm^{-1} as well as the blue shift of the band at 1000 cm^{-1} indicate the amount of silica formed.

also for nanocrystalline material. Missing Bragg reflections in the respective XRD patterns suggest that AZP stays amorphous during encapsulation and also that no other crystalline compounds (*e.g.*, crystalline SiO_2 or zinc silicates) form. In addition, ATR-FTIR spectroscopy revealed a broad, non-split band centered between 1000 and 1050 cm^{-1} depending on the synthetic conditions which is assigned to the asymmetric phosphate stretching mode ν_{as}(P–O). The band is non-split due to lower lattice site symmetry and the absence of factor group splitting. (For the IR spectrum of crystalline hopeite see Figure 3.5 B.) IR bands between 3000–3500 and at 1600 cm^{-1} are assigned to coordinating water. In the IR spectrum of encapsulated AZP, a band at 1448 cm^{-1} was observed additionally. Hudgen *et al.* explained this band in a P_2O_5-silica glass as corresponding to P=O stretching vibrations.[243] Furthermore, the arrow in Figure 7.3 indicates the barely visible ν_s(Si–O–Si) band at 792 cm^{-1}. For higher concentrations of TEOS or/and NH_3 this band was more and more pronounced due to the larger amount of silica formed (see Figure 7.4). The asymmetric Si–O–Si stretching mode of silica is reported to appear at 1105 and 1020 cm^{-1}.[244] The superposition of the asymmetric Si–O–Si stretching mode and the asymmetric stretching mode of phosphate may lead to a continuous shifting of the absorption maximum of the IR band at approximately 1000 cm^{-1} which was observed for different synthetic conditions. For large quantities of silica formed the band was blue shifted.

7.3.2 Characterization

The achieved results are indicative for a successful synthesis of amorphous AZP@SiO_2 particles. In order to clarify the effect of the silica shell on the thermally induced crystallization process and to determine possible differences in the level of hydration, a combination of TGA and DTA was performed (Figure 7.5). Both AZP and AZP@SiO_2 displayed a weight loss of about 10.5%. Under the assumption that the hydration state of AZP particles dispersed encapsulated by SiO_2 does not change, it is proposed that the silica phase reveal the same percentage loss of water than AZP. This explanation leads to a composition of the silica phase of $SiO_2 \times 0.4\ H_2O$. In addition, TGA display the evaporation of coordinating water at higher temperatures for AZP@SiO_2 than for AZP. This may be explained by the fact that coordinating water within the amorphous zinc phosphate hydrate has to diffuse through the silica shell first. Further, evaporation of coordinating water at higher temperatures results in a less intense but broader endothermic signal detected in the DTA curve in the range of 90 to 300 °C for AZP@SiO_2 in comparison to AZP. The onset of thermally induced crystallization of AZP and AZP@SiO_2 to anhydrous *a*-$Zn_3(PO_4)_2$ was observed by two exothermic signals between 480 and 550 °C. (In fact, for AZP@SiO_2 also weak reflections which were assigned to tridymite (SiO_2) were observed in the corresponding XRD pattern.). AZP@SiO_2 crystallizes at a slightly lower temperature than AZP.

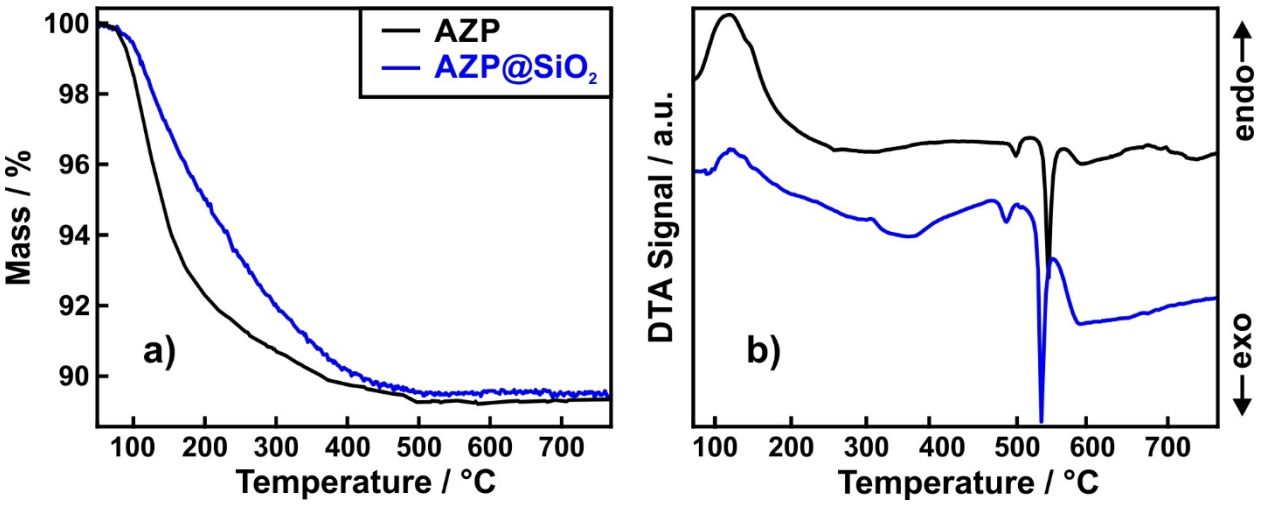

Figure 7.5. a) TGA and **b)** DTA of AZP nanoparticles and AZP@SiO_2 nanoparticles in comparison.

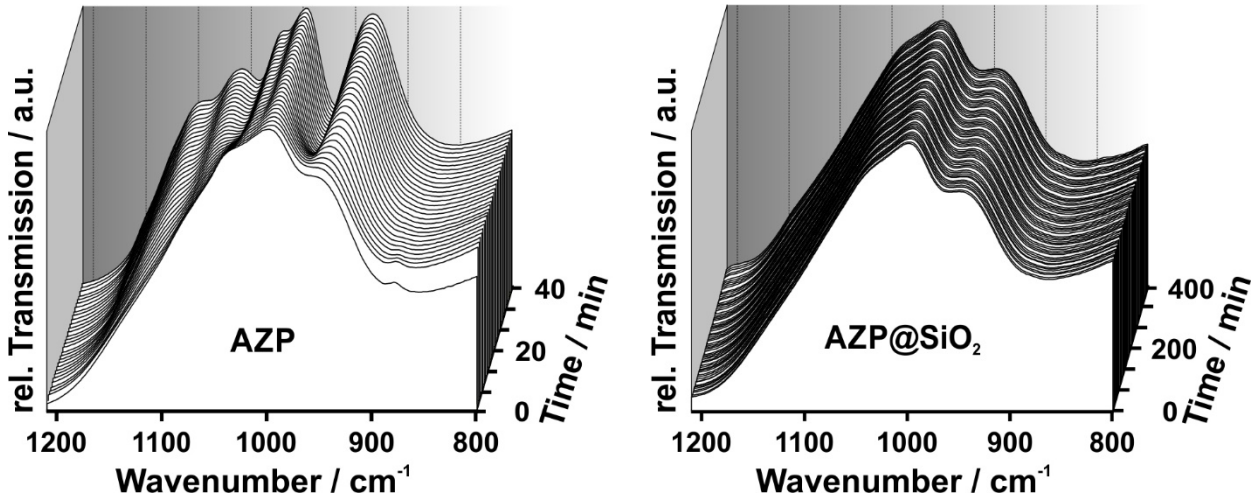

Figure 7.6. IR spectra of wet AZP and AZP@SiO_2 measured *in situ*. Splitting of the asymmetric phosphate stretching mode shows the ongoing crystallization of AZP to hopeite. Note that the time scale of the crystallization experiment with AZP@SiO_2 is ten times larger than for the AZP experiment.

7.3.3 Crystallization Behavior in Water

As pointed out in Chapter 3, AZP crystallizes very fast in the presence of water provided by aqueous solutions or even moisture. A shell of silica may limit the diffusion of additional water that is needed for crystallization to hopeite towards the AZP cores: Therefore, we expect different crystallization behavior. In order to determine recrystallization kinetics, ATR-FTIR spectroscopy with wet AZP and AZP@SiO_2 was performed *in situ* on the ATR element of an IR spectrometer. AZP starts to crystallize instantly, which is observable by the increasing splitting of asymmetric stretching mode of phosphate due to factor group splitting and increased lattice site symmetry (Figure 7.6). In order to have a quantitative access to the kinetics of the crystallization process, IR spectra of mixtures with known ratios of AZP and crystalline hopeite were measured, and the respective splitting of the asymmetric phosphate stretching mode was used for a standardization (Figure 7.7). Results for the quantitative analysis of AZP's crystallization kinetics determined by ATR-FTIR spectroscopy are displayed in Figure 7.8 a). The crystallization of AZP synthesized by precipitation displayed a sigmoidal curve with low crystallization rates in the beginning and the end but rapid crystallization at intermediate times. This is typical for systems that show an incubation period. The slow initial crystallization is due to the activation barrier that must be overcome to form crystalline nuclei within the 20 nm particles. During the intermediate period, the crystallization is rapid as the crystalline regions grow throughout the particles and consume the amorphous phase while new nuclei continue to form in the remaining parent phase. The crystallization eventually stagnates when little

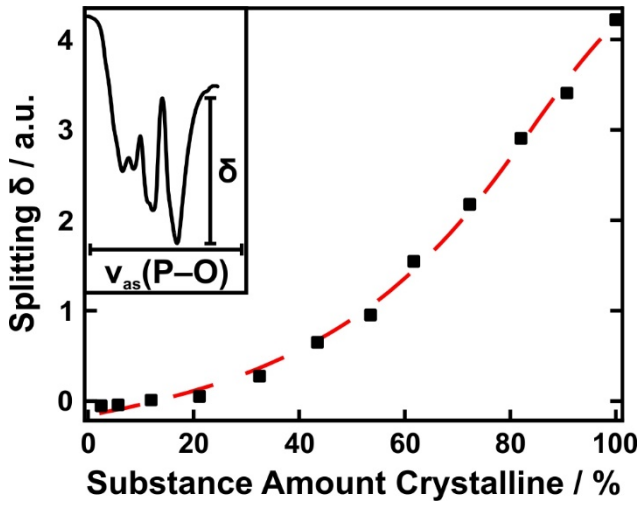

Figure 7.7. Splitting of the asymmetric phosphate stretching mode for mixtures of AZP and hopeite measured by ATR-FTIR spectroscopy.

material is left for crystallization. Furthermore, the crystalline regions begin to touch one other and fuse into bigger crystals. In essence, the nucleation and growth follows an Avrami type kinetics which is indicative of an autocatalytic crystal growth.

A non-linear least-squares fit of this evolution to the Avrami form[245–247] $s=1-\exp(-[k(t-t_0)]^n)$ yields the best results for $t_0=0$ indicating that crystallization starts initially. A value of 1.17 for the exponent n and 2.67×10^{-4} s^{-1} for the Avrami constant k was obtained by fitting[248,249,303] The fit is not suitable at longer reaction times, and in the manner in which the curve saturates. This is perhaps because of the number of different steps in the data analysis procedure with each step introducing some error. We are unable to simultaneously

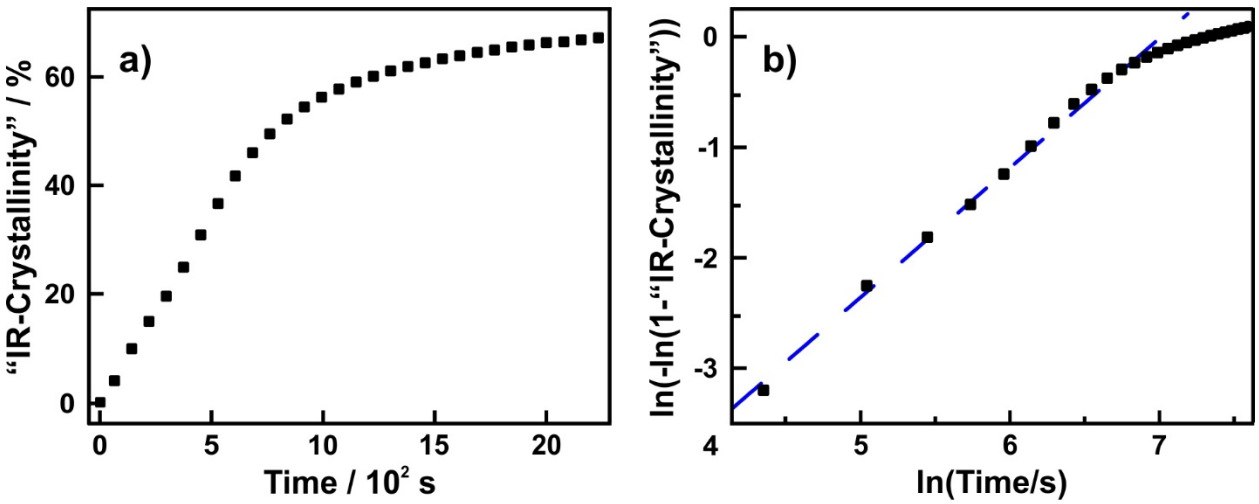

Figure 7.8. a) Quantitative analysis of AZP crystallization kinetics by ATR-FTIR spectroscopy. **b)** Double-logarithmic plot of crystallization kinetics showing the underlying Avrami mechanism.

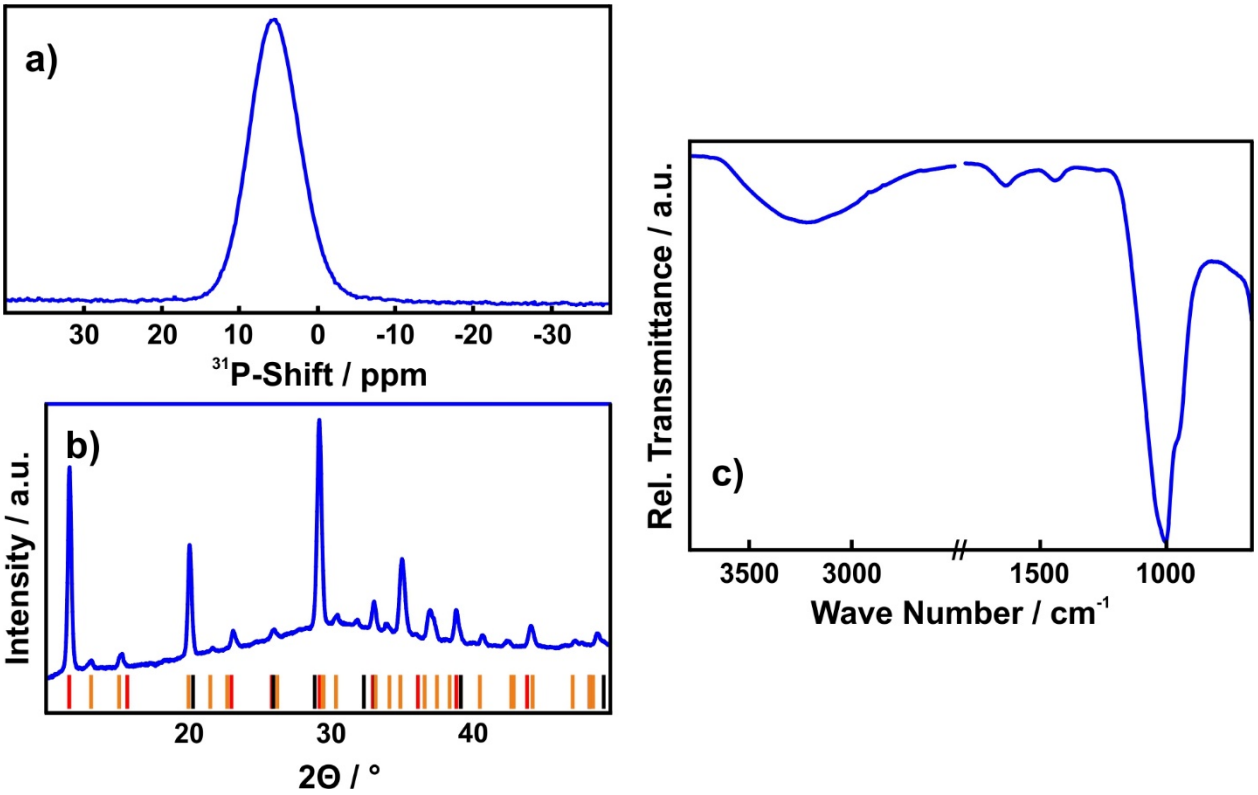

Figure 7.9. AZP@SiO_2 nanoparticles after incubation in water for one week. **a)** ^{31}P MAS NMR spectrum, **b)** XRD pattern (literature reflections: red - coesite (SiO_2), orange - SiO_2 (calculated), black - *a*-$H_2Si_2O_5$) (literature reflections with less than 1% intensity of the most intense reflection are not shown for a better overview), and **c)** ATR-FTIR spectrum. All measurements suggest that silica encapsulation inhibits crystallization of hopeite.

refine k, n and t_0 in the fitting procedures. The small value for n suggest that the process is, in keeping with expectation, diffusion controlled and that nuclei form in the early stages. A continuous formation of new nuclei should not take place.[245–248]

For AZP@SiO_2, the original IR band does not split further. Even for reaction times of 400 min (10 times longer than the entire experiment for AZP), no crystallization is detectable. Extension to longer reaction times in water of 1 week suggested that silica shells prevented crystallization of AZP. An XRD pattern of AZP@SiO_2 after incubation in water for one week is displayed in Figure 7.9 b). While the pattern displays reflections that indicate crystalline material, none of the reflections arise from hopeite, rather they can be all assigned to different crystalline SiO_2 and $H_2Si_2O_5$ species. This result shows that besides AZP@SiO_2, a small amount SiO_2 particles formed as side phase by homogeneous nucleation, which crystallized in the presence of water. In addition, a significant amorphous hump was observable in the XRD pattern, indicating the presence of amorphous phases, most probably AZP@SiO_2. Additional hints for the suppressed crystallization were achieved by ATR-FTIR spectroscopy and

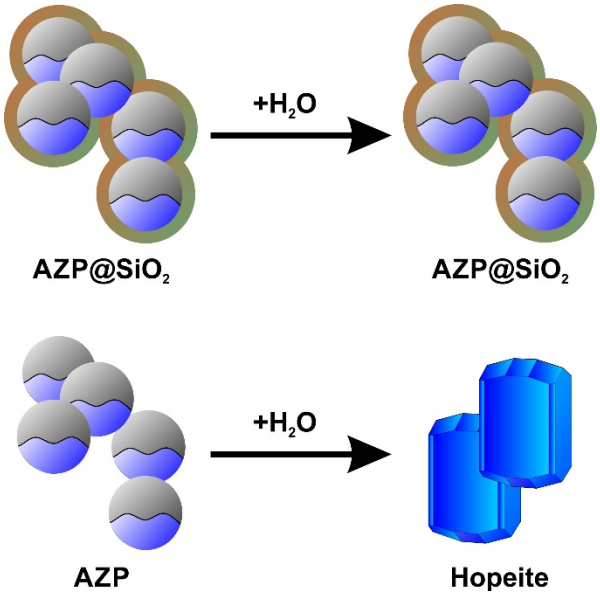

Figure 7.10. Scheme how silica shell may prohibit further uptake of water which is needed to crystallize hopeite.

^{31}P MAS NMR spectroscopy, as the spectra were identical to those of AZP@SiO_2 prior to incubation in water (see Figure 7.9 a) and c). These results strongly suggest that application of a silica shell prohibit the crystallization of AZP to hopeite by offering protection against the contact with surrounding water (see Figure 7.10).

7.4 Conclusion

In summary, we have determined the crystallization kinetics of AZP in water by applying *in situ* ATR-FTIR spectroscopy. AZP crystallizes to hopeite by uptake of water which cis described by an Avrami mechanism with an Avrami exponent of approximately 1. Water and the connected hydrogen-bonded network are proposed to determine the crystallization kinetics in accordance with the results of Chapter 3. Water plays a significantly different role during the crystallization process of hopeite than for crystallization of anhydrous crystal modifications like calcite. For systems with anhydrous crystal modifications, it is reported that water has to be expelled before crystallization. Water acts as a mineralizer that accelerates the mobility of ions involved in the process.[238] In the hopeite system water molecules are building blocks of the crystal structure what makes an uptake of water essential for a crystallization process.

Our results strongly suggest that crystallization of hopeite can be prohibited effectively in the absence of water. One possibility to limit the contact of amorphous nanoparticles with surrounding water is encapsulation in a silica shell. We successfully synthesized AZP@SiO_2 nanoparticles with homogeneous 15–20 nm shells that covered the AZP agglomerates. Results of XRD, SS-NMR, and ATR-FTIR spectroscopy indicate that AZP@SiO_2 does not crystallize in water to a significant amount within a period of one week. In contrast, crystallization of non-encapsulated AZP in water is completed within 60 min. The diffusion of surface water into the AZP cores may be limited by the silica shell. As AZP requires additional coordinating water as a building block for the crystal lattice of hopeite, the silica shell may prohibit the crystallization induced by water. These observations, combined with the very high temperature for thermally induced crystallization (480 °C), make AZP an interesting extreme example for how the thermodynamic pathway from a metastable state to its stable modification can be efficiently blocked.

8

FORMATION OF LIQUID-CONDENSED PHASES AT HIGH SUPERSATURATION

8.1 Introduction

The previous chapters pointed out the possibilities to stabilize amorphous solids of 3d metal phosphate hydrates against crystallization by applying a non-aqueous solvent or silica shells. However, the nanosized amorphous solids precipitate from solution. The question arises if it is possible to synthesize stable nanofluids where the metal phosphates are dispersed as nanoscale colloidal suspensions in aqueous solution. For this purpose, the nanomaterial has to be stabilized in order to prevent agglomeration leading to crystallization and phase separation.

Nanofluids display a variety of possible applications including energy storing materials,[250,251] heat transfer fluids,[252–254] drug delivery systems,[255,256] and advanced lubricants.[257] As they reveal an enhanced thermal conductivity, heat transfer processes applying nanofluids have attracted great attention for the last 15 years. The transfer of heat is essential to achieve high cooling rates for automotive engines, electronic components, and nuclear reactors.[258–260] However, a universal model how the nanometer-sized materials (nanoparticles, nanodroplets, nanorods, …) are stabilized in the respective fluids does not exist yet.

Nanomaterial tend to agglomerate in fluids due to their high-energy surfaces. In order to prevent agglomeration which may lead to phase separation, nanomaterials have to be stabilized sterically by applying surfactants. Another possibility is electrostatic stabilization, *e.g.*, by adsorption of charged species on nanomaterial's surface.

Several reports exist basically dealing with zinc phosphating which suggest indirectly the formation of stable nanofluids in the presence of high concentrations of HPO_4^{2-}/$H_2PO_4^-$.[133–139] It is reported that solutions containing Na_2HPO_4 or K_2HPO_4 has an increased potential to

dissolve zinc orthophosphates.[261] Furthermore, most of the synthesis procedures for zinc phosphate coatings refer on $Zn(H_2PO_4)_2$ concentrates in which $ZnCl_2$ is dissolved.[262,263]. The reports are focused on the phosphate coatings which should be nanocrystalline or amorphous. No satisfying models have been established dealing with nucleation and crystallization on the provided surface at high concentrations of zinc and phosphate present in the phosphating baths. Unfortunately, the authors do not provide any information concerning the pH values present during preparation of concentrates and the phosphating process. The question whether dissolution of the respective zinc species without precipitation of zinc phosphate appears due to the low present pH or due to the formation of nanofluids in highly concentrated (di)hydrogen phosphate solutions, remains unanswered.

These reports, basically technically oriented, inspired us to investigate the performance of 3d metal phosphates in highly concentrated hydrogen phosphate solutions. We choose zinc and cobalt phosphate as model systems making up a complementary couple. SS-NMR spectroscopy can be applied for the zinc phosphate system that may provide essential information about the chemical environment of phosphate species in the concentrates. Further, the color of cobalt phosphates provides insights into the coordination of Co^{2+} and its hydration state. Investigation of nucleation and precipitation events in the presence enormous supersaturation (probably leading to the formation of networks and enhanced viscosity) will help to improve our knowledge about nanofluids and nucleation processes in general.

The expression liquid-condensed phase (LCP) is used instead of nanofluids for the following experimental procedures and discussions for the following reasons: (i) The term nanofluid refers to a two-phase system composed of a (usually saturated) solution with dispersed nanoparticles. The presence of nanoparticles could not be evidenced. (ii) LCP is a more general term referring to an one-phase system.

In literature, the term LCP basically refers to metastable nanoscaled liquid-droplets occurring during precipitation and not to liquid bulk phases.[25,26] However, the term LCP is assumed to fit best for describing the results of this chapter.

8.2 Experimental

8.2.1 Synthesis of liquid phase

0.5 M K_2HPO_4 solution was prepared by solving 21.78 g solid K_2HPO_4 (≥98%, Sigma Aldrich) in 250 mL deionized water. Afterwards 250 mL reagent-grade ethanol (≥99.8%, Sigma Aldrich) were added resulting in the formation of a two-phase system (highly concentrated aqueous K_2HPO_4 solution and water-ethanol mixture). The upper ethanol phase was removed by decantation and by repeated pipetting. In addition, 68.0 g $ZnCl_2$ (99.999%, Sigma Aldrich) were solved in 100 mL reagent-grade ethanol (500 mM solution). Different amounts of $ZnCl_2$ solution (1–40 mL) were added to the aqueous K_2HPO_4 solution by a pipette and the mixture was homogenized by shaking. Analogous experiments were performed with $CoCl_2$ (≥98%, Sigma Aldrich) instead of $ZnCl_2$.

In order to determine the amount of Co and Zn in the viscous down phase, atomic absorption spectroscopy was performed (AAS).

8.2.2 Structural Analysis

In order to gain a structural model for the synthesized liquid species, we performed ^{31}P MAS NMR spectroscopy with the initial solution highly concentrated in K_2HPO_4 as well as after adding different amounts of $ZnCl_2$.

8.2.3 Further Analysis

Viscosity of the liquid species was determined by a Couette viscometer. The number of revolutions was varied in the range of 100–175 min^{-1}.

We used a Microtrac NANO-flex to measure dynamic light scattering in the backscattering mode (180° heterodyne DLS). For this purpose, a 5 mW laser was used at 780 nm. Signals were evaluated with the software Microtrac FLEX 11.0.0.2.

Conventional TEM measurements were carried out by dropping the viscous liquid on a copper coated carbon-grid. In addition, a setup with an *in situ*-liquid cell TEM flow holder was used. Measurements were done on a TEM 2011 FS with between two SiN chips in distance of 5 μm, which are mounted in a crossed geometry.

In addition, ATR-FTIR spectra were recorded and SAXS was measured.

For experimental details see Chapter 13.

8.2.4 Potential for Dissolving Crystalline Phosphates

In order to investigate the potential of the highly concentrated K_2HPO_4 solution for dissolving already formed crystals, 10 mg of $Co_3(PO_4)_2 \times 8\ H_2O$ (synthesized according to Chapter 4), hopeite (synthesized according to Chapter 3), fluorapatite (see below), and $CePO_4$ (American Elements, 99%) were stirred in 10 mL of solution for 1 d respectively.

Synthesis of fluorapatite:

2.5 mmol $CaCl_2 \times 2\ H_2O$ (≥99%, Sigma Aldrich) and 0.25 mmol NH_4F (≥99.99%, Sigma Aldrich) were dissolved in ethylene glycol (≥99.8%, Sigma Aldrich) by treatment with a sonication probe for 2 h (solution 1) as well as 1.5 mmol $(NH_4)_2HPO_4$ (≥99%, Sigma Aldrich) in ethylene glycol (solution 2). Both solutions were mixed and again treated with a sonication probe for 2 h. The precipitate was separated by centrifugation (9000 rpm, 5 min) and dried *in vacuo* ($p=3\times10^{-3}$ mbar) for 2 d.

8.3 Results and Discussion

8.3.1 Synthesis

0.5 M aqueous K_2HPO_4 solution was mixed with reagent-grade ethanol. As ethanol and water are mixable in any ratio, one would expect an one-phase system as a result. However, a two-phase system was formed. ATR-FTIR spectroscopy displayed ethanol and water vibrations with no bands arising from HPO_4^{2-} in the upper phase (see Figure 8.1 A). In the down phase no ethanol bands were observed (see Figure 8.1 B). Therefore, it is assumed that a phase separation took place resulting in an aqueous $KHPO_4$ solution and a water-ethanol mixture. This phenomenon has similarity to other ternary systems like water/ethanol/toluene[264] or water/methanol /styrene.[265] In these cases, the authors referred to the *Louche effect* or "Ouzo effect". Our ternary system is composed of two solvents (ethanol and water) which are miscible in all proportions and a third compound (K_2HPO_4) which is soluble in the first solvent (water) and nearly insoluble in the second solvent (ethanol). As the initial system is brought into the metastable region of the corresponding phase diagram by the addition of ethanol, the mixture is supersaturated with respect to ethanol probably leading to homogeneous nucleation. The nuclei may form spontaneously from small local concentration fluctuations. The droplets grow in order to reduce surface tension via Ostwald ripening leading resulting in a two-phase system. The down phase reveals the maximum concentration in terms of K_2HPO_4 not leading to nucleation as all additional water is transferred to the ethanol phase. Therefore, adding ethanol to an aqueous solution where the solved salt is insoluble in ethanol

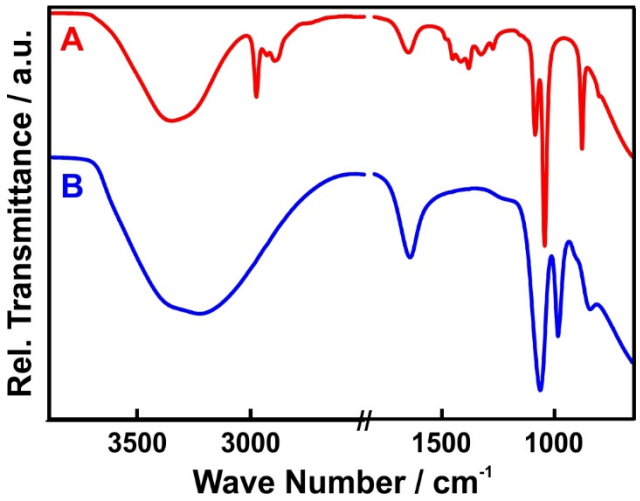

Figure 8.1. IR spectra of the ternary system K_2HPO_4, H_2O, EtOH. **(A)** In the upper phase only EtOH and H_2O are detectable, no HPO_4^{2-} vibrations. **(B)** In the down phase HPO_4^{2-} vibration are detected without any bands arising from ethanol.

may be a synthetic method to achieve a maximum concentrated solution without nucleation of particles.

The two phases were separated and an ethanol solution containing Zn^{2+} or Co^{2+} is added. In the following, experiments were performed basically with Zn solution as it can be analyzed by ^{31}P MAS NMR spectroscopy in contrast to Co solution due to the paramagnetic character of Co^{2+}. For illustration of the respective reactions, the experiments were performed again with Co instead. Co^{2+} is a transition metal ion and its coloring provides essential information about its coordination surrounding and hydration state. $CoCl_2$ reveals a red color if solved in water ($[Co(H_2O)_6]^{2+}$) and a blue color in ethanol as it exists as chlorido complex ($CoCl_4^{2-}$). Adding a solution of $CoCl_2$ in ethanol to the down phase results in a deep blue viscous liquid (Co-LCP) while again a second phase forms as ethanol is not soluble in the down phase. The degree of viscosity depends on the amount of added Co solution. The deep blue color should arise from Co^{2+} coordinated by phosphate because (i) no bands arising from ethanol are present in the corresponding IR spectrum of the down phase, (ii) coordination by water results in a red color, and (iii) amorphous cobalt phosphate species appear with deep blue color (see Chapter 4). The ongoing changes in coordination become clearer by adding an aqueous solution of $CoCl_2$ (red colored) to the two-phase system without removing the upper phase (see Figure 8.2). After the addition, the upper phase was colored red initially as there was a water-ethanol mixture solving the Co^{2+} which was still coordinated by water. Shortly after, the down phase started to turn blue at the phase boundary what is a hint that Co^{2+} is diffusing to the down phase. Also particles formed at the phase boundary which dissolved shortly after in the down phase. The hydration shells of Co^{2+} may be peeled away and displaced by phosphate. The upper phase was colorless afterwards indicating that the absence of Co^{2+}. AAS

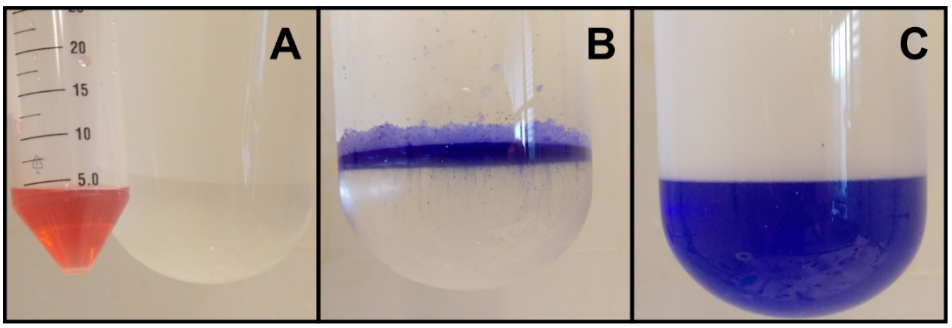

Figure 8.2. Synthesis of LCP: **(A)** Aqueous solution of $CoCl_2$ is added to the two-phase system water $+K_2HPO_4$/ethanol (Note the slightly visible phase boundary!) and results in **(B)** precipitation slightly above the phase boundary which is dissolving in the aqueous K_2HPO_4 solution leading to **(C)** cobalt phosphate hydrate-LCP.

Table 8.1. Amount of Zn and Co located in the down phase during different experiments as determined by AAS.

experiment	species	total amount / 10^{-3} mol	amount measured by AAS in the down phase / 10^{-3} mol
1	Zn	0.5	0.498
2	Zn	2.5	2.501
3	Zn	5.0	4.999
4	Zn	20.0	19.989
5	Co	2.5	2.500

experiments were performed with the down phases of several similar experiments varying the added amount of Co solution and Zn solution (resulting in Zn-LCP) as displayed in Table 8.1. More than 99% of the added amount of Zn/Co was located in the down phase in any case. Again, experiments with Co solutions help to visualize the ongoing reactions.

A driving force should be present for locating Zn/Co which is soluble in both phases in the down phase against the present diffusion. The free enthalpy of hydration has to be overcome due to the change in coordinating ligands. In addition, the precipitation of $Zn_3(PO_4)_2 \times 4\ H_2O$/$Co_3(PO_4)_2 \times 8\ H_2O$ (probably via an intermediate amorphous phase) has to be blocked although supersaturation is $S \approx 10^{37}$ with respect to $Co_3(PO_4)_2 \times 8\ H_2O$.

It is assumed that a hydrogen-bonded phosphate network with a fixed amount of coordinating water is responsible for this very uncommon behavior. This is supported by the following facts: (i) The respective LCP dissolved and solid particles (ACP or AZP) were formed by further addition of water. Additional water in between the network higher as the fixed amount may destroy the network resulting in nucleation of particles. (ii) By adding a solution of MCl (M=Zn, Co) in ethanol to an already formed LCP, the LCP phase shrank by expelling water which is mixed with the ethanol phase. The metal ion M^{2+} may be coordinated by HPO_4^{2-} which is then probably not available for the formation of the network. The decreased number of HPO_4^{2-} anions being part of the network may affect the water molecules in between which were expelled and transferred to the ethanol phase.

8.3.2 Structural Analysis

^{31}P NMR spectroscopy was applied under static and MAS conditions on the Zn-LCP samples as this type of spectroscopy is a powerful tool to provide information concerning the local environment of phosphorous in solution/solid state (Figure 8.3). Our aim was to gather information about a structure model which may explain the observed spectra of the synthesized LCP phases. A number of NMR experiments was conducted at different spinning frequency in order to determine the isotropic ^{31}P chemical shifts related with the samples as well as to gain further information about the anisotropy of these shifts (in the liquid condensed phase state). The latter we achieved by analyzing so called spinning sideband patterns which provides the parameters of the shielding tensor. Modulation of the magnetic field at the

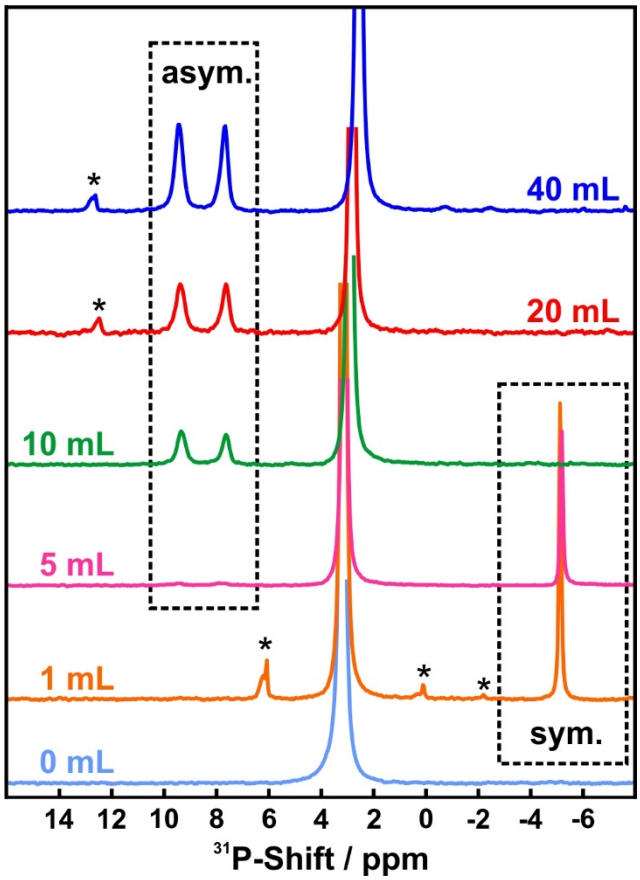

Figure 8.3. ^{31}P MAS NMR spectra of highly concentrated K_2HPO_4 solution (prepared by adding ethanol to solution with moderate concentration) (0 mL) and of liquid-condensed phases of zinc phosphate. Upfield shifting of the main HPO_4^{2-} signal is due to an increased shielding of free HPO_4^{2-} in the presence of complexes formed. For high amounts of zinc (5–40 mL) two signals at approximately 7.6 and 9.4 ppm are observed in the ^{31}P MAS NMR spectra indicating the formation of an asymmetric complex. For lower amounts of zinc (1–5 mL), one signal at approximately -5.1 ppm is present indicating a symmetric complex. (For 5 mL the two very weak ^{31}P signals are still detectable.) The asterisks mark spinning side bands.

spinning frequency results in these spurious kind of signals, which are also a sign of incomplete averaging of the anisotropic interaction.

The most intense signal in the ^{31}P NMR spectra was observed between 2.6 and 3.1 ppm and is associated to free HPO_4^{2-} in aqueous solution. For relatively small amounts of added Zn solution (1 and 5 mL), an additional sharp resonance at -5.1 ppm was detected in the static (not shown) as well as in the MAS ^{31}P NMR spectra. In literature, similar cases including molybdic and tungstic heteropolyanions are explained by the formation of a symmetric phosphate complex.[266] Increasing the amount of added Zn solution led to a gradual decrease in the signal at 5.1 ppm and thus to a reduction of the amount of the symmetric complex present in the LCP. Instead, a broad signal with a maximum at ca. 8.6 ppm and a full width at half maximum (FWHM) of ca 1200 Hz appeared in the static ^{31}P spectra, which under MAS conditions split into two signals with equal intensity. These signals resonated respectively at 7.6 and 9.4 ppm and are most probably an indication of the formation of an asymmetric complex with two inequivalent phosphorous atoms in its structure. Further addition of Zn solution (in ethanol) resulted in increased peak intensity. For 5 mL added, both the symmetric complex as well as the asymmetric complex (though barely detectable at this Zn concentration) were observed in solution. This indicates that a critical amount of Zn exists which leads to a transformation of the symmetric complex to the asymmetric one.

The ^{31}P NMR spectrum of the highly concentrated K_2HPO_4 exhibited a single sharp resonance signal related with the free HPO_4^{2-}. Increasing the amount of added Zn solution resulted in a slight upfield shift of this signal, which is most probably related with an increased number of complexes present in the LCP, which reinforced the shielding of HPO_4^{2-} and most probably interfere the present hydrogen-bonded network. The presence of a hydrogen-bonded network was suggested by comparing the ^{31}P NMR shifts of a highly concentrated HPO_4^{2-} solution with a diluted one. The signal of the highly concentrated solution was downfield shifted as the formation of hydrogen bonds results generally in a significant deshielding. This is due to the presence of the electric dipole field of the hydrogen bonds although an interaction with the free electron pair of the acceptor atom should have the opposite effect.[267]

Summarizing the results of the ^{31}P NMR experiments is that on increasing the amounts of Zn^{2+} solution added to the highly concentrated K_2HPO_4/water phase, different types of complexes (initially a symmetric and at higher Zn concentrations most probably an asymmetric one) were formed. Furthermore, a slight upfield shift of the signal of the free HPO_4^{2-} was

detected that allowed indirectly to monitor the hydrogen-bonded network present (Figure 8.3). The question what is the structure of the complexes in solution remains so far unanswered. We try to understand their organization by simulating the NMR spectra of different possible complex structures at room temperature including different hydrogen-bonded phosphate networks as well as number of water molecules which take part in the complex formation.

8.3.3 Further Analysis

The highly concentrated HPO_4^{2-} solution (before adding Zn^{2+}) revealed an increased viscosity (4.59 Pa·s) in comparison to pure water (≈1 Pa·s at 20 °C) which may be explained by the formation of a hydrogen-bonded network including HPO_4^{2-} accompanied with removal of water. The degree of viscosity depended on the added amount of Zn^{2+} (or Co^{2+}) sensitively. Viscosity measurements with a Couette viscometer showed an exponential dependence of the viscosity on the amount of added Zn^{2+} (see Figure 8.4). The increased viscosity may be explained by the expelling of water in between the HPO_4^{2-}network when additional complexes of Zn^{2+} and HPO_4^{2-} are formed. No significant effect was observed by variation of the number of revolutions.

Using a liquid cell TEM holder enabled us to investigate the LCP species *in situ*. The LCP is not homogeneous but particles were observed. Figure 8.5 (A) displays small particles 10 nm in size which are slightly dense with no reflections indicating crystallinity under electron diffraction. In addition, a second kind of particles was present (Figure 8.5 B). These particles are very dense aggregates showing characteristic reflections (Figure 8.5 C). Unfortunately, it was not possible to identify the present crystalline phase. A mixed potassium cobalt (hydrogen)

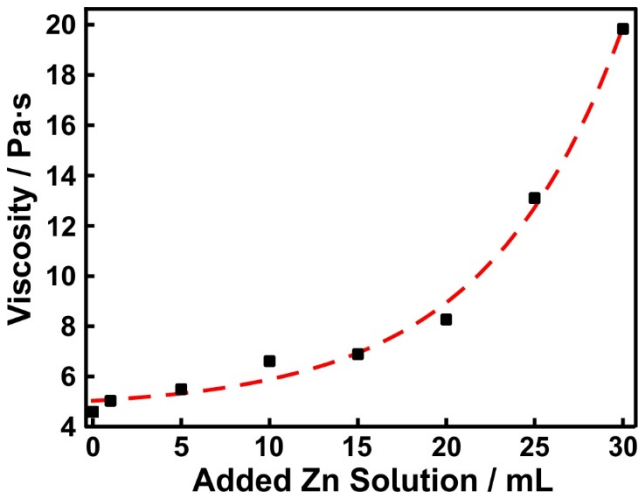

Figure 8.4. Viscosity of the liquid phase in dependence of the amount of added Zn solution (500 mM). In red exponential fit of the results.

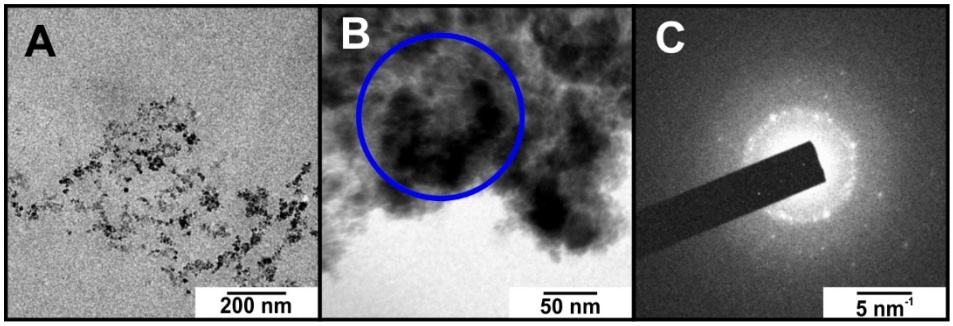

Figure 8.5. Results of liquid-TEM measurements: **(A)** Particles approximately 10 nm in size, which are not dense. **(B)** Very dense aggregates with **(C)** e-diffraction indicating the presence of a crystalline phase (blue circle in (B) shows the diffraction area.)

phosphate may be one explanation. However, irradiation with electron accompanied with an increase in temperature may lead to evaporation of water. A result may be disturbance in the hydrogen phosphate network and probably crystallization.

Further experiments with the aim to detect possible particles were not successful. Using a special light scattering setup with backscattering geometry did not display any clusters in solution, neither did SAXS measurements.

Interestingly, the highly concentrated HPO_4^{2-} solution does not only solve Zn^{2+} and Co^{2+} without precipitation of a solid species, but also allows dissolution of already formed crystals (Figure 8.6 B) despite present pH is determined to be 9. We used $Co_3(PO_4)_2 \times 8\ H_2O$ as the surrounding of Co^{2+} as well as its hydration state can be qualitatively monitored by the color of solution. Dissolution of $Co_3(PO_4)_2 \times 8\ H_2O$ in highly concentrated $KHPO_4$ solution led to the formation of a blue LCP whose color intensity depended on the amount of solved material. In contrast, dissolution of $Co_3(PO_4)_2 \times 8\ H_2O$ conventionally by applying a dilute acid (H_2SO_4, pH=3.5) results in the red colored $[Co(H_2O)_6]^{2+}$ complex (Figure 8.6 C). In

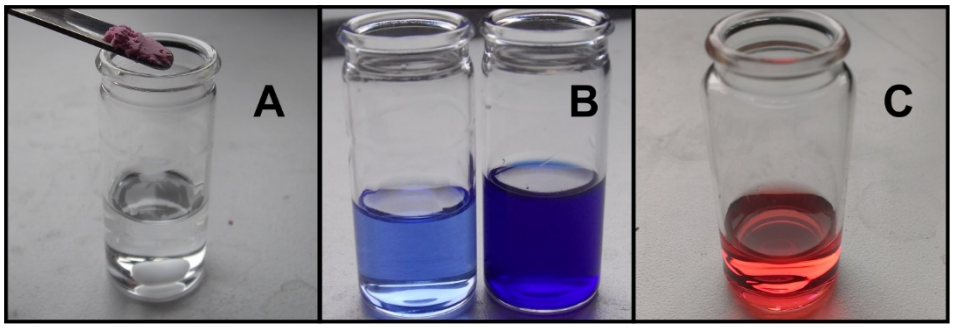

Figure 8.6. (A) Crystalline $Co_3(PO_4)_2 \times 8\ H_2O$ is added to the highly concentrated HPO_4^{2-} solution. **(B)** $Co_3(PO_4)_2 \times 8\ H_2O$ is dissolved in the HPO_4^{2-} network effecting the characteristic blue coloring (increase in the amount of crystalline substance results in a more intensive color). **(C)** In contrast, dissolving $Co_3(PO_4)_2 \times 8\ H_2O$ in diluted H_2SO_4 results in the characteristic red $[Co(H_2O)_6]^{2+}$ complex.

Figure 8.7. After annealing Co-LCP **(A)** for 2 d at 130 °C, a gel has formed covered by a "skin" **(B)**. Exposing (B) to humidity for 1 d results in **(C)** which appears liquid-like again.

addition, hopeite, fluorapatite, and $CePO_4$ were successfully solved in the highly concentrated medium. For the hopeite system, the situation may be more complicated because zinc phosphates may dissolve in basic solutions anyway by the formation of a $[Zn(OH)_4]^{2-}$ complex. However, solid ($Zn(OH)_2$) precipitates from aqueous solution at pH=9 so that possible formation of a hydroxo complex does not explain the appearance of an one-phase system at this pH in highly concentrated HPO_4^{2-}. At the current state of our research, the question remains what is the driving force for dissolving the crystalline material despite its enormous free enthalpy of formation. It is assumed that it is an entropic driven reaction by incorporation of M^{n+} (n=2 for M=Co, Zn, Ca; n=3 for M=Ce) in the HPO_4^{2-} network that beats the respective lattice energy.

Heating up Co-LCP for 2 d at 130 °C leads to the evaporation of water and the formation of a gel covered by a slightly solid "skin" (Figure 8.7 B). Under the "skin", the material appeared still liquid-like with increased viscosity. 1 d after the heating process, the hardened Co-LCP became liquid again due to humidity (Figure 8.7 C). As a large amount of K_2HPO_4, which is highly hygroscopic, is present in the Co-LCP, this may result in an affinity to water provided by humidity. Decomposition of Co-LCP into a denser and a less dense phase was also observed afterwards (see Figure 8.7 C).

8.4 Conclusion

This chapter demonstrates the formation of liquid-condensed phases (LCP) of cobalt and zinc phosphate in highly concentrated $KHPO_4$ solution in most probably within a viscous network. Application of sufficiently high concentrated K_2HPO_4 solutions allows (i) to synthesize Zn- and Co-LCP from solutions containing Zn^{2+}/Co^{2+} and (ii) to dissolve already precipitated phosphate hydrates despite their enormous lattice energy.

We assume that a dynamic network of HPO_4^{2-} with water molecules in between forms at sufficiently high concentrations HPO_4^{2-} leading to a viscous liquid. By incorporation of metal ions in the network, water may be expelled resulting in an increased viscosity. Heating up leads to the formation of a kind of gel as the water in between the LCP is evaporated. Exposed to humidity, the gel liquefies again due to the uptake of water.

Experiments with Co^{2+} as metal ion gave qualitatively insights into the respective coordination environment and the hydration state present due to its characteristic color. Co^{2+} should be coordinated by phosphate species in the liquid-condensed species due to its intensive blue color. The formation of an LCP induced by enormous concentration of HPO_4^{2-} was suggested by reference solubility experiments of $Co_3(PO_4)_2 \times 8\ H_2O$ at pH=3.5 and pH=9.

Results of SS-NMR measurements on Zn-LCP indicated the formation of HPO_4^{2-} complexes within a hydrogen-bonded network to be responsible for the stabilization of the respective LCP without nucleation of solid particles. For low amounts of present zinc ions a symmetric complex may be formed, whereas high amounts may result in the formation of asymmetric complexes.

Various experiments including SAXS, TEM, and light scattering suggested the absence of solid particles in the respective LCP.

The formation of LCP in the presence of high HPO_4^{2-} concentration accompanied with the dissolution of solid metal phosphates display an interesting phenomenon, which has been studied very little. However, to this point of time we have no sufficient explanation for the processes appearing in the highly concentrated and viscous solutions. Simulation of SS-NMR data will help to understand the species/complexes formed in solution and the present network. Analysis of PDF data might provide information about short range order in the liquid phases. Furthermore, X-ray absorption spectroscopy (EXAFS and XANES) may display the first coordination spheres of the respective metals in LCP.

9

PRENUCLEATION CLUSTERS OF COPPER PHOSPHATE HYDRATE

9.1 Introduction

Mixing solutions that contain a 3d metal (Fe^{2+}, Co^{2+}, Ni^{2+}, Cu^{2+}, Zn^{2+}) and PO_4^{3-} results in precipitation of crystalline hydrated metal phosphates while amorphous metal phosphates occur as intermediates (see Chapter 3–5). The appearance of amorphous intermediates is not directly in conflict with classical nucleation theory. Nonetheless, CNT is based on equilibrium thermodynamics, and amorphous precursors are normally precipitated at high supersaturations under non-equilibrium conditions. Thus, the application of CNT to amorphous intermediates may be limited.[28] The question remains whether the amorphous particles form according to CNT or whether prenucleation clusters (PNC) are involved. For example, the results of Posner *et al.*[8] suggest the formation of clusters (so-called Posner clusters) with a composition of $Ca_9(PO_4)_6$ as precursors in the formation of amorphous calcium phosphate which may be also valid for 3d metal phosphate hydrates. Hydroxylapatite and the intermediate amorphous calcium phosphate are predicted to form by close packing of the initial clusters, which clearly contradicts CNT. Nonetheless, the assignment of clusters is solely based on analysis of X-ray pair distribution functions and thus not fully satisfying.[8]

Inspired by experiments by Gebauer *et al.*,[7] who used a titration setup with an ion-selective electrode (ISE) in order to visualize the underlying nucleation processes, we performed analogous experiments for the copper phosphate system. The copper phosphate system was used as a prototype for the 3d metal phosphates due to the practical reason that ISEs are only commercially available for Cu. Gebauer *et al.* explained a pH dependent systematic deficiency in measured ion concentration through formation of prenucleation clusters. The PNC are predicted to be a thermodynamically stable species that exhibits highly dynamical character in undercritical and even in undersaturated solutions. As the interaction

between a sufficiently high number of ions/molecules in solution forming a critical nucleus is in fact a highly unlikely event, this model with dynamically ordered units (DOLLOP) may be more probable.

Unfortunately, it was not possible to monitor the undersaturated region during titration of $CuSO_4$ in a phosphate buffer due to limits of detection.

This chapter has the intention to clarify the following questions:

(i) Do PNC exist for 3d metal phosphates?
This question was addressed by titration experiments and analytical ultracentrifugation (AUC). Titration of Cu^{2+} in a phosphate buffer was monitored with a Cu ISE to determine if Cu^{2+} is bound due to cluster formation and to quantify the amount if applicable. Based on these results the following additional questions were addressed:

(ii) What is the structure and composition of copper phosphate PNC? Are they a solved species or exhibit a solid-liquid interface? Are different cluster compositions and sizes present in solution?
For this purpose, the amount of bound PO_4^{3-} was calculated by the amount of NaOH added at any point of time in a constant-pH setup. PO_4^{3-} acts as a base and the consumption of PO_4^{3-} can be correlated to a decrease in pH. As our precipitation experiments generated amorphous copper orthophosphate hydrates (see Chapter 5), we initially assume PO_4^{3-} as active species.

(iii) What is the first solid species formed in solution under these conditions?

9.2 Experimental

9.2.1 Titration Setup

The titration experiments were performed with a TITRANDO 905 (Metrohm No. 2.905.0020) using the Tiamo 2.4 software. Two dosing units DOSINO 807 (Metrohm No. 6.3032.120) with a 2 mL glass cylinder volume (minimal dosage volume 0.2 μL) were used to titrate the different solutions into a glass titration vessel (Metrohm No. 6.1415.250). A Cu sensitive electrode (Metrohm No. 6.0502.140) combined with a pH reference electrode (Metrohm No. 6.0258.010) was utilized. The pH electrode was calibrated with Metrohm buffers (pH=9.0 – No. 6.2307.120; pH=7.0 – No. 6.2307.110; pH=4.0 – No. 6.2307.100) once a week to correct for the drift in electrode slope and intercept. In order to minimize the possible deviations, we performed the measurements in the dark as changing light conditions influenced the Cu ISE. Furthermore, we sealed the titration vessel hermetically to reduce the amount of dust and to perform measurements under exclusion of CO_2, which could affect the pH value.

9.2.2 Solutions Used for Experiments

To adjust the pH to a permanent constant value, 1 mM NaOH was used. For this purpose, a 200 mM standard solution (Sigma-Aldrich) was diluted in a 1:200 ratio. A 1 mM $CuSO_4$ solution was prepared by diluting 0.1 M $CuSO_4$ standard solution (Sigma-Aldrich) in a 1:100 ratio, and a 1 mM phosphate buffer was prepared from a 0.1 M standard (Sigma) by diluting 1:100. KCl solution for the reference experiments was prepared from anhydrous KCl (≥99%, Sigma-Aldrich). All solutions were prepared with deionized water and used at room temperature.

9.2.3 Further Analysis

In order to visualize the first particles and clusters, we performed TEM measurements on the solutions of interest. Aliquots of the solutions were dropped on a TEM grid and dried for 1 da under vacuum.

Analytical ultracentrifugation was applied to detect ions, clusters, and solids in solution. Aliquots of 330 μL of the solutions of interest were taken for the measurements, and 350 μL of the 1 mM phosphate buffer were used as reference solution.

Solid particles which were isolated by centrifuging were analyzed by XRD and ATR-FTIR spectroscopy.

For further experimental details see Chapter 13.

9.3 Results and Discussion

9.3.1 Titration of Cu^{2+} in Water and a Phosphate Buffer

For titrations experiments, 1 mM $CuSO_4$ solution was added to 50 mL of 1 mM phosphate buffer at a rate of 0.01 μL/min at different fixed pH values (6.00; 6.25; 6.50; 6.75; 7.00). Depending on the desired pH value during the titration experiment, dilute NaOH or H_2SO_4 solutions were used to set the initial value. As $CuSO_4$ behaves acidic, 1 mM NaOH was used to keep the pH value constant during titration. Before the actual experiment, 0.2 mL of $CuSO_4$ solution were pipetted into the stirring vessel in order to have a certain starting concentration of copper, which is necessary for reliable measurements with the Cu ISE. The initial region (0.0–0.2 mL $CuSO_4$) was modelled by extrapolating the results of the linear region (*vide infra*). Experiments did not use a true calibration for the Cu. Each titration experiment was carried out multiple times in the absence of phosphate buffer and multiple times with the phosphate buffer adjusted for each pH value.

As the slope and intercept of the Cu electrode are sensitive to the ionic strength of the solution, which varies with pH value, a titration curve of Cu^{2+} in water was measured for each individual pH value. A KCl solution was used to simulate the ionic strength due to the phosphate buffer and the NaOH/H_2SO_4 used to adjust the starting pH value during the actual experiment. The maximum ionic strength was I=5 mM, and it is worth to mention that varying the ionic strength in this range did not have a significant effect on the measured voltages. As the dosage of Cu^{2+} was known, the "theoretical" concentration of Cu^{2+} was calculated at any point during titration under the assumption that all ions are detected by the ISE. The true concentration of free Cu^{2+} in solution was determined from the measured voltage of the Cu ISE according to the Nernst equation:

$$E = E^0 + \frac{\mathrm{R}T}{2\mathrm{F}} \ln a \qquad 9.1$$

Linear regression of the data collected at each individual pH value (individual ionic strength) was used to determine optimal parameters for intercept and slope of the theoretical curve that adequately describes the electrode. The resulting parameters are summarized in Table 9.1, and these individual calibrations of the Cu electrode were used to perform quantitative measurements in the phosphate buffer.

Titration of Cu^{2+} in 1 mM phosphate buffer at various pH values resulted in the curves displayed in Figure 9.1. All titration curves can be divided into three stages:

Table 9.1. Intercept and slope for the Cu sensitive electrode determined by titration of Cu^{2+} in deionized water.

pH	intercept / mV	slope / mV
6.00	344.5	33.6
6.25	335.5	31.5
6.50	328.2	30.6
6.75	313.5	28.7
7.00	291.5	25.0

Stage I: During stage I, a linear increase in measured concentration in solution was observed. The slope is significantly different from the theoretical one (based on the amount of $CuSO_4$ added, dotted line), which suggests the formation of clusters, a new species that does not precipitate (*e.g.*, is soluble) and is not detectable as single ions by the Cu ISE. With increasing pH, more PO_4^{3-} is present in solution, leading to a higher binding tendency of Cu^{2+} resulting in a smaller slope of the respective titration curve.

Stage II: The measured concentration is nearly constant (very small slope) despite the fact that additional Cu^{2+} is titrated, which is indicative for the formation of a second species of solute clusters or nucleation of a new phase. The local maxima in measured concentration accompanied by a slight decrease in concentration rather suggest a nucleation process.

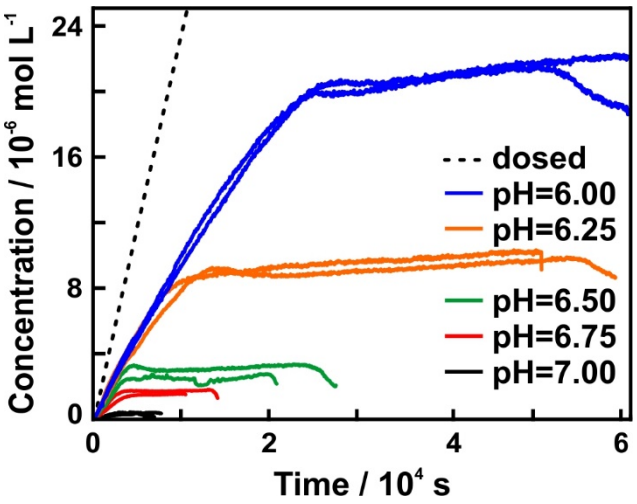

Figure 9.1. Titration of Cu^{2+} in 1 mM phosphate buffer. The dotted line represents the "theoretical" curve obtained by calculating the concentration based on the amount of Cu^{2+} added. Colored lines represent the measured concentrations at the respective pH values.

Stage III: The concentration decreases due to precipitation of solid copper phosphate, which represents the post-nucleation state. The concentration of Cu^{2+} in solution is determined by the solubility product ($K_{SP}=1.4\times10^{-37}$ mol^5/L^5) to be 1.67×10^{-8} mol/L. As the detections limit of the Cu ISE is 10^{-8} mol/L, the concentration of Cu^{2+} in solution is not sufficient to result in a quantifiable signal, but fluctuates strongly.

It is possible that the differences in actual and theoretical slope during titration experiments are due to experimental errors and not caused by cluster formation. However, the significant second region with nearly constant concentrations strongly contradicts classical nucleation theory. It is crucial to note that theses titration experiments were performed in supersaturated solution from the very early stages due to the very small solubility product of copper phosphate. As explained in Chapter 1, supersaturation is not sufficient to cause nucleation but a critical supersaturation has to present. Following this, we investigated the occurrence of PNC in the copper phosphate system in undercritical solution, as observation of the undersaturated region was not possible due to limits of detection.

In order to detect possible solid species during the titration experiments, aliquots of the solutions of interest were dropped onto a TEM grid and analyzed by electron microscopy. Figure 9.2 displays TEM images collected during the titration of Cu^{2+} in a phosphate buffer at the three different stages. During stage I, no solid particles were observed, which agrees with the formation of solute clusters at this stage. Stage II resulted in a less dense species that gave limited contrast to the carbon coated grid. No clear morphology seems to be present, the species appears to be a liquid-condensed phase (LCP) at the nm scale. Arrows in the corresponding TEM image indicate small spherical spots 5 nm in size with higher contrast, which may be a hint that the LCP formed by aggregation of small subunits that were PNC in

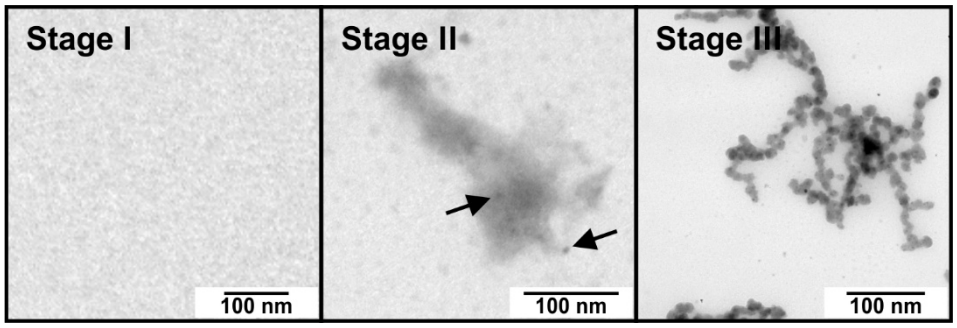

Figure 9.2. TEM images collected at different stages of the titration of Cu^{2+} in a phosphate buffer. **Stage I**: no particles are present; **stage II**: a liquid-like species occurs; arrows indicate particles of higher contrast (approximately 5 nm in size); **stage III**: precipitation stage – solid amorphous copper phosphate precipitates.

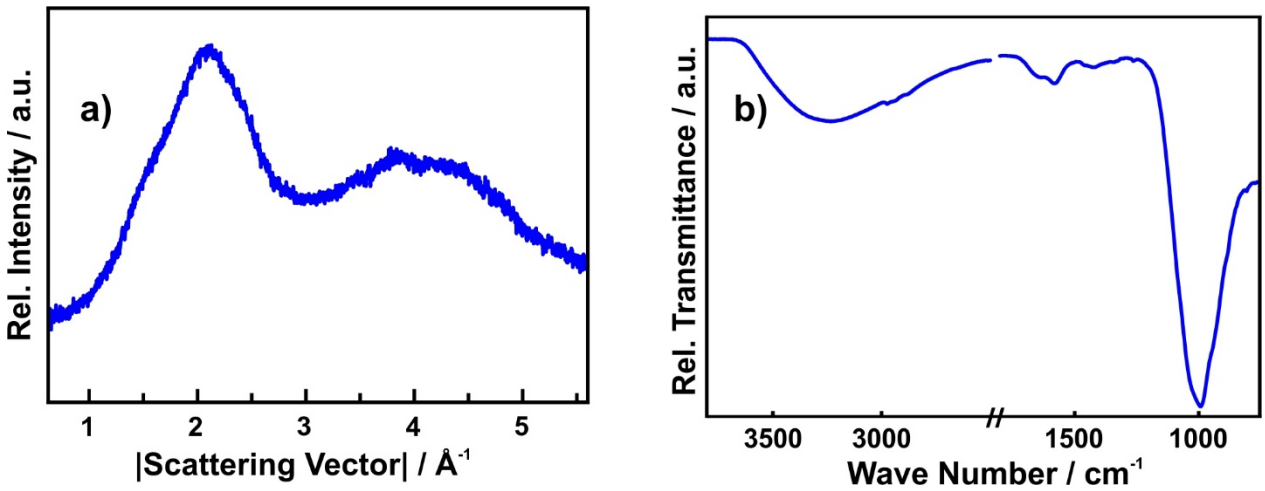

Figure 9.3. a) X-ray diffractogram and **b)** corresponding IR spectrum of species isolated from the third stage of the titration experiment.

earlier stages. Furthermore, centrifuging the solution at 9,000 rpm does not lead to any visible phase separation during stage I and II. We assume that PNC are present in stage I and thus the measured Cu^{2+} concentration is lower than it should be according to the amount added. In stage II, a LCP is generated, most likely by densification of PNC in stage II. This liquid-like species may grow by the addition of further Cu^{2+}, which leads to a nearly complete consumption of newly added Cu^{2+}.

During stage III, a solid species was precipitated. Centrifugation and isolation of the very small amount of solid particles allowed further analysis. XRD measurements showed broad modulated intensity features without defined reflections (see Figure 9.3 a). ATR-FTIR spectroscopy display a broad phosphate stretching mode without splitting due to factor group splitting and lower site symmetry (see Figure 9.3 b). Both diffraction and spectroscopic methods suggest that an amorphous copper phosphate is the first solid species formed during the titration experiment. TEM images collected during stage III (see Figure 9.2, stage III) display amorphous nanoparticles 15 nm in size. Some particles may crystallize partially in the TEM due to the irradiation with electrons accompanied with an increase in temperature. Different alignment of the crystalline regions determines how the Laue condition is satisfied resulting in different contrast. The appearance of particles with a stronger contrast indicates this formation of crystalline regions.

9.3.2 Cluster Composition

In order to determine the cluster composition, which is likely changing at the transition from stage I to stage II, it is necessary to calculate the quantity of phosphate ions bound due

to cluster formation. The fully deprotonated species PO_4^{3-} was chosen for calculations based on the nature of the final product of the titration experiment, amorphous copper phosphate hydrate as indicated by ATR-FTIR spectroscopy. However, for the following explanation it is irrelevant whether PO_4^{3-} or another phosphate species present in solution is removed as free species by the formation of clusters. Assuming an aqueous phosphate solution, the following equilibria have to be considered:

$$H_3PO_4 \rightleftharpoons H^+ + H_2PO_4^- \rightleftharpoons 2H^+ + HPO_4^{2-} \rightleftharpoons 3H^+ + PO_4^{3-} \qquad 9.2$$

with the corresponding pK_a values: $pK_{a,1}$=2.14, $pK_{a,2}$=7.207, and $pK_{a,3}$=12.346.

The fraction a_3 of PO_4^{3-} (degree of dissociation) in relation to all "phosphate species" (a_2 - HPO_4^{2-}, a_1 - $H_2PO_4^-$, a_0 - H_3PO_4) can be calculated according to Equations 9.3:

$$\alpha_0 = \frac{[H^+]^3}{[H^+]^3 + K_{a1}[H^+]^2 + K_{a1}K_{a2}[H^+] + K_{a1}K_{a2}K_{a3}}$$

$$\alpha_1 = \frac{K_{a1}[H^+]^2}{[H^+]^3 + K_{a1}[H^+]^2 + K_{a1}K_{a2}[H^+] + K_{a1}K_{a2}K_{a3}}$$

$$\alpha_2 = \frac{K_{a1}K_{a2}[H^+]}{[H^+]^3 + K_{a1}[H^+]^2 + K_{a1}K_{a2}[H^+] + K_{a1}K_{a2}K_{a3}} \qquad 9.3$$

$$\alpha_3 = \frac{K_{a1}K_{a2}K_{a3}}{[H^+]^3 + K_{a1}[H^+]^2 + K_{a1}K_{a2}[H^+] + K_{a1}K_{a2}K_{a3}}$$

$[H^+]$ is the concentration of protons in solution and K_{ai} (i=1, 2, 3) the constants of the respective equilibria. The relative quantities of the different protonated phosphate species are determined by the pH, resulting in a specific ratio of the four species at any given pH value (see Figure 9.4). While it is desirable to carry out experiments with the highest possible PO_4^{3-} concentration (at a given total concentration of all phosphate species), precipitation of $Cu(OH)_2$ at pH>7.00 would interfere with the titration experiments. As a compromise, the pH range between 6.00 and 7.00 was chosen for the titration experiments.

Formation of clusters composed of PO_4^{3-} and Cu^{2+} removes PO_4^{3-} from the equilibrium. Because the pH is kept constant during the titration experiments, the equilibrium is reestablished through the generation of PO_4^{3-} by deprotonation of HPO_4^{2-}. The loss of HPO_4^{2-} in turn affects the other phosphate species. Assuming that a single PO_4^{3-} is bound by clusters and equilibrium is reestablished, the amount of PO_4^{3-}, a_3, is effectively reduced by the fractional number ω_3 ($0<\omega_3<1$). Furthermore, the amount of HPO_4^{2-} a_2 is reduced by ω_2, the

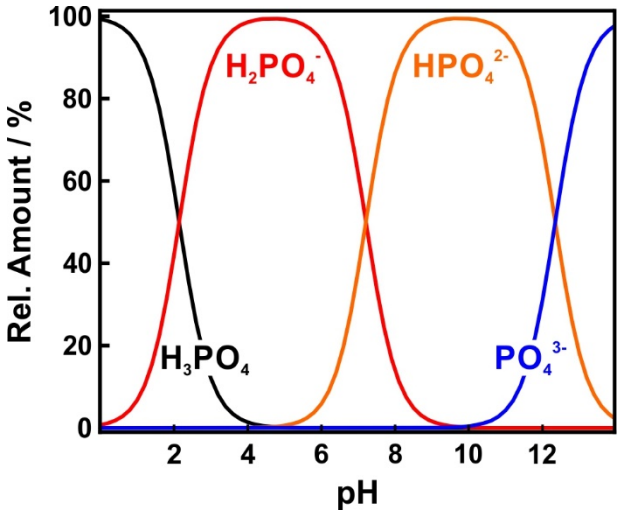

Figure 9.4. Distribution of the different phosphate species (phosphoric acid, dihydrogen phosphate, hydrogen phosphate, and phosphate) as a function of pH value according to Equations 9.3.

amount of $H_2PO_4^-$ a_1 is reduced by ω_1, and the amount of H_3PO_4 a_0 is reduced by ω_0. Assuming constant ratios of the individual species in solution, this leads to:

$$\frac{\alpha_3}{\alpha_2} = \frac{\alpha_3 - \omega_3}{\alpha_2 - \omega_2}$$
$$\frac{\alpha_2}{\alpha_1} = \frac{\alpha_2 - \omega_2}{\alpha_1 - \omega_1} \qquad 9.4$$
$$\frac{\alpha_1}{\alpha_0} = \frac{\alpha_1 - \omega_1}{\alpha_0 - \omega_0}$$

Rearrangement of Equations 9.4 combined with the fact that the sum of the losses of all species must correspond to the loss of 1 phosphate anion ($\omega_3+\omega_2+\omega_1+\omega_0=1$) gives:

$$\omega_3 = \frac{\alpha_3}{\alpha_3 + \alpha_2+\alpha_1+\alpha_0}$$
$$\omega_2 = \frac{\alpha_2}{\alpha_3 + \alpha_2+\alpha_1+\alpha_0} \qquad 9.5$$
$$\omega_1 = \frac{\alpha_1}{\alpha_3 + \alpha_2+\alpha_1+\alpha_0}$$
$$\omega_0 = \frac{\alpha_0}{\alpha_3 + \alpha_2+\alpha_1+\alpha_0}$$

As the ratios of all phosphate species together are equal to one ($a_3+ a_2+ a_1+ a_0=1$), Equations 9.5 are simplified to:

$$\omega_3 = \alpha_3$$

$$\omega_2 = \alpha_2 \qquad 9.6$$

$$\omega_1 = \alpha_1$$

$$\omega_0 = \alpha_0$$

According to this, the distribution of bound PO_4^{3-} among all present species underlies the same conditions than the equilibrium itself. According to the phosphate equilibrium (see Equation 9.2), the loss of one PO_4^{3-} requires the loss of three H^+ to keep the pH value constant and thus three OH^- have to be titrated. For the other phosphate species one proceeds analogously giving Equation 9.7:

$$\omega_{OH} = 3\omega_3 + 2\omega_2 + 1\omega_1 \qquad 9.7$$

where ω_{OH} is the number of OH^- that have to be titrated when one PO_4^{3-} is bound due to cluster formation.

The amount of bound PO_4^{3-} is then calculated by Equation 9.8 during constant pH-titration:

$$n_{bound}(PO_4^{3-}) = \frac{c(\mathrm{NaOH}) \cdot V(\mathrm{NaOH})}{\omega_{OH}} \qquad 9.8$$

Figure 9.5 displays a plot of ω_{OH} versus pH, which exhibits three pronounced steps. At high pH values, PO_4^{3-} is the main species present in solution, binding of which requires titration of 3 OH^-. At very low pH values, non-dissociated H_3PO_4 is the main species whose loss does not need to be compensated by addition of OH^-. Again, there is no difference

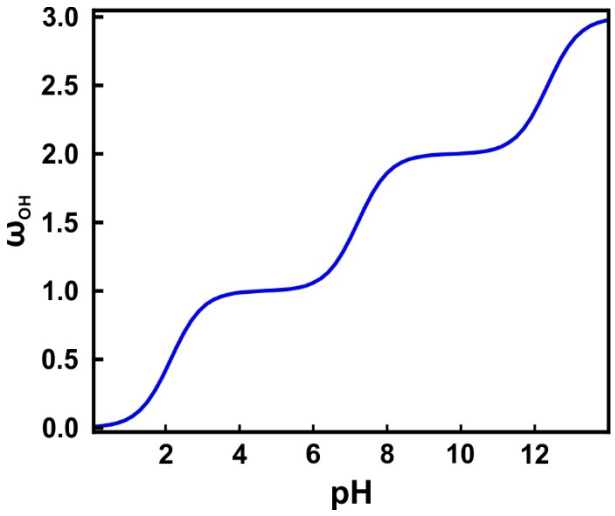

Figure 9.5. Number of OH^- equivalents ω_{OH} necessary to keep the pH constant when one PO_4^{3-} is removed from equilibrium due to cluster formation.

regarding the phosphate species bound by cluster formation. Removing PO_4^{3-} or H_3PO_4 results in the same change in pH value and thus in the same amount of NaOH necessary for titration.

In addition, the decrease in pH due to the titration of $CuSO_4$ has to be taken into consideration. $CuSO_4$ forms $[Cu(H_2O)_6]^{2+}$ in solution, which acts as a Brønsted acid with $pK_a(Cu^{2+})=7.49$.

$$[Cu(H_2O)_6]^{2+} \rightleftharpoons [Cu(H_2O)_5(OH)]^{+} + H^{+} \qquad 9.9$$

The degree of dissociation $a(Cu^{2+})$ can be calculated similarly to the phosphate equilibrium:

$$\alpha(Cu^{2+}) = \frac{K_a(Cu^{2+})}{[H^{+}] + K_a(Cu^{2+})} \qquad 9.10$$

Comparison of Equation 9.10 and Equilibrium 9.9 shows that for every Cu^{2+} one OH^- has to be titrated. Thus, the number of bound PO_4^{3-} due to cluster formation (see Equation 9.8) has to be corrected to:

$$n_{bound}(PO_4^{3-}) = \frac{c(NaOH) \cdot V(NaOH) - c(Cu^{2+}) \cdot V(Cu^{2+}) \cdot \alpha(Cu^{2+})}{\omega_{OH}} \qquad 9.11$$

The amounts of phosphate bound due to cluster formation during constant pH titration (calculated by Equation 9.11) and bound copper (difference between theoretical and measured amount of copper) as a function of time are displayed in Figure 9.6. Measurements were corrected by applying an offset due to initial electrode tune-in. It can be clearly seen that the amount of bound copper and phosphate is nearly equal during stage I of the titration, corresponding to a cluster composition of "PO_4^{3-}":Cu^{2+}=1:1. In order to maintain charge

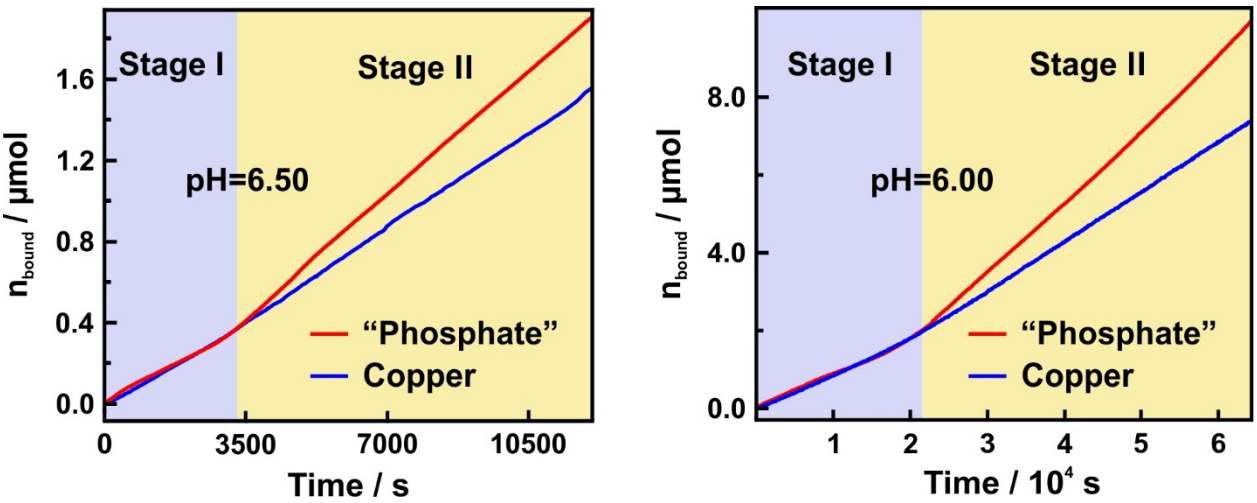

Figure 9.6. Amount of phosphate and copper bound due to cluster formation during constant pH titration at two selected pH values. Offset corrections were performed due to initial electrode tune-in.

neutrality, clusters should not be formed by PO_4^{3-}, but by HPO_4^{2-}, which is present in higher concentrations in this pH range.

At the transition point between stage I and stage II, a change in slope for the amount of NaOH added is observed, which corresponds to an increased number of "PO_4^{3-}" ions bound per unit time (see red curves in Figure 9.6). In contrast, the measured concentration of Cu^{2+} in solution reaches "a plateau" (see Figure 9.1), suggesting that all newly added copper is bound. The amount of bound Cu^{2+} continues to increase almost linearly with only a slight kink at the transition time. This indicates that the phosphate to copper ratio is no longer constant, but increases linearly during stage II. As a result, the liquid-like species should become more and more enriched with phosphate. This is typical behavior for growing clusters/aggregates in solution. In the beginning (stage I), small clusters form with a nearly 1:1 ratio of components that are coordinated by surrounding water. In later stages, the solution interface of the growing clusters is dominated by one of the respective species, in this case probably HPO_4^{2-}. Negative charges may be compensated by protonation. Furthermore, it is possible that attractive forces between clusters may lead to coalescence and growth, although uncompensated negative

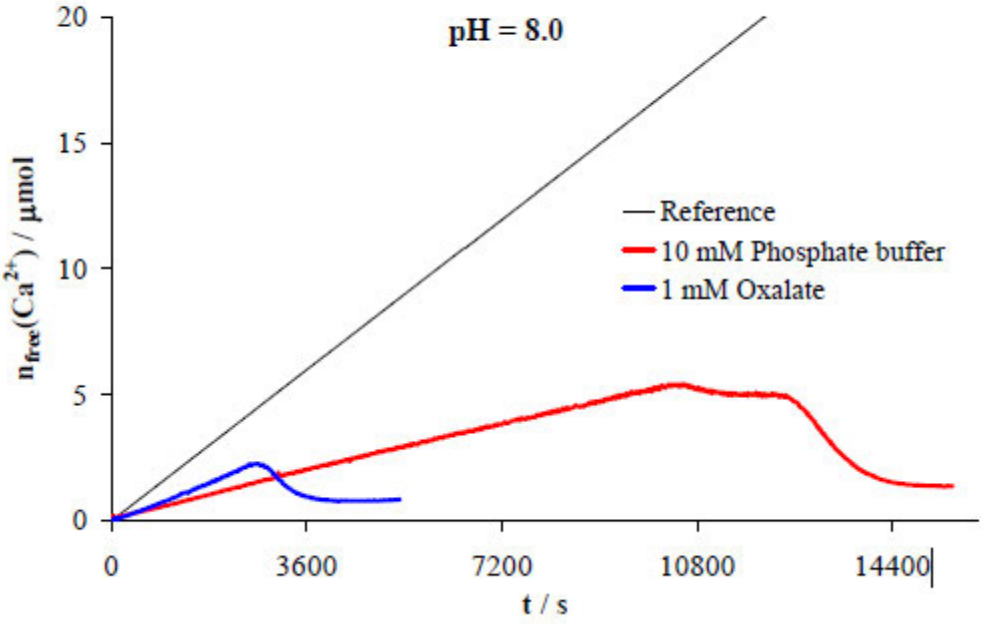

Figure 9.7. Amount of free calcium ions in 10 mM phosphate buffer (red) and 1 mM oxalate (blue) at pH=8.0, respectively. The reference line (black) gives the amount of calcium added. From [7] reprinted with permission from AAAS.

surface charges should result in repulsion. There are several literature reports about this uncommon coalescence at the nanoscale, which cannot be explained by theories based on field approximations like the D.L.V.O. theory.[268,269]

Additional qualitative experiments that were performed during the initial work of Gebauer *et al.*[7] suggested the existence of PNC of CaC_2O_4 and $Ca_3(PO_4)_2$. Similarly to our results, their phosphate titration curve exhibited a plateau with only a slight increase in concentration (see Figure 9.7). Both results indicate that this prenucleation behavior with the occurrence of a LCP may be a general phenomenon for the nucleation of metal phosphates $M_3(PO_4)_2$ for metals that form divalent cations with moderate charge density like Ca, Fe, Co, Ni, Cu, or Zn.

9.3.3 Analytical Ultracentrifugation

In order to corroborate the formation of clusters in solution during the titration experiment, analytical ultracentrifugation (AUC) was performed. AUC is a powerful tool to analyze macromolecular samples[270] and has been used to prove the existence of PNC within the $CaCO_3$ system.[7] Applying a centrifugal field leads to a sedimentation equilibrium distribution along the axis of rotation characterized by Boltzmann distributions. These distributions are monitored by a Rayleigh interferometer.[271] Unfortunately, the concentrations of clusters in solution were insufficient to obtain a quantifiable signal, as cluster concentrations of 1 mg/mL should be present for reliable measurements. Even for the phosphate buffer itself, no quantifiable signal could be detected. This is likely due to the fact that $Cu_3(PO_4)_2$ has a very low solubility product of $K_{SP}=1.4\times10^{-37}$ mol^5/L^5, thus our experiments were limited to concentrations one order of magnitude lower than those in the initial experiments of Gebauer *et al.*[7]

9.4 Conclusion

In this chapter, the prenucleation stage and the early nucleation stages of the copper phosphate hydrate system were studied. Nucleation of copper phosphate hydrates in solution most probably proceeds via PNC followed by a LCP, as shown by a constant pH titration setup with a Cu ISE and by TEM. PNC clusters contain a 1:1 ratio of bound Cu^{2+} to phosphate in good agreement with small copper hydrogen phosphate clusters. An increase in the constant pH value during titration lead to higher concentrations of HPO_4^{2-} in solution and thus to enhanced binding of Cu^{2+} due to cluster formation. By the formation of a LCP, which in fact displays a nucleation event, the copper hydrogen phosphate species may become more and more enriched in hydrogen phosphate. The LCP was shown to nucleate amorphous nanoparticles 15 nm in size.

This work demonstrates that copper phosphate is a well-suited model system to study nucleation processes via PNC. The occurrence of PNC in undercritical solution is not restricted to calcium systems, and could constitute a general phenomenon that appears to other slightly soluble compounds with a cation comparable to Ca^{2+} with respect to polarizability. The exploration of additional systems that display a PNC controlled nucleation event may enable determination of the limitations of CNT.

Part II

10

AMORPHIZATION OF $Co_3(PO_4)_2 \times 8\ H_2O$ UNDER MECHANICAL STRESS

10.1 Introduction

Structural phase transitions in solids are of fundamental importance as they reflect the lattice thermodynamics and kinetics of atomic motion, which in turn provide insights into structure-property relations and chemical reactivity. From a practical point of view, phase-specific properties are not only key for many technical applications of electronic,[272] magnetic,[273] or structural materials,[274] but also for catalysis[275] and energy storage materials.[276–278] Amorphous solids are conventionally made by supercooling of liquids, bypassing crystallization, but can be formed readily as well by rapid condensation from the vapor phase, solution precipitation, or via decomposition or polymerization reactions.[276] Furthermore, electrochemical insertion of ions into or the anodization of solids can lead to amorphization. Irradiating solids with electrons, neutrons or high-energy ions leads to radiation damage, *i.e.*, a largely increased number of vacancies and defects,[279,280] and eventually to the formation of amorphous materials. Hydrostatic pressure can cause amorphization under special circumstances:[281,282] Compounds with negative thermal expansion (NTE)[283–285] and metal-organic frameworks[286,287]undergo irreversible amorphization at high hydrostatic pressures due to their open network structure, and often amorphize at much lower pressures under non-hydrostatic conditions.[288,289] The application of non-hydrostatic pressure and mechanical stress to solids, either by mechanical grinding and milling or in the form of ultrasound, can lead to strain energy not uniformly distributed. Instead, strain is concentrated in holes, corners, and cracks, leading to large structural changes and eventually to amorphization.[289–291] In (planetary) ball mills, short-term temperature and pressure variations

occur when the grinding balls hit the charge or the walls, with maximum local temperature peaks up to 1500 °C and local pressures of up to several thousand bars.[292–294] However, these conditions are intermittent in time and space, *i.e.*, the synthesis does not occur under equilibrium conditions. Therefore, the structural evolution of materials by such processes like electrochemistry, radiation, or milling does not necessarily reflect the thermodynamic sequence of events and may lead to the formation of metastable products.[295] As a result, mechanochemistry may be a synthetic approach to compounds that can otherwise only be obtained from solid state reactions under extreme conditions (high pressure or temperature).[296–298] An example of unusual reactions under pressure is the observation that layered hydrated structures may be exfoliated due to the squeezing out of structural water induced by the enormous shear forces within ball mills.[299]

A large body of research has been carried out concerning the optimization of ball mill performance for industrial applications, mainly focusing on particle size and homogeneity of the material used.[300,301] Monitoring the processes occurring during ball milling is very challenging. Recently *in situ* studies of mechanochemically induced transformations using synchrotron X-ray diffraction[102–104] and Raman spectroscopy[104] were reported, where high reaction rates (equal or greater than in solution) and the catalytic influence of additives were observed.[299] However, we are still far from an overall understanding of the mechanical processes occurring during ball milling. A particularly challenging aspect to describe is the combination of static pressure and high shearing forces in a ball mill that maybe are accompanied by the formation of a plasma.[101] In the magma-plasma model it is assumed that highly energetic impacts between particles create short-lived (10^{-7} s) excited plasma-like states. This may result in chemical reactions, emission of light and electrons, local rise of temperature and pressure, and amorphization.[302]

The amorphization of crystalline hydrates represents an important group of solid-state transformations.[303] Their crystal structure may be destabilized by breaking of hydrogen bonds between crystal water molecules and other lattice constituents. Therefore, dehydration of hydrated polymorphs may lead to amorphization of the material.[304,305] Especially, dehydration and amorphization of zeolites are well-studied cases.[290,291,306] Various kinds of structural transformations may result from this destabilization including the formation of polymorphic metastable phases,[307] or a transformation to a stable crystalline phase of the anhydrous compound.[308] Alternatively, crystal to glass transformations may take place, which can lead to a single amorphous phase, or to polyamorphic states like those assumed to occur in ice[309] or triphenyl phosphite.[310,311]

In this chapter, we show that cobalt phosphate octahydrate ($Co_3(PO_4)_2 \times 8\ H_2O$) undergoes amorphization upon ball milling, monitored *ex situ* by powder XRD with high-intensity synchrotron radiation, ATR-FTIR, and UV-Vis spectroscopy. SEM and TEM allowed tracking of the particle size during the amorphization process, while a combination of TGA and DTA gave insights into the thermal stability of the corresponding phases. It turned out that dehydration of the crystalline phosphate is a key step to achieve amorphization. The composition and morphology of the final amorphous cobalt phosphate hydrate (mech-ACP) was determined with the aid of EDX spectroscopy, ICP-MS and ICP-OES, TGA, and DTA. The final amorphous compound has a different coordination of Co^{2+} based in EXAFS, XANES, and UV-Vis spectroscopy measurements. In order to gain knowledge about the complex processes that occur during ball milling, we performed a comparative hydrostatic compression experiment. *In situ* X-ray diffraction under high-pressure in a diamond anvil cell revealed that static pressure itself does not induce dehydration and amorphization. Lattice parameters and strain present in the sample were determined. Amorphous solids with various amounts of coordinating water are retained during annealing of mech-ACP at elevated temperatures. Recrystallization of mech-ACP can be induced by dissolution and recrystallization, which was monitored with the aid of ATR-FTIR spectroscopy.

10.2 Experimental

10.2.1 Amorphization

800 mg of cobalt phosphate octahydrate (Sigma Aldrich) were treated with a planetary ball mill (PULVERISETTE 7 classic, Fritsch) for different time intervals ranging from 0 to 260 min. The milling was interrupted for 10 min after 20 min of treatment to avoid heating of the grinding jars, milling balls, and the charge. 15 mg of grinding balls (1 mm diameter) were used. The grinding balls and jars consisted of ZrO_2. The number of revolutions was 600 min^{-1}. Ethanol was used as a medium for dissipating heat, pressure, and friction.

10.2.2 Amorphization Kinetics

Cobalt phosphate hydrates with varying degrees of hydration and crystallinity were obtained after different milling times. The compounds were qualitatively investigated by a combination of UV-Vis spectroscopy and TGA/DTA. Quantitative analyses were performed by ATR-FTIR spectroscopy and high-energy synchrotron XRD.

For IR spectroscopy, the splitting of the asymmetric phosphate stretching mode was used as a measure for the degree of ordering ("IR-crystallinity") (see Chapter 4). Mixtures of known ratios of completely amorphous product mech-ACP and the starting material $Co_3(PO_4)_2 \times 8\ H_2O$ served as standards for quantitative IR spectroscopy.

Diffraction patterns were recorded at beamline 11-BM (ANL) using 30 keV radiation. Sample compositions were determined using the PONKCS approach.[312] In this method, the diffraction halo of pure mech-ACP was modeled with Pawley fits using a tetragonal cell (*P4*, a=0.1 Å, b=0.1 Å, c=20.740821 Å). In addition, background due to the Kapton tube was modelled. The cell mass was calibrated to a known mixture of amorphous cobalt phosphate and $Co_3(PO_4)_2 \times 8\ H_2O$.

Reflection profiles were handled by the Whole Powder Pattern Modelling (WPPM)[313] approach assuming a log-normal distribution of spherical crystallites. Profile asymmetry was taken care of by standard models of strain.[314] All refinements were performed with Topas Academic V5 (Coelho Software, Brisbane Australia). The relative contents of crystalline $Co_3(PO_4)_2 \times 8\ H_2O$ and the amorphous solid were freely refined for all individual diffraction patterns. The sample that was ball milled for 40 min showed a small number of additional reflections in the synchrotron diffraction pattern at 5.739°, 7.828°, 10.404°, 11.352°, 14.841° 2Θ. These reflections could not be attributed to a known phase, and may result from the

grinding media. The impurity peaks were not present in other ball milled samples. Thus, they were treated as individual reflections without phase information.

10.2.3 High-Pressure *in situ* Diffraction Studies

Cobalt phosphate octahydrate was investigated by *in situ* high pressure diffraction measurements at beamline 17-BM at the Advanced Photon Source at Argonne National Laboratory. The beamline uses an area detector for rapid 2-D data acquisition. The wavelength used was 0.72808 Å, and the detector distance was set at 400 mm based on calibration with LaB_6. Data were collected with a Perkin Elmer a-Si C-window CCD detector with 2048×2048 pixels of 100 micron. The sample was mixed with NaCl as an internal pressure standard, and packed inside a membrane diamond anvil cell (DAC) with a 500 micron culet face. A stainless steel gasket with an opening of 250 microns was used as a sample chamber, and isopropanol served as a pressure transmitting fluid (PTF), providing a hydrostatic environment up to 4.2 GPa. A methanol pump was used to apply pressures up to 8.1 GPa. The NaCl reflections were used to determine the pressure inside the DAC based on the Birch equation of state.[315] Lattice constants for the standard and sample phases were extracted by Rietveld refinement using the fundamental parameter approach.

10.2.4 Further Characterization

Cobalt phosphate samples with different degrees of crystallinity were analyzed by electron microscopy to evaluate the evolution of particle size and morphology, while ICP-MS, ICP-OES, and EDX were used to determine their compositions. EXAFS and XANES spectroscopy at a synchrotron gave insights into short-range order and bond lengths of the amorphous compound. For experimental details see Chapter 13.

10.2.5 Recrystallization Kinetics

The crystallization kinetics of ACP were determined by quantitative IR spectroscopy. For this process, mech-ACP was stored in a climate-controlled chamber (70% humidity, 50 °C) for different time intervals. In order to prevent further crystallization during drying processes, all samples were measured in the wet state.

10.3 Results and Discussion

10.3.1 Amorphization Process in Ball Mill

The transformation from crystalline $Co_3(PO_4)_2 \times 8\ H_2O$ to mech-ACP was monitored by XRD (Figure 10.1). Diffractogram C in Figure 10.1 shows sharp intensities in the diffraction patterns of $Co_3(PO_4)_2 \times 8\ H_2O$.[186] The absence of reflections after 260 min of ball milling indicates the absence of any crystalline material (Figure 10.1 A).

The kinetics of the transition from the crystalline to the amorphous state were monitored by quantitative analysis of the intensity profiles using the PONKCS approach,[312] which revealed not only the degree of crystallinity, but also the strain within the samples. The high-intensity synchrotron radiation allowed detecting even very broad reflections arising from small and only partially crystalline samples. Figure 10.2 displays refinement results for three representative diffractograms.

Figure 10.3 shows IR spectra of $Co_3(PO_4)_2 \times 8\ H_2O$ after different durations of milling. IR spectroscopy probes a material at a molecular level and therefore provides insights into the short-range order. Initially, the asymmetric stretching mode of phosphate υ_{as} in the region 900–1100 cm^{-1} is split due to lower site symmetry and factor group splitting. This splitting vanishes gradually during the milling process. Again, physical mixtures with different ratios of completely amorphous and crystalline compound were used as standards, allowing us to follow the amorphization kinetics (see Chapter 4*)*. We know that the physical mixtures does not exactly represent uniform solids with a decreased degree of crystallinity, but they are an

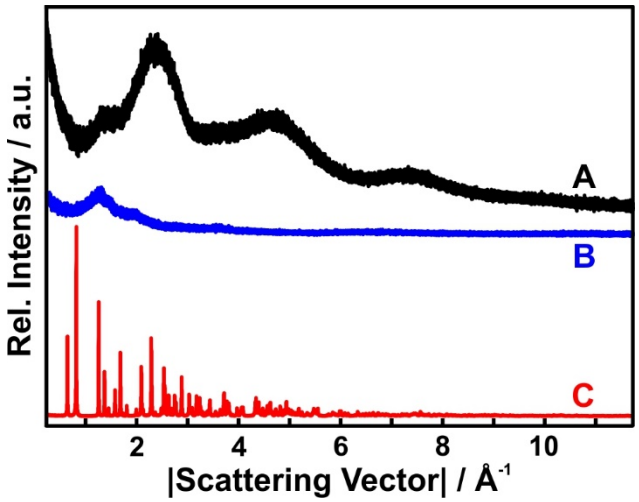

Figure 10.1. XRD patterns recorded with high-intensity synchrotron radiation of **(A)** mech-ACP synthesized by 260 min ball milling of **(C)** $Co_3(PO_4)_2 \times 8\ H_2O$, **(B)** empty Kapton capillary.

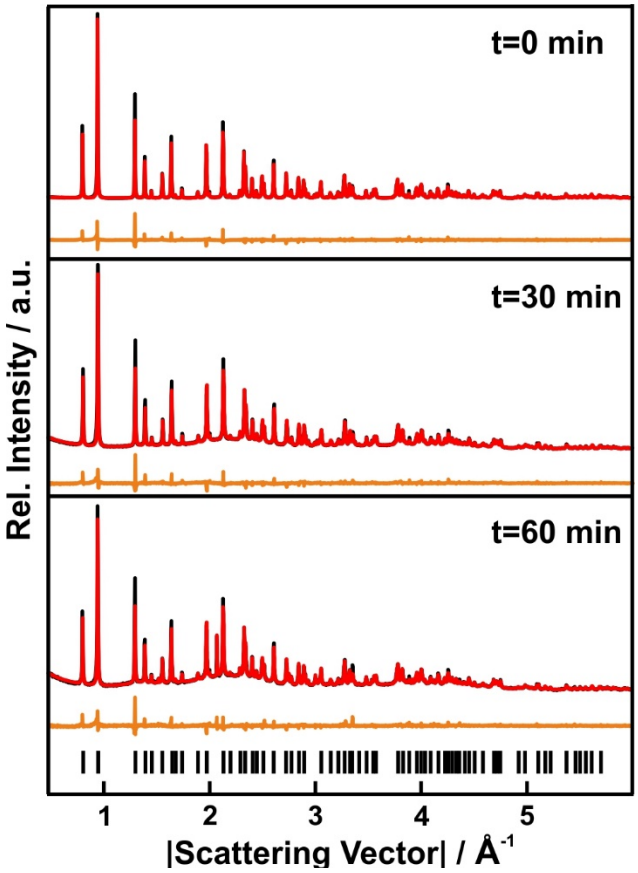

Figure 10.2. 11-BM XRD data of $Co_3(PO_4)_2 \times 8\ H_2O$ after different milling durations. Black: Measured intensities, red: simulated intensities using PONKCS,[312] orange: difference between observed and simulated intensities.

adequate reference. After 260 min of milling the sample was completely amorphous. Furthermore, the amount of structural water decreased during ball milling what was monitored by the decrease in water vibrations. The hydrogen-bond network is destroyed due to the enormous (shear) forces in the planetary ball mill leading to a release of water. One can assume that a plasma is formed during milling as reported in literature.[101,302] However, there was no possibility to observe plasma formation during milling *in situ*. Further, ACP synthesized from aqueous solution (Figure 10.3 D/Chapter 4) revealed a significant higher amount of structural water than mech-ACP.

Figure 10.4 shows the amorphization kinetics of $Co_3(PO_4)_2 \times 8\ H_2O$ as deduced from XRD and IR spectroscopy. It should be noted that IR spectroscopy and XRD do not describe the same kind of long-range order (therefore we use the expression "IR-crystallinity") as explained before. Both methods display an exponential decay for the crystalline material with similar decay constants, which demonstrates that the loss of crystallinity (XRD) and the local ordering monitored by ATR-FTIR spectroscopy ("IR-crystallinity") are strongly correlated.

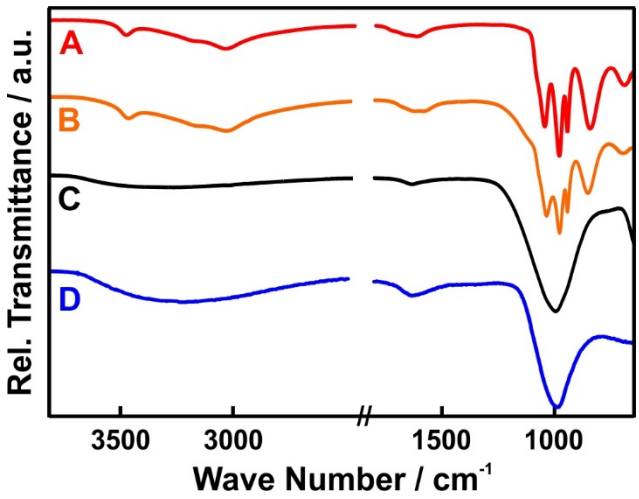

Figure 10.3. IR spectra normalized to the phosphate stretching mode. $Co_3(PO_4)_2 \times 8\ H_2O$ before milling **(A)**, after 60 min of milling **(B)** and after 260 min of milling (mech-ACP) **(C)**. For comparison, **(D)** displays the IR spectra of AZP synthesized in aqueous solution. The bands of $Co_3(PO_4)_2 \times 8\ H_2O$ are split because of lattice symmetry constraints.

The combination of diffraction and spectroscopy gives complementary methods for determination of amorphization kinetics.

Figure 10.5 a) displays the DTA curves recorded while heating the milled samples under argon flow (100 to 0% amount of crystalline phase as measured by IR spectroscopy). An exothermic signal in the range of 578 to 596 °C (minimum of curve) can be attributed to recrystallization of anhydrous crystalline $Co_3(PO_4)_2$. A corresponding signal cannot be observed for crystalline $Co_3(PO_4)_2 \times 8\ H_2O$ during heating. This signal was observed even after 20 min of milling. With increasing milling time the recrystallization signal was shifted to

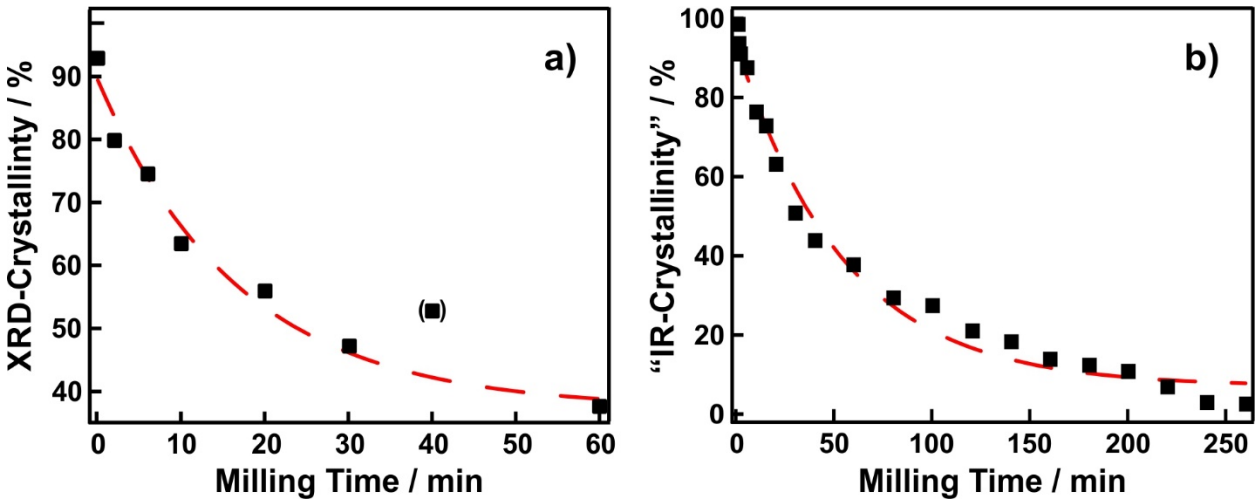

Figure 10.4. Amorphization kinetics of $Co_3(PO_4)_2 \times 8\ H_2O$ in a planetary ball mill monitored with **a)** XRD and **b)** ATR-FTIR spectroscopy. Both methods indicate an exponential decay for the crystalline phase. The point in brackets was determined to be an outlier and not used for fitting.

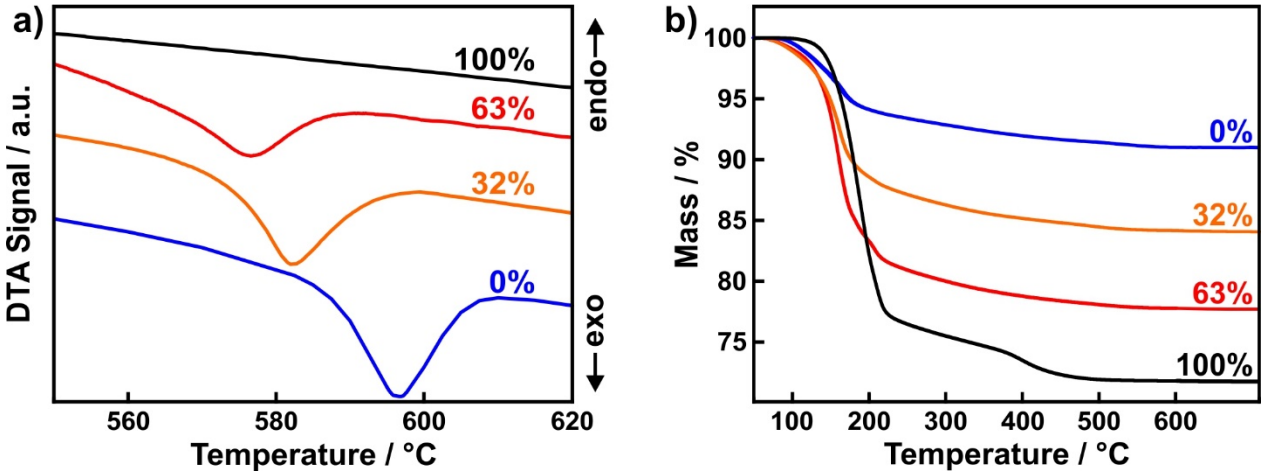

Figure 10.5. a) DTA curves of cobalt phosphate hydrates after different milling durations (displayed on the right side) with different degrees of "IR-crystallinity" (displayed on the left side). **b)** Corresponding TG curves.

higher temperatures. This demonstrates that the resulting solids after different periods of time in the ball mill represent not simply physical mixtures of crystalline and amorphous solids but rather uniform solids with a decreased degree of crystallinity. Furthermore, the signal became increasingly stronger, in good agreement with the progressive amorphization caused by ball milling.

In addition, simultaneously measured TG curves (Figure 10.5 b) show that with increasing milling time and the corresponding increasing amorphous content the mass loss of the samples is reduced, revealing that coordinating water is expelled continuously during the amorphization process. This is in good agreement with the results of ATR-FTIR spectroscopy. The loss of coordinating water during ball milling is assumed not to cause the stronger inhibition of thermally induced crystallization. As reported in Part I, the amount of coordinating water within amorphous phases does not significantly influence the thermally induced crystallization as the differences in free enthalpy of formation are very small for different amorphous phosphates only varying in their degree of hydration. In contrast, the products after different milling durations are only partially amorphous and thus crystallize and different temperatures.

UV-Vis spectra measured after different milling times (with their corresponding degrees of crystallinity determined by IR spectroscopy) are plotted in Figure 10.6. Starting from reflectance in the region of 430 to 600 nm (pink colored $Co_3(PO_4)_2 \times 8\ H_2O$), the final mech-ACP has a broader reflectance in the region of 430 to 710 nm (corresponding to blue color). UV-Vis spectra of partially crystalline samples appear as superposition of the spectra

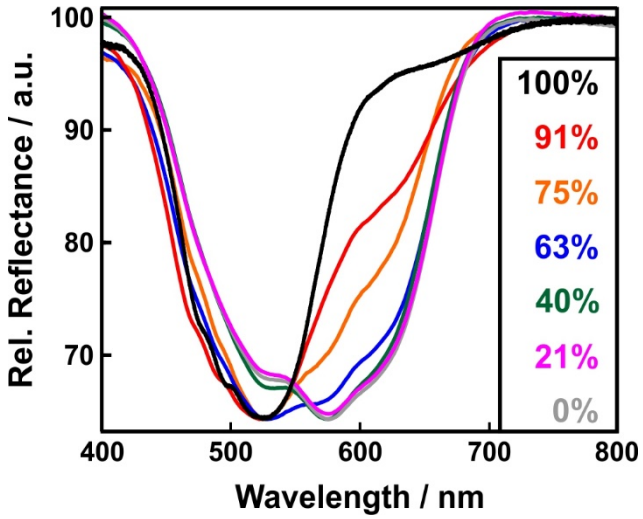

Figure 10.6. UV-Vis spectra of cobalt phosphate hydrates with different degrees of "IR-crystallinity".

of $Co_3(PO_4)_2 \times 8\ H_2O$ and mech-ACP. As already explained in Chapter 4, the absorption of visible light strongly depends on the coordination of Co^{2+} within the compound and its hydration state. Lower coordination numbers are realized within mech-ACP, which result in reflectance at lower energies or higher wavelengths. Furthermore, there is a broader region of reflectance due to a broad distribution of coordination numbers and hydration states within mech-ACP. Reflectances of mech-ACP are stronger than for $Co_3(PO_4)_2 \times 8\ H_2O$ because the LaPorte forbiddance is only valid for optical transmissions within octahedral surroundings.

10.3.2 Comparison to Static Pressure

In situ high-pressure synchrotron XRD patterns of $Co_3(PO_4)_2 \times 8\ H_2O$ were collected in order to distinguish between the shearing forces in the planetary ball mill and high isotropic pressure. Figure 10.7 shows typical X-ray profiles at different hydrostatic pressures obtained by integrating 2D data from an image plate. Due to the decrease in unit cell volume under pressure, the reflections shift to higher values of the scattering vector. Only the low q sections of the respective XRD patterns are plotted because the most intense reflections are in this region, and all reflections from the NaCl standard lie outside this q window. No abrupt changes in peak positions are observed, indicating that no crystalline high pressure polymorphs are formed. The profile broadening at very high pressures is caused by the non-hydrostatic behavior of isopropanol in this region. The sharpening of reflections in the diffraction patterns collected after decompression indicates (i) the retention of a crystalline state and (ii) the absence of any irreversible processes. No evidence of significant amorphization under static pressure was detected. In contrast, amorphization in a ball mill can be interrupted at any

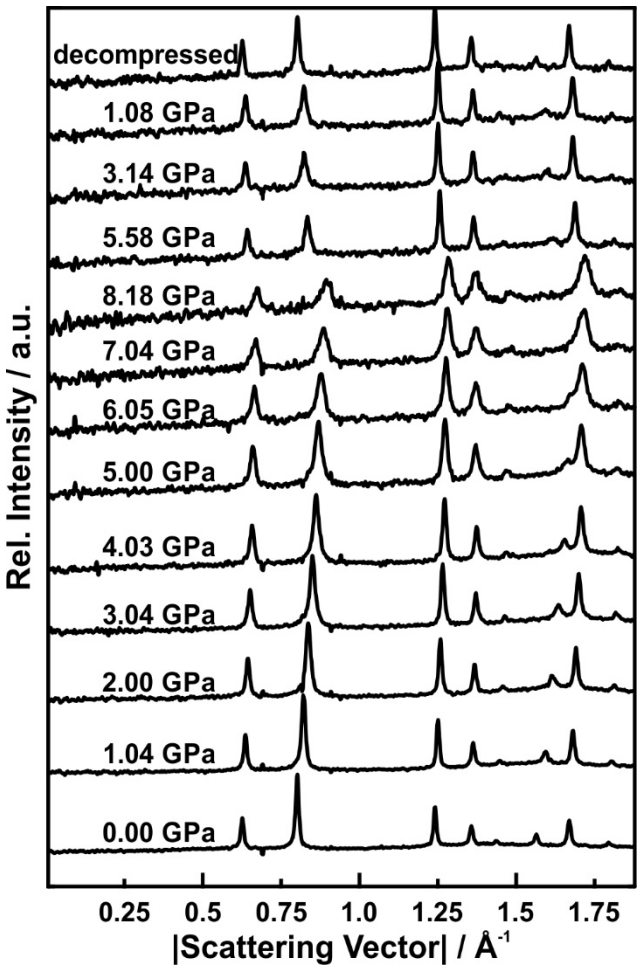

Figure 10.7. Evolution of the X-ray powder diffraction patterns of $Co_3(PO_4)_2 \times 8\ H_2O$ at pressures up to 8.18 GPa. Patterns are represented as a function of scattering vector *q*.

point in time, and the degree of amorphization present is permanent and irreversible. Anisotropic peak shapes also suggest that there is a higher strain remaining within the crystal lattice. Comparison of the results obtained by ball-milling and static pressure suggests that shear forces are the main cause of amorphization, as the local pressures in a planetary ball mill only reach peak values of several thousand bar (0.1 GPa).[292] The retention of crystalline material at much higher pressures shows that hydrostatic pressure by itself is not sufficient to cause amorphization. The shear forces cause removal of water molecules, which seems to drive the amorphization. In contrast, application of static pressure in a pressure transmitting fluid is unlikely to allow coordinated water molecules to be expelled (see Figure 10.8).

The refinement for the first dataset was carried out using soft distance constraints and a single atomic displacement parameter per phase. For subsequent sequential refinements, atomic positions were fixed to avoid potentially disastrous changes. The ambient pressure pattern was recorded in the diamond-anvil cell before the start of the experiment to determine

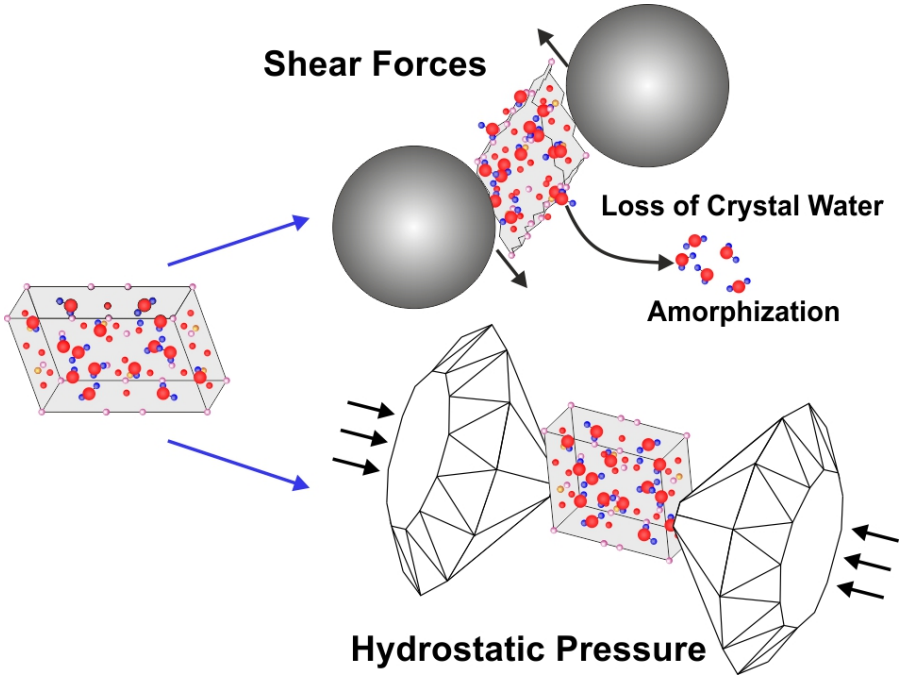

Figure 10.8. Illustration of performed experiments. High hydrostatic pressure does not induce irreversible changes in unit cells and thus amorphization. High shear forces in a ball mill results in deformation of unit cells followed by expelling of structural water which finally causes amorphization.

the reference volume. The ambient pressure parameters of $Co_3(PO_4)_2 \times 8\ H_2O$, a=10.040 Å, b=13.350 Å, c=4.679 Å, and β=104.818° are in good agreement with those given in the literature.[186] After decompression, $Co_3(PO_4)_2 \times 8\ H_2O$ was recovered with its initial structure and cell parameters. However, some residual pressure on the cell is retained even after decompression, which could be seen by slightly shifted NaCl reflections. The relative axial compressibilities a/a_0, b/b_0, and c/c_0 are plotted as a function of pressure in Figure 10.9 A. It was found that the b-axis is more compressible than the a- and c-axes. This is not surprising, as $Co_3(PO_4)_2 \times 8\ H_2O$ is layered along the b-direction.

Linear regressions in the pressure range up to 4 GPa yield mean axial compressibilities for *a, b,* and *c* of $4.97(4)\times10^{-3}$ GPa^{-1}, $1.16(16)\times10^{-2}$ GPa^{-1}, and $2.89(3)\times10^{-3}$ GPa^{-1}. As isopropanol becomes non-hydrostatic above 4.2 GPa, deviations from linear behavior occurred at higher pressures. As a result, the volume of the unit cell decreases linearly in the pressure range up to 4 GPa, but shows deviations at higher pressures (see Figure 10.9 b).

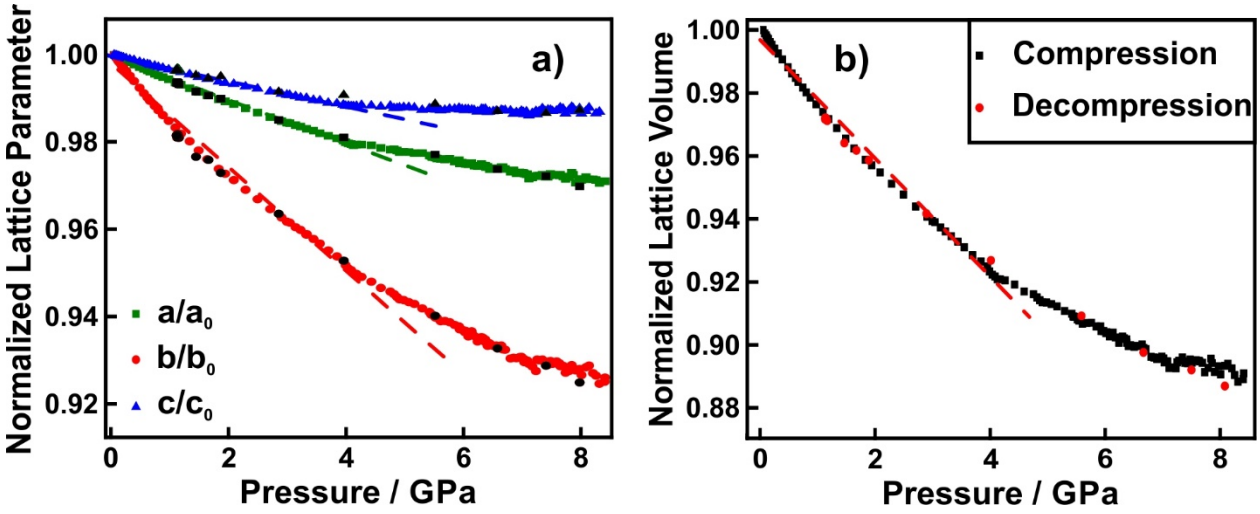

Figure 10.9. a) Relative change in unit cell axis length a/a_0, b/b_0, and c/c_0 as a function of pressure in $Co_3(PO_4)_2 \times 8\ H_2O$ up to 8.18 GPa. Dashed lines represent linear fits in the pressure region up to 4.2 GPa. Black triangles, squares, and circles represent lattice parameters during relaxation. Pressures are measured with a maximum relative error of ±1%. **b)** Corresponding unit cell volumes.

10.3.3 Further Characterization

The mechanochemically synthesized mech-ACP obtained by treating $Co_3(PO_4)_2 \times 8\ H_2O$ in the planetary ball mill for 260 min was characterized using a number of additional techniques. ICP-MS, ICP-OES, and EDX gave an average ratio of Co to P of 3:2.1

Table 10.1. Results of ICP-MS, ICP-OES, and EDX of mech-ACP after 260 min of milling of $Co_3(PO_4)_2 \times 8\ H_2O$.[a]

ICP-MS	^{59}Co	^{31}P
mean conc. / µg L^{-1}	116.5±3.0	43.1±1.0
mean conc. / µmol L^{-1}	1.97±0.05	1.39±0.03
ratio	3.00:2.11	
ICP-OES	Zn	P
mean conc. / µg L^{-1}	113	40
mean conc. / µmol L^{-1}	1.92	1.29
ratio	3.0:2.0	
EDX	CoK	PK
at%	23.6±2.3	17.3±1.7
ratio	3.0:2.2	

[a]Mean concentrations (µg L^{-1}) and standard deviations for Co and P in mech-ACP; estimated standard deviations of all the samples (ESD) are included.

(Table 10.1). The errors for EDX analysis are large due to the presence of rough surfaces and charging of the samples. Based on all results, we assume an average composition of $Co_3(PO_4)_2 \times x\ H_2O$.

IR spectroscopy and thermogravimetric analysis were used to determine the amount of water in the amorphous structure. Assuming that all surface water and ethanol were removed by drying in vacuo, the loss of weight during the heating process is only caused by structural water. This suggests a chemical composition of $Co_3(PO_4)_2 \times 2.0\ H_2O$ for mech-ACP (see Table 10.2). Quantitative analysis of the IR spectra was performed by comparing the extinctions of the water bands of crystalline and amorphous cobalt phosphate, which are (according to Lambert-Beer's law) proportional to the concentration of water in the compound. Interestingly, mech-ACP reveals a significant lower content of coordinating than ACP isolated as intermediate in solution. As the release of water is a hint for the degree of disorder in the respective solids, we conclude that the enormous shearing forces effect the formation of a highly disordered solid with probably less short-range order than in ACP.

The presence of a high pressure, in combination with large shear strains, is essential for producing high densities of lattice defects, in particular dislocations, which lead to a significant reduction in grain size and concomitant increase in surface area. However, TEM and STEM

Table 10.2. Water content (in formula units) of mech-ACP and HT-mech-ACP determined by IR spectroscopy[a] and TGA.

IR spectroscopy		
substance	E(δ(H–O–H))	water content
$Co_3(PO_4)_2 \times 8\ H_2O$	0.096	8.0
mech-ACP	0.024	2.0
HT-mech-ACP	0.002	0.1
TGA		
substance	mass loss / %	water content
$Co_3(PO_4)_2 \times 8\ H_2O$	28.3	8.0
mech-ACP	8.8	2.0
HT-mech-ACP	0.9	0.2

[a]For IR spectroscopy the extinction of $Co_3(PO_4)_2 \times 8\ H_2O$ was assumed to correspond to a water content of 8 formula units.

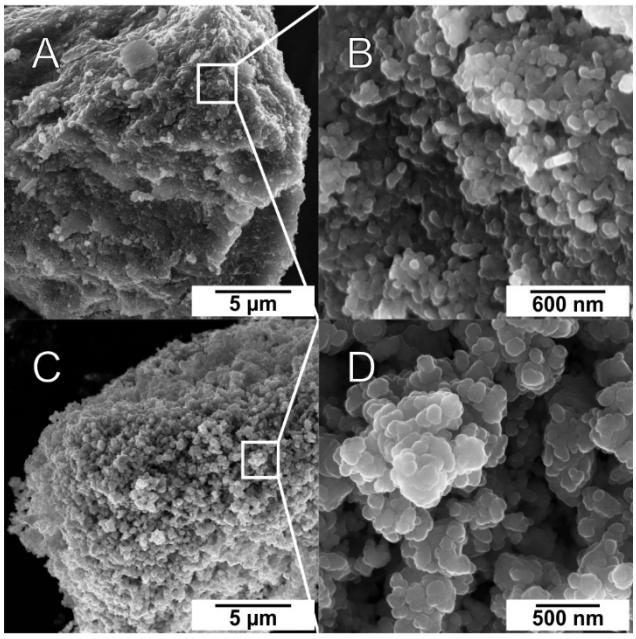

Figure 10.10. (A, B) SEM image of mech-ACP after 260 min of ball milling $Co_3(PO_4)_2 \times 8\ H_2O$. **(C, D)** SEM image of HT-mech-ACP after annealing mech-ACP at 450 °C for 5 d.

revealed that the ball-milled samples were very heterogeneous after all milling durations. Images taken after 30 min of milling (corresponding to 50% crystalline sample determined by IR spectroscopy) showed agglomerates of crystalline particles in the size range of 100 nm to 1 µm as well as agglomerates of amorphous particles approximately 10 to 70 nm in size (see Figure 10.11). Agglomerates may form because of the high-energy surfaces of particles produced under mechanical stress. The amorphous nanoparticles seemed to adopt a "molten" state reminiscent of amorphous particles synthesized by precipitation (Figure 10.11 B). It was not possible to visualize defects or lattice strain because the partially crystalline particles amorphized under high-resolution conditions due to radiation damage by the electron beam. Mech-ACP after 260 min of milling contained a large amount of the small "molten" particles, but still revealed several bigger ones. Electron diffraction carried out on a large agglomerate of particles showed some weak reflections besides the amorphous halo. We assume that due to the inherent error in determining the amorphous fraction by IR spectroscopy of ±2%, there could still be a very small fraction of partially crystalline particles within mech-ACP. This fraction is too small to be detectible by XRD, but is visible by electron diffraction for large scattering volumes. SEM images mainly show nearly spherical particles 50 to 100 nm in size (see Figure 10.10 A, B). The small number of bigger plate-like particles consists of smaller, tightly agglomerated nanoparticles. A possible model for the amorphization of $Co_3(PO_4)_2 \times 8\ H_2O$ might be the following multi-step process: (i) Dislocations, which are

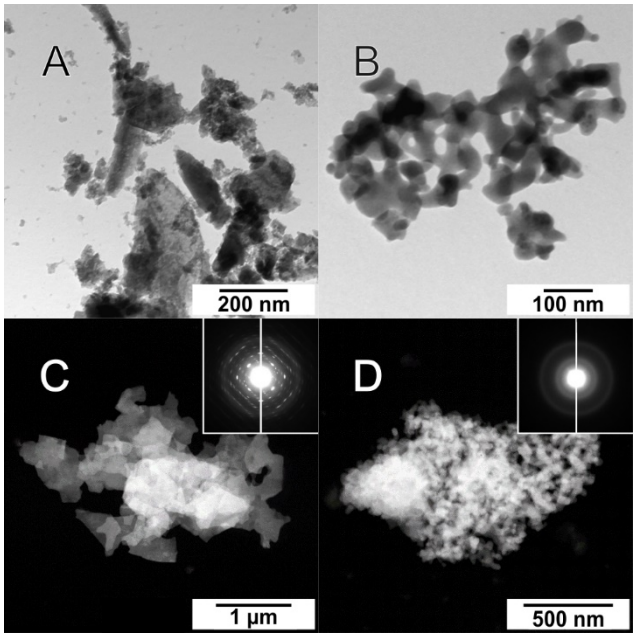

Figure 10.11. (A, B) TEM images **(C, D)** STEM images of cobalt phosphate hydrate after 30 min of milling corresponding to 50% amorphous fraction. Images B and D additionally are most likely representative for mech-ACP. Electron diffraction patterns shown in the insets C and D demonstrate their crystalline or amorphous character.

initially distributed throughout the grains, rearrange and group together into dislocation clusters to reduce the strain energy. (ii) As deformation continues and more dislocations are generated, misorientations develop between the clusters, forming smaller sub-clusters. (iii) The process is repeated within the subgrains until the size becomes sufficiently small such that the subgrains can rotate. (iv) Additional deformation causes the subgrains to rotate into high-angle grain boundaries, typically with an equiaxed shape.[316] The generation of smaller sub-clusters induced by ball-milling may support the amorphization of hydrated material as the Laplace pressure increases for smaller radii of surface curvature. Thus, coordinated water is expelled more easily leading to loss of crystallinity.

In order to gain further insights into the coordination of Co^{2+} in mech-ACP and the bond length distribution, we performed EXAFS and XANES measurements at a synchrotron beamline (Figure 10.12). Using $Co_3(PO_4)_2 \times 8.0\ H_2O$ as standard, XANES verified that there were no differences in oxidation state between crystalline and amorphous compounds, as the edge positions at 7723 eV (mech-ACP) and 7727 eV ($Co_3(PO_4)_2 \times 8.0\ H_2O$) are nearly identically. Furthermore, XANES provided first insights into coordination of Co in mech-ACP by observing the "white line" and the pre-edge region. As explained in Chapter 4, quadrupole transitions between the 1s and 3d states are known to result in pre-edge features. In the absence of inversion symmetry around the transition metal center, 3d and 4p wave functions can mix

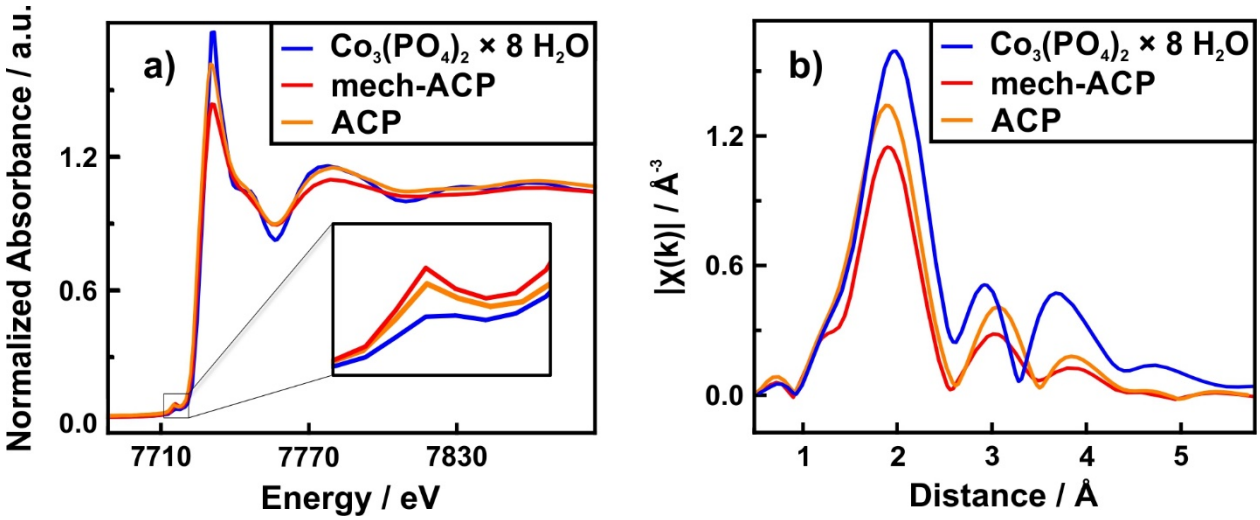

Figure 10.12. a) XANES spectra of $Co_3(PO_4)_2 \times 8\ H_2O$, ACP, and mech-ACP. Inset shows the pre-peak region. **b)** EXAFS profile-amplitude of the Fourier transform.

and result in pre-edge peaks. In contrast, a strong "white line" without pre-edge features is characteristic of a centrosymmetric structure (*e.g.* octahedral coordination). As the coordination polyhedra of the Co^{2+} species in $Co_3(PO_4)_2 \times 8.0\ H_2O$ are not perfect, a weak pre-edge peak is observable. The distinct pre-edge peak for mech-ACP suggests a less centrosymmetric environment for Co^{2+}. In addition, mech-ACP also has a more pronounced pre-edge peak and a weaker "white line" than ACP precipitated from aqueous solution (see Chapter 4).

EXAFS measurements were performed to further investigate the local environment of the Co atoms in mech-ACP. The amplitude of peaks present reflects the coordination number, and comparison of the Fourier transforms for both samples confirms that mech-ACP has a lower coordination number than $Co_3(PO_4)_2 \times 8.0\ H_2O$ (octahedral). In addition, peak positions give insights into the bond lengths within the structure. Single scattering of the nearest neighbor oxygens leads to the first peak at around 2.1 Å. While the first peak in the EXAFS FT-spectra appears at similar distances for both mech-ACP and $Co_3(PO_4)_2 \times 8.0\ H_2O$, the average distance for mech-ACP is slightly larger, which is in accordance with a lower coordination number. The differences observed for the second and third coordination shell are even more significant, confirming that mech-ACP and $Co_3(PO_4)_2 \times 8.0\ H_2O$ have different short-range order, and that mech-ACP shows decreased order beyond the first coordination shell. Furthermore, mech-ACP has lower coordination numbers for the first three coordination shells in comparison to ACP precipitated from solution. The results of EXAFS and XANES together with the lower content of coordinated water (2.0 formula units in comparison to 5.0

formula units water per formula unit $Co_3(PO_4)_2$) suggest that mech-ACP's short-range order is different from the one of ACP. Lower coordination numbers and a lower level of hydration is present.

10.3.4 High-Temperature Mech-ACP

Mech-ACP loses its structural water during heating under argon flow as seen during thermal analysis (see Figure 10.5). As a result, heating mech-ACP at 450 °C for 5 d leads to an amorphous cobalt phosphate with less structural water than mech-ACP. IR spectroscopy and TGA measurements suggested a composition of $Co_3(PO_4)_2 \times 0.15\ H_2O$ (see Figure 10.13 and Table 10.2). SEM confirmed that HT-mech-ACP still consisted of nanoparticles 50 to 100 nm in size (see Figure 10.10). Qualitatively, the particles were less agglomerated than mech-ACP.

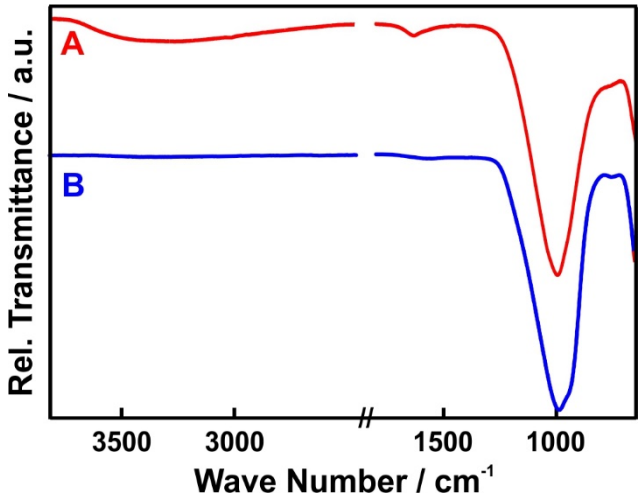

Figure 10.13. IR spectra of **(A)** mech-ACP and **(B)** HT-mech-ACP after annealing mech-ACP at 450 °C for 5 d.

10.3.5 Crystallization Kinetics

The crystallization kinetics of the ball-milled ACP were investigated by IR spectroscopy (Figure 10.14 a), which turned out to be the most suitable method for following the crystallization process starting from an amorphous compound and ending up with $Co_3(PO_4)_2 \times 8.0\ H_2O$. Mech-ACP samples were measured after different periods of time in a climate chamber with fixed temperature and humidity (40 °C and 70%). A double-logarithmic plot resulted in a linear trend, which indicates that the crystallization of mech-ACP follows an Avrami mechanism (Figure 10.14 b)[317] The Avrami exponent was determined to be 1.8, which is characteristic for a two-dimensional growth rate with heterogeneous nucleation of crystalline

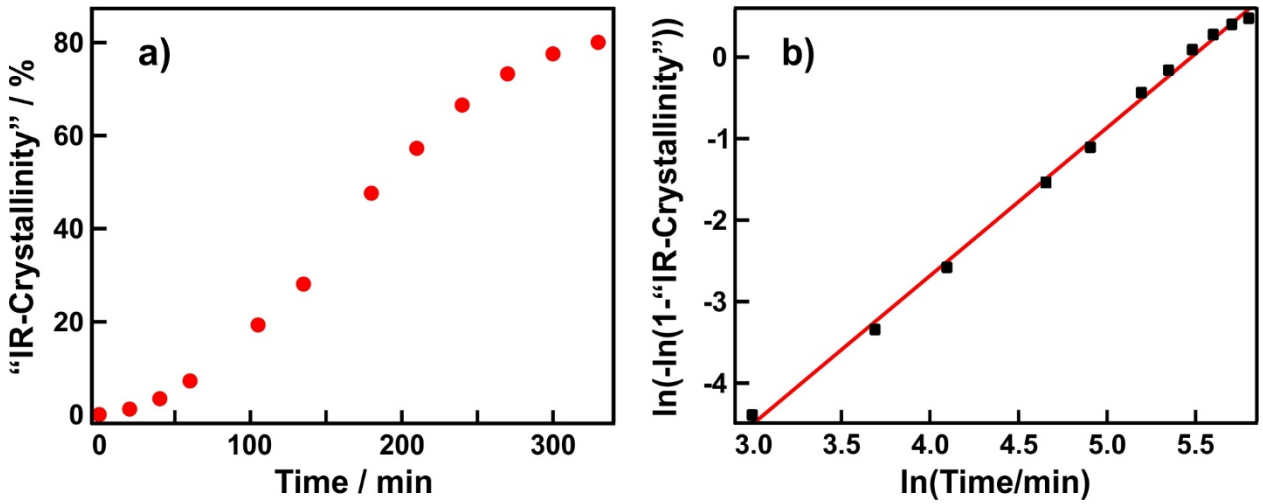

Figure 10.14. a) Crystallization kinetics of mech-ACP synthesized by ball milling. Crystallization was measured after different time periods in a climate chamber by IR spectroscopy. **b)** Double-logarithmic plot of crystallization kinetics showing the validity of an Avrami mechanism.

seeds on the amorphous surface of mech-ACP. As mech-ACP does not only exhibit a destroyed crystalline structure with a high defect density, but also a considerably different particle shape consisting of coalesced nanoparticles, there is no healing process of the amorphous structure in the narrower sense. In the beginning, the amorphous nanoparticles form a few crystalline regions. As these regions start to grow, the crystallization velocity increases until nearly all material is crystalline, at which point crystallization slows down, giving rise to the typical sigmoidal curve shape. Another reason for the induction period in the beginning may be the necessity to take up water, which has to take place before formation of the octahydrate. As Avrami kinetics give only phenomenological descriptions they should not be overrated.

10.4 Conclusion

We have successfully amorphized crystalline $Co_3(PO_4)_2 \times 8.0\ H_2O$ by high energy ball milling. The amorphization process was monitored by two complementary methods, XRD with high-intensity synchrotron radiation and quantitative ATR-FTIR spectroscopy. TGA and ATR-FTIR spectroscopy proved that coordinating water is expelled during the amorphization process. This suggests that coordinating water is essential for the degree of crystallinity in this hydrated system. The amount of remaining water in the amorphous solid was lower than for ACP isolated from aqueous solution. The morphology of mech-ACP appeared "molten"-like and was very similar to ACP synthesized in aqueous solution.

While the application of hydrostatic pressure in isopropanol does not lead to amorphization at pressures up to 8.2 GPa, the combination of local pressure with intense shearing forces (maybe accompanied with the formation of a magma-plasma) during ball milling causes this uncommon effect. EXAFS and XANES measurements revealed different cobalt coordination environments in mech-ACP and the starting crystalline phase. Furthermore, mech-ACP's short range order is different from ACP synthesized in aqueous solution. The recrystallization process of mech-ACP induced by water follows Avrami kinetics and was monitored *in situ* by ATR-FTIR spectroscopy.

High-resolved XRD pattern of $Co_3(PO_4)_2 \times 8.0\ H_2O$ before and after grinding in a mortar will help to verify whether shearing forces are sufficient to cause amorphization or whether amorphization is explained by the formation of a magma-plasma.

11

RECRYSTALLIZATION OF AMORPHOUS ZINC PHOSPHATE PREPARED BY BALL-MILLING

11.1 Introduction

Zinc phosphate $Zn_3(PO_4)_2$ is an important anti-corrosive pigment on metal surfaces, where it acts as anodic inhibitor by forming a dense phosphate surface film.[114,318,319] In addition, it is frequently used as cement in dentistry for luting permanent metal restorations.[320,321] The formation of the cement is due to non-crystalline zinc phosphate containing small particles of unreacted ZnO. Although no crystalline phosphate is involved in the setting of the cement, its surfaces are modified by small hopeite ($Zn_3(PO_4)_2 \times 4\ H_2O$) crystallites, and metastable (crystalline or amorphous) intermediates are assumed to be important during the kinetically controlled hardening.[322] Amorphous zinc phosphate may be thermodynamically stable at the nanoscale due to a crossover in thermodynamic stability arising from dominating surface effects,[145] but it is inherently labile and appears to serve (as other amorphous phases)[323,324] as a reservoir for the formation of crystalline polymorphs.

Zinc phosphate has also been reported to form protective films on rubbing surfaces.[325] As many other metal phosphates, it adopts a network structure where PO_4^{3-} tetrahedrons are interconnected through Zn^{2+} cations.[326–328] The stiffness of the tribofilm is determined by the coordination of the metal atoms.[329,330] By increasing the coordination number of the Zn^{2+} cations under pressure or shear (which may occur during asperity collision) the material may change from an initially open network structure with viscoelastic properties to a more densely packed and therefore stiffer structure.[331] Because of its coordinative flexibility Zn^{2+} can even switch back four-coordination during decompression after having adopted five and

six-coordinate structures at higher pressure. Therefore, an understanding of the phase transformations (and grain size refinement) of zinc phosphate under pressure or shear is important as it provides insights into its chemical reactivity and structure-property relations.

Phase transformations of metal phosphates (or oxides in general) can occur easily during ball-milling,[295,332] a process central to the processing of nanoparticles.[289,303] Milling generates disordering, amorphization, and polymorphic transformations, defects (*e.g.*, point defects and crystallographic shear (Wadsley defects)). Especially for hydrated or porous compounds, milling can lead to dehydration with a concomitant collapse of ordered linkages between the building blocks.[285,286,290 ,291,299,333] Amorphization by ball-milling is a multi-step process where random dislocations are formed in an initial step and strain energy is reduced by rearranging lattice dislocations to clusters. [332,334,335] By progressively reducing the cluster size nanopowders containing amorphous/disordered regions with nanocrystalline grains embedded in amorphous grain boundaries are formed. Therefore the structure of ball-milled nanopowders may by very different from that of nanopowders synthesized by wet chemical routes.[336] Polymorphs may appear transiently after short milling times,[337] and materials formed under milling conditions may be metastable at ambient temperature and pressure; they exist in thermodynamic equilibrium only at high temperature or/and pressure. In essence, polymorphic transformations depend on the dynamical conditions of grinding.[338] In addition, they may depend on the nature (steel, zirconia) of the grinding tools,[339] and metastable phases may be stabilized either by structural distortions induced through the milling process[340] or by incorporating impurities (*e.g.*, Fe^{2+}, Fe^{3+} and Cr^{3+} from steel) into the sample due to the wear and oxidation of the milling media.[341]

Despite the surge of studies by high-energy ball-milling,[299–301] little attention has been paid to the effect of impurities and contaminations introduced during the grinding process on the products, their properties and reactivity, in particular considering the importance of ball-milling for the large-scale production of nanoparticles. During the preparation of amorphous zinc phosphate, the recrystallization to hopeite turned out to be very different for materials prepared in stainless steel and zirconia containers, although the container had only a minor effect on the amorphization itself. We have pursued and analyzed this abrasion effect by intentionally adding ^{57}Fe impurities to simulate the abrasion effect and to understand the inhibiting effect of Fe on the stability of zinc phosphate and its crystallization at the nanoscale. Fe impurities (2 mol%) increase the stability of ball-milled amorphous zinc phosphate (mech-AZP) tremendously. Its thermal stability with respect to $Zn_3(PO_4)_2$ increases by up to 65 °C in the presence of Fe impurities (5 mol %) under Ar. Mech-AZP is metastable, as

"Fe-doped" γ-$Zn_{3-x}Fe_x(PO_4)_2$ was formed in the presence, but α-$Zn_3(PO_4)_2$ in the absence of iron, while annealing in air lead to the oxidation of Fe and to the formation of α-Fe_2O_3 impurities, as shown by Mössbauer spectroscopy and magnetic susceptibility measurements.

ATR-FTIR spectroscopy indicated that in the absence of Fe the kinetics of the re-crystallization of amorphous mech-AZP in water follows a classical Avrami behavior,[245–248] whereas the reaction of mech-AZP in the presence of Fe impurities proceeds *via* a different mechanism. ^{57}Fe Mössbauer spectroscopy with ^{57}Fe-enriched samples revealed the short-range order within the amorphous solids: During ball-milling Fe is oxidized to Fe^{2+} and Fe^{3+} species, which can be located in tetrahedral and octahedral sites. The Fe^{3+} sites are located close to the particle surfaces, where they bind water because of their higher Pearson hardness (compared to Fe^{2+} and Zn^{2+}) thereby reducing its mobility and inhibiting the re-crystallization to hopeite. EPR studies showed the incorporation of Fe^{3+} to be coupled with the formation of Zn^{2+} vacancies. Our findings reveal the amorphization mechanism of $Zn_3(PO_4)_2$ in stainless steel ball mills at the molecular scale and highlight how the reactivity of the amorphous product is determined by impurities associated with the preparation method. Our results provide insights and also theoretical guidance for the preparation of amorphous oxide.

11.2 Experimental

11.2.1 Synthesis of Hopeite

Hopeite was synthesized by mixing 300 mM $Zn(NO_3)_2$ solution ($Zn(NO_3)_2 \times 6\ H_2O$ in Milli-Q water, >98%, Sigma-Aldrich) and 200 mM Na_3PO_4 solution (>96%, Sigma-Aldrich). The mixture was stirred for 1 week at room temperature, centrifuged (9000 rpm), and dried by re-suspending in reagent-grade ethanol (≥99.5%, Sigma-Aldrich), centrifuging again, and finally drying under dynamic vacuum for 3 d.

11.2.2 Amorphization of Hopeite

800 mg of hopeite were dispersed in reagent-grade ethanol (m=7.1 g) in order to dissipate heat, pressure, and friction during milling. The dispersions were treated with a planetary ball mill (Retsch PM100) in jars made of stainless steel (for different time intervals 81 mg of stainless steel grinding balls (5 mm diameter) were used. The number of revolutions was set to 600 min^{-1}.

In comparison, ZrO_2 grinding balls and jars were used (to lower the contamination of the samples caused by abrasion of the grinding tools because of their hardness). 15 mg of grinding balls (1 mm diameter) were used (PULVERISETTE 7 classic, Fritsch). The number of revolutions was set to 600 min^{-1}. The reaction was carried out with different amounts (0 to 80 mg) of iron powder (>99.99%, Chempur) in order to quantify the effect of iron on the amorphization process and properties of the final products.

11.2.3 Amorphization Kinetics

Depending on the milling time, samples varied in their degree of crystallinity as determined by quantitative ATR-FTIR spectroscopy and powder XRD. For IR spectroscopy again the splitting of the asymmetric stretching mode of the phosphate group (occurring in crystalline hopeite) was analyzed. The IR measurements were calibrated with standards containing physical mixtures of crystalline hopeite and amorphous zinc phosphate with different ratios of the two components. The crystallinity of the samples could be evaluated quantitatively at any point during the transformation from the band splitting.

11.2.4 Crystallization Kinetics in Water

The reactivity of the amorphous products was examined by recrystallization in water. The reactions were monitored IR spectroscopically. The measurements were carried out on an

ATR crystal of a Fourier transform infrared spectrometer by adding Milli-Q water. Spectra were recorded every 80 s and analyzed quantitatively using a MATLAB script. The splitting of the asymmetric stretching mode of the phosphate group is an indicator for the crystallinity. The phosphate band of crystalline zinc phosphate is split, whereas the band of amorphous zinc phosphate is non-split/broadened. As the (same area of the) sample is located constantly in the beam path of the evanescent wave, the fluctuations are low and the crystallization kinetics are determined precisely

11.2.5 Physical Characterization

The final products were investigated by a combination of TGA and DTA in order to determine the amount of water within mech-AZP as well as the crystallization temperature during annealing in dependence on the amount of added iron. Composition of the products was determined by ICP-MS, ICP-OES, and quantitative ATR-FTIR spectroscopy. The coordination of ^{57}Fe within mech-AZP was investigated by Mössbauer spectroscopy as well as EPR spectroscopy. For experimental details, see Chapter 13.

11.3 Results and Discussion

Phase-pure hopeite was particle sizes in the µm-range was synthesized by precipitation from aqueous solutions of $Zn(NO_3)_2$ and Na_3PO_4. Phase identity was confirmed by PXRD and IR spectroscopy.

11.3.1 Amorphization Kinetics

Amorphous zinc phosphate was prepared by crystalline hopeite treated in a planetary ball mill. The amorphization was complete after 340 min of milling, as indicated by a broad, non-split phosphate band in the FTIR spectra (Figure 11.1 a). The splitting only occurs in crystalline hopeite due to factor group splitting and the lower site symmetry. The respective reaction rate was determined by interrupting the milling process after given time intervals, taking samples and recording their FTIR spectra *ex situ*.[342,343] The band splitting is a measure for the progress of the amorphization reaction (Figure 11.1 b). The "IR-crystallinity" reflects the local (short-range) order within the sample, whereas diffraction data (reflection width or profile) provide information concerning particle size, long-range order ("X-ray-crystallinity") and strain. The advantage of IR spectroscopy is that it is a laboratory method. In addition, it is very fast and yields information even for highly distorted lattices close to the end of the reaction.

The progress of the milling reaction in the presence of iron impurities (2 mol%, Figure 11.2) was very similar. The transformation from hopeite to mech-AZP was monitored by XRD

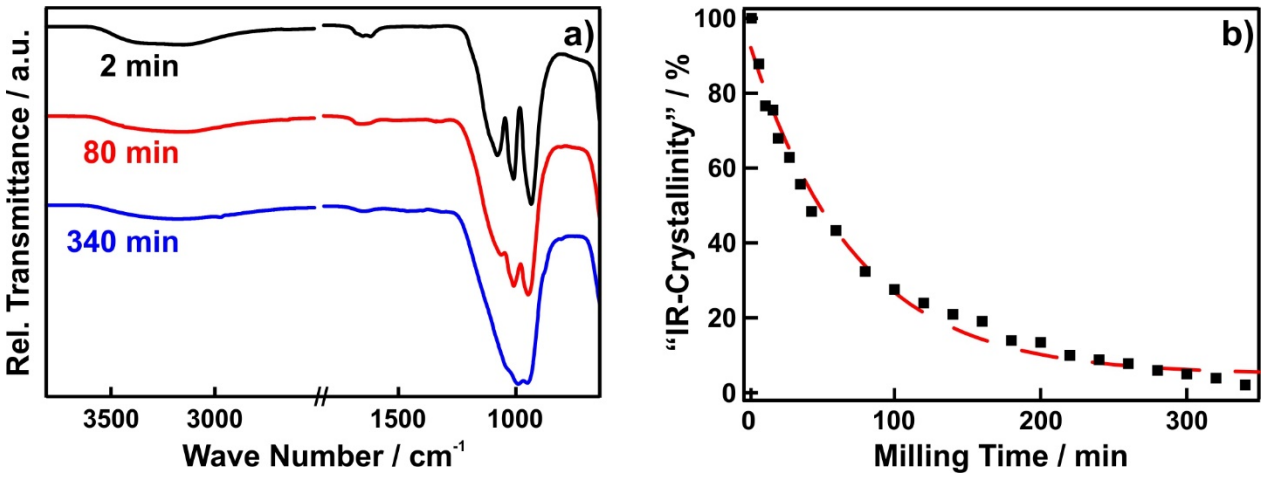

Figure 11.1. a) IR spectra of $Zn_3(PO_4)_2 \times 4\ H_2O$ (hopeite) after different process (milling) times of 2, 80, and 340 min in the absence of Fe impurities, normalized to the phosphate stretching mode. The bands of crystalline hopeite are split because of lattice symmetry constraints **b)** Amorphization kinetics derived by quantitative analysis of the IR spectra.

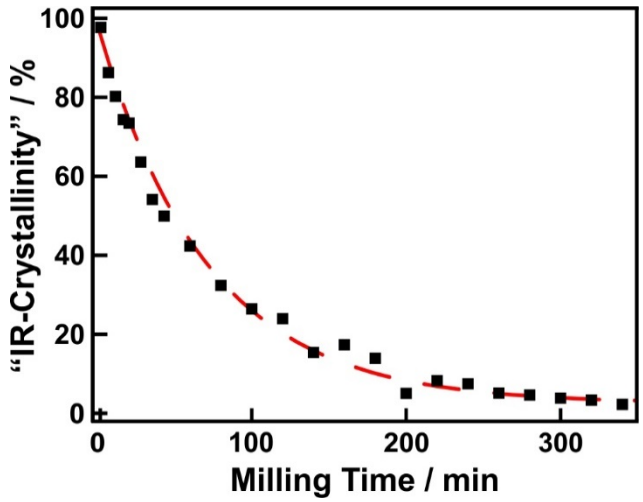

Figure 11.2. Amorphization kinetics derived by quantitative analysis of the respective IR spectra after different milling times of $Zn_3(PO_4)_2 \times 4\ H_2O$ in the presence of iron impurities (2 mol%).

(Figure 11.3). The diffractogram in Figure 11.3 shows sharp intensities in the diffraction patterns of hopeite after 2 min of milling (orange trace). The pronounced reflection broadening after 80 min of ball milling (red trace) indicates the loss of crystallinity, and after 340 min (blue trace) the amorphization was complete as demonstrated by the absence of reflections in the X-ray diffractogram. The most intense reflection of Fe appears at 11.72° in 2Θ (indicated by the black arrow in Figure 11.3). As Mössbauer spectroscopy indicated 7% content of unreacted *a*-Fe (Table 11.4, *vide infra*), we conclude that no other crystalline FeO_x or ZnO_x phases were present in mech-AZP.

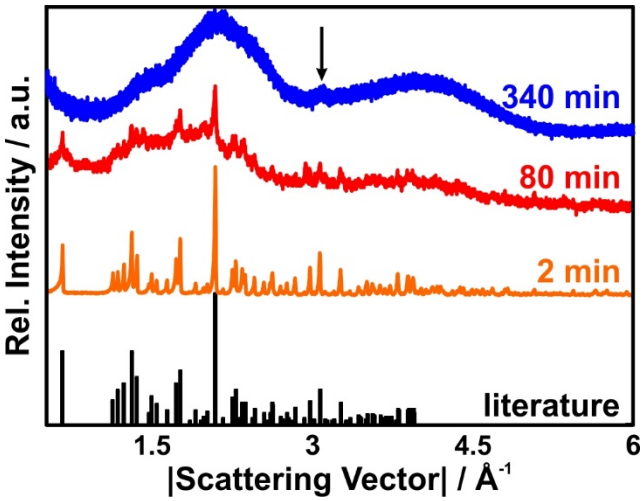

Figure 11.3. X-ray diffractograms of hopeite in the presence of Fe impurities (2 mol%) after different milling times. The sample of mech-AZP (340 min) was measured with high-intensity synchrotron radiation. The black arrow indicates the most intense reflection of elemental *a*-Fe.

Table 11.1. Milling reaction with different amounts of iron.

Amount of Fe used during milling / mol%	Milling time until complete amorphization[a] / min	"IR-Crystallinity" after 60 min of milling / %
0	340	56.8
1	320	59.2
2	340	59.6
4	360	57.8
5	320	56.5
10	340	59.0

[a]determined by quantitative ATR-FTIR spectroscopy

The kinetics of the transition from the crystalline to the amorphous state were monitored again by quantitative analysis of the band splitting of the IR spectra.[342,343] Table 11.1 (summarizing the results of experiments with different amounts of iron added during the milling) displays no recognizable effect of iron on the reaction. The amorphization kinetics follows an exponential decay, and it is very similar to that of the reaction in the absence of Fe, regardless of the amount of Fe impurities, *i.e.*, there is no discernable effect of Fe on the amorphization process.

11.3.2 Characterization

The composition of the final amorphous products was characterized by EDX, ICP-MS, and ICP-OES. Table 11.2 shows the results for mech-AZP synthesized without iron. An average Zn:P composition of 3.0:2.0 was determined. The different initial iron concentration was found in the later measurements with a deviation of ±3% although a distinction between iron integrated in the amorphous structure and iron outside the structure was not possible. EDX showed Fe to be distributed homogeneously within the samples. The water of hydration in mech-AZP corresponds to an average formula of $Zn_3(PO_4)_2 \times 1.5\ H_2O$ as determined by quantitative IR spectroscopy ($Zn_3(PO_4)_2 \times 0.8\ H_2O$, Table 11.3, *vide infra*) based on the Beer-Lambert law (extinctions of the O–H bands are proportional to the water content) and TGA ($Zn_3(PO_4)_2 \times 2.1\ H_2O$, Figure 11.6, *vide infra*). This suggests that coordinating water is essential for the degree of crystallinity in this hydrated system, *i.e.*, the dehydration of hydrated structures requires large structural re-arrangements and therefore leads to amorphization. [303–

Table 11.2. ICP-MS, ICP-OES, and EDX results of mech-AZP synthesized without Fe by milling hopeite for 340 min.

ICP-MS	^{64}Zn	^{66}Zn	^{31}P
mean conc. / μg L^{-1}	570.7±7.0	580.7±4.7	179.4±1.4
mean conc. / μmol L^{-1}	8.73±0.11	8.88±0.07	5.79±0.04
ratio		3.00:1.97	
ICP-OES	Zn		P
mean conc. / μg L^{-1}	2440		790
mean conc. / μmol L^{-1}	37.3		25.5
ratio		3.0:2.1	
EDX	ZnK	PK	
at%	15,78	10.73	
ratio		3.0:2.0	

[a]Mean concentrations (μg L^{-1}) and standard deviations for Zn and P in mech-AZP; estimated standard deviations of all the samples (ESD) are included.

305] In fact, the amorphization of crystalline hydrates represents an important group of solid-state transformations.[343]

The mech-AZP crystallites formed by ball milling in the absence of Fe have a plate-like morphology with diameters between 500 nm and 3 μm (Figure 11.4). At higher magnification the plates appear to consist of agglomerates of nearly spherical particles with diameters of 50 to 150 nm. As synthetic hopeite contains micro-plates with diameters in the μm range (see

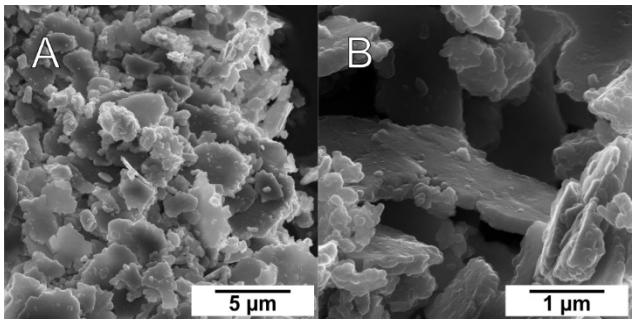

Figure 11.4. SEM images of mech-AZP after ball milling of hopeite for 340 min in the absence of iron.

Figure 3.4 E and F, Chapter 3), we can assume that the particles of mech-AZP were formed in two separate processes: small particles are produced by the milling followed by fusing these smaller particles to plate-like aggregates to reduce surface energy.

11.3.3 Crystallization Kinetics in Water

As mech-AZP contains much less structural water than hopeite recrystallization to hopeite should occur in aqueous solution or even atmospheric moisture as water (i) is a structural building block (ii) is known to act as a mineralizer. A plausible explanation reason for this behavior is the significantly lower activation energy for surface diffusion compared to solid state diffusion.[163] In fact, crystalline hopeite was obtained after short reaction times (approx. 1 min) by re-suspending mech-AZP (ball-milled in the absence of iron) in water, and it is stable for months under dry conditions. Figure 11.5 displays the crystallization kinetics of mech-AZP, ball-milled in the absence and in the presence of iron (0 to 5 m%) as determined by quantitative *in situ* ATR-FTIR spectroscopy.

Mech-AZP synthesized in the absence of Fe is very unstable with respect to crystallization in water. After only 2 min more than 80% of the sample had transformed to hopeite. The reaction profile showed a Langmuir-like behavior, which suggests that the proceeds *via* the adsorption/desorption of water to distinct surface sites capable of binding the H_2O adsorbate with a subsequent transformation to the crystalline product. This reaction therefore would yield an adsorbed complex $H_2O(ads)$ with an associated equilibrium constant K_e, according to this mechanism the reaction approaches a "saturation" limit for longer reaction times. In the presence of iron the recrystallization slowed down significantly with

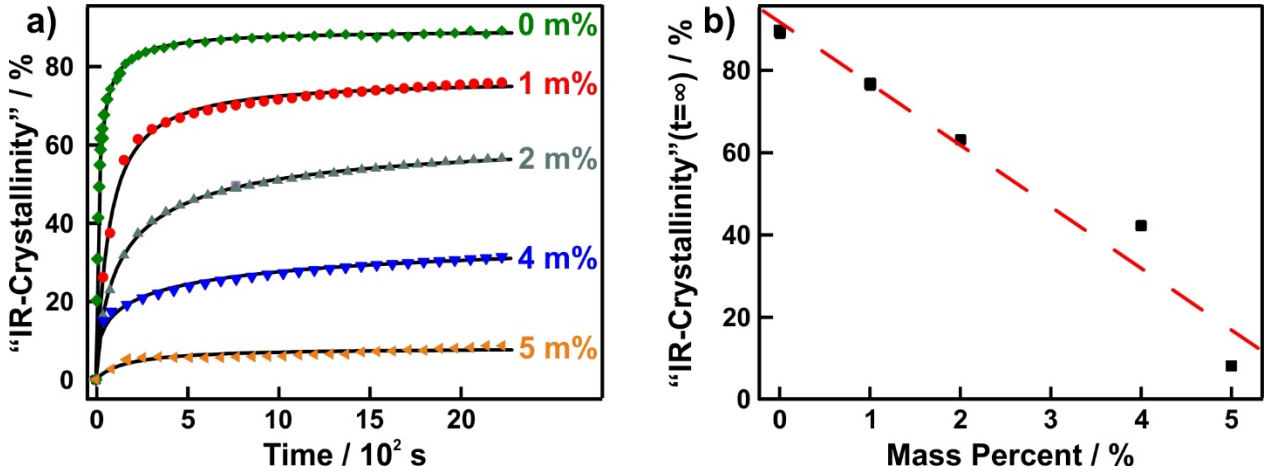

Figure 11.5. a) Crystallization kinetics in water of mech-AZP with different amounts of iron (mass %) during milling (black lines represent Langmuir plots) **b)** "IR-Crystallinity" at saturation limit according to the respective Langmuir plot.

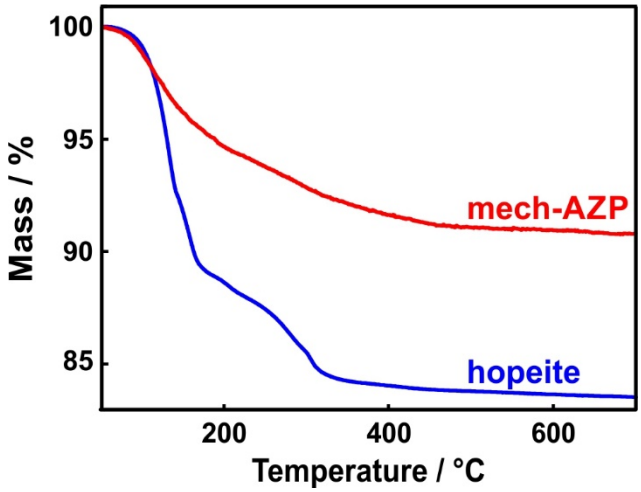

Figure 11.6. TGA measurement of mech-AZP(0 m% Fe) showing the continuous loss of weight upon heating (red line). In contrast, hopeite loses its structural water in defined steps and contains a higher amount of structural water.

increasing Fe content, and a major portion of the sample remained amorphous. With 5 mol% of Fe the crystallinity only increases towards 10% even after 2 d, and with 10 mol% of Fe added during ball-milling mech-AZP was stable with respect to crystallization even after 2 months. In the absence of water, mech-AZP is stable (even at 350 °C) for several months, *i.e.*, water acts appears to act as a mineralizer imparting enhanced mobility to the surface ions.

In contrast, the reaction rate of AZP prepared by precipitation (see Chapter 7) can be described by an Avrami kinetics, which is indicative of the growth of crystals being autocatalytic. The transformation of both materials to hopeite is assumed to occur *via* a dissolution-recrystallization process. We attribute the differences in the reactivity of mech AZP and AZP to their different compositions and structures, in particular to differences of the hydration networks.

Mech-AZP particles have an inhomogeneous and plate-like appearance. The plates are composed of smaller coalesced nanoparticles; the strong aggregation can be rationalized by the reduction of surface energy. The water content of mech-AZP is much lower than that of AZP, *i.e.*, the tendency for hydration should be much more pronounced. The abrasion of Fe, which was simulated here by intentionally adding Fe particles to the mill-charge, leads to the integration of Fe ions into the AZP lattice. The Fe impurities should be incorporated preferentially at surface defect sites (unsaturated), and surface- bound Fe^{2+} can oxidize to Fe^{3+} easily. As Fe^{2+} and in particular Fe^{3+} are more oxophilic than Zn^{2+}, hydrated $[Fe(H_2O)_x]^{2+}$ and $[Fe(H_2O)_x]^{3+}$ surface sites will form locally, and Fe^{3+}-bound water may prevent further surface migration of the water molecules required for lattice rearrangement and crystallization. In

Table 11.3. Water content (formula units)[a] of zinc phosphates based on the extinctions of the water bands in normalized IR spectra.

substance	E(ν(O–H)) / a.u.	water content	E (δ(H–O–H)) / a.u.	water content
hopeite	0.125	4.0	0.070	4.0
mech-AZP	0.021	0.7	0.015	0.9
HT-mech-AZP	0.001	0.0	0.003	0.4

[a]The water content of hopeite was set to 4.0.

addition, $[Fe(H_2O)_6]^{3+}$ is a strongly acidic (pK_s=2.22) and therefore protonate surface phosphate groups, thereby acting as crystallization inhibitor.

Mech-AZP(0 m% Fe) loses structural water continuously upon heating, but remains non-crystalline up to 468 °C (see Figure 11.6). Even after annealing at 350 °C for 5 d under argon, mech-AZP stays non-crystalline. Quantitative IR spectroscopy indicated a composition $Zn_3(PO_4)_2 \times 0.2\ H_2O$ (HT-mech-AZP) after annealing (see Table 11.3).

Milling increases the portion of mech-AZP; as a result, the intensity of the exothermic signal increases as well. In addition, the transformation temperature, *i.e.*, the stability of the balled-milled product, increases with increasing milling time (Figure 11.7 a). The effect of Fe is also evident from the thermally induced crystallization. An increasing Fe content (up to 8%)

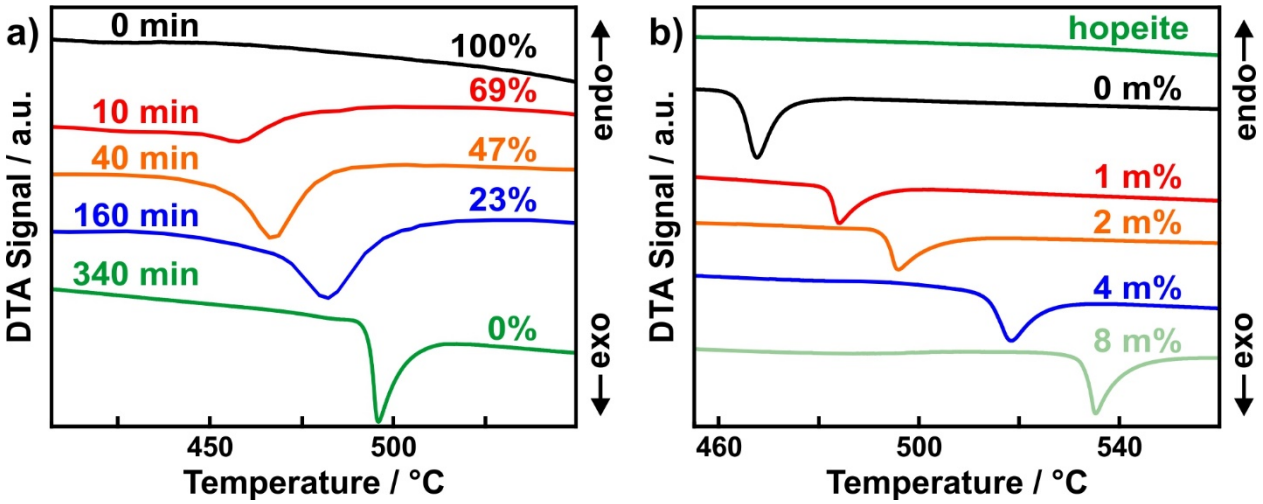

Figure 11.7. a) DTA of hopeite milled with 2 m% of Fe for different milling durations (displayed on the left side) corresponding to different degrees of "IR-crystallinity" (displayed on the right side). **b)** DTA of hopeite and its milling end products (mech-AZP) with different amounts of Fe used during reaction (in m% beside the curves).

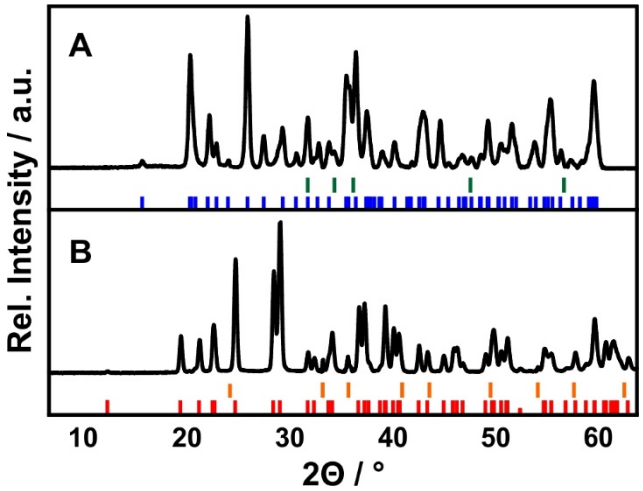

Figure 11.8. (A) X-ray diffractogram γ-$Zn_{3-x}Fe_x(PO_4)_2$ formed by heating a sample mech-AZP in the presence of 2 mol% ^{57}Fe at 700 °C under argon (in blue: literature reflections of γ-$Zn_3(PO_4)_2$, in green: literature reflections of ZnO). **(B)** Heating up on air leads to α-$Zn_3(PO_4)_2$ (red literature reflections) containing α-Fe_2O_3 impurities (orange literature reflections).

increases the transformation temperature (amorphous-crystalline) from 468 to 535 °C (Figure 11.7 b).

"Fe-doped" γ-$Zn_{3-x}Fe_x(PO_4)_2$ was formed after annealing mech-AZP under Ar (Figure 11.8 A). γ-$Zn_{3-x}M_x(PO_4)_2$ forms only as a solid solution in the presence of divalent transition metals (>5 mol%).[344–346] The transition metal atoms replace the Zn^{2+} species at the tetrahedral sites. Excess Zn^{2+} phase separates as ZnO. In fact, weak reflections of zincite (ZnO) could be observed in the X-ray diffractogram. In addition, γ-$Zn_3(PO_4)_2$ is one of the rare cases where may be Zn^{2+} is located at the tetrahedral and octahedral sites.

Calvo *et al.*[117] reported that the "doping metal" occupies the octahedral position because Zn^{2+} prefers a tetrahedral rather than an octahedral coordination. Annealing in air leads to the formation of α-$Zn_3(PO_4)_2$ containing α-Fe_2O_3 impurities as a side phase, as shown by X-ray diffraction (Figure 11.8 B), Mössbauer spectroscopy (Figure 11.9 d), and magnetic susceptibility measurements (Figure 11.10).

The hopeite structure contains two different zinc sites with tetrahedral and octahedral coordination in a ratio of 2:1. The Zn^{2+} cations at the tetrahedral sites are coordinated by four oxygen atoms of different phosphate groups, while the environment of the octahedral sites consists of oxygen atoms of two different water molecules and four different phosphate groups. Accordingly, the Mössbauer spectra of mech-AZP (2% ^{57}Fe, Figure 11.9) show two iron signals in a ratio 2:1: one doublet (doublet 1) corresponding to high-spin Fe^{2+} and a second doublet (doublet 2) corresponding to high-spin Fe^{3+} (besides a small sextet arising from traces

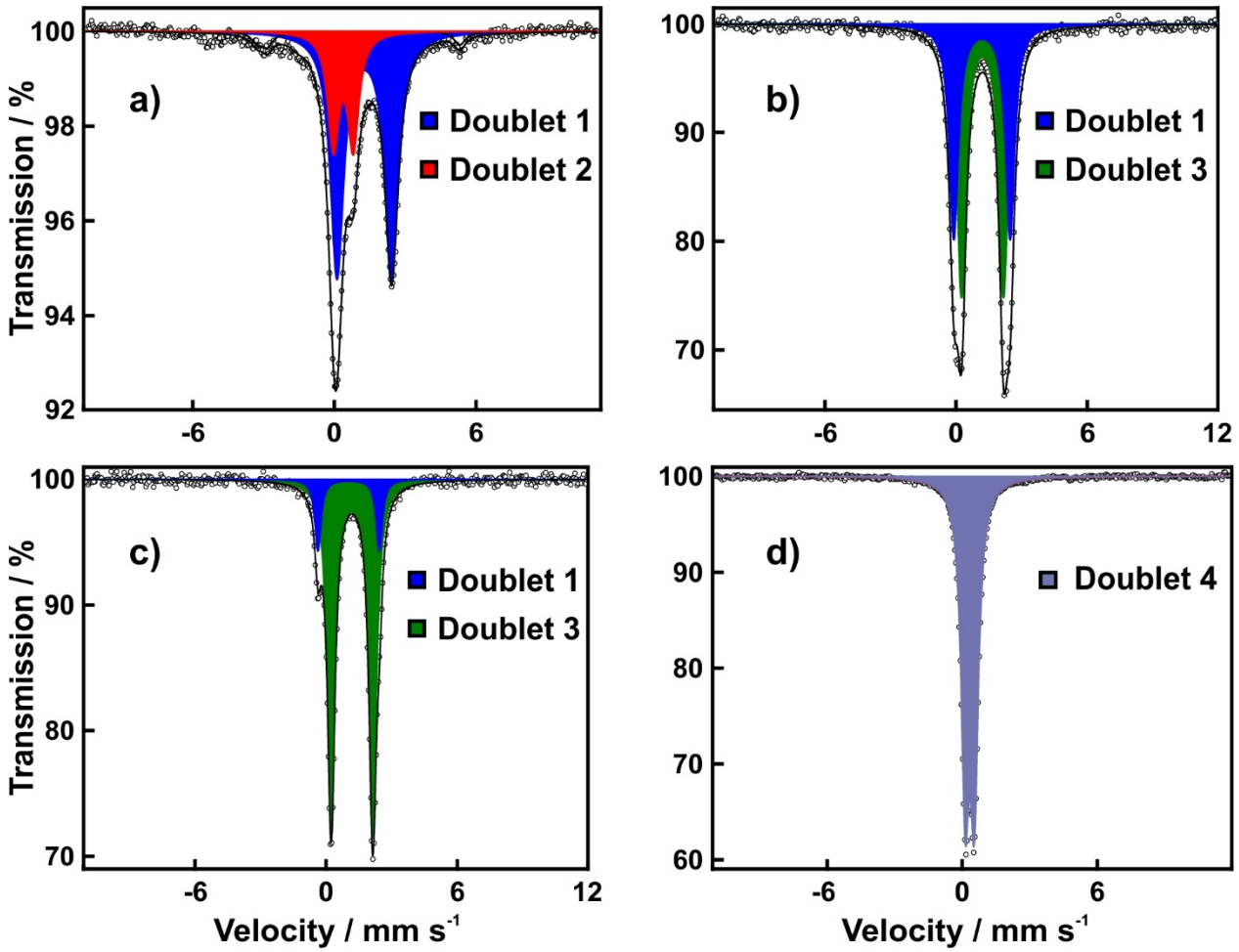

Figure 11.9. Mössbauer spectra of **a)** mech-AZP, and the annealing products: **b)** 400 °C under argon, **c)** 700 °C under argon, and **d)** 700 °C on air.

of elemental ^{57}Fe). Based on the isomer shifts and quadrupole splittings the Fe^{2+} species are located at the tetrahedral and the Fe^{3+} cations at the octahedral sites (see Table 11.4). According to these results, Fe is oxidized and occupies the respective positions of Zn in the hopeite structure. Under equilibrium conditions, it is expected that Fe prefers octahedral coordination and Zn the tetrahedral coordination leading to a phosphophyllite-like structure ($Zn_2Fe(PO_4)_2 \times 4\ H_2O$).[347] This trend is not observed as the chemical reaction during ball milling are under non-equilibrium conditions.

During annealing (400 °C, 700 °C), doublet 2 vanishes completely whereas a new doublet can be observed (see Figure 11.9 b) and c). The total signal (doublet 3) of the Mössbauer spectrum of mech-AZP sample after annealing 400 °C can be assigned to high-spin Fe^{3+} in octahedral sites of the γ-$Zn_3(PO_4)_2$ structure. It is not surprising that Fe^{2+} occupies the preferred octahedral positions in the γ-$Zn_3(PO_4)_2$ structure as the crystallization process is under equilibrium conditions. The principal signal (doublet 3) in the Mössbauer spectrum of

Table 11.4. Hyperfine parameters of ^{57}Fe in Fe substituted $Zn_{3-x}Fe_x(PO_4)_2 \times n\ H_2O$.[a]

signal	isomer shift / $mm \cdot s^{-1}$	quadrupole splitting / $mm \cdot s^{-1}$	species	amount / %
mech-AZP (2 m% ^{57}Fe)				
1	1.315(3)	2.744(5)	Fe^{2+}, hs	65(1)*
2	0.532(9)	0.73(1)	Fe^{3+}, hs	28(1)*
mech-AZP (2 m% ^{57}Fe, 400 °C for 5 d, Ar)				
1	1.195(3)	2.58(2)	Fe^{2+}, hs	45(3)
3	1.221(3)	1.92(1)	Fe^{2+}, hs	55(3)
mech-AZP (2 m% ^{57}Fe, 700 °C for 5 d, Ar) (γ-$Zn_{3-x}Fe_x(PO_4)_2$)				
1	1.100(1)	2.81(2)	Fe^{2+}, hs	14(2)
3	1.253(2)	1.905(4)	Fe^{2+}, hs	86(2)
mech-AZP (2 m% ^{57}Fe, 700 °C for 5 d, on air) (α-$Zn_3(PO_4)_2$)				
4	0.344(1)	0.410(1)	Fe^{3+}, hs	100

[a]Isomer shifts are given in relation to *a*-Fe at ambient temperature. *The difference to 100% is due to 7% of unreacted *a*-Fe, identified by its typical sextet.

mech-AZP sample after annealing at 400 °C corresponds to high-spin Fe^{2+} in octahedral sites of γ-$Zn_3(PO_4)_2$. Doublet 1 can be assigned to non-crystalline mech-AZP(Fe) as the sample was not fully crystalline. The decrease in the relative intensity of doublet 1 due to crystallization of the sample after annealing at 700 °C corroborates this assignment. Reducing the annealing temperature to 400 °C results in the formation of smaller amounts of γ-$Zn_{3-x}Fe_x(PO_4)_2$. In contrast, annealing in air leads to the formation of α-$Zn_3(PO_4)_2$ with minor (5%) amounts of hematite (α-Fe_2O_3) side phase, as demonstrated by PXRD (Figure 11.8 B) and Mössbauer spectroscopy (only Fe^{3+}, hs species arising from α-Fe_2O_3, see Figure 11.9 d). Furthermore, this was supported by collective magnetization at 5 K, observed in the magnetic susceptibility and magnetization measurements (Figure 11.10), whereas a solid solution of γ-$Zn_{3-x}Fe_x(PO_4)_2$ with Fe^{2+} cations replacing Zn^{2+} in the γ-$Zn_3(PO_4)_2$ structure show only paramagnetic behavior.

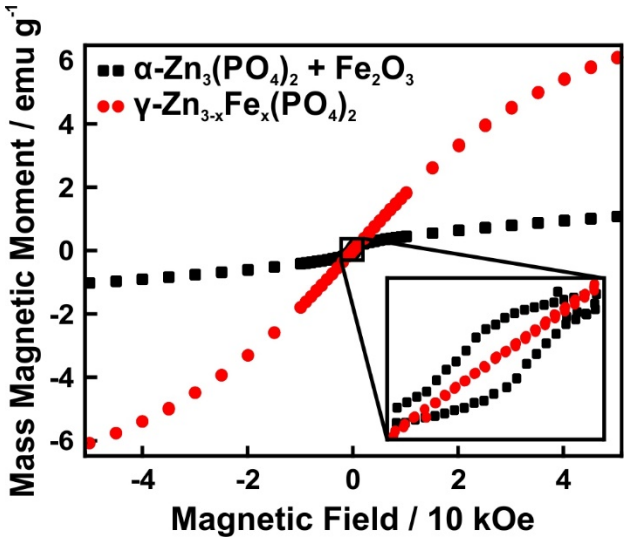

Figure 11.10. Hysteresis loops (5 K) for mech-AZP ball-milled in the presence of 2 mol% ^{57}Fe after annealing at 700 °C under Ar (red spheres) and in air (black squares).

As Fe is present in its di- and trivalent states (Fe^{2+} and Fe^{3+}) we also performed EPR spectroscopy with mech-AZP, in order to examine whether the presence of Fe^{3+} is associated with Zn^{2+} vacancies ("hole doping") or due to free unpaired electrons or radicals (Figure 11.11), which would lead to a sharp signal at g=2.0 (not observed). We observed several signals at g≈4.0 with temperature-dependent signature, which are characteristic for Fe-substituted ZnO ($Zn_{1-x}Fe_xO$).[348] The transitions are spin forbidden (Δm_s=2) and attributed to the presence of isolated Fe^{3+} ions ($^6S_{5/2}$, S=5/2) with uncoupled Fe^{3+} species near-by, leading to a ferromagnetic coupling over a small area. A weaker signal at g≈2.0 (a so-called half-field signal) is due to the coupling of spin functions and an associated violation of the selection rules. The

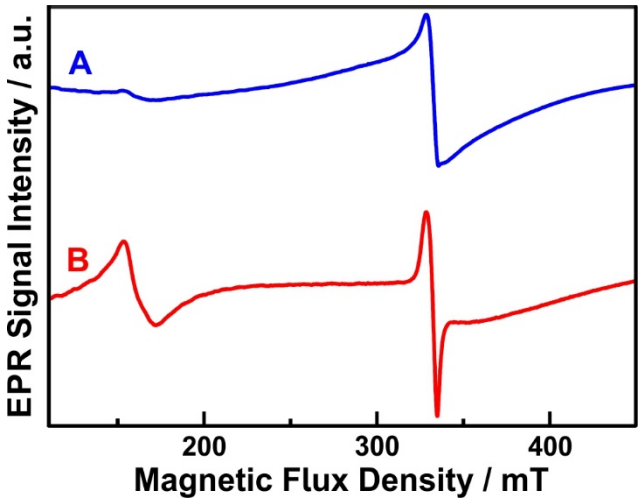

Figure 11.11. EPR spectra of mech-AZP (synthesized with 2 mol% of ^{57}Fe) at room temperature **(A)** and cooled with N_2 **(B)**.

EPR signal of the Fe^{2+} ions cannot be resolved due to the small value of spin lattice relaxation time. Although an exact analysis of the EPR signal is too complex, no free unpaired electrons or radicals are present[348–350] in mech-AZP.

11.4 Conclusion

We have shown that metastable amorphous polymorphs of zinc phosphate can be generated by mechanosynthesis (ball-milling). In particular, the metastable products were stabilized by the incorporation impurities due to wear of the milling media (stainless steel balls). We could demonstrate this here by an amorphization study of hopeite ($Zn_3(PO_4)_2 \times 4\ H_2O$) in a planetary ball mill and its subsequent recrystallization. Abrasion of the milling tools was simulated by addition of pure ^{57}Fe. The amorphization process and its kinetics were monitored by X-ray powder diffraction with high-intensity synchrotron radiation and quantitative ATR-FTIR spectroscopy. Inductively coupled plasma mass spectrometry (ICP-MS), optical emission spectrometry (ICP-OES), and thermal analysis revealed the release of coordinated water to be a key step during the formation amorphous zinc phosphate (mech-AZP) by ball-milling. Quantitative IR spectroscopy proved useful for the *in situ* determination of the re-crystallization kinetics of mech AZP in water. The crystallization of mech-AZP (formed in the absence or presence of Fe) followed a Langmuir-like behavior. This is significantly different from AZP isolated from aqueous solution that crystallizes according to classical Avrami kinetics. Simulations of C-REDOR curves for mech-AZP will help to understand the different crystallization behavior based on the present water network. However, Fe impurities increased the stability of mech-AZP tremendously. Also its thermal stability with respect to $Zn_3(PO_4)_2$ increased by up to 70 °C in the presence of Fe impurities (8 mol%) under Ar.

Due to the ability of the ^{57}Fe Mössbauer spectroscopy to probe the environment of the Fe nuclei, insights on a local atomic scale into the mechanically induced changes were obtained. Metastable mech-AZP was stabilized as "Fe-doped" γ-$Zn_{3-x}Fe_x(PO_4)_2$ with Fe^{2+} and Fe^{3+} incorporated at the tetrahedral and octahedral sites of the $Zn_3(PO_4)_2$ structure. Annealing in air lead to the oxidation of Fe and to the formation of α-$Zn_3(PO_4)_2$ containing α-Fe_2O_3 impurities, as shown by Mössbauer spectroscopy and magnetic susceptibility measurements. EPR studies showed the incorporation of Fe^{3+} γ-$Zn_{3-x}Fe_x(PO_4)_2$ to be coupled with the formation of Zn^{2+} vacancies. The Fe^{3+} defect sites are assumed to bind water strongly because of their higher oxophilicity (Pearson hardness) compared to Fe^{2+} and Zn^{2+}. As a result, hydrated $[Fe(H_2O)_x]^{3+}$ surface complexes are assumed to form locally, which prevent surface migration of Fe^{3+}-bound water that is required for lattice rearrangement and crystallization.

Our findings reveal the amorphization mechanism of $Zn_3(PO_4)_2$ in planetary ball mills at the atomic scale and highlight how the reactivity of the amorphous product is determined by

impurities associated with the preparation method. The results provide insights and theoretical guidance for the preparation of complex amorphous phosphates.

12

CONCLUSION AND OUTLOOK

The aim of this work was the examination of metastable solid states of 3d metal phosphates. These metal phosphates display very interesting model systems for general investigations concerning nucleation, crystal growth, and stabilization of metastable states which is still poorly understood. First, these non-equilibrium phases were isolated from solution as precursors during the formation of crystalline modifications (bottom-up). Second, we investigated a mechanochemical top-down approach starting with thermodynamically stable modifications and ending up with metastable phases via ball milling.

The first part of the present thesis covers the occurrence of different intermediates during precipitation of 3d metals phosphate hydrates in solution. Amorphous solids, prenucleation clusters, and liquid-condensed phases were observed as metastable precursors of the crystalline 3d metal phosphate hydrates. A key point was their comprehensive characterization and their subsequent recrystallization. Additionally, we placed emphasis on the role of coordinating water during the formation and stabilization of intermediates.

In the first step, we presented the synthesis and comprehensive characterization of amorphous zinc phosphate hydrate nanoparticles from aqueous solution (AZP). The nanomaterial (20 nm in size) was isolated prior to the formation of the thermodynamically stable hopeite ($Zn_3(PO_4)_2 \times 4\ H_2O$). By resuspending the amorphous material in water, hopeite was formed by a dissolution-recrystallization process. Thermogravimetric measurements, quantitative ATR-FTIR spectroscopy, and ^1H SS-NMR spectroscopy displayed a lower water content in the amorphous solid compared to hopeite. The water-deficient, amorphous solid was stabilized kinetically in the absence of water, even at elevated temperatures. Heating up leads to a range of different hydrated amorphous solids upon crystallization of anhydrous *a*-$Zn_3(PO_4)_2$ at about 500 °C. Simulations of C-REDOR NMR curves showed a rather rigid hydrogen-bonded network for amorphous zinc phosphate hydrate and hopeite to be responsible for the inhibition of crystallization.

Besides AZP, an amorphous precursor phase prior to the formation of $Co_3(PO_4)_2 \times 8\ H_2O$ was isolated (ACP). Co^{2+} is colorimetrically active due to its transition metal character so that coloring of the respective solids allows distinguishing between different hydrated modifications and amorphous solids qualitatively. EXAFS and XANES measurements suggested different short-range order in amorphous cobalt phosphate hydrate and $Co_3(PO_4)_2 \times 8\ H_2O$: The amorphous phase realizes smaller coordination numbers (in direction 4 (tetrahedral) instead of 6 (octahedral)) and the distances of Co^{2+} to its neighbors of the second and third coordination shell are larger than for $Co_3(PO_4)_2 \times 8\ H_2O$. Automated quantitative ATR-FTIR spectroscopy with a self-written MATLAB script and external standards, allowed to follow the recrystallization process time dependent *in situ*. Recrystallization of $Co_3(PO_4)_2 \times 8\ H_2O$ was described by an exponential relation.

Further, the occurrence of amorphous solids prior to the formation of iron, nickel, and copper phosphate hydrate in aqueous solution suggested that this may be a general phenomenon for late 3d metal phosphates. The results support the idea that phosphates of cations with the potential to bind water reversibly crystallize via a multi-stage process including the formation of different hydrated (amorphous) intermediates. A first hint for possible candidates for this crystallization pathway is given by a moderate Pearson of the respective cation. All prepared amorphous solids were water-deficient in relation to the respective hydrated crystalline modification.

Next, we established a facile synthetic approach for an anhydrous amorphous cobalt phosphate (MeOH-ACP) precipitating from methanol. TEM displayed coalesced ("molten") particles at the nm and μm scale. ATR-FTIR and XRD measurements (under exclusion of air) suggested MeOH-ACP to be amorphous. ICP-MS, ICP-OES, and EDX revealed its composition to be $Co_3(PO_4)_2$. MeOH-ACP rapidly adsorbs moisture from the air, which was investigated by ATR-FTIR spectroscopy *in situ* and described according to a Langmuir-like behavior. The uptake of water led to a certain saturation level of hydration but still without crystallization. Crystallization proceeded via dissolution and recrystallization at high degrees of humidity provided by a climate chamber and was described by an exponential relation.

Furthermore, the crystallization of AZP to hopeite in aqueous solution was monitored by using *in situ* ATR-FTIR spectroscopy. Crystallization was described by an Avrami-like behavior. Subsequently heterogeneous nucleation of silica on the surface of AZP nanoparticles resulted in encapsulation by a shell of silica. The silica shell (15–20 nm thick) formed over entire agglomerates of AZP and blocked the diffusion of adsorbed surface water

to the amorphous core effectively as indicated by ATR-FTIR spectroscopy. As AZP has to incorporate additional water for crystallization to hopeite, no crystallization event was observed for AZP@SiO_2 in aqueous solution.

In addition, macroscopic liquid-condensed phases (LCP) were prepared by adding $ZnCl_2$/$CoCl_2$ to a highly concentrated HPO_4^{2-} solution. The LCP revealed an increased viscosity and SS-NMR measurements suggested the presence of complexes embedded in a hydrogen-bonded network. Low concentrations of Zn^{2+} resulted in the formation of a symmetric complex whereas high concentrations led to an asymmetric complex. The essential role of water in between the network was indicated by (i) densification of LCP by evaporation of water and (ii) dissolution of LCP accompanied with precipitation of solid particles through additional water. The highly concentrated HPO_4^{2-} solution had the potential to dissolve phosphate crystals with enormous lattice energy that displayed a novel effect with still unexpected possibilities of structural investigations.

Further, prenucleation clusters (PNC) were detected by an ionic sensitive electrode prior to the formation of an amorphous solid phase for the copper phosphate system. The measured concentration in solution differed from the theoretical values significantly during a constant pH titration of Cu^{2+} in a phosphate buffer. Higher pH values that correspond to a higher amount of PO_4^{3-} and HPO_4^{2-} in solution resulted in an increased binding of Cu^{2+} in PNC. The titration was divided into three stages based on the results of the titration measurements and TEM. It is assumed that PNC form in undercritical solution during stage I, followed by the formation of a nanoscopic LCP in stage II. Reaching a critical supersaturation, the precipitation of an amorphous solid was observed in stage III, most probably an amorphous copper phosphate hydrate. The amount of phosphate species bound by clusters were determined time dependent based on the constant pH titration. The results suggested a 1:1 composition of Cu^{2+} to HPO_4^{2-} in stage I and an enrichment in HPO_4^{2-} in stage II probably due to termination of the LCP surface by HPO_4^{2-}. The formation of PNC in undercritical solution for slightly soluble phosphates may be a general phenomenon which is in conflict with classical nucleation theory.

The second part of this thesis covers a mechanistic study of the amorphization of thermodynamically stable crystalline phosphate hydrates under mechanical stress. $Co_3(PO_4)_2 \times 8\ H_2O$ was amorphized mechanochemically by treatment with a planetary ball mill (mech-ACP). Amorphization kinetics were described by an exponential decay as determined by quantitative ATR-FTIR spectroscopy and XRD at a synchrotron beamline.

Further, coordinating water was expelled during the amorphization process which was demonstrated by ATR-FTIR spectroscopy and TGA. The final product were analyzed in terms of composition and short-range order. XANES and EXAFS measurements revealed Co^{2+} to have a lower coordination number in mech-ACP (approximate formula $Co_3(PO_4)_2 \times 2\ H_2O$) than in $Co_3(PO_4)_2 \times 8\ H_2O$ and also in ACP (isolated from solution). In addition, we showed that hydrostatic pressure did not cause amorphization by an *in situ* reference experiment in a diamond anvil at a synchrotron beamline. However, the enormous shearing forces present in a planetary ball mill (maybe accompanied with the formation of a plasma) are responsible for the amorphization. Recrystallization by dissolution and recrystallization was induced by exposing the amorphous solid to humidity in a controlled way using a climate chamber. Recrystallizations kinetics were described by an Avrami-like behavior.

Furthermore, we examined the stabilization of amorphized products by incorporating impurities due to wear of the milling media as demonstrated by a study of the amorphization of hopeite in a planetary ball mill and its subsequent recrystallization. Abrasion was simulated by addition of pure ^{57}Fe. The amorphization process and its kinetics were monitored by XRD with high-intensity synchrotron radiation and quantitative ATR-FTIR spectroscopy and determined to follow an exponential decay. The release of coordinated water turned out to be a key step during the amorphization process from hopeite to ball-milled amorphous zinc phosphate (mech-AZP). The recrystallization kinetics of mech-AZP in water follow a classical Langmuir behavior and thus, are significantly different from AZP isolated from solution following an Avrami-like crystallization. Fe impurities increase the stability of mech-AZP tremendously. ^{57}Fe Mössbauer spectroscopy and XRD revealed that during ball-milling Fe is oxidized to Fe^{2+} and Fe^{3+} and incorporated at the tetrahedral and octahedral sites of hopeite's structure under non-equilibrium conditions. During heating, mech-AZP crystallizes to γ-$Zn_{3-x}Fe_x(PO_4)_2$ under inert atmosphere while annealing on air leads to α-$Zn_3(PO_4)_2$ with impurities of α-Fe_2O_3. EPR studies showed the incorporation of Fe^{2+}/Fe^{3+} to be coupled with the formation of Zn^{2+} vacancies. The Fe^{3+} defect sites are suggested to bind water due to their higher Pearson hardness (compared to Fe^{2+} and Zn^{2+}) thereby reducing its mobility and inhibiting the recrystallization to hopeite. Our findings reveal the amorphization mechanism of hopeite in planetary ball mills at the atomic scale and highlight how the reactivity of the amorphous product is determined by impurities associated with the preparation method.

In conclusion, this thesis illuminates different metastable intermediates during precipitation of 3d metal phosphate hydrates from solution including amorphous solids, prenucleation clusters, and liquid-condensed phases. The structures of the chosen crystalline phosphate hydrates were simple enough to provide well-suited model systems to study nucleation and crystal growth. The moderate charge densities of the divalent metals and PO_4^{3-} allowed reversible hydration leading to different hydrated intermediates accompanied by the formation of hydrogen-bonded networks. The isolation as well as the recrystallization kinetics of the precursors presented in this thesis displayed the essential role of water as active reaction partner during nucleation and crystal growth events. The great variety of solid metal phosphates with plenty of industrial applications (*e.g.*, tooth cements, corrosion resistance coatings, lubricant base layers) make them promising candidates for materials science. Design of functional structures with controlled morphology, size distribution, and purity is one of the main goals. Future work will comprise examination of the intermediates under influence of various additives (*e.g.*, polymers) and solvents in order to control the degree of hydration. Stepwise adjustment of hydration and coordination environment might be a systematic approach to understand solvation and desolvation processes during nucleation and crystal growth. Control and stabilization of the individual precursors occurring during precipitation will provide the potential to crystallize the intermediates selectively and controlled to the aimed structures. This thesis represents a first step towards this aim.

Another area for intensive work will be the understanding of metastable states occurring during mechanosynthesis. Reactions take place under non-equilibrium conditions and are therefore difficult to access. Different *in situ* techniques might provide insights into the complex mechanisms induced by pressure and mechanical stress. Especially the stabilization of the occurring metastable phases by defects and impurities will be body of research for future work. Understanding the role of the present non-equilibrium phases will be the key for designing solid bodies with tailored properties.

A further outlook is provided by the fact that the investigated crystalline and amorphous phosphate hydrates revealed a different degree of hydration depending on the respective cation. Systematic doping of the 3d metal phosphate hydrates with other cations (by precipitation experiments or by mechanosynthesis) will help to understand the influence of cations/impurities with different abilities of hydration on crystal structures, the formation of amorphous precursor phases, and inhibition of recrystallization. The doping of hopeite with Fe during ball milling presented in this thesis displays first results on this topic.

13

SUPPORTING INFORMATION

Instrumental Details

Analytical Ultracentrifugation. AUC Measurements were performed on an Optima XL-I analytical ultracentrifuge (Beckman-Coulter, Palo Alto, CA, United States) using Rayleigh interference optics in 12 mm double-sector titanium centerpieces (Nanolytics, Potsdam, Germany). Samples were investigated at 25 °C and 60,000 rpm, corresponding to a centrifugal force as high as 280,000 g, for 8 h experiment duration.

Measurements were carried out by Rose Rosenberg (group of Prof. Dr. Cölfen). No quantifiable signals were achieved.

Atomic Absorption Spectroscopy. AAS was measured using a Perkin Elmer atomic absorption spectrometer equipped with the S100 ZL with Zeeman Furnace Module. $CoCl_2$ (1.000±0.002 g, Merck) and $ZnCl_2$ (1.000±0.002 g, Merck) were standards for calibration.

Data were collected by Dr. Mihail Mondeshki. Interpretation and presentation of the results were performed on my own.

Attenuated Total Reflection-Fourier Transformed Infrared Spectroscopy. ATR-FTIR spectra were measured with a Bruker Alpha-P FT-IR spectrometer or a Nicolet™ iS™10 FT-IR spectrometer from Thermo scientific with platinum ATR. The spectra were recorded 64 times with a resolution of 4 cm^{-1}. For measuring intervals <1 min, spectra were recorded 16 times.

All measurements were carried out independently. Analysis of data, interpretation, and presentation were performed by myself.

Density measurements. The density of the amorphous sample was determined by AccuPyc 1330 He pycnometer (Micrometrics GmbH). The measuring volume of 100 cm^3 was

decreased to 50 cm^3 by a stainless steel calibration sphere. We measured the sample 25 times in order to get a low standard deviation.

Density measurements were recorded by Markus Schedel at the Technical University of Darmstadt (service measurements). Interpretation of data were performed by myself.

Dynamic Light Scattering. A Microtrac NANO-flex was used to measure dynamic light scattering in the backscattering mode (180° heterodyne DLS). For this purpose, a 5 mW laser was used at 780 nm. Signals were evaluated with the software Microtrac FLEX 11.0.0.2.

Measurements were performed by myself at the Fraunhofer ICT IMM under the supervision of Dr. Christoph Bantz. Data were evaluated by Dr. Christoph Bantz – no quantifiable signals were achieved.

Electron parametric resonance spectroscopy. EPR spectra were recorded on a Miniscope MS 300 X-band CW spectrometer (Magnettech GmbH, Germany). Values of *g* are referenced against Mn^{2+} in ZnS as external standard (*g*=2.118, 2.066, 2.027, 1.986, 1.946).

EPR spectra were recorded by Christoph Kreitner. Interpretation and presentation of the results were performed by myself.

Inductively Coupled Plasma Mass Spectrometry. For ICP-MS measurements, a precisely weighed amount of sample was solubilized with 5 mL sub-boiled conc. HNO_3 in a Teflon vessel by a microwave digestion. The digestion solution was filled up to 100 mL with deionized water and subsequently diluted with 3.3% HNO_3 1 to 1000. Blanc values for 5 mL conc. HNO_3 filled up to 100 mL with deionized water were subtracted. The measurements were performed on an ICP-sector field-MS device – Thermo element 2 (Thermo Scientific, Bremen, Germany) (medium resolution R=4500). The sample was conducted to the ICP-SF-MS by a PFA nebulizer (gas flow: 1.22 L min^{-1}, cooling gas: 16 L min^{-1}) through a Peltier-cooled PFA-cyclone-spray chamber PC^3 (4 °C) (Elemental Scientific Inc., Omaha, NE, USA). The sample were analyzed ten times for 70 s with a dwell time of 10 s. Quantification was performed with external calibration (standard solutions prepared with 3.3% HNO_3).

Inductively Coupled Plasma Optical Emission Spectroscopy. ICP-OES was performed using a PerkinElmer Optima 8300 (power 1300 W). Therefore, the same diluted solutions were used as for the ICP-MS measurements. Samples were conducted to the ICP-OES by a MiraMist nebulizer (Burgener Canada) (gas flow: 0.55 L min^{-1}, auxiliary gas flow: 0.2 L min^{-1}). Samples were ionized trough a plasma flow of 13 L min^{-1}. It was measured at wavelengths of 206.200 (Zn), 228.616 (Co), and 178.223 nm (P), each time for 10 s.

ICP-MS and ICP-OES measurements were performed by Dr. Björn Meermann at the Federal Institute of Hydrology. Analysis of data as well as their interpretation and presentation were performed independently.

Mössbauer Spectroscopy. Mössbauer spectra were obtained at room temperature with a constant acceleration transmission Mössbauer spectrometer and a ^{57}Co (Rh) source. An α-Fe foil was used to calibrate the Mössbauer spectrometer in a velocity range of ±10 mms^{-1}.

Mössbauer spectra were recorded and analyzed by Sergii Shylin under supervision of Dr. Vadim Ksenofontov. Interpretation and presentation of data were performed by myself.

Optical Spectroscopy. UV-Vis spectra were recorded with a Cary 5 G UV-Vis-NIR spectrophotometer equipped with an Ulbricht sphere. The solid phosphates were fixed with a scotch tape and the diffuse reflectance of the samples was measured in the range of 400 to 800 nm with a scan rate of 1 nm/s. The spectra were corrected by subtraction of the scotch tape background.

All spectra were recorded on my own. Analysis, interpretation, and presentation of data were performed independently.

Raman Spectroscopy. Raman spectra were recorded with a Horiba Jobin Yvon spectrophotometer equipped with a Nd:YAG laser for the region between 150 and 1500 cm^{-1}. The scan rate was 2700 cm^{-1} min^{-1}.

All measurements were performed by myself, also analysis of data, their interpretation, and presentation.

Scanning Electron Microscopy. SEM analysis was performed with a Zeiss Gemini Supra 40 microscope. The acceleration voltage was chosen to be between 15 kV and 30 kV, the working distance was 2.8 mm. Samples were sputtered with carbon or silver. Samples were fixed on an aluminum stub by using adhesive carbon tape. Energy dispersive X-ray (EDX) spectra were recorded by a Bruker QUANTAX 400 X-ray spectrometer.

Electron micrographs and EDX spectra were recorded at the Federal Institute for Materials Research and Testing in Berlin as service measurements. Interpretation of data and their presentation were performed independently.

Scanning Transmission Electron Microscopy. Electron micrographs were collected using a Tecnai F30 in the STEM mode. The acceleration voltage was set to 120 kV. The Tecnai F30 was equipped with a LaB_6 cathode. Samples for STEM were prepared by dispersing

samples in reagent-grade ethanol. Samples were prepared on a carbon-coated copper grid and vacuum-dried at room temperature.

Electron micrographs were collected by Dr. Tatiana Gorelik. Analysis, interpretation, and presentation of results were performed independently.

Small-Angle X-ray Scattering. SAXS measurements were performed with a SAXSess device of Anton Paar using monochromated CuKα radiation and a CCD camera (SCX-TE: 4300K/2; Pixel size: 24×24 μm^2). Samples were dispersed in water-free ethanol and treated with a sonication probe (Diameter 7 mm, max. amplitude 175 μm, acoustic power density 300 W/cm^2) for 15 min.

SAXS curves were recorded at the Federal Institute for Materials Research and Testing in Berlin by Dr. Ralf Bienert. He also analyzed and interpreted the data. Presentation of results was performed by myself.

Solid State-Nuclear Magnetic Resonance spectroscopy. NMR spectra were recorded on a Bruker Advance DSX 400 MHz NMR spectrometer with B_0 field corresponding to ^1H resonance frequency of 399.87 MHz. A commercial 3 channel 4 mm Bruker probe head was used at 10 kHz magic angle spinning (MAS) for the solid samples. A 30° 4 μs pulse averaging 128 scans with 20 s recycle delay and a two pulse phase modulation (TPPM) heteronuclear decoupling scheme were used for all ^{31}P experiments. All ^{31}P spectra were referenced to external $NH_4H_2PO_4$ at 0.9 ppm as a secondary shift reference.

All SS-NMR spectra (except spectra of Chapter 3) were recorded and analyzed by Dr. Mihail Mondeshki. Interpretation and presentation of results were performed independently. The SS-NMR spectra of Chapter 3 were measured by Vinicius Celinski under supervision of Prof. Dr. Jörn Schmedt auf der Günne (see also there for experimental details). He also performed analysis, interpretation, and presentation of the results.

Superconducting quantum interference device magnetometry. The magnetic measurements were done with a Quantum Design MPMS-XL SQUID magnetometer. The grinded powder was pressed in a plastic capsule, which was fixed in a straw. Measurements of possible hysteresis curves were performed from -50 kOe to 50 kOe at 5 K by cooling with liquid He and at 300 K.

Data were collected by Kristina Wichmann. Analysis, interpretation, and presentation of the results were performed independently.

Thermal analysis. DTA and TGA were carried analysis were carried out on a Netzsch STA 449 F3 Jupiter. Samples were deposited in an ALOX crucible and heated from 20 to 800 °C under argon with a heating rates of 1 K min^{-1} to 10 K min^{-1} and a flow rate of 10 mL min^{-1}.

All measurements were carried out by my own. Analysis, interpretation, and presentation of results were also performed by myself.

Transmission Electron Microscopy. TEM analysis was carried out on a Philips EM-420 microscope (acceleration voltage 120 kV) equipped with a LaB_6 cathode. Samples for TEM snapshots were prepared by taking aliquots of samples directly from solution or by dispersing samples in reagent-grade ethanol. Samples were prepared on a carbon-coated copper grid and vacuum-dried at room temperature.

All electron micrographs were recorded by myself. Further, their interpretation and presentation were performed independently.

In addition, a setup with an *in situ*-liquid cell TEM flow holder was used. Measurements were done on a TEM 2011 FS with between two SiN chips in distance of 5 μm, which are mounted in a crossed geometry.

Measurements were performed by Dr. Teresa Roncal-Herrero at the University of York. Analysis, interpretation, and presentation of results were done independently.

Viscosity Measurements. Viscosity of samples was determined by a Couette viscometer. The number of revolutions was varied in the range of 100–175 min^{-1}.

Measurements as well as interpretation and presentation of data were performed by myself.

X-ray absorption spectroscopy. XANES and EXAFS measurements were performed at the BAM*line* (BESSY-II) at the Co-K edge (7709 eV) in transmission, according to the sketch below (Figure 13.1).

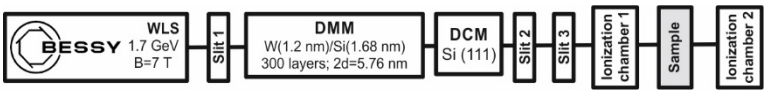

Figure 13.1. Schematics of the experiments for XANES/EXAFS in transmission.

All samples were measured four times and merged in μ(E) to increase signal to noise ratio. For data analysis and evaluation, the open source software packages Athena and Artemis

based on IFEFFIT were used.[i] For background subtraction the Rbkg value was set to 1.0. All spectra were normalized to the post-edge region, free from absorption features. A Hanning-type Fourier window for forward Fourier transform was set to the *k*-range between 1–7.5 $Å^{-1}$ with a dk value of 1.0. Furthermore, a crystal identification file (CIF) from $Co_3(PO_4)_2 \times 8\ H_2O$ was used for simulation, using FEFF, under Artemis, as a comparison basis and fitted to the experimental EXAFS spectra.

Measurement and analysis of data were performed by Dr. Ana Buzanich. Interpretation and presentation of the results were carried out by myself.

X-ray Diffraction. XRD measurements of crystalline and amorphous samples of zinc phosphate were conducted with a Bruker AXS D8 Discover equipped with a Highstar Detector and using monochromated CuKα (1.54 Å) radiation. Each sample was analyzed for 8 h. Samples containing iron, cobalt, nickel, or copper were measured with a Stoe Stadi-P diffractometer in Debye-Scherrer geometry and operating with MoKα radiation (0.709 Å). Each sample was analyzed for 13 h.

A XRD pattern of MeOH-ACP was collected in a fused capillary. Hydr-MeOH-ACP stored for 2 weeks under air was measured as well. Both XRD measurements were performed at synchrotron beamline BESSY II (λ=1.010 Å). The distance between sample and detector was set to be 206.59 mm. Each sample was analyzed for 300 s.

XRD measurements at the Bruker AXS D8 Discover were carried out by Regine Jung-Pothmann, measurements at the Stoe Stadi-P diffractometer by Christine Stefani (Max Planck Institute for Solid State Research in Stuttgart). Synchrotron measurements at BESSY II were performed in cooperation with Dr. Franziska Emmerling (service measurement). Analysis, interpretation, and presentation of data were performed by myself.

High-resolution XRD. HR-XRD synchrotron powder diffraction data were collected using beamline 11-BM at the Advanced Photon Source (APS), Argonne National Laboratory, using an average wavelength of 0.414 Å. Discrete detectors covering an angular range from -6 to 16° 2Θ were scanned over a 34° 2Θ range, with data points collected every 0.001° 2Θ and scan speed of 0.01 °/s.

The 11-BM instrument uses X-ray optics with two platinum-striped mirrors and a double-crystal Si(111) monochromator, where the second crystal has an adjustable sagittal bend.[351] Ion chambers monitor incident flux. A vertical Huber 480 goniometer, equipped with a Heidenhain encoder, positions an analyzer system comprised of 12 perfect Si(111) analyzers

and 12 Oxford-Danfysik $LaCl_3$ scintillators, with a spacing of 2° 2Θ.[352] Analyzer orientation can be adjusted individually on two axes. A three-axes translation stage holds the sample mounting and allows it to be spun, typically at ~5400 rpm (90 Hz). A Mitsubishi robotic arm is used to mount and dismount samples on the diffractometer. An Oxford Cryosystem Cryo-stream Plus device allows sample temperatures to be controlled over the range 80–500 K when the robot is used.

The diffractometer was controlled via EPICS.[353] Data were collected while continually scanning the diffractometer 2Θ arm. A mixture of NIST standard reference materials Si (SRM 640c) and Al_2O_3 (SRM 676) is used to calibrate the instrument, where the Si lattice constant determines the wavelength for each detector. Corrections are applied for detector sensitivity, 2Θ offset, small differences in wavelength between detectors, and the source intensity, as noted by the ion chamber before merging the data into a single set of intensities evenly spaced in 2Θ.

Samples were sent to the 11-BM synchrotron via mail-in service and measured there. Analysis of data was performed independently as well as interpretation and presentation.

Quantitative analysis of the XRD pattern (generated at the 11-BM synchrotron beamline) of cobalt phosphate octahydrate after different milling durations in a planetary ball mill were performed by Dr. Martin Panthöfer using the PONKCS approach[312] (see Chapter 10).

In situ high pressure diffraction measurements were performed at beamline 17-BM at the Advanced Photon Source at Argonne National Laboratory in cooperation with Prof. Dr. Cora Lind-Kovacs. For experimental details see Chapter 10. She analyzed and interpreted the data, presentation of results was performed on my own.

Additional Declaration

All syntheses, all crystallization experiments, and all titrations presented in this thesis were performed by myself.

All parts of the thesis were written on my own except the NMR part of Chapter 3 as this was a cooperation with Prof. Dr. Jörn Schmedt auf der Günne. Chapter 3 contains an adapted reproduction of *Journal of the American Chemical Society* **2015**, *136*, 2285–2294[105] reproduced with permission of the American Chemical Society Copyright 2015. I was the main author writing the manuscript.

The general idea for the isolation of amorphous zinc and cobalt phosphate hydrate from solution (see Chapter 3 and 4) was developed during my diploma thesis. No data recorded

during my diploma studies were used in this thesis except TEM and SEM images of AZP and ACP.

I did not use any unnamed sources or aid.

14

BIBLIOGRAPHY

[1] De Yoreo, J. J.; Vekilov, P. G. *Rev. Mineral. Geochem.* **2003**, *54*, 57–93.

[2] Ehrenfest, P. *Z. Physik.* **1927**, *45*, 455–457.

[3] Rie, E. *Z. Phys. Chem.* **1923**, *104*, 354–362.

[4] Arrhenius, S. A. *Z. Physik. Chem.* **1889**, *4*, 96–116.

[5] LaMer, V. K.; Dinegar, R. H. *J. Am. Chem. Soc.* **1950**, *72*, 4847–4854.

[6] Ostwald, W. *Z. Phys. Chem.* **1897**, *22*, 289–330.

[7] Gebauer, D.; Völkel, A.; Cölfen, H. *Science* **2008**, *322*, 1819–1822.

[8] Posner, A. S.; Betts, F. *Acc. Chem. Res.* **1975**, *8*, 273–281.

[9] Lentz, C. W. *Inorg. Chem.* **1964**, *3*, 574–579.

[10] Harris, R. K.; Knight, C. T. G.; Hull, W. E. *J. Am. Chem. Soc.* **1981**, *103*, 1577–1578.

[11] Bass, J. L.; Turner, G. L. *J. Phys. Chem. B* **1997**, *101*, 10638–10644.

[12] Cornell, R. M.; Giovanoli R.; Schneider W. *J. Chem. Technol. Biotechnol.* **2007**, *46*, 115–134.

[13] Flynn, C. M. *Chem. Rev.* **1984**, *84*, 31–41.

[14] Murray, K. S. *Coordin. Chem. Rev.* **1974**, *12*, 1–35.

[15] Beecher, A. N.; Yang, X.; Palmer, J. H.; LaGrassa, A. L.; Juhas, P.; Billinge, S. J. L.; Owen, J. S. *J. Am. Chem. Soc.* **2014**, *136*, 10645–10653.

[16] Keggin. J. F. *Proc. Roy. Soc., A* **1934**, *144*, 75–100.

[17] Le Chatelier, H.; Boudouard, O. *Bull. Soc. Chim. Fr.* **1898**, *19*, 483–488.

[18] Gebauer, D.; Kellermeier, M.; Gale, J. D.; Bergstöm, L.; Cölfen, H. *Chem. Soc. Rev.* **2014**, *43*, 2348–2371.

[19] Demichelis, R.; Raiteri, P.; Gale, J. D.; Quigley, D.; Gebauer, D. *Nat. Commun.* **2011**, *2*, 590–598.

[20] Vekilov, P. G. *Cryst. Growth Des.* **2004**, *4*, 671–685.

[21] Leunissen, M. E.; Christova, C. G.; Hynninen, A. –P.; Royall, C. P.; Campbell, A. I.; Imhof, A.; Dijkstra, M.; van Roij, R.; van Blaaderen, A. *Nature* **2005**, *437*, 235–240.

[22] Garetz, B.; Matic, J.; Myerson, A. S. *Phys. Rev. Lett.* **2002**, *89*, 175501–175504.

[23] Vekilov, P. G. *Nanoscale* **2010**, *2*, 2346–2357.

[24] Bewernitz, M. A.; Gebauer, D.; Long, J.; Cölfen, H.; Gower, L. B. *Faraday Discuss.* **2012**, *159*, 291–312.

[25] Gower, L. B.; Odom, D. J. *J. Cryst. Growth* **2000**, *210*, 719–734.

[26] Gower, L. A.; Tirrell, D. A. *J. Cryst. Growth* **1998**, *191*, 153–160.

[27] Wolf, S. E.; Mueller, L.; Barrea, R.; Kampf, C. J.; Leiterer, J.; Panne, U.; Hoffmann, T.; Emmerling, F.; Tremel, W. *Nanoscale* **2011**, *3*, 1158–1165.

[28] Lewis, A. E.; Mangere, M. *Chem. Eng. Technol.* **2011**, *34*, 517−524.

[29] Gower, L. B. *Chem. Rev.* **2008**, *108*, 4551–4627.

[30] Aizenberg, J.; Weiner, S; Addadi, L. *Connect. Tissue Res.* **2003**, *44*, 20–25.

[31] Briones, M. J. I.; López, E.; Méndez, J.; Rodríguez, J. B.; Gago-Duport, L. *Mineral. Mag.* **2008**, *72*, 227–231.

[32] Lee, M. R.; Hodson, M. E.; Langworthy, G. N. *Mineral. Mag.* **2008**, *72*, 257–261.

[33] Raz, S.; Testeniere, O.; Hecker, A.; Weiner, S.; Luquet, G. *Biol. Bull.* **2002**, *203*, 269–274.

[34] Ziegler, A. *J. Struct. Biol.* **1994**, *11*, 110–116.

[35] Wilt, F. H. *Zool. Sci.* **2002**, *19*, 253–261.

[36] Addadi, L.; Raz, S., Weiner, S. *Adv Mater* **2003**, *15*, 959–970.

[37] Dorvee, J. R.; Veis, A. *J. Struct. Biol.* **2013**, *183*, 278–303.

[38] Smith, J.; Hamilton, R.; McCulloch, I.; Stingelin.Stutzmann, N.; Heeney, M.; Bradley, D. D. C.; Anthopoulos, T. D. *J. Mater. Chem.* **2010**, *20*, 2562–2574.

[39] Wulff, G. *Z. Krystallogr.* **1901**, *20*, 449–530.

[40] Gregor, H. P.; Luttinger, L. B.; Loebl, E. M. *J. Phys. Chem.* **1955**, *59*, 990−991.

[41] Frank, F. C.; van der Merwe, J. H. *Proc. R. Soc.* **1949**, *198*, 205–216.

[42] Volmer, M.; Weber, A. *Z. phys. Chem.* **1926**, *119*, 277–301.

[43] Pina, C. M.; Becker, U.; Risthaus, P.; Bosbach, D.; Putnis, A. *Nature* **1998**, *395*, 483–486.

[44] Penn, R. L.; Banfield, J. F. *Science* **1998**, *281*, 969–971.

[45] Cölfen, H.; Mann, S. *Angew. Chem. Int. Ed.* **2003**, *42*, 2350–2365.

[46] Cölfen, H.; Antonietti, M. *Mesocrystals and Non-Classical Crystallization*; Wiley-VCH: Weinheim, Germany, 2008.

[47] Cölfen, H.; Yu, S. H. *MRS Bulletin* **2005**, *30*, 727–735.

[48] Pacholski, C.; Kornowski, A.; Weller, H. *Angew. Chem. Int. Ed.* **2002**, *41*, 1188–1191.

[49] Zitoun, D.; Pinna, N.; Frolet, N.; Belin, C. *J. Am. Chem. Soc.* **2005**, *127*, 15034–15035.

[50] Penn, R. L.; Banfield, J. F. *Geochim. Cosmochim. Acta* **1999**, *63*, 1549–1557.

[51] Li, S. Q.; Wu, C. Y.; Sassa, K.; Asai, S. Mater. Sci. Eng., A 2006, 422, 227–231.

[52] Tian, Z. R.; Liu, J.; Voigt, J. A.; Mckenzie, B.; Xu, H. Angew. Chem. Int. Ed. 2003, 42, 413–417.

[53] Addadi, L.; Joester, D.; Nudelman, F.; Weiner, S. Chem. Eur. J. 2006, 12, 981–987.

[54] Oaki, Y.; Kotachi, A.; Miura, T.; Imai, H. *Adv. Funct. Mater.* **2006**, *6*, 612–615.

[55] Cuif, J. P. Dauphin, Y. *Biogeosciences* **2005**, *2*, 61–73.

[56] Kulak, A. N.M; Iddon, P.; Li, Y.; Armes, S. P.; Cölfen, H.; Paris, O.; Wilson, R. M.; Meldrum, F. C. *J. Am. Chem. Soc.* **2007**, *129*, 3729–3736.

[57] Nassif, N.; Pinna, N.; Gehrke, N.; Antonietti, M.; Jäger, C.; Cölfen, H. *Proc. Nat. Acad. Sci. USA* **2005**, *102*, 12653–12655.

[58] Cölfen, H.; Antonietti, M. *Angew. Chem., Int. Ed.* **2005**, *44*, 5576–5591.

[59] Liu, Y.; Wang, S.; Tao, D.; Dai, Y.; Yu, J. *Materials Characterization* **2015**, *107*, 189–196.

[60] Rui, X.; Li, C.; Liu, J.; Cheng, T.; Chen, C. *Electrochim. Acta* **2010**, *55*, 6761–6767.

[61] Rui, X.; Yesibolati, N.; Chen, C. *J. Power Sources* **2011**, *196*, 7715–7720.

[62] Rui, X.; Ding, N.; Liu, J.; Li, C.; Chen, C. *Electrochim. Acta* **2010**, *55*, 2384–2390.

[63] Yin, S.-C.; Grondney, H.; Strobel, P.; Anne, M.; Nazar, L. *J. Am. Chem. Soc.* **2003**, *125*, 10402–10411.

[64] Chen, X.-B.; Zhou, X.; Abbott, T. B.; Easton, M. A.; Birbilis, N. *Surf. Coat. Technol.* **2013**, *217*, 147–155.

[65] Han, E. H.; Zhou, W. Q.; Shan, D. Y.; Ke, W. *Mater. Sci. Forum* **2003**, *419–422*, 879–882.

[66] Zhou, W. Q.; Tang, W.; Zhao, Q.; Wu, S. W.; Han, E. H. *Mater. Sci. Forum* **2011**, *686*, 176–180.

[67] Cui, X.-J.; Zhou, J.-X.; Lin, X.-Z.; Luo, H.; Gong, M. *Chin. J. Nonferrous Met.* **2012**, *22*, 15–21.

[68] Bhaumik, A. *Proc. Indian Acad. Sci.* **2002**, *114*, 451–460.

[69] Yu, J. C.; Zhang, L. Z.; Zheng, Z.; Zhao, J. C. *Chem. Mater* **2003**, *15*, 2280–2286.

[70] Mahendra, P. K.; Inagaki, S.; Yoshida, H. *J. Phys Chem B* **2005**, *109*, 9231–9238.

[71] Lu, M.; Wang, F.; Liao, Q.; Chen, K.; Qin, J.; Pan, S. *J. Mol. Struct.* **2015**, *1081*, 187–192.

[72] Bingham, P. A.; Hand, R. J.; Forder, S. D. *Mater Res. Bull.* **2006**, *41*, 1622–1630.

[73] Karabulut, M.; Yuce, B.; Bozdogan, O.; Ertap, H.; Mammadov, G. M. *J. Non-Cryst. Solids* **2011**, *357*, 1455–1462.

[74] Moguš-Milanković, A.; Pavić, L.; Ertap, H.; Karabulut, M. *J. Am. Ceram. Soc.* **2012**, *95*, 2007–2014.

[75] Gier, T. E.; Stucky, G. D. *Nature* **1991**, *349*, 508–510.

[76] Gier, T. E.; Bu, X.; Feng, P.; Stucky, G. D. *Nature* **1998**, *359*, 154–157.

[77] Feng, P.; Bu, X.; Stucky, G. D. *Angew. Chem. Int. Ed.* **1995**, *34*, 1745–1747.

[78] Bu, X.; Gier, T. E.; Stucky, G. D. *Microporous Mesoporous Mater.* **1998**, *26*, 61–66.

[79] Durif, A. *Crystal Chemistry of Condensed Phosphates*, Springer Science + Business Media, New York 1995.

[80] Glaum, R. Neue Untersuchungen an wasserfreien Phosphaten der Übergangsmetalle. Postdoctoral thesis, Liebig University Giessen, 1999.

[81] Wang, L.; Nancollas, G. H. *Chem. Rev.* **2008**, *108*, 4628–4669.

[82] Driessens, F. C. M.; van Dijk, J. W. E.; Borggreven, J. M. P. M. *Calcif. Tiss.* **1978**, *26*, 127–137.

[83] Weiner, S.; Traub; W.; Wagner, H. D. *J. Struct. Biol.* **1999**, *126*, 241–255.

[84] Olszta, M. J.; Cheng, X.; Jee, S. S.; Kumar, R.; Kim, J. J., Kaufmane, M. J.; Douglas, E. P.; Gower, L. B. *Mater. Sci. Eng. R* **2007**, *58*, 77–116.

[85] Cai, Y.; Tang, R. *J. Mater Chem.* **2008**, *18*, 3375–3787.

[86] Kirkham, J.; Brookes, S. J.; Shore, R. C.; Wood, S. R.; Smith, D. A.; Zhang, J.; Chen, H. F. ; Robinson, C. *Curr. Opin. Colloid Interface Sci.* **2002**, *7*, 124–132.

[87] Daculsi, G.; Mentanteau, J.; Kerebel, L. M.; Mitre, D. *Calcif. Tissue Int.* **1984**, *36*, 550–555.

[88] Boskey, A. L.; Posner, A. S. *J. Phys. Chem.* **1973**, *77*, 2313–2317.

[89] Eanes, E. D.; Posner, A. S. *Mater. Res. Bull.* **1974**, *9*, 907–916.

[90] Johnsson M. S.; Nancollas G. H. *Crit. Rev. Oral. Biol. Med.* **1992**, *3*, 61–82.

[91] Tsortos, A.; Nancollas, G. H. *J. Colloid. Interface Sci.* **2002**, *250*, 159–167.

[92] Rey, C.; Combes, C.; Drouet, C.; Glimcher, M. *Osteoporos. Int.* **2009**, *20*, 1013–1021.

[93] Dorozhkin, S. V.; Epple, M. *Angew. Chem. Int. Ed. Engl.* **2002**, *41*, 3130–3146.

[94] Treboux, G.; Layrolle, P.; Kanzaki, N.; Onuma, K.; Ito, A. *J. Phys. Chem.* **2000**, *104*, 5111–5114.

[95] Termine, J. D.; Posner, A. S. *Arch. Biochem. Biophys.* **1970**, *140*, 307–317.

[96] Kabybya, S.; Gal, A.; Kahil, K.; Weiner, S.; Addadi, L.; Schmidt, A. *J. Am. Chem. Soc.* **2015**, *137*, 990–998.

[97] Akiva-Tal, A.; Kababya, S.; Balazs, Y. S.; Glazer, L.; Berman, A.; Sagi, A.; Schmidt, A. *Proc. Natl. Acad. Sci. U. S. A.* **2011**, *108*, 14763−14768.

[98] Beniash, E.; Addadi, L.; Weiner, S. *J. Struct. Biol.* **1999**, *125*, 50−62.

[99] Ramirez, A. P. *Nature* **2003**, *421*, 483.

[100] Kohn, M. *Anal. Chim. Acta* **1953**, *9*, 226–228.

[101] Heinecke, G. *Tribochemistry*. Akademie-Verlag: Berlin, 1984.

[102] Friščić, T.; Halasz, I.; Beldon, P. J.; Belenguer, A. M.; Adams, F.; Kimber, S. A. J.; Honkimäki, V.; Dinnebier, R. E. *Nat. Chem.* **2013**, *5*, 66–73.

[103] Halasz, I.; Kimber, S. A. J.; Beldon, P. J.; Belenguer, A. M.; Adams, F.; Honkimäki, V.; Nightingale, R. C.; Dinnebier, R. E.; Friščić, T. *Nat. Protocols* **2013**, *8*, 1718–1729.

[104] Batzdorf, L.; Fischer, F.; Wilke, M.; Wenzel, K. J.; Emmerling, F. *Angew. Chem. Int. Ed.* **2015**, *54*, 1799–1802.

[105] Bach, S.; Celinski, V. R.; Dietzsch, M.; Panthöfer, M.; Bienert, R.; Emmerling, F.; Schmedt auf der Günne, J.; Tremel, W. *J. Am. Chem. Soc.* **2015**, *136*, 2285–2294.

[106] Dey, A.; Bomans, P. H.; Müller, F. A.; Will, J.; Frederik, P. M.; de With, G.; Sommerdijk, N. A. *Nat. Mater.* **2010**, *9*, 1010–1014.

[107] van Driessche, A. E. S.; Benning, L. G.; Rodriguez-Blanco, J. D.; Ossorio, M.; Bots, P.; Garcia-Ruiz, J. M. *Science* **2012**, *336,* 69–72.

[108] Weiss, H.; Bräu, M. F. *Angew. Chem. Int. Ed.* **2009**, *48*, 3520–3524.

[109] *Kristallisation in der industriellen Praxis*; Hofmann, G.; Wiley-VCH: Weinheim, Germany, 2004.

[110] Arnaud, Y.; Sahakian, E.; Romand, M.; Charbonnier, J. C. *Appl. Surf. Sci.* **1988**, *32*, 281–295.

[111] Gardner, P. J.; McArn, I. W.; Bartob, V.; Seydt, G. M. *Surf. Coat. Int.* **1990**, *74*, 16–17.

[112] Haussühl, S.; Middendorf, B.; Dörfel, M. *J. Solid State Chem.* **1991**, *93*, 9–16.

[113] Pawlig, O.; Trettin, R. *Mater. Res. Bull.* **1999**, *34*, 1959–1966.

[114] Del Amo, B.; Romagnoli, R.; Vetere, V. F.; Hernández, L. S. *Progr. Org. Coat.* **1998**, *33*, 28–35.

[115] Herschke, L.; Enkelmann, V.; Lieberwirth, I.; Wegner, G. *Chem. Eur. J.* **2004**, *10*, 2795–2803.

[116] Liebau, F. *Acta Crystallogr.* **1965**, *18*, 352-354.

[117] Calvo, C. *Can. J. Chem.* **1965**, *43*, 436-445.

[118] Whitaker, A. *Acta Crystallogr.* **1975**, *B31*, 2026-2035.

[119] Hill, R. J.; Jones, J. B. *Am. Mineral.* **1976**, *61*, 987-995.

[120] *NBS Monogr. (U.S.)* **1979**, *25* (16), 80.

[121] *NBS Monogr. (U.S.)* **1979**, *25* (16), 81.

[122] *NBS Monogr. (U.S.)* **1979**, *25* (16), 83.

[123] Yuan, A. -Q.; Wu, J.; Huang, Z. -Y.; Zhou, Z. -G.; Wen, Y. X.; Tong, Z. -F. *Chin. J. Chem.* **2007**, *25*, 857-862.

[124] Liu, W.; Liu, Y.; Shi, Z.; Pang, W. *J. Mater. Chem.* **2000**, *10*, 451-455.

[125] Cheetham, A. K.; Ferey, G.; Loiseau, T. *Angew. Chem., Int. Ed.* **1999**, *38*, 3268-3292.

[126] Oliver, S.; Kuperman, A.; Ozin, G. A. *Angew. Chem., Int. Ed.* **1998**, *37*, 46-62.

[127] Li, J.; Yu, J.; Yan, W.; Xu, Y.; Xu, W.; Qiu, S.; Xu, R. *Chem. Mater.* **1999**, *11*, 2600-2606.

[128] Bohlsen, F.; Kern, M. *Quintessence Int.* **2003**, *34*, 493-496.

[129] Squier, R. S.; Agar, J. R.; Duncan, J. P.; Taylor, T. D. *Int. J. Oral Maxillofac Implants* **2001**, *16*, 793-798.

[130] Milutinovic-Nikolic, A. D.; Medic, V. B.; Vukovic, Z. M. *Dental Mater.* **2007**, *23*, 674-678.

[131] Day, R. M.; Boccaccini, A. R. *J. Biomed. Mater., Res. A* **2005**, *73*, 73-79.

[132] Pawlig, O.; Trettin, R. *Chem. Mater.* **2000**, *12,* 1279-1287.

[133] Meyer, G. *Farbe Lack* **1963**, *69*, 528-532.

[134] Meyer, G. *Farbe Lack* **1965**, *71*, 113-119.

[135] Clay, M. F.; Cox, G. H. *J. Oil Colour Chem. Assoc.* **1973**, *56*, 13-16.

[136] Yoshihara, T.; Okita, H. *Trans. Iron Steel Inst. Jpn.* **1983**, *23*, 984-993.

[137] Adrian, G.; Bittner, A. *J. Coat. Technol.* **1986**, *58*, 59-65.

[138] Romagnoli, R.; Vetere, V. F. *Corrosion* **1995**, *51*, 216-223.

[139] Sankara Narayanan, T. S. N. *Rev. Adv. Mater. Sci.* **2005**, *9*, 130-177.

[140] Calvo, C. *J. Phys. Chem. Solids* **1963**, *24*, 141-149.

[141] Berkowitz, J. K.; Olsen, J. A. *J. Lumin.* **1991**, *50*, 111-115.

[142] Wang, J.; Wang, S.; Su, Q. *J. Mater. Chem.* **2004**, *14*, 2569-2574.

[143] Navrotsky, A.; Mazeina, L.; Majzlan, L. *Science* **2008**, *319*, 1635–1638.

[144] McHale, J. M.; Auroux, A.; Perrotta, A. J.; Navrotsky, A. *Science* **1997**, *277*, 788–791.

[145] Navrotsky, A. *Geochem. Trans.* **2003**, *4*, 34–37.

[146] Yuan, A. Q.; Liao, S.; Tong, Z. F.; Wu, J.; Huang, Z. Y. *Mater. Lett.* **2006**, *60*, 2110–2114.

[147] Smith, A. L. *J. Electrochem. Soc.* **1951**, *98*, 363–368.

[148] Roming, M.; Feldmann, C.; Avadhut, Y. S.; Schmedt auf der Günne, J. *Chem. Mater* **2008**, *20*, 5787–5795.

[149] Avadhut, Y. S.; Weber, J.; Hammarberg, E.; Feldmann, C.; Schellenberg, I.; Pöttgen, R.; Schmedt auf der Günne, J. *Chem. Mater.* **2011**, *23*, 1526–1538.

[150] Avadhut, Y. S.; Schneider, D.; Schmedt auf der Günne, J. *J. Magn. Reson.* **2009**, *201*, 1–6.

[151] Chan, J. C. C.; Eckert, H. J. *Chem. Phys.* **2001**, *115*, 6095–6105.

[152] Chan, J. C. C. *Chem. Phys. Lett.* **2001**, *335*, 289–297.

[153] Michel, F. M.; MacDonald, J.; Feng, J.; Phillips, B. L.; Ehm, L.; Tarabrella, C.; Parise, J. B.; Reeder, R. J. *Chem. Mater.* **2008**, *20*, 4720–4728.

[154] Wolf, G.; Gunther, C. *J. Therm. Anal. Calorim.* **2001**, *65*, 687–698

[155] Harris, R. K.; Becker, E. D.; Cabral de Menezes, S. M.; Granger, P.; Hoffman, R. E.; Zilm, K. W. *Pure Appl. Chem.* **2008**, *80*, 59–84.

[156] Herschke, L.; Rottstegge, J.; Lieberwirth, I.; Wegner, G. *J. Mater. Sci.: Mater. Med.* **2006**, *17*, 81–94.

[157] Faatz, M.; Gröhn, F.; Wegner, G. *Adv. Mater.* **2004**, *16*, 996–1000.

[158] Reichle, R. A.; McCurdy, K. G.; Hepler, L. G. *Can. J. Chem.* **1975**, *53*, 3841–3845.

[159] Herschke, L. Polymer controlled mineralization of zinc phosphate hydrates and applications in Corrosion Protection, Catalysis and Biomedicine. Ph.D. Thesis, Johannes Gutenberg University Mainz, June 2004.

[160] Wolf, S. E.; Leiterer, J.; Emmerling, F.; Tremel, W. *J. Am. Chem. Soc.* **2008**, *130*, 12342–12347.

[161] Cartwright, J. H. E.; Checa, A. G.; Gale, J. D.; Gebauer, G.; Sainz-Diaz, C. I. *Angew. Chem. Int. Ed.* **2012**, *51*, 11960–11970.

[162] Mangalam, G.; Das, S. J. *Arch. Phys. Res.* **2010**, *1*, 54–61.

[163] Schäfer, H. *Angew. Chem.* **1971**, *83*, 35–42.

[164] Navrotsky, A. *Proc. Natl. Acad. Sci. U.S.A.* **2004**, *101*, 12096–12101.

[165] MacKenzie, K. J. D.; Smith, M. E. *Multinuclear Solid-State Nuclear Magnetic Resonance of Inorganic Materials*; Elsevier Science, Ltd.: Oxford, U.K., 2002.

[166] Gullion, T.; Schaefer, J. *J. Magn. Reson.* **1989**, *81*, 196–200.

[167] Saalwächter, K.; Spiess, H. W. *J. Chem. Phys.* **2012**, *114*, 5707–5728.

[168] Haeberlen, U.; Waugh, J. S. *Phys. Rev.* **1968**, *175*, 453–467.

[169] Brouwer, E. B.; Gougeon, R. D. M.; Hirschinger, J.; Udachin, K. A.; Harris, R. K.; Ripmeester, J. A. *Phys. Chem. Chem. Phys.* **1999**, *1*, 4043–4050.

[170] Goetz, J. M.; Schaefer, J. *J. Magn. Reson.* **1997**, *127*, 147–154.

[171] Celinski, V. R.; Weber, J.; Schmedt auf der Günne, J. *Solid State Nucl. Magn. Reson.* **2013**, *49–50*, 12–22.

[172] Schmedt auf der Günne, J. *J. Magn. Reson.* **2003**, *165*, 18–32.

[173] Van Vleck, J. H.; *Phys. Rev.* **1948**, *74*, 1168–1183.

[174] Brunner, E.; Sternberg, U. *Prog. Nucl. Magn. Reson. Spectrosc.* **1998**, *32*, 21–57.

[175] Pedersen, B. F.; Semmingsen, D. *Acta Crystallogr.* **1982**, *B38*, 1074–1077.

[176] Bacon, G. E.; Curry, N. A. *Proc. R. Soc. A* **1962**, *266*, 95–108.

[177] Mikuli, E.; Grad, B.; Medycki, W.; Hołderna-Natkaniec, K. *J. Solid State Chem.* **2004**, *177*, 3795–3804.

[178] Holcomb, D. F.; Pedersen, B. *J. Chem. Phys.* **1962**, *36*, 3270–3278.

[179] Pake, G. E. *J. Chem. Phys.* **1948**, *16*, 327–336.

[180] Migdał-Mikuli, A.; Mikuli, E.; Hetmańczyk, J.; Hetmańczyk Ł.; Hołderna-Natkaniec, K.; Natkaniec, I. *J. Alloys Compd.* **2009**, 469, 73–81.

[181] Mishima, O.; Stanley, E. *Nature* **1998**, *396*, 329–335.

[182] Smith, K. H.; Shero, E.; Chizmeshya, A.; Wolf, G. H. *J. Chem. Phys.* **1995**, *102*, 6851–6857.

[183] Poole, P. H.; Grande, T.; Sciortino, F.; Stanley, H. E.; Angell, C. A. *Comput. Mater. Sci.* **1995**, *4*, 373–382.

[184] Gnielinski, V.; Mersmann, A.; Thurner, F. *Verdampfung, Kristallisation, Trocknung*; Springer: Germany, 1993.

[185] Bach, S.; Panthöfer, M.; Bienert, R.; Buzanich, G.; Emmerling, F.; Tremel, W. *Cryst. Growth Des.* **2015**, submitted.

[186] Yakovenchuk, V. N.; Ivanyuk, G. Y.; Mikhailova, Y., A.; Selivanova, E. A.; Krivovichev, S. V. *Can Mineral* **2006**, *44*, 117–123.

[187] Lee, Y. H.; Clegg, J. K.; Lindoy, L. F.; Lu, G. Q. M.; Park, Y.-C.; Kim, Y. *Acta Crystallogr. Sect. E*, **2008**, *E64*, i67–i68.

[188] Anderson, J. B.; Kostiner, E.; Ruszala, F. A. *Inorg. Chem.*, **1976**, 15, 2744–2748.

[189] Badsar, M.; Edrissi, M. *Mater. Res. Bull.* **2010**, *45*, 1080–1084.

[190] Corbeil, M. C.; Charland, J. P.; Moffatt , E. A. *Stud. Conserv.* **2002**, *47*, 237–249.

[191] Kram, T.; El-Rassy, H.; Zaknoun, F.; Moussa, Z.; Sultan, R. *Chem. Phys. Lett.* **2012**, *525–526*, 54–59.

[192] Surendranath, Y.; Kanan, M. W.; Nocera, D. G. *J. Am. Chem. Soc.* **2010**, *132*, 16501–16509.

[193] Surendranath, Y.; Luttermann, D. A.; Liu, Y.; Nocera, D. G. *J. Am. Chem. Soc.* **2012**, *134*, 6326–6336.

[194] Li, Y.; Zhao, Y.; Zhang, Z. *Electrochem. Commun.* **2014**, *48*, 35–39.

[195] Ge, L.; Han, C.; Xiao, X.; Guo, L. *Appl. Catal., B.* **2013**, *142–143*, 414–422.

[196] Casadio, F.; Bezúr, A.; Fiedler, I.; Muir, K.; Trad, T.; Maccagnola, S. *J. Raman Spectrosc.* **2012**, *43*, 1761–1771.

[197] Binnewies, M.; Glaum, R.; Schmidt, M.; Schmidt, P. *Chemical Vapor Transport Reactions*, De Gruyter, Berlin, 2012.

[198] *Handbook of Chemistry and Physics*; CRS publisher: 2014.

[199] Alvarez, S. *Dalton Trans.* **2013**, *42*, 8617-8636.

[200] Lis, D.; Backus, E. H. G.; Hunger, J.; Parekh, S. H.; Bonn, M. *Science* **2014**, *344*, 1138–1142.

[201] Finlayson, B.; Hench, L. L.; Smith, L. H. *Urolithiasis: Physical Aspects*, Washington, 1972.

[202] Guillou, N.; Gao, Q.; Forster, P. M.; Chang, J. S.; Nogues, M.; Park, S. E.; Ferey, G.; Cheetham, A. K. *Angew. Chem., Int. Ed.* **2001**, *40*, 2831–2834

[203] Yu, J.; Wang, A.; Tan, J.; Li, X.; van Bokhoven, J. A.; Hu, Y. K. *J. Mater. Chem.* **2008**, *18*, 3601–3607.

[204] Yang, J.-H.; Tan, J.; Ma, D. *J. Power Sources* **2014**, *260*, 169–173.

[205] Tan, J.; Yang, J.-H.; Liu, X.; Yang, F.; Li, X.; Ma, D. *Electrochem. Commun.* **2013**, *27*, 141–143.

[206] Yang, J.; Tan, J.; Yang, F.; Li, X.; Liu, X.; Ma, D. *Electrochem. Commun.* **2012**, *23*, 13–16.

[207] Boericke, W.; Dewey, W. A. *The Twelve Tissue Remedies of Schüssler*, Philadelphia, F. E. Boericke, Hahnemann Pub. House 1988.

[208] Behbahani, F. K.; Yektanezhad, T.; Khorrami, A. R. *Heterocycles* **2010**, *81*, 2313–2321.

[209] Cao, F.; Li, D. X. *Bioinsp. Biomim.* **2010**, *5*, 16005–16010.

[210] Cai, R.; Du, Y. P.; Zhang, W. Y.; Tan, H. T.; Zeng, T.; Huang, X.; Yang, H. F.; Chen, C. P.; Liu, H.; Zhu, J. X.; Peng, S. J.; Chen, J.; Zhao, Y. L.; Wu, H. C.; Huang, Y. Z.; Xu, R.; Lim, T. M.; Zhang, Q. C.; Zhang, H.; Yan, Q. Y. *Chem. Eur. J.* **2013**, *19*, 1568–1572.

[211] Wang, B. F.; Qiu, Y. L.; Ni, S. Y. *Solid State Ion.* **2007**, *178*, 843–847.

[212] Vu, A.; Stein, A. *Journal of Power Sources* **2014**, *245*, 48–58.

[213] Shen, W.; Wang, Y.; Yan, J.; Wu, H.; Guo, S. *Electrochimica Acta* **2015**, *173*, 310–315.

[214] Heravi, M. M.; Behbahani, F. K. Zadsirjan, V. *Heterocycl. Commun.* **2006**, *12*, 369–372.

[215] Behbahani, F. K., Farahani, M. *Lett. Org. Chem.* **2011**, *8*, 431–435.

[216] Hajipour, A. R.; Karimi, H. *Chinese J. Catal.* **2014**, *35*, 1529–1533.

[217] Khemthong, P.; Daorattanachai, P.; Laosiripojana, N.; Faungnawakij, K. *Catal. Commun.* **2012**, *29*, 96–100.

[218] Doyle, R. P.; Kruger, P. E.; Moubaraki, B.; Murray, K. S.; Nieuwenhuyzen, M. *Dalton Trans.* **2003**, *22*, 4230–4237.

[219] Zhu, H.; Jin, L.; Cheng, D.; Zheng, Y. *Inorg. Chim. Acta* **2012**, *388*, 37–45.

[220] Wang, C.; Lii, K. *J. Solid State Chem.* **2013**, *197*, 456–459.

[221] ElBatal, H. A.; ElMandouh, Z. E.; Zayed, H. A.; Marzouk, S. Y.; Elkomy, G. M. *J. Mol. Struct.* **2013**, *1054–1055*, 57–64.

[222] Dorozhkin, S. V. *Acta Biomater.* **2012**, *6*, 4457–4475.

[223] Posner, A. S. *Arch Biochem Biophys.* **1968**, *124*, 604–615.

[224] Pauling, L. *The Nature of Chemical Bond*, Cornell University Press: Ithaca, U.S.A., 1960.

[225] Shannon, R. D. *Acta Cryst.* **1976**, *A32*, 751–767.

[226] Klockmann, F.; Ramdohr, P.; Strunz, H. *Klockmanns Lehrbuch der Mineralogie*, Enke: Stuttgart, 1978.

[227] Richens, D. T. *Chemistry of Aqua Ions*, Wiley, New York, 1997

[228] Addadi, L.; Weiner, S. *Angew. Chem. Int. Ed.* **1992**, *31*, 153–169.

[229] Welton, T. *Chem. Rev.* **1999**, *99*, 2071–2083.

[230] Dietzsch, M. Precipitation of $CaCO_3$, $MgCO_3$ and $Ca_{(1-x)}Mg_xCO_3$ in aqueous solution and ionic liquids. Ph.D. Dissertation, Johannes Gutenberg University of Mainz, 2014.

[231] Sawada, K. *Pure & Appl. Chem* **1987**, *69*, 921–928.

[232] Rodriguez-Blanco, J. D.; Shaw, S.; Benning, L. G. *Nanoscale* **2011**, *3*, 265–271.

[233] Morse, J. W.; Arvidson, R. S.; Lüttge, A. *Chem. Rev.* **2007**, *107*, 342–381.

[234] Weiner, S.; Sagi, I.; Addadi, L. *Science* **2005**, *309*, 1027–1028.

[235] Radha, A. V.; Forbes, T. Z.; Killian, C. E.; Gilbert, P.U.P.A.; Navrotsky, A. *Proc. Natl. Acad. Sci. USA* **2010**, *107*, 16438–16443.

[236] Lam, R. S. K.; Charnock, J. M.; Lennie, A.; Meldrum, F. C. *Cryst. Eng. Comm.* **2007**, *9*, 1226–1236.

[237] Bentov, S.; Weil, S.; Glazer, L.; Sagi, A.; Berman, A. *J. Struct. Biol.* **2010**, *171*, 207–215.

[238] Ihli, J.; Wong, W. C.; Noel, E. H.; Kim, Y.-Y.; Kulak, A. N.; Christenson, H. K.; Duer, M. J.; Meldrum, F. C. *Nat. Commun.* **2014**, *5*, 3169–3170.

[239] Graf, C.; Gao, Q.; Schütz, I.; Noufele, C. N.; Ruan, W.; Posselt, U.; Korotianskiy, E.; Nordmeyer, D.; Rancan, F.; Hadam, S.; Vogt, A.; Lademann, J.; Haucke, V. Rühl, E. *Langmuir* **2012**, *28*, 7598–7613.

[240] Stöber, W.; Fink, A. *J. Colloid Interface Sci.* **1968**, *26*, 62–69.

[241] Chang, C.-L.; Fogler, H. S. *AlChE J.* **1996**, *42*, 3153–3163.

[242] Brinker, C.; Scherer, W. *The Physics and Chemistry of Sol-Gel Processing*, Academic Press: San Diego, 1990.

[243] Hudgens, J. J.; Martin, S. W. *J. Am. Ceram. Soc.* **1993**, *76*, 1691–1696.

[244] Yang, H.; Zhuang, Y.; Hu, H.; Du, X.; Zhang, C.; Shi, X.; Wu, H.; Yang, S. *Adv. Funct. Mater.* **2010**, *20*, 1733–1741.

[245] Avrami, M. *J. Chem. Phys.* **1939**, *7*, 1103–1112.

[246] Avrami, M. *J. Chem. Phys.* **1940**, *8*, 212–224.

[247] Avrami, M. *J. Chem. Phys.* **1941**, *9*, 177–184.

[248] Johnson, W. A.; Mehl, R. F. *Trans. AIME* **1939**, *135*, 416–458.

[249] Bartz, M.; Küther, J.; Vaughan, G.B.M.; Seshadri, R.; Tremel, W. *J. Mater. Chem.* **2001**, *11*, 503–506.

[250] Demirbas, M. F. *Energ. Source Part B* **2006**, *1*, 85–95.

[251] Wu, S.; Zhu, D.; Zhang, X., Huang, J. *Energ. Fuel* **2010**, *24*, 1894–1898.

[252] Ma, H. B.; Wilson, C.; Borgmeyer, B. *Appl. Phys. Lett.* **2006**, *88*, 14116.

[253] Naphon, P.; Assadamongkol, P.; Borirak, T. *Int. Commun. Heat Mass* **2008**, *35*, 1316–1319.

[254] Xie, H.; Chen, L. *Phys. Lett. A* **2009**, *373*, 1861–1864.

[255] Vonarbourg, A.; Passirani, C.; Saulnier, P.; Benoit, J. P. *Biomater.* **2006**, *27*, 4356–4373.

[256] Singh, R.; Lillard, J. W. *Exp. Mol. Pathol.* **2009**, *86*, 215–223.

[257] Zhou, J.; Wu, Z.; Zhang, Z.; Liu, W.; Yue, Q. *Tribol. Lett.* **2000**, *8*, 213–218.

[258] Wang, X. Q.; Mujumdar, A. *S. Int. J. Therm. Sci.* **2007**, *46*, 1–19.

[259] Xie, H.; Yu, W.; Chen, W. *J. Exp. Nanosci.* **2010**, *5*, 463–472.

[260] Yu, W.; France, D. M.; Singh, D.; Timofeeva, E. V.; Smith, D. S. Routbort, J. L. *J. Nanosci. Nanotechnol.* **2010**, *10*, 4824–4849.

[261] Clever, H. L.; Drrick, M. E.; Johnson, S. A. *J. Phys. Chem. Ref. Data.* **1992**, *21*, 941–966.

[262] Henricks, J. A., *Phosphate Coating Compositions and Methods of Making and Using the Same*, United States Patent Office 1965, 3178319.

[263] Henricks, J. A., *Method of Providing Ferrous Articles with Phosphate Coatings and Compositions Therefor*, United States Patent Office 1961, 2975082.

[264] Ruschak, K. J.; Miller, C. A. *Ind. Eng. Chem. Fundam.* **1972**, *11*, 534–540.

[265] McCracken, J. R.; Daytner, A. *J. Appl. Polym. Sci.* **1974**, *18*, 3365–3372.

[266] Massart, R.; Contant, R.; Fruchart, J.-M.; Ciabrini, J.-P. *Inorg. Chem.* **1977**, *16*, 2916–2921.

[267] *NMR Spectroscopy, Basic principles. Concepts, and Applications in Chemistry*, Harald Günther, Wiley, 2013, 117–118.

[268] Labbez, C.; Jönsson, B.; Pochard, I.; Nonat, A.; Cabane, B. *J. Phys. Chem. B* **2006**, *110*, 9219–9230.

[269] Plassard, C.; Lesniewska, E.; Pochard, I.; Cabane, B. *Langmuir* **2004**, *21*, 6702–6709.

[270] Cole, J. L.; Lary, J. W.; Moody, T.; Laue, T. M. *Methods Cell Biol.* **2008**, *84*, 143–179.

[271] Ghirlando, R. *Methods* **2011**, *54*, 145–156.

[272] Hartmann, L.; Tremel, K.; Uttiya, S.; Crossland, E.; Ludwigs, S.; Kyunkid, N.; Vergnat, C.; Brinkmann, M. *Adv. Funct. Mater.* **2011,** *21*, 4047–4057.

[273] Phu, N. D.; Ngo, D. T.; Hoang, L. H; Luong, N. H.; Chau N.; Hai, N. H. *J. Phys. D: Appl. Phys.* **2011**, *44*, 345002.

[274] Granchini, G.; Marras, S.; Prato, M.; Giannini, C.; Quarti, C.; De Angelis, F.; De Bastini, M.; Eperon, G. E.; Snaith, H. J.; Manna, L.; Petrozza, A. *J. Phys. Chem. Lett.* **2014**, *5*, 3836–3842.

[275] Indra, A.; Menezes, P. W.; Sahraie, N. R.; Bergmann, A.; Das, C.; Tallarida, M.; Schmeißer, D.; Strasser, P.; Driess, M. *J. Am. Chem. Soc.* **2014**, *136*, 17530–17536.

[276] Kang, S.-H.; Goodenough, J. B.; Rabenberg, L. K. *Chem. Mater.* **2001**, *13* , 1758–1764.

[277] Ravnsbæk, D.; Filinchuk, Y.; Cerenius, Y.; Jakobsen, H. J.; Besenbacher, F.; Skibsted, J.; Jensen, T. R. *Angew. Chem. Int. Ed.* **2009**, *48*, 6659–6663.

[278] Huot, J.; Ravnsbæk, D.B.; Zhang, J.; Cuevas, F.; Latroche, M.; Jensen, T.R. *Progr. Mater. Sci.* **2013**, *58*, 30–75.

[279] Angell C. A. *Science* **1995**, *267*, 1924–1935.

[280] Ewing, R. C. *Proc. Natl. Acad. Sci. U.S.A.* **1999**, *96*, 3432–3439.

[281] Bai, X.-M.; Voter, A. F.; Hoagland, R. G.; Nastasi, M.; Uberuaga, B. P. *Science* **2010***, 327,* 1631–1634.

[282] Ackland, G. *Science* **2010**, 327, 1587–1588.

[283] Garg, N.; Panchal, V.; Tyagi, A. K.; Sharma, S. M. *J. Solid State Chem.* **2005**, *178*, 998–1002.

[284] Varga, T.; Wilkinson, A. P.; Lind, C.; Bassett, W. A.; Zha, C.-S. *Phys. Rev. B* **2005**, *71*, 214–106.

[285] Lock, N.; Christensen, M.; Kepert, C. J.; Iversen, B. B. *Chem.Commun.* **2013**, *49*, 789–791.

[286] Bennett, T. D.; Cheetham, A. K. *Acc. Chem. Res.* **2014**, *47*, 1555−1562.

[287] Coudert, F. X. *Chem. Mater.* **2015**, *27*, 1905−1916.

[288] Lind, C.; VanDerveer, D. G.; Wilkinson, A. P.; Chen, J.; Vaughan, M. T.; Weidner, D. J. *Chem. Mater.* **2001**, *13*, 487–490

[289] Baláž, P. *Mechanochemistry in Nanoscience and Minerals Engineering*, Springer-Verlag: Berlin, Germany, 2008.

[290] Cao, S.; Bennett, T. D.; Keen, D. A.; Goodwind, A. L.; Cheetham, A. K. *Chem. Commun.* **2012**, *48*, 7805–7807.

[291] Bennett, T. D.; Saines, P. J.; Keen, D. A.; Tan, J.-C.; Cheetham, A. K. *Chem. Eur. J.* **2013**, *19*, 7049–7055.

[292] Urakaev, F. K.; Boldyrev, V. V. *Powder Technol.* **2000**, *107*, 93–107.

[293] Urakaev, F. K.; Boldyrev, V. V. *Powder Technol.* **2000**, *107*, 197–206.

[294] Machon, D.; Meersman, F.; Wilding, M. C.; Wilson, M.; McMillan, P. F. *Progr. Mater. Sci.* **2014**, *61*, 216–282.

[295] Šepelák, V., Bégin-Colin, S.; Le Caër, G. *Dalton Trans.* **2012**, *41*, 11927–11948.

[296] Kipp, S.; Šepelák, V.; Becker, K. D. *Chem. unserer Zeit* **2005**, *39*, 384–392.

[297] Xu, H.; Zeiger, B. W.; Suslick, K. S. *Chem. Soc. Rev.* **2013**, *42*, 2555–2567.

[298] Cliffe, M. J., Mottilo, C., Stein, R.S., Bučar, D.-K. & Friščić, T. *Chem. Sci.* **2012**, *3*, 2495–2500.

[299] Ziadeh, M.; Chwalka, B.; Kalo, H.; Schütz, M. R.; Breu, J. *Clay Miner.* **2012**, *47*, 341–353.

[300] Schnatz, R. *Int. J. Min. Proc.* **2004**, *74*, S55–S63.

[301] Clermont, B.; de Haas B. *J. S. Afr. Inst. Min. Metall.* **2010**, *110*, 133–140.

[302] Takacs, L. *Chem. Soc. Rev.* **2013**, *42*, 7649–7659.

[303] Willart, J. F.; Descamps, M. *Mol. Pharmaceutics* **2008**, *5*, 905–920.

[304] Wang, H.; Xu, B.; Smith, P.; Davies, M.; DeSilva, L.; Wingate, C. *J. Phys. Chem. Solid* **2006**, *67*, 2567–2582.

[305] Brantut, N.; Schubnel, A.; Rouzaud, J.-N.; Brunet, F.; Shimamoto, T. *J. Geophys. Res.* **2008**, *113*, B10401.

[306] Kim, H., N.; Lee, S. K. *Am. Min.* **2014**, *99*, 1996–2007.

[307] Tian, F.; Qu, H.; Louhi-Kultanen, M.; Rantanen, J. *Chem. Eng. Technol.* **2010**, *33*, 833–839.

[308] Zhang, Q.; Kasai, E.; Saito, F. *Powder Technol.* **1996**, *87*, 67–71.

[309] Loerting, T.; Giovambattista, N. *J. Phys.: Condens. Matter* **2006**, *18*, R919–R977.

[310] Tanaka, H.; Kurita, R.; Mataki, H. *Phys. Rev. Lett.* **2004,** *92***,** 025701.

[311] Kurita, R.; Tanaka, H. *Science* **2004,** *306***,** 845–848.

[312] Scarlett, N. V. Y.; Madsen, I. C. *Powder Diffraction* **2006**, *21*, 278–284.

[313] Scardi, P.; Leoni, M. *Acta Crystallogr., Sect. A* **2002**, *58*, 190–200.

[314] Cheary, R. W.; Coelho, A. *J. Appl. Cryst.* **1992**, 25, 109–121.

[315] Birch, F. *J. Geophys. Res. Solid* **1986**, *91*, 4949–4954.

[316] Mishra, A; Kad, B; Gregori, F; Meyers, M. *Acta Mater.* **2007**, *55*, 13–28.

[317] Pradell, T.; Crespo, D.; Clavaguera, N.; Clavaguera-Mora, M. T. *J. Phys.: Condens. Matter* **1998**, *10*, 3833–3844.

[318] Etzrodt, G. *Ullmann's Encyclopedia of Industrial Chemistry*, Wiley-VCH: Weinheim, Germany, 2011.

[319] Wenig, D.; Jokiel, P.; Uebleis, A.; Boehni, H. *Surf. Coatings Technol.* **1997**, *88*, 147–156.

[320] Pameijer, C. H. *Int. J. Dent.* **2012**, *752861*, 1–7.

[321] Hill, E. E.; Lott, J. *Austr. Dent. J.* **2011**, *56*, Suppl. 67–76.

[322] Davidson, C. L. *Adv. Eng. Mater.* **2001**, *3*, 763–767.

[323] Dove, P. M.; Han, S.; Wallace, A. F.; DeYoreo, J. J. *Proc. Natl Acad. Sci U.S.A.* **2008**, *105*, 9903–9908.

[324] Becker, A.; Bismayer, U.; Epple, M.; Fabritius, H.; Hasse, B.; Shi, J.; Ziegler, A. *Dalton Trans.* **2003**, *4*, 551–555.

[325] Shakhvorostov, D.; Nicholls, M. A.; Norton, P. H.; M.H. Müser, M. H. *Eur. Phys. J. B* **2010**, *76*, 347–352.

[326] Brow, R. K. *J. Non-Cryst. Solids* **2000**, *263–264*, 1–28.

[327] Schüth, F. *Chem. Mater.* **2001**, *13*, 3184–3195.

[328] Cheetham, A. K.; Rao, C. N. R.; Feller, R. K. *Chem. Commun.* **2006**, 4780–4795.

[329] Mosey, N. J.; Müser, M. H.; Woo, T. K. *Science* **2005**, *307*, 1612–1615.

[330] Shakhvorostov, D.; Müser, M.H.; Mosey, N. J.; Song, Y.; Norton, P. R. *Phys. Rev. B* **2009**, *79*, 094107.

[331] Pawlak, Z.; Yarlagadda, P. K.; Hargreaves, D.; Frost, R. L.; Rauckyte, T.; Zak, S *J. Achiev. Mater. Manufact. Eng.* **2009**, *33*, 35–40.

[332] Šepelák, V.; Düvel, A.; Wilkening, M.; Becker, K. D.; Heitjahns, P. *Chem. Soc. Rev.* **2013**, *42*, 7507–7520.

[333] Bennett, T. D.; Cao, S.; Tan, J. C.; Keen, D. A.; Bithell, E. G.; Beldon, P. J. *J. Am. Chem. Soc.* **2011**, *133*, 14546–14549.

[334] James, S. L.; Adams, C. J.; Bolm, C.; Braga, D.; Collier, P.; Friščić, T., Grepioni, F.; Harris, K. D. M.; Hyett, G.; Jones, W.; Krebs, A.; Mack, J.; Maini, L.; Orpen, A. G.; Parkin, I. P.; Shearouse, W. C.; Steed, J. W.; Waddel, D. C. *Chem. Soc. Rev.* **2012**, *41*, 413–447.

[335] Boldyrev, V. V. *Russ. Chem. Rev.* **2006**, *75*, 177–189.

[336] Šepelák, V.; Bergmann, I.; Indris, S.; Feldhoff, A.; Heitjans, P.; Becker, K. D. *Transworld Research Network, Kerala* **2010**, 191–206.

[337] Bégin-Colin, S.; Le Caër, G.; Mocellin, A.; Zandona, M. *Philos. Mag. Lett.* **1994**, *69*, 1–7.

[338] Bégin-Colin, S.; Le Caër, G.; Zandona, M.; Bouzy, E.; Malaman, B. *J. Alloys Compd.* **1995**, *227*, 157–166.

[339] Boldyrev, V. V.; Lyakhov, N. Z.; Pavlyukhin, Yu. T.; Boldyreva, E. V.; Ivanov, E. Yu.; Avvakumov, E. G. *Sov. Sci. Rev. B. Chem.* **1990**, *14*, 105–161.

[340] Gateshki, M.; Petkov, V.; Williams, G.; Pradhan, S. K.; Ren, Y. *Phys. Rev. B* **2005**, *71*, 224107.

[341] Štefanić, G.; Musić, S.; Gajović, A. *Mater. Res. Bull.* **2006**, *41*, 764–777.

[342] Pawlig, O.; Schellenschläger, V.; Lutz, H. D.; Trettin, R. *Spectrochim. Acta A Mol. Biomol. Spectrosc.* **2001**, *57*, 581–590.

[343] Zedler, L.; Hager, M. D.; Schubert, U. S.; Harrington, M. J.; Schmitt, M.; Popp, J.; Dietzek, B. *Mater. Today* **2014**, *2*, 57–69.

[344] Thomas, I. M.; Weller, M. T. *J. Mater. Chem.* **1992**, *2*, 1123–1126.

[345] Baran, E. J.; Nord, A. G.; Diemann, E. *J. Phys. Chem. Solids* **1989**, *50*, 983–984.

[346] Sørensen, M. B.; Hazell, R. G.; Bentien, A.; Bond, A. D.; Jensen, T. R. *Dalton Trans.* **2005**, *3*, 598–606.

[347] Hill, R. J. *J. Appl. Crystallogr.* **1976**, *9*, 503–504.

[348] Tong, T.; Zhang, J.; Tian, B.; Chen, F.; He, D. *J. Hazard. Mater.* **2008**, *155*, 572–579.

[349] Karmakar, D.; Mandal, S. K.; Kadam, R. M.; Paulose, P. L.; Rajarajan, A. K.; Nath, T. K.; Das, A. K.; Dasgupta, I.; Das, G. P. *Phys. Rev. B* **2007**, *75*, 144404.

[350] Grätzel, M.; Howe, R. *J. Phys. Chem.* **1990**, *94*, 2566–2572.

[351] Wang, J.; Toby, B. H.; Lee, L. P.; Ribaud, L.; Antao, S.; Kurtz, C.; Ramanathan, M.; von Dreele, R. B.; Beno, M. A. *Rev. Sci. Instrum.* **2008**, *79*, 085105.

[352] Lee, P. L.; Shu, D.; Ramanathan, M.; Preissner, C.; Wang, J.; Beno, M. A.; von Dreele, R. B.; Ribaud, L.; Kurtz, C.; Antao, S. M.; Jiao, X.; Toby, B. H. *J. Synchr. Rad.* **2008**, *15*, 427-432.

[353] Dalesio, L. R.; Hill, J. O.; Kraimer, M.; Lewis, S.; Murray, D.; Hunt, S.; Watson, W.; Clausen, M.; Dalesio, J. *Nucl. Instrum. Methods Phys. Res., Sect. A* **1994**, *352*, 179-184.

[354] Bach, S. *Charakterisierung von amorphen Cobaltphosphathydraten und Zinkphosphathydraten*. Diploma Thesis., Johannes Gutenberg University of Mainz, 2012.

[redacted]

CURRICULUM VITAE

[redacted]